Department of Chemical and Environmental Engineering

CONTROLLABLE SYNTHESIS FOR FABRICATION OF MICRO/NANO-STRUCTURED MESOPOROUS PRECURSOR PARTICLES FOR HIGH PERFORMANCE LITHIUM-ION BATTERIES

By

Bin DONG BEng MSc (Hon)

Thesis submitted to the University of Nottingham for the degree of Doctor of Philosophy

January 2018

Abstract

Increasingly global warming and air pollution caused by the consumption of fossil fuel have imposed the priority of using green energy. As a result, the use of rechargeable lithium-ion batteries (LIBs) has increased rapidly

Olivine-structured $LiFePO_4$ is considered as one of the most promising positive electrode materials owing to its significant advantages of nontoxicity, low cost of raw materials, good structural stability at high temperature, excellent safety performance, and relatively high theoretical specific capacity (170 $mAhg^{-1}$) with a flat discharge-charge potential (3.45V vs. Li^+/Li). Therefore, $LiFePO_4$ battery becomes a reliable material for energy storage system used in hybrid electric vehicles (HEVs), full electric vehicles (EVs), plug-in hybrid electric vehicles (PHEVs), and portable devices. However, the poor rate performance of $LiFePO_4$, resulting from its intrinsic low Li^+ diffusivity (10^{-17} to 10^{-14} cm^2s^{-1}) and low electronic conductivity (10^{-9} to 10^{-8} S cm^{-1}), has become a technical bottleneck to confine its widely practical applications.

Following previous studies, a systematic study on controllable preparation of $LiFePO_4$ positive electrode material with nanoscale size, or hierarchical micro/nano mesoporous structure has been carried out using various synthesis methods, including impinging stream reaction (ISR), ultrasonic-intensified impinging stream reaction (UISR), two-step co-precipitation method, and two-step hydrothermal method (UIHT). The physical and chemical properties of as-synthesized products are measured by XRD, FTIR, SEM, TEM, BET, Mastersizer, CV, and charge-discharge test. Based on these observations, the relationship

among particle morphology, electrochemical performance, and impacts of fluid dynamics is evaluated in this work.

Preface

This work reported in this PhD thesis is solely the work of the author and has not been published elsewhere except for the following parts:

Journal papers:

Dong B., Li G.*, Yang X.* Chen L., and Chen G.Z., 2018, Controllable Synthesis of $(NH_4)Fe_2(PO_4)_2(OH)\cdot 2H_2O$ Using Two-Step Route: Ultrasonic-intensified Impinging Stream Pre-treatment Followed by Hydrothermal Treatment, Ultrasonics Sonochemistry, 42, 452-463.

Dong B., Huang X., Yang X.*, Li G., Xia L., and Chen G.Z., 2017, Rapid Preparation of High Eletrochemical Performance $LiFePO_4$/C Composite Cathode Material with an Ultrasonic-intensified Micro-impinging Jetting Reactor, Ultrasonics Sonochemistry, 39, 816-826.

Ezeh I.C., Dong B., Yang X., Sun C., Snape C., Facile Synthetic Route, Calcination Temperature and Heating Rate: Study on Optimum Thermal Performance of CuO/ZrO_2 Catalysts for Methanol Synthesis (Under Review).

Conferences:

Dong B., Li G., Xia L., Chen G.Z. and Yang X.G.*," Synthesis of $FexMn_{1-x}PO_4$ (x = 1, 0.96, 0.93, and 0.90) nanocomposites by Ultrasound-intensified Impinging Stream Microreactor" AEMC 2018, Stockholm Sweden, 25-28 March 2018.

Dong B., Li G., Xia L., Chen G.Z. and Yang X.G. *," Mesoscale Investigation of Hierarchical Micro/Nano-structured porous $FePO_4$ and $LiFePO_4$ prepared by a

two-step heterogeneous growth technology" CIESC 2017, Beijing China, 14-15 October 2017.

Dong B., Li G., Xia L., Zhang J.W., Ni C., Song M.X., Wang P.C., Chen G.Z. and Yang X.G.*, Synthesis By Two-step Growth Scheme For Fabrication of Hierarchical Micro/Nano-structured Mesoporous $FePO_4$ Particles for High Performance Lithium-Ion Batteries, Nanotech 2017 Conference & Expo, Washington D.C. USA, 14-17 May 2017.

Dong B., Li G., Xia L., Chen G.Z. and Yang X.G.*, Synthesis of $FePO_4 \cdot 2H_2O$ nanocomposites for fabrication of Lithium Ion Battery using impinging stream reactor, 14th International Conference on Nanomaterials and Nanotechnology, Madrid Spain, 30-31 March 2017.

Chinese Patents:

1. Yang X.G., Dong B. and Li G., A Method to Prepare Near-Spherical Mesoporous FePO4 precursor and $LiFePO_4$ Positive Electrode Materials, Application number: 2017103872903

2. Yang X.G., Dong B. and Li G., Controllable Synthesis of $Fe_2(NH_4)(OH)(PO_4)_2(H_2O)_2$ and $FePO_4$ for High Performance Lithium-ion Batteries by Two-step Hydrothermal Method, Patent number: CN107275593 A

3. Yang X.G., Dong B. and Li G., Synthesis of Hierarchical Micro/Nano-structured Porous $FePO_4$ for High Performance Lithium-ion Batteries Using a Two-step Co-precipitation Method, Patent number: CN106876700 A

Acknowledgements

Firstly, I would like to thank my supervisors, Professor Xiaogang Yang, Professor George Zheng Chen, and Dr. Guang Li for their wisdom, patience and guidance during my entire PhD study.

Special thanks to all members of the Chemical and environmental Engineering Departments, most especially Dr. Jun He, Dr. Jie Yang, Dr. Lan Xia, Dr. Linpo Yu, Dr. Di Hu, Dr. Bencan Tang, Dr. Binjie Hu and Dr. Chenggong Sun for their kind supports and advices.

A greater appreciation goes to all the members in Flow and Surface Transport (FAST) and Electrochemical Technology (ETG) groups, most especially Dr. Yiyi Wu. Dr. Luming Chen, Dr. Ezeh Collins I., Mr. Weibin Shi, Mrs. Xiani Huang, Mr. Chenyang Xue, Miss Lu Liu, Miss Yanqing Guo, Miss Xinyue Cai, Mr. Bin Li, Mr. Xingyi Qian, Mr. Bamidele Akinwolemiwa and Miss Chaohui Wei, for their unfathomable supports.

I would like to thank Jane Zhang, Julian Zhu, Helen Xu, Karey Shan, John Xu, Xiao Hua, Guanghua Yang, and Keli Zhang for their expertise and support during the entire project.

I also appreciate the financial support from the funding institutions: International Doctoral Innovation Centre (IDIC), National Natural Science Foundation of China (NSFC) (Grant No. 21576141, 91534118), Zhejiang Provincial Natural Science Foundation (Grant No. LY15B060001), Engineering and Physical Sciences Research Council (Grant No. EP/J000582/1, GR/R68078) and Ningbo Municipal Government (3315 Plan, 2014A35001-1).

I would also like to thank all my friends, especially Dr. Ning Xue, Dr. Jingsha Xu, Dr. Yao Li, Dr. Feicheng Wang, Min Hui Yap, Zheng Lian, Bin Wang, Chaohui Wei, Yanfei Xiong, Jiawei Zhang, Liming Xu, Zeping Wang, and Zhibin Ma. It will be very boring without them during PhD study.

Finally and most importantly, I would like to express my love and appreciation to my wife—Mrs. Xiangting Yin, my parents, and my parents-in-law for their immense support and encouragement. Without their love, support, and encouragement, I will not be this inspired.

Table of Contents

List of Figures

Chapter 1

Chapter 2

Chapter 3

Chapter 4

Chapter 5

Chapter 6

List of Tables

Chapter 2

Chapter 3

Chapter 4

Chapter 5

Chapter 6

List of Abbreviations and Symbols

Abbreviations:

LIBs	Lithium-Ion Batteris
HEVs	Hybrid Electric Vehicles
EVs	Electric Vehicles
PHEVs	Plug-in Hybrid Electric Vehicles
PSD	Particle Size Distribution
RT	Room Temperature
SEI	Solid Electrolyte Interface
LIS	Liquid-continuous Impinging Streams
CFD	Computational Fluid Dynamics
PLIF	Planar Laser Induced Fluorescence
MRT	Micro Reaction Technology
CV	Cyclic Voltammetry
EIS	Electrochemical Impedance Spectroscopy
PEG	Polyethylene Glycol
CTAB	Hexadecyltrimethylammonium Bromide
HSM	High Shear Mixer
CI	Conventional Impeller
FP	$FePO_4$
LFP	$LiFePO_4$
SEM	Scanning Electron Microscope
TEM	Transmission Electron Microscope
XRD	X-ray Diffraction
BET	Brunauer Emmett Teller
FTIR	Fourier transform infrared spectroscopy
PTFE	Polytetrafluoroethylene
UIHT	Ultrasound-assisted CITJ and hydrothermal treatment
CITJ	Confined impinging T-jet mixer

Symbols

L	Diffusion distance
T:	Intercalation time of lithium ion within electrode
D	Diffusion coefficient
R_m	Electrode resistance per unit mass
k	Specific reaction rate constant
Q	Volumetric feeding rate
D_{eddy}	Eddy diffusivity of the reactant solutions
λ	Kolmogorov length
t_M	Micromixing time
ε	Micromixing turbulent energy dissipation rate
ν_{ms}	Kinematic viscosity of the mixed solution,
α	The ratio of the volumetric flow rate
P	Input power
P_{IS}	Input power for impinging stream
P_{UI}	Input power for ultrasonic irradiation
V_T	Mixing volume of the T-type micromixer
ρ	Densities of the impinging stream solutions
u	Velocity of stream
ξ_T	Local loss coefficient
q_T	Discharge ratio
φ	Ratio of the cross-sectional areas of the inlet 1 to outlet
t_R	Mean residence time
t_M	Micromixing homogenization time
t_N	Nucleation time
k_l	Mass transfer coefficient
C_o	Reagent initial concentration
d_{32}	Mean diameter over the surface distribution, also called Sauter mean diameter
F_c	Shape factor
d_{43}	Mean diameter over the volume distribution

$\boldsymbol{P}$	pressure drop in the impinging stream reactor
$\boldsymbol{n}$	Rotation speed (rps)
$\boldsymbol{Da}$	Impeller diameter
$\boldsymbol{\rho}$	Density of reaction solution
$\boldsymbol{m}$	Mass of solution in the reactor
$\boldsymbol{N_P}$	N_P Power number

CHAPTER 1: Current Status of Controllable Synthesis of Lithium-ion Battery Electrode Precursor Materials and Fabrication Approaches

1.1 Lithium ion battery

1.1.1 Introduction

Increasingly global warming and air pollution caused by the consumption of fossil fuel have imposed the priority of using green energy. As a result, the use of rechargeable lithium-ion batteries (LIBs) has increased rapidly (Shu *et al*., 2013; Gibot *et al*., 2008). The research about lithium ion battery was begun from 1950s due to the stability of lithium metal in a number of non-aqueous electrolytes. In 1992, Sony firstly introduced lithium ion battery into market.

Compared with other commercial positive electrode materials, such as $LiCoO_2$, $LiNiO_2$, $LiMn_2O_4$ and their derivatives, olivine-structured $LiFePO_4$ is considered as one of the most promising positive electrode materials owing to its significant advantages of nontoxicity, low cost of raw materials, good structural stability at high temperature, excellent safety performance, and relatively high theoretical specific capacity (170 $mAhg^{-1}$) with a flat discharge-charge potential (3.45V vs. Li^+/Li) (Ding *et al*.,2010; Park *et al*., 2003; Padhi *et al*.,1997). Therefore, $LiFePO_4$ battery becomes a reliable material for energy storage system used in hybrid electric vehicles (HEVs), full electric vehicles (EVs), plug-in hybrid electric vehicles (PHEVs), and portable devices (Dai *et al*.,2010) . However, the

poor rate performance of LiFePO4, resulting from its intrinsic low Li^+ diffusivity (10^{-17} to 10^{-14} cm^2s^{-1}) and low electronic conductivity (10^{-9} to 10^{-8} S cm^{-1}), has become a technical bottleneck to confine its widely practical applications (Shin *et al*., 2008; Chung, Bloking and Chiang, 2002; Guo *et al*.,2015) before these drawbacks being overcome fundamentally.

1.1.2 Methods to overcome drawbacks

Fe-based lithium ion battery has been considered as reliable energy storage material. However, some drawbacks, including poor intrinsic electronic conductivity (10^{-9} to 10^{-8} S cm^{-1}), ionic conductivity (10^{-11} to 10^{-9} S cm^{-1}) and ionic diffusivity (10^{-17} to 10^{-14} cm^2 s^{-1}) affect the application of $LiFePO_4$ in high-rate lithium ion batteries significantly (Shin *et al*.,2008; Wang *et al*.,2005). Surface and interface engineering have been used to improve the low intrinsic electronic conductivity, including the reduction of particle size and particle size distribution (PSD) (Saravanan *et al*.,2009; Choi and Kumta, 2007), controlling the particle morphology, introducing porous and hierarchical structure (Wang, Li and Chen, 2015), coating the particles with fine electronic conductive materials (Shi *et al*., 2012; Zhang *et al*., 2011; Park *et al*., 2004; Hu *et al*., 2007), or doping with selective supervalent cations (Shu *et al*., 2013; Bilecka *et al*., 2011; Wang *et al*., 2008; Ge *et al*., 2010) .

Size effect

The low ionic diffusivity of lithium ion in battery system leads to that large amount of lithium ion will stay on the interface of electrode particles and electrolyte, result in relatively low mass-transport efficiency and rate capacity

(Wang, Li and Chen, 2015). The improvement on the active surface will help to generate more paths for lithium ion, and increase the permeation of lithium ion between solid electrode and electrolyte.

Wang *et al.* (2010) and Zhou *et al.* (2005) have demonstrated the diffusion of lithium ions within the electrode materials is influenced by both diffusion coefficient and diffusion distance. The relationship between intercalation time of lithium ion within electrode and diffusion distance is as follows:

$$L = (Dt)^{1/2} \rightarrow t = \frac{L^2}{D}$$

where L is diffusion distance; t is intercalation time of lithium ion within electrode; D is diffusion coefficient, which is constant for a particular material.

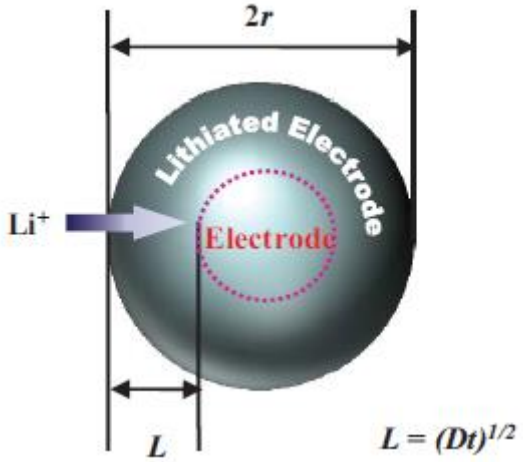

Figure 1- 1 Schematic representation of the effective diffusion length in electrode-active materials (Wang, Li and Chen, 2015).

In this equation, diffusion coefficient D is constant for each material, so that the decrease of diffusion distance of lithium ion is an effective method to reduce diffusion time and improve rate capacity. As ionic conductivity of $LiFePO_4$ (10^{-11}-

10^{-10} S cm^{-1} at RT) is much lower than its electronic conductivity (>10^{-9} S cm^{-1} at RT), Gaberscek *et al*. (2007) have found the reduction of diffusion distance, or minimization of particle size, can improve electrochemical performance more significantly than carbon coating. They evaluated the publications from nine different groups and found an empirical law which can imply the correlation between $LiFePO_4$ particle size and the electrode resistance. Based on this investigation, they found that there is a square correlation between electrode resistance and particle size: $R_m \propto d^n$ (n=1.994). And particle size minimization is more sufficient to improve electrochemical performance for $LiFePO_4$.

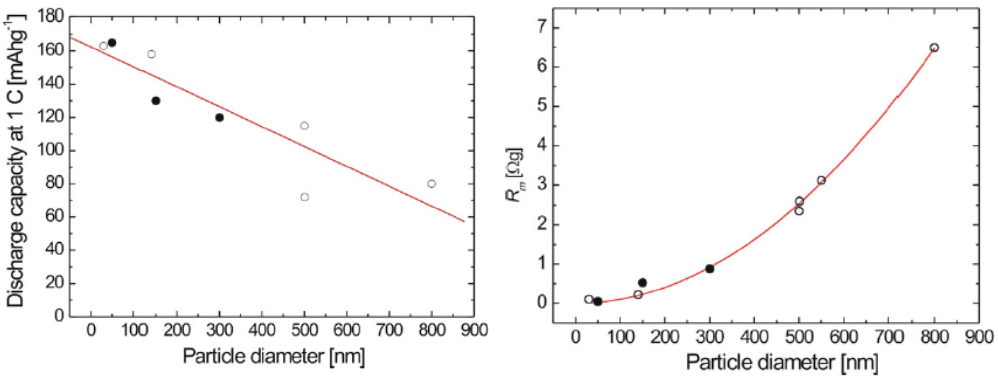

(a) (b)

Figure 1- 2 (a) Discharge capacity as a function of average particle diameter of various $LiFePO_4$ samples and linear regression of the data indicating that the capacity drops linearly with increasing particle diameter (solid line). (b) Dependence of electrode resistance per unit mass, R_m, on average particle diameter of various $LiFePO_4$ samples and NLS fit of the data using a general power law relationship based on the equation: $R_{m,exp} = Ad^n$. The values of fitting parameters are: $A = 9.620 \times 10^{12} \Omega\, g\, m^{-n}, n = 1.994$

Pore effect

Materials with porous structure have been widely used in different areas, including catalysis, adsorption and separation, gas storage and sensing (Schüth, 2005). Electrode materials, such as $LiFePO_4$, can profit from porous structure and have drawn attention in the past decade. Vu *et al.* (2012) had summarized important benefits of porous electrode:

- Porousity can create more channels and provide good access of the electrolyte to the electrode surface, as well as facilitating the penetration of electrolyte inside the electrode.
- Porousity can improve specific surface area of electrode material, provide a large electrode/electrolyte interface and ensure an effective charge transfer across the interface.
- The diffusion distances for lithium ion is reduced by the very thin active material (nanometers to tens of nanometers) surrounding the pores.
- The utilization of active material is increased effectively by the small feature sizes, and leading to improved specific capacities, especially at high charge/discharge rates.
- The bicontinuous effect of active phase (walls) and electrolyte phase (pores) in porous electrode can provide continuous transport pathway for lithium ion.
- Porous structure has negative influence on tap density and volumetric capacity of an electrode, there are still some examples that porosity can increase volumetric capacity compared to packed nanoparticles which caused by a better inter-particle contact.

Based on the synthesis method, porous materials can be classified as template and non-template (Wan, Shi and Zhao, 2007; Hatton *et al*., 2005; Lu and Schuth, 2006; Stein, Li and Denny, 2008; Jeffryes *et al*., 2011).

According to the pore size, porous materials can be classified as micropores <2nm, mesopores 2-50 nm, and macropores >50nm. And different pore size influences the performance of electrode significantly. Micropores can provide larger specific surface area. However, the small size of pores leads to narrow channels and restricting the moving of electrolyte. Doherty *et al*. (2010) demonstrated that high micropore concentration limited conductivity of electrode. While Lee *et al.* (1993) found that positive electrode pore diameter influenced the utilization of positive electrode significantly. The electrode utilization can benefit from a higher porosity electrode materials at high discharge rate. However, volumetric energy density may be decreased by large pore size. Therefore, it is necessary to identify the optimal pore size range. In addition, the electrode with uniform pore size can optimize the open volume and lead to better mass transport without wasted space (Jiao *et al*., 2008).

Structural Hierarchy Effect

Hierarchical structure was usually referred as micro/nanoscale aggregates with well-defined morphologies through self-assembling of smaller blocks, including nanorods, nanoflakes, nanowires, nanoparticles, and nanoplates (Lakes, 1993; Chen, Kuang, and Su, 2012). Generally, hierarchical structure can provide smaller primary grains, higher specific surface area, larger void spaces, and accessible porous system. It can help to enhance mass diffusion on the interface between electrolyte and electrode, shorten diffusion distance of Li ions, improve cycling

stability, and retain relatively high tap density. Therefore, previous researchers have synthesised electrode materials with hierarchical structure through careful control of reaction and rational selection of reactants (Uchiyama *et al*., 2009; Wu, Wen, and Li, 2011; Sun *et al*., 2011; Jin *et al*., 2011; Saravanan *et al*., 2010; Yuan *et al*., 2011; Li, Fu, and Su, 2012; Fang *et al*., 2013).

Surface Modification and Functionalization

LiF_6-based electrolyte is widely used in lithium ion battery. The decomposition reaction of LiF6 is inevitable and generates PF_5 and LiF. PF_5 is strong Lewis acid, which can react with water and release HF. HF will attack active material and affect electrochemical performance of electrode materials (Edström, Gustafsson and Thomas, 2004).

The energy separation of highest occupied molecular orbital (HOMO) and lowest unoccupied molecular orbital (LUMO) determines the electrochemical potential windows of electrolytes (Goodenough and Kim, 2010). Electrolyte will be oxidized if the electrochemical potential of cathode is below HOMO, as well as it will be reduced if electrochemical potential of anode is above LUMO. The electrochemical potential of electrode should be within the window of electrolyte to maintain the thermodynamic stability. Otherwise passivation layer will be generated on the electrode and block the electron transfer from the electrolyte HOMO to the cathode or from the anode to the electrolyte LUMO. A solid electrolyte interface (SEI) thin films (insoluble ionic Li compounds) can be generated on the electrode surface from the oxidation or reduction of non-aqueous electrolyte molecules. SEI can help to increase the stability of electrolyte and electrode, but if its thickness exceeds tunnelling capacity of electrons, SEI will

block efficient mass transport into active electrode, and affect rate performance (Lee *et al.,* 2014). Therefore, it is essential to modify or functionalize the electrode. Wang *et al*. (2014) has summarized the advantages, which include:

- Suppress the surface reactions between HF and active materials
- Alleviate the decomposition of electrolyte
- Improve ionic and electronic conductivities of the electrode
- Accommodate the huge volume change upon cycling
- Modify the electrochemical properties of SEI films

HF can attack active electrode material, dissolve transition metal cations, lessen the electrical contact of the particles with the conducting work, and leading to the fading of electrode capacity (Myung, Amine and Sun, 2010). Metal oxides (Al_2O_3, ZrO_2, TiO_2, B_2O_3, MgO, $Li_2O{\cdot}2B_2O_3$), fluorides (AlF_3), and organic compounds (PEDOT, polypyrrole, PPy doped with PEG) have been applied to modify the surface of electrode materials to suppress the attack from HF, and leading to improved cycleability and capacity retention (Meng, Yang and Sun, 2012; Zhao and Wang, 2013) . The reasons are that, metal oxides can react with HF and transform into fluoride layer. This fluoride layer is resistant to HF and prevents the attack from HF attack. Fluoride coating which is inactive to HF has the same effect. Therefore, metal oxides and fluoride can protect active materials and reduce interfacial charge transfer resistance. Electrochemically stable organic compounds with good electronic conductivity can be coated on the surface of electrode and restrain the side reaction. Apart from that, most of these organic compounds are conductive polymers and can assist to generate highly continuous surface with controllable nanoscale thickness.

The ionic conductivity of electrode materials determines rate capacity. Comparing to metal oxides, fluorides (AlF_3), and organic compounds, the coating surface of amorphous lithium phosphate compounds can not only suppress side surface reaction, but also improve lithium-ion conductivity. Because most of metal oxides, fluorides (AlF_3), and organic compounds coating are insulators for lithium ion conduction, and lithium phosphates is electrochemically stable lithium-ion conductors and they can form surface protect layer.

1.1.3 Research Aims and Objectives

Therefore, to prepare $LiFePO_4$ particle with nanoscale primary grains, meso-porous, and hierarchical structure, which can guarantee this positive electrode material have both excellent electrochemical performance and high tap density, it is necessary to control crystallisation process. The crystallization (or precipitation) process of particles is consisted of two consecutive steps: nucleation and particle growth. The particle size, distribution, shape unpredictability, and purity of particles are affected by both nucleation and particle growth steps significantly (Kulmala, 2003; Dirksen and Ring, 1991).

It has been recognised that rapid and homogeneous micromixing of feeding streams would be beneficial to the preparation of nanoparticles. However, a rapid micromixing is very difficult to be realised when employing the traditional stirring reactor due to the poor mixing and mass transfer performance (Baldyga, Bourne and Hearn, 1997; Bhattacharya and Kresta, 2004). However, impinging stream and ultrasound irradiation have important impacts on micromixing during nucleation process.

Agglomeration is an important procedure in crystallization and involved in the process of powder production, separation, and purification. During powder production process, agglomeration influences the particle size, distribution, and shape unpredictability. Moreover, agglomerate particles may contain impurities which are from mother liquor, and affect the purification process negatively. Many researches have demonstrated that physical adhesion of the crystals (aggregation) and molecular growth of the aggregates are two consecutive steps in agglomeration mechanism (Ilievski and White, 1994; Ilievski and Hounslow, 1995; Ilievski and White, 1995; Kucher *et al.*, 2006; Brunsteiner *et al.*, 2004). Based on the different physic-chemical characteristics of the crystal material, agglomeration process is dictated by different factors, including turbulent agitation (agitation speed), supersaturation, and salt addictive. Turbulent fluid motion of the suspension leads to crystal collision, breaking and re-dispersion of the adhered crystals, and the promoting of mass transfer for molecular growth. In many cases, there is a certain agitation speed which agglomerate particle size increases when increasing the agitation speed until to this certain speed, then decreases with any further increase of the agitation speed (Sung *et al.*, 2000; Wojcik and Jones, 1998; Kim *et al.*, 2004). Supersaturation can generate a large population of particles, inducing that the possibility of crystal collisions is increasing in an agitated suspension (Wojcik and Jones, 1997; Jung *et al.*, 2000). Thus the molecular growth can be facilitated and lead to the producing of large agglomerate particles. Salt addictive can also control agglomeration (Kucher *et al.*, 2006). The principle is that, crystals can adsorb salt ions, cause the creation of a surface charge and induce a repulsive interaction among the crystals, results in the inhibiting of crystal agglomeration and reducing of the agglomerated particle size.

Additionally, the polarity of crystal also influences agglomeration. Crystals are significantly agglomerated when using low polar solvent. On the contrary, the crystal agglomeration is reduced as the increasing of solvent polarity, due to the inhibition of crystal adhesion, which caused by the strongly adsorbing of polar solvent on the crystals (Alander and Rasmuson, 2007; Alander *et al.*, 2003). Many methods have been developed to prepare micro-sized $LiFePO_4$, including co-precipitation, sol-gel method, solid state reaction, hydrothermal synthesis, spray pyrolysis, and some other methods. In this study, we focus on hydrothermal and co-precipitation methods.

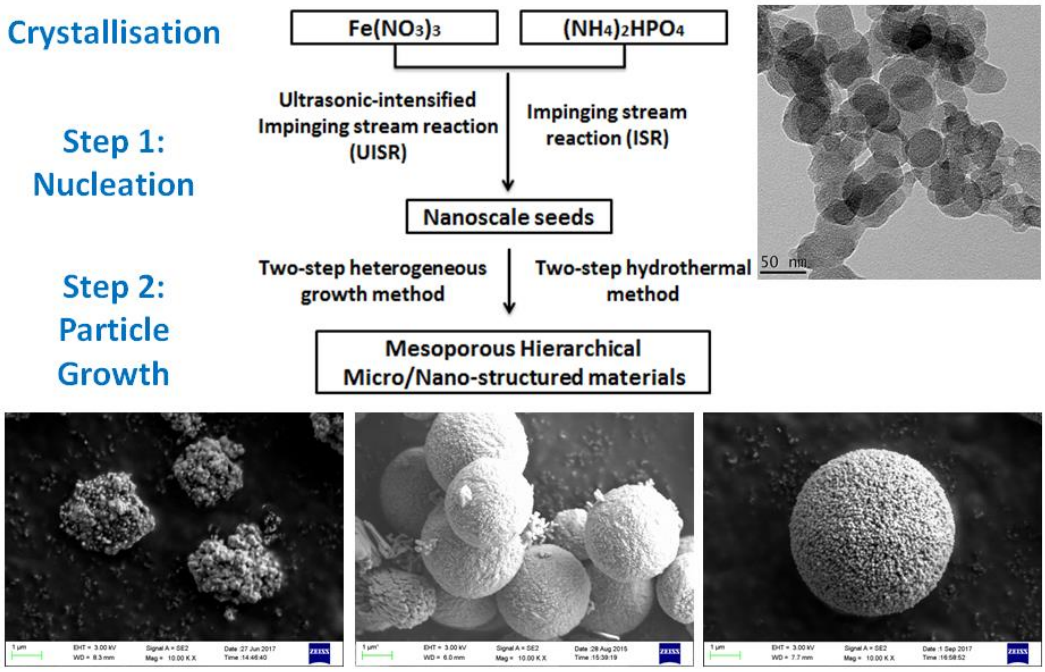

Figure 1-3 Schematic illustration of main procedures and technologies used in this work.

Therefore, in this work, we tried to controllable synthesise $LiFePO_4$ with nanoscale primary grains, meso-porous, and hierarchical structure. Meanwhile, the effects of different technologies (including impinging stream reaction, ultrasonic

irradiation, hydrothermal reaction, and co-precipitation) affect particle size, distribution, shape unpredictability, purity, and electrochemical performance of as-synthesised samples in nucleation and particle growth processes were systematically investigated respectively. A brief schematic illustration (Figure 1-3) is used to show the main procedures and technologies in this work.

1.2 Impinging Stream Reaction

It has been recognised that rapid and homogeneous micromixing of feeding streams would be beneficial to the preparation of nanoparticles. However, a rapid micromixing is very difficult to be realised when employing the traditional stirring reactor due to the poor mixing and mass transfer performance (Baldyga, Bourne and Hearn, 1997; Bhattacharya and Kresta, 2004). Some micromixers, such as impinging jet stream reactor and T-type micromixer, have been proved to be able to significantly intensify the mixing, especially micromixing, within extremely short time. Thus it has been applied for the preparation or synthesis of catalysts (Zhang *et al.*, 2015; Zhang *et al.*, 2016), chitosan (Huang *et al.*, 2015), light conversion materials (Zhou, Liu and Liu, 2012), drugs (valente *et al.*, 2012), and energy storage materials (Xiao *et al.*, 2013; Yan *et al.*, 2013). Generally, impinging stream reactor and T-mixer are simplest component that two inlet tubes and one outlet tube join the main channel (Yan *et al.*, 2015; Krupa *et al.*, 2014). The difference between impinging stream reactor and T-mixer is that, impinging jet stream reactor has sufficient space in outlet so that pressure energy can be released and translated in kinetic energy. In these components, a local intensive micro-mixing can be generated by the collision between two high speed impinging streams. The existing understanding to the impinging streams has

revealed that the adoption of liquid-continuous impinging streams (LIS) has two major features: local pressure fluctuations and homogeneous micromixing. In a synthesis process, efficient micromixing due to turbulent eddy motion can remarkably improve the mass transfer rate between the mixed solutions and increase the reaction rate. As a result, the probability of crystal nucleus collision increases significantly. The local pressure fluctuations can also influence the energy and mass transfer in the solution (Huang *et al.*, 2015). Comparing with conventional stirred tanks, an impinging stream reactor or T-type micromixer has fixed and confined volume, leading to several orders of magnitude higher mixing intensity and uniform residence time when the feeding rate is kept to be steady. This kind of hydrodynamic reaction environment will be beneficial to the control of the mixing conditions and local reactant concentrations (Siddiqui *et al.*, 2009).

The use of impinging stream in micromixer for material synthesis has been documented in many previous researches for various applications. $CuO/ZnO/Al_2O_3$ catalysts used for methanol synthesis, prepared by impinging steam reactor, has shown superior physicochemical properties and higher catalytic activity compared with the preparation method of conventional batch processing (Simson *et al.*, 2013; Kaluza *et al.*, 2011). Zhang *et al.* (2015) prepared $CuO/ZnO/Al_2O_3$ catalysts by using a similar method and have investigated the effects of reagent concentration, volumetric flow rates and aging time on the catalyst structure and catalytic performance. Jiang *et al.* (2015) applied a dual impinging jet mixer to investigate the effect of jet velocity on crystal size distribution of pharmaceutical ingredients. Yan *et al.* (2013) have found that the use of impinging stream reaction with the pH of the working solution being 1.3

can achieve the molar ratio of nFe to nP to be equal 1 in the obtained amorphous FP and uniform particle size in the range of 40-60 nm. They considered the hexagonal FP to be the preferred form for synthesising the LFP/C with good electrochemical performance. They also attribute the use of the impinging stream to give rise to the low possibility of ionic disorder and stacking faults in LFP nanoparticles, and the capability of the highly pure LFP (Yan *et al.*, 2013). Casanova and Higuita (2011) adopted a specially designed high pressure jet homogenizer to investigate the effect of total pressure drop, pH value, temperature, and protein concentration on the formation of calcium carbonate nanoparticles. Tari *et al.* (2015) have revealed that the crystal size of glycine can be reduced by using impinging stream. Wu *et al.* (2006) also demonstrated that the function of the impinging stream reaction is to assist to gain homogeneous mixing and to reduce the particle size of barium sulfate. Li *et al.* (2015) synthesized ZnO/Ag micro/nanospheres using microwave-assisted impinging stream microreactor and found that the photocatalytic and antibacterial properties of ZnO/Ag can be enhanced. Kumar *et al.* (2013) synthesized nanocrystalline MgO by impinging stream micromixing, and investigated the effect of jet impingement angle and jet velocity (Reynolds number). Additionally, the use of computational fluid dynamics (CFD) modelling approach has been applied to study the micromixing efficiency of impinging stream by adopting Villermaux-Dushman parallel competing reaction system as indicators (Liu *et al.*, 2014; Siddiqui *et al.*, 2009; Liu and Fox, 2006). Planar Laser Induced Fluorescence (PLIF) technique is also used to investigate the impact of Reynolds number on mixing (Fonte *et al.*, 2015; Shi *et al.*, 2015). For T-mixer, Borukhova *et al.* (2016) used T-mixer to convert bulk alcohols into the corresponding chlorides. Polyzoidis *et al.* (2016) developed

a micro reaction technology (MRT) with T-mixer to prepared metal-organic framework ZIF-8. Due to the highly controlled mas and heat transport conditions provided by MRT, the productivity and repeatability in the preparation of ZIF-8 can be enhanced significantly. Kolmykov *et al.* (2017) also synthesize ZIF-8 crystals via microfluidic technology by using T-micromixer. Wong *et al.* (2004) demonstrated that, in a micro T-mixer, rapid mixing can be achieved when the Reynolds number is between 400 and 500, because liquid streams can break up into striations and then these striations will disappear into uniform concentration across the mixing channel. Moreover, the mixing characteristics of T-type mixer are also investigated with gas phase (Soleymani, Kolehmainen and Turunen, 2008), liquid phase (Gobby, Angeli and Gavriilidis, 2001) and for the generation of nanoparticles (Gradl *et al*., 2006).

1.3 Ultrasonic Irradiation

Ultrasound intensified synthesis methods have been applied in industrial manufacturing process and material synthesis due to its fast, cost-effective and environmentally-friendly. There are several types of ultrasonic-intensified reactors, which can be divided into probe-horn (including vertical probe horn and longitudinal horn) reactor and cup-horn (ultrasonic bath) reactor (Asgharzadehahmadi *et al*., 2016). Comparing with cup-horn reactor, probe-horn reactor requires less energy cost during synthesis process (Monnier, Wilhelm and Delmas, 1999). When liquid medium is irradiated by ultrasound, ultrasonic wave can introduce acoustic cavitation and generate large amount of cavitation bubbles. Because the instantaneous collapse of the cavitation bubbles an create extremely high pressures (up to 1000 atm), temperature (up to 5000K), and the heating and

cooling rate greater than 10^{10} Ks^{-1} inside the cavitation zone, the chemical and physical changes in solution are enhanced by the imploding of cavitation bubbles significantly (McNamara, Didenko and Suslick, 1999; Mason and Cordemans, 1996). In addition, ultrasound can help to prevent the agglomeration among particles and interaction between particles and reactor surface (Noël *et al.*, 2011). Therefore, high intensity ultrasonic-irradiation is a promising technology which can enhance micromixing, as well as overcome clogging and slurry transport difficulties problem, especially in ISR (Noël *et al*., 2011; Rivas and Kuhn, 2016; Sedelmeier *et al.*, 2010; Horie *et al*., 2010; Zhang *et al*., 2012). However, most of these research only treatment outlet tube (Noël *et al*., 2011; Zhang *et al*., 2012), or use extra gas (Horie *et al*., 2010), which increase the operation cost.

The ultrasound-assisted chemical reaction is significantly influenced by operation parameters, such as ultrasound intensity, frequency, pulse and so on (Sancheti and Gogate, 2017). Generally, an increase in ultrasound intensity will facilitate the generation of active cavitation bubbles, drive the reaction in faster way till optimum level and reduce reaction time. The optimum power dissipation is determined by the specific application and reactor configuration (Gutierrez and Henglein, 1990). In addition, the product yield and conversion rate can be improved as the increasing of ultrasound intensity (Bansode and Rathod, 2014; Khan, Jadhav and Rathod, 2015; Waghmare, Vetal and Rathod, 2015; Ammar *et al.*, 2015; Safari and Javadian, 2015; Li *et al.*, 2014; Rabiei and Naeimi, 2015; Dange, Kulkarni and Rathod, 2015).

Ultrasound frequency influences bubble critical size, collapse time, as well as the dominance of the chemical or physical effects significantly (Sancheti and Gogate,

2017). Generally, dominating physical effects, including liquid circulation and turbulence, can be produced under lower frequencies (20 kHz to 50 kHz), while dominating chemical effects can be observed at relatively higher frequencies. In addition, the increasing of frequency leads to the reduction of bubbles size (Li *et al.*, 2014; Thompson and Doraiswamy, 1999; Gogate, 2008; Son, Lim and Khim, 2009). The effect of frequency on chemical reaction rate and yield is strongly determined by the system type. In a homogeneous reaction or even heterogeneous reaction, chemical reaction rate can be improved under higher frequency due to the dominant chemical effects which can intensify the oxidation reaction (Vivekanand and Wang, 2011; Francony and Pétrier, 1996; Entezari, Heshmati and Sarafraz-Yazdi, 2005; Kruus *et al.*, 1997; Vichare *et al.*, 2000). In comparison, lower frequencies are preferred in enzyme catalysed reaction or heterogeneous reactions because dominant physical effects result in increased mass transfer rate and conversion rate (Bansode and Rathod, 2014; Khan, Jadhav and Rathod, 2015; Ammar *et al.*, 2015; Li *et al*., 2014).

Pulsed ultrasound, or duty cycle of ultrasonic operation, decides the time which solution is irradiation by ultrasound in one cycle. The cycle time of pulsed ultrasound is consisted of pulse duration time ("on") and interval time ("off") of the sonicator.

As the using of continuous ultrasound without cooling may damage sonicator due to excessive heating, the using of pulsed ultrasound can not only reduce energy consumption, but also prolong the life of sonicator though decreasing local temperature rise rate (Raskar, Avhad and Rathod, 2014; Avhad, Niphadkar and Rathod, 2014). Moreover, in enzymatic reaction, prolonged exposure time of

ultrasound can reduce the enzyme activity due to the increased shear force caused by turbulence (Delgado-Povedano and Luque de Castro, 2015). Therefore, the optimum mode of pulsed ultrasound should be established based on the reactor configuration and specific application. Furthermore, temperature and agitation speed also play a vital role in ultrasound-assisted reaction system (Sancheti and Gogate, 2017).

1.4 Co-precipitation Reaction

Synthesis of $FePO_4$ precursor and $LiFePO_4$ composites has been documented in many previous researches. Ying *et al.* (2006) reported a controllable crystallization method to synthesize spherical amorphous $FePO_4 \cdot xH_2O$ and spherical olivine $Li_{0.97}Cr_{0.01}FePO_4$ /C powders with high tap density by co-precipitation method. In the synthesis process, $Fe(NO)_3$ (1.0 mol L^{-1}), H_3PO_4 (1.0 mol L^{-1}) and NH_3 (3.0 mol L^{-1}) solutions are using as raw materials. The schematic diagram of the reactor is shown in Figure 1-4, and the reaction equation is as follows:

$$Fe(NO_3)_3 + H_3PO_4 + 3NH_3 + xH_2O = FePO_4 \cdot xH_2O + 3NH_4NO_3$$

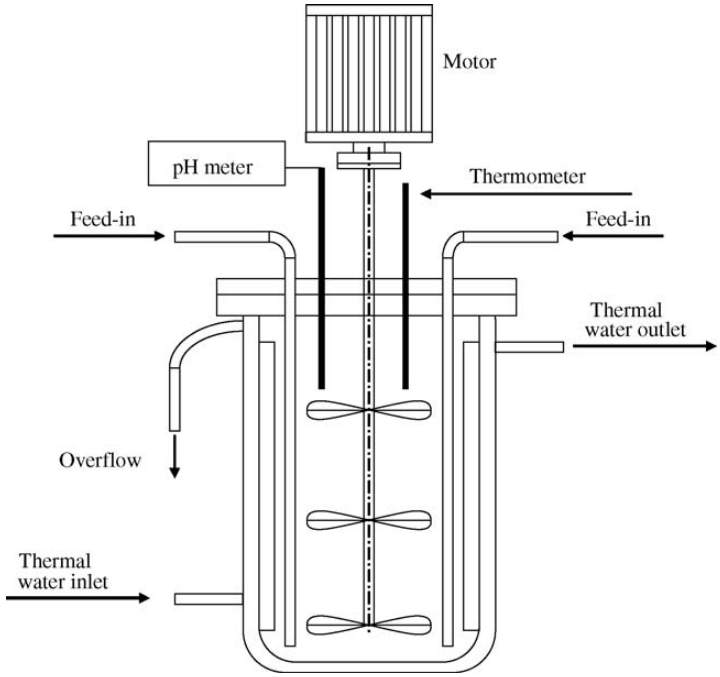

Figure 1-4 Schematic diagram of the reactor for controlled crystallization process (Ying *et al.*, 2006).

The agitating intensity was maintained at 50-60 W L^{-1}. The mean residence time was 8-12 h. The temperature was 45 ℃. When the solution's pH value increases, Fe^{3+} is very easy to hydrolyze to $Fe(OH)^{2+}$, $Fe(OH)_2^{+}$, and $Fe(OH)_3$. On the contrary, the decreasing of pH value results in the formation of HPO_4^{2-}, and H_2PO^{4-}. Figure 1-5 shows the relationship between Fe/P molar ratio of the precursors and solution's pH value. When pH is between 1.95 and 2.25, the Fe/P molar ratio is closed to 1, which is necessary to the synthesis of spherical $FePO_4$ powder. Thus, the pH value was kept at 2.1 in this experiment.

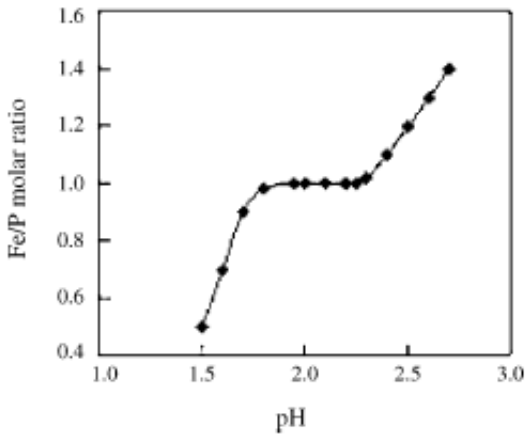

Figure 1-5 The Fe/P molar ratio of the precursors prepared at different pH (Ying *et al.*, 2006).

In the synthesis process of $Li_{0.97}Cr_{0.01}FePO_4$ /C powder, $FePO_4$, $LiCO_3$, $Cr(NO_3)_3$ and sucrose are sintered in N_2. Li^+ and Cr^{3+} diffuse into $FePO_4$ spheres and insert into $FePO_4$ framework. In the meantime, the sucrose will pyrolyse and generate hydrogen and carbon, which will create a strong reductive atmosphere for the reduction of Fe^{3+} to Fe^{2+}, results in the generation of $Li_{0.97}Cr_{0.01}FePO_4$. Furthermore, the residual pyrolytic carbon will coat on the spherical $Li_{0.97}Cr_{0.01}FePO_4$ particles and form $Li_{0.97}Cr_{0.01}FePO_4$ /C.

The SEM images in Figure 1-6 show the morphology of $FePO_4 \cdot xH_2O$, $FePO_4$, and $Li_{0.97}Cr_{0.01}FePO_4$/C. Both of $FePO_4 \cdot xH_2O$ and $FePO_4$ particles show well-dispersed spherical shape. $Li_{0.97}Cr_{0.01}FePO_4$ /C powders are similar to the $FePO_4$ precursors, although there is slight agglomeration and small amount of fragments. The spherical particle shape leads to a higher tap-density (1.8 g cm $^{-3}$), so that the batteries' energy density will be improved significantly.

The prepared $Li_{0.97}Cr_{0.01}FePO_4$/C sample shows excellent cycling performance, which can be attributed to the enhancement of the electronic conductivity by the

Cr^{3+} substitution, carbon coating, and the excellent cycle ability of $LiFePO_4$. However, the results also show the rate capacity should be further improved. The discharge capacity is only 110 mAh g^{-1} at 1.0 C. The reasons why $Li_{0.97}Cr_{0.01}FePO_4$ /C spheres have high electronic conductive surface but poor electronic conductive core may be explained as that, during the sintering process, the sucrose and pyrolytic carbon are difficult to diffuse into the close-grained $FePO_4$ spheres, so that they are only coated on the surface. Additionally, the high position charge density of Cr^{3+} results in the difficult diffusion and insertion process.

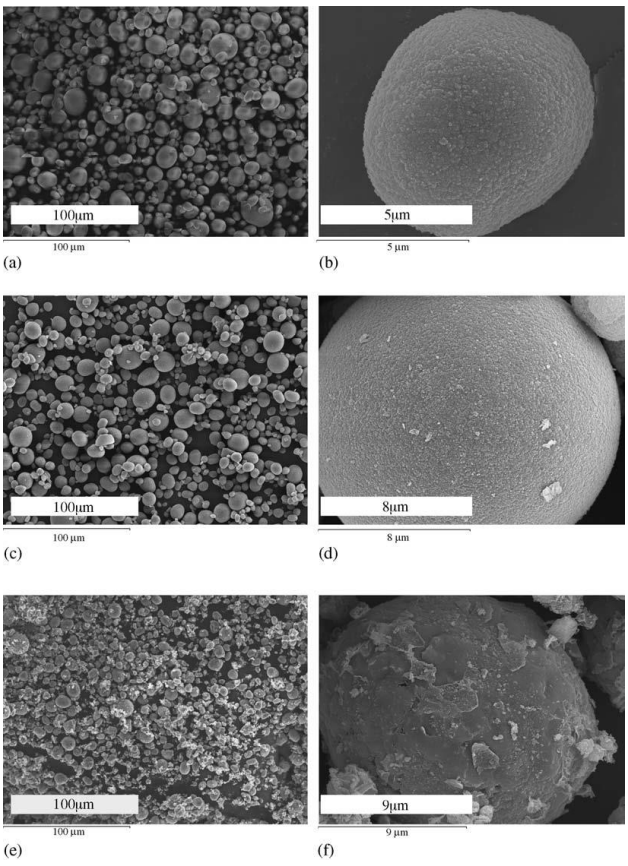

Figure 1-6 SEM images of the spherical $FePO_4 \cdot xH_2O$, $FePO_4$, and $Li_{0.97}Cr_{0.01}FePO_4$ /C: (a) and (b) $FePO_4 \cdot xH_2O$ particles, (c) and (d) $FePO_4$ particles, (e) and (f) $Li_{0.97}Cr_{0.01}FePO_4$ /C particles (Ying *et al.*, 2006).

Shin *et al*. (2008) also evaluated the effect of Cr-doping on LFP nanocomposites. Wang *et al*. (2008) reported an in situ polymerization restriction method to synthesise nanoscale $FePO_4$ and $LiFePO_4$/carbon composites. Sun *et al.* (2010) investigated how Cl ion influenced electrochemical property of $LiFePO_4$/C samples.

Cl-doped $LiFePO_4$/C sample is synthesized by $LiNO_3$, $Fe(NO_3)_3 \cdot 9H_2O$, NH_4Cl, $NH_4H_2PO_4$, and glucose. All these chemicals are mixed and stirred, then dried in an oven at 100℃.

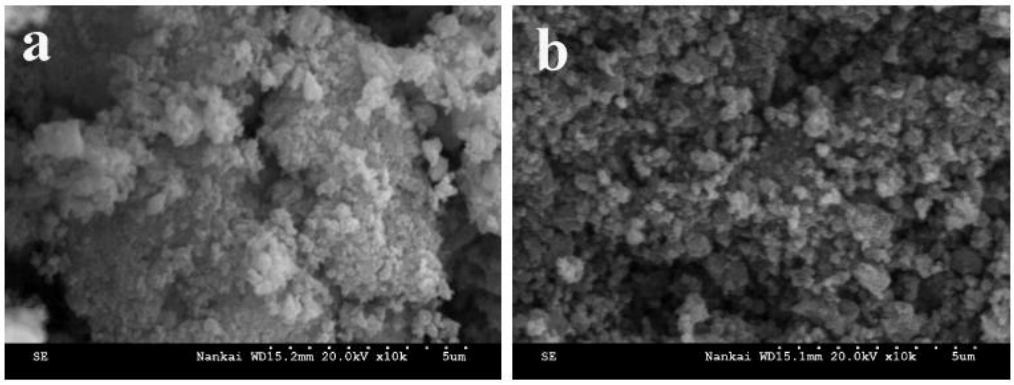

Figure 1-7 SEM images of (a) $LiFePO_4$/C and (b) Cl-doped $LiFePO_4$/C (Ying *et al.*, 2006).

The primary grain size of normal $LiFePO_4$ and Cl-doped $LiFePO_4$ are 100-200nm, but normal $LiFePO_4$ particles is agglomerated significantly. Additionally, the discharge capacity of normal $LiFePO_4$/C and Cl-doped $LiFePO_4$/C is 132.1 and 162 mAh g^{-1} respectively. The reason is that, Cl-doping can improve the stability of $LiFePO_4$ framework through reducing the lengths of P-O. Meanwhile, Cl-doping can facilitate the extraction of Li due to the weakness of interaction between Li and O.

Hong *et al*. (2012) synthesised $LiFePO_4$/C nanocomposites and evaluated how sucrose amount influences electrochemical performance of $LiFePO_4$/C. Hsieh *et al.* (2012) prepared nanoscale $FePO_4$ precursor at different pH value using co-precipitation method to investigate how pH value influenced the co-precipitation synthesis of $FePO_4$, and the electrochemical performance of resultant $LiFePO_4$/C positive electrode. $FeSO_4 \cdot 7H_2O$, equimolar solution of H_3PO_4 (85%), and concentrated H_2O_2 are using as starting materials. $NH_3 \cdot H_2O$ was used as neutralizer to control the desired pH value of the solution, which is 1, 2, 3 and 4 respectively.

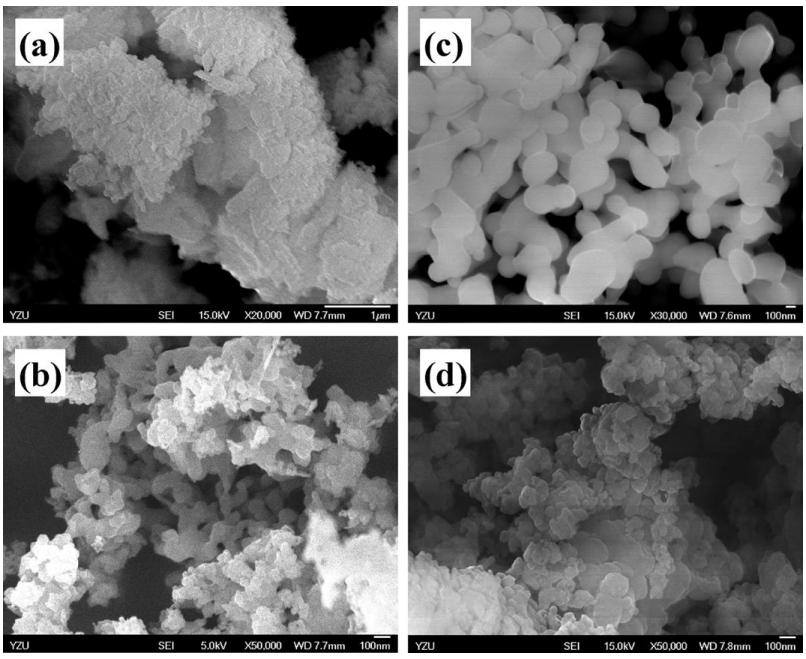

Figure 1-8 SEM images of various $FePO_4$ precursors at different pH values: (a) 1, (b) 2, (c) 3, and (d) 4 (Hong *et al*., 2012).

As can be seen from Figure 1-8, the $FePO_4$ precursor synthesized at pH 3 shows nearly spherical-like shape with well uniformity. According to Figure 1-9, the particle size and shape of $LiFePO_4$/C powders are similar to those of their

precursors. The average size of $FePO_4$ precursor and $LiFePO_4$/C powder synthesized at pH=3 are 200-350 nm and 200-400 nm, respectively. But the other $LiFePO_4$/C samples become to be agglomeration. Additionally, the tap density of this precursor (pH=3) is 1.34 g cm $^{-1}$, which is higher than other samples.

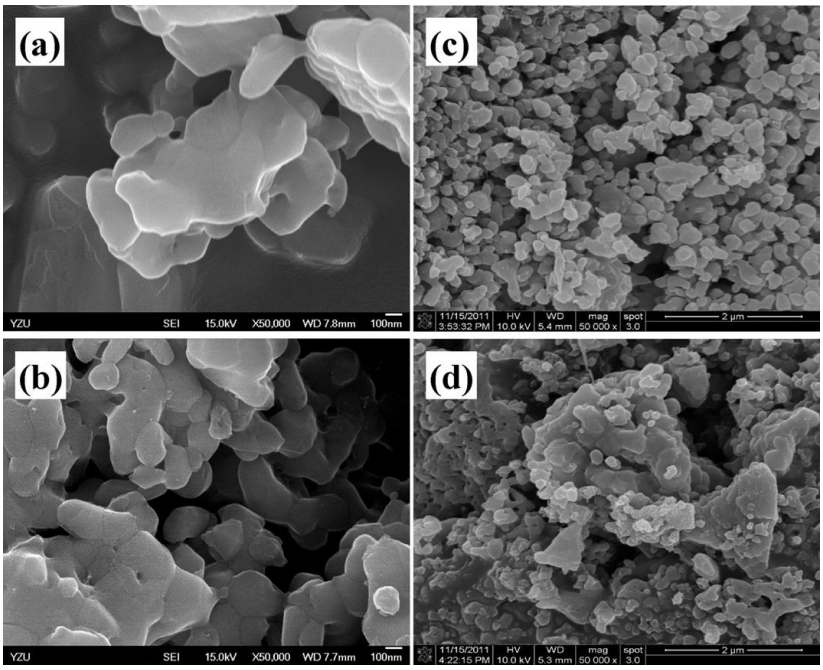

Figure 1-9 SEM images of various $LiFePO_4$/C powders synthesized by different $FePO_4$ precursor (a) 1, (b) 2, (c) 3, and (d) 4 (Hong *et al*., 2012).

In terms of electrochemical properties, CV curve, cyclic performance and rate capability all demonstrate that the $FePO_4$ precursor synthesized at pH 3 had the best performance. It has the highest coulombic efficiency (96%) at the first cycle, and the discharge capacity at 0.1 and 5 C are 162.1 and 119.7 mAh g^{-1} respectively.

All of these results reveal that pH affects the morphology of $FePO_4$, as well as the electrochemical performance significantly. $FePO_4$ precursors are core material in controlling the crystallization and shape of $LiFePO_4$/C composites. When the pH value is low (pH=1, 2), the XRD patterns show a poor crystallinity of as-synthesized powders. On the other side, when the pH value is from 3.8 to 8, the solubility diagram reveals that a three phase precipitation including $FePO_4 \cdot xH_2O$, $Fe(OH)_3$, and liquid would coexist, so that some impurities are produced and caused the generation of irregular-shaped powders. Furthermore, based on the electrochemical property analysis, particle morphology affects specific capacity and rate capability significantly. In conclusion, the results indicate that the optimum pH value should be about 3 (Hsieh *et al*., 2012).

Zhu *et al.* (2014) reported the use of a facile co-precipitation method to prepare nanoscale $FePO_4$ precursor and have revealed that reagent concentration can affect both of the morphology and electrochemical performance of positive electrode material. In this study, $Fe(NO_3)_3$ (0.1 mol L^{-1}) and $(NH_4)_2HPO_4$ (0.1 mol L^{-1}) solutions in a stoichiometric ratio were used as material. The pH value was maintained at the range from 2 to 5 through the adding of concentrated NH_3H_2O solution. The temperature is kept at 60 ℃ to avoid the formation of $Fe(OH)_3$. Additionally, the concentration of $Fe(NO_3)_3$ and $(NH_4)_2HPO_4$ was increased from 0.1 mol L^{-1} to 1 mol L^{-1}, to investigate the effect of supersaturation.

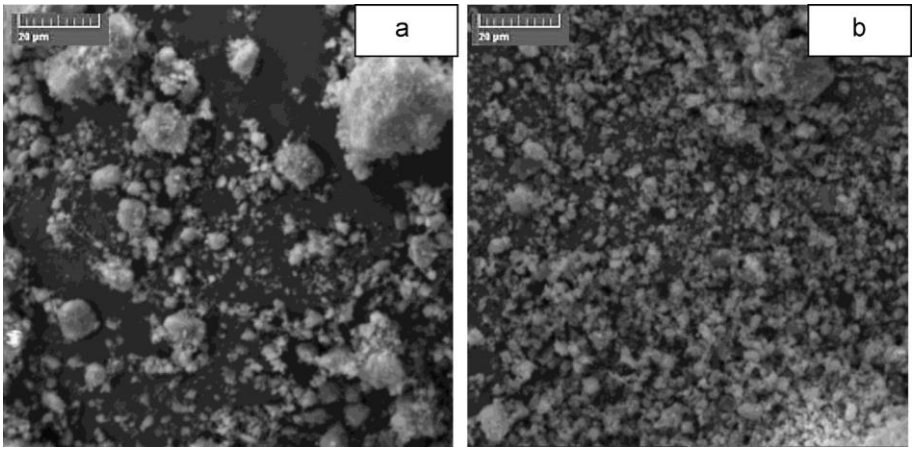

Figure 1-10 SEM image of $LiFePO_4$/C samples (a) obtained with 0.1 mol/L raw materials and dried at 80℃ (b) obtained with 1.0 mol/L raw materials and dried at 80℃ (Zhu *et al.*, 2014).

The electrochemical performances of $LiFePO_4$/C were determined by cyclic voltammetry (CV), electrochemical impedance spectroscopy (EIS), and electrochemical capacity measurement. Based on the results, the $LiFePO_4$/C sample obtained with 1.0 mol/L raw materials and dried at 80℃ has the best electrochemical performance. It can deliver discharge capacities of 162.5mAh g^{-1}, 147.3mAh g^{-1}, 133.0mAh g^{-1}, 114.7mAh g^{-1}, 97.2mAh g^{-1}, 91.3mAh g^{-1}, and 88.5mAh g^{-1} at rate of 0.1C, 0.2 C, 0.5 C, 1 C, 2 C, 3 C and 4 C respectively.

Qian *et al.* (2012) applied an electrochemical method to synthesise $FePO_4$ nanoparticles and found that electrochemical performance of $LiFePO_4$/C can be improved if $FePO_4$ precursor has mesoporous structure. By using Fe(II) salts, Arnold *et al.* (2003) synthesised $LiFePO_4$ nanoflates by aqueous co-precipitation method . A microwave heating assisted co-precipitation method was adopted by Park *et al.* (2003) to prepare $LiFePO_4$ nanocomposites. Ni *et al.* (2005) prepared $LiFePO_4$ nanocomposites by co-precipitation method, and the effects of ion

doping (Mg^{2+}, Cu^{2+}, and Zn^{2+}) on physical and chemical properties of LFP were evaluated. Ding *et al.* (2010) reported a novel co-precipitation method to prepare nano-structured LFP/graphene composites, and indicated that the electrochemical performance of LFP can be improved by adding graphene nanosheets. Liu *et al.* (2014) evaluated how the graphene nanosheet content affects the morphology and electrochemical performance of LFP. Shi *et al.* (2012) investigated the effect of graphene on the rate capability, illustrating that the rate capability can be enhanced through graphene wrapping. Bai *et al.* (2015) also synthesised LFP/C microspheres by co-precipitation method. Han *et al.* (2013) have demonstrated that the use of two step heterogeneous growth technology can produce porous and coarse LFP/C composites with improved electrochemical performance.

Zhu *et al.* (2006) reported an aqueous precipitation and carbothermal reduction method to synthesize $LiFePO_4$. $FeSO_4 \cdot 7H_2O$ (99 wt%), H_2O_2 (99 wt%) and $NH_4H_2PO_4$ (30 wt%) are using as starting materials for the synthesis of $FePO_4 \cdot 2H_2O$ precursor . Then stoichiometric amount of $FePO_4 \cdot 2H_2O$ mixed with Li_2CO_3 and carbon to synthesize $LiFePO_4$/C. The molar ratio of $FePO_4 \cdot 2H_2O$: Li_2CO_3: C was 2:1:3.92.

Figure 1-11 shows the SEM micrographs of $FePO_4 \cdot 2H_2O$ prepared at different temperatures. It indicates that higher synthesizing temperature results in smaller particle. When the synthesis temperature is 100 ℃, the average particle size is about 0.1 μm.

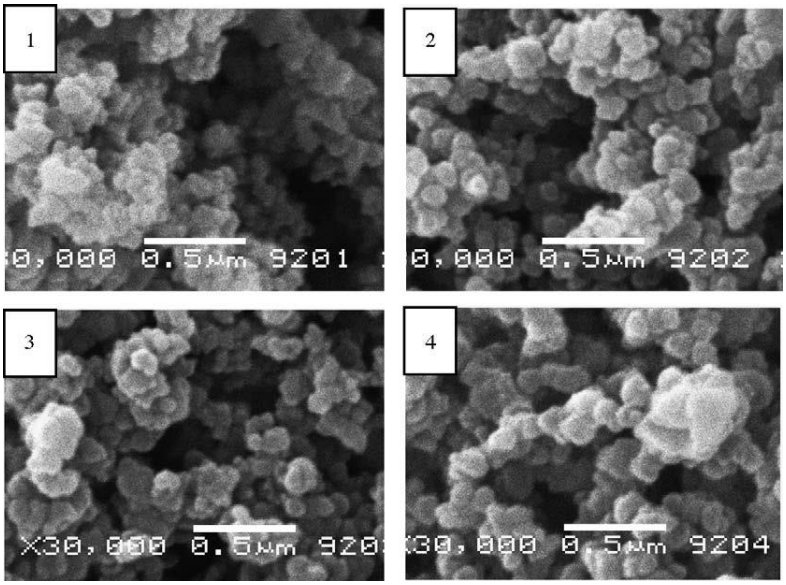

Figure 1-11 SEM micrographs of $FePO_4 \cdot 2H_2O$ prepared at different temperatures: 1. 100℃; 2. 70℃; 3. 40℃; 4. 20℃ (Zhu *et al.*, 2006).

Figure 1-12 indicates that sintering temperature and time influence the particle size of $LiFePO_4$. Longer sintering time and higher sintering temperature can generate larger $LiFePO_4$ particles.

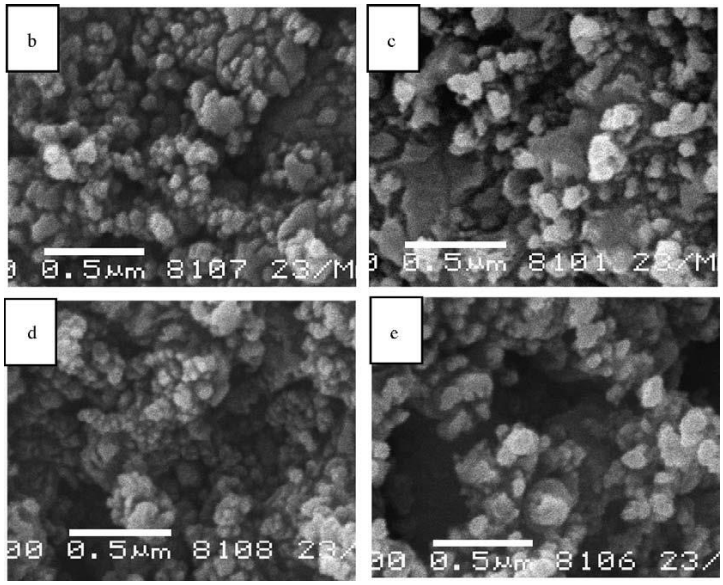

Figure 1- 12 SEM micrographs of $LiFePO_4$/C for sample (b), (c), (d), and (e) (Zhu *et al.*, 2006).

In terms of electrochemical properties, sample (b), which is synthesized at 560 ℃ for 12 h, shows the best electrochemical performance. The discharge capacity is 152 mAh g^{-1} at 0.1 C and 129 mAh g^{-1} at 1 C, respectively.

Comparing to Fe(II), Fe(III) material need an electrochemical or chemical reduction step. However, Fe(III) material is more cheap than high-cost Fe(II) salt. And Fe(II) salt is so easy to be oxidized that it should be in an excellent preservation state.

1.5 Hydrothermal synthesis method

Hydrothermal synthesis method is a low-cost and energy saving method. It has been widely used to generate lithium iron phosphate positive electrode materials due to its mild operation temperature, simple process and has the potential for large-scale production. In 2001, Yang *et al.* firstly reported lithium iron phosphate can be synthesized hydrothermally. In order to avoid the generation of $Fe(OH)_2$, $FeSO_4$ and H_3PO_4 were mixed and stirred firstly, then LiOH was added into the mixture. And the stoichiometric ratio of $FeSO_4$, H_3PO_4 and LiOH is 1:1:3. The mixture was hydrothermally synthesized at 120 ℃ for up to 5 hours. However, the relatively lower synthesis temperature (120 ℃) lead to lower capacity (100 Ah/kg at 0.14 mA/cm^2), and the reason is that some lithium/iron disorder with around 7% iron on the lithium sites (Yang *et al*., 2002). Higher reaction temperature (exceed 175 ℃) can help to minimize iron disorder and generate lithium iron phosphate with correct volume and lattice parameters (Jin and Gu, 2008). And the adding of reactant (ascorbic acid or sugar) can avoid the formation of surface ferric films (Chen *et al*., 2008).

1.5.1 Hydrothermal mechanism

In 2010, Qin *et al*. reported a dissolution-precipitation mechanism for the formation of $LiFePO_4$ platelets under hydrothermal synthesis condition. In their research, $FeSO_4 \cdot 7H_2O$, H_3PO_4 and $LiOH \cdot H_2O$ were used as starting materials. Three experimental phenomenons can be observed apparently, including precursor dissolution, hydrothermal formation of $LiFePO_4$, and reduction of particle size with the addition of alcohol and carbon black.

Figure 1-13 shows the changing of $LiFePO_4$ morphology in dissolution-precipitation process in hydrothermal condition. In the beginning, the initial agglomerated precursor (Figure 1-13a) dissolved into small aggregates with irregular sheet-like shape (Figure 1-13b). As the increasing of temperature (from 165°C to 180°C), these irregular aggregates transformed to $LiFePO_4$ precursor with nanoleaflet structure (Figure 1-13c), and finally to plate-like $LiFePO_4$ powders (Figure 1-13d).

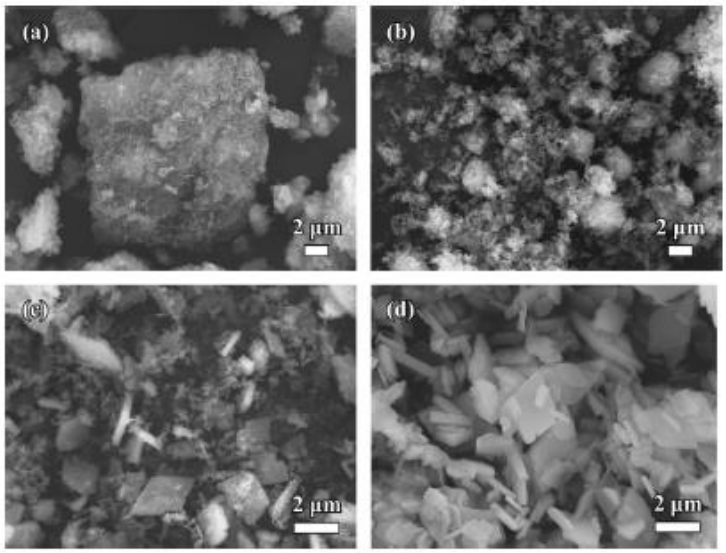

Figure 1-13 SEM images of $LiFePO_4$ (LFP): (a) LFP precursor, (b) LFP precursor reacted hydrothermally at 165 ℃, (c) LFP precursor reacted hydrothermally at 180 ℃ without holding time, (d) LFP precursor reacted hydrothermally at 180 ℃ for 5 min. (Qin *et al*., 2010)

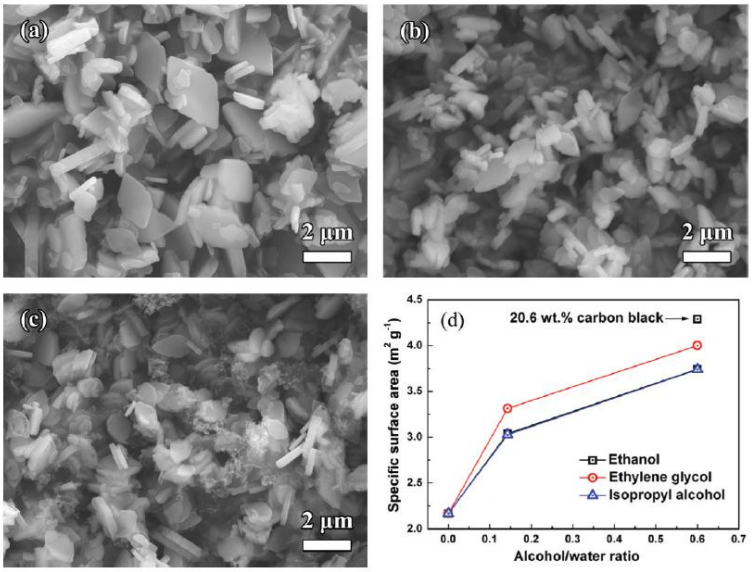

Figure 1-14 SEM images of $LiFePO_4$: (a) the precursor heated up to 180 °C for 3 h, (b) with ethanol/water (3:5, v/v), (c) with ethanol/water (3:5, v/v) and carbon black (20.6 wt % vs $LiFePO_4$), and (d) the evolution of the specific

surface areas for $LiFePO_4$ powders synthesized hydrothermally with various alcohols and contents in the reaction system and 20.6 wt % carbon black in reaction medium of ethanol/water (3:5, v/v).

In 1999, Pinceloup *et al*. reported the particle size was influenced by the content of water and the amount of nuclear sites with large surface area significantly. Therefore, Qin *et al*. (2010) induced various alcohol and/or carbon black to investigate this phenomenon. Figure 1-14 showed the introducing of ethanol to reduce the content of water (Figure 1-14b), and carbon black with large surface area (62 $m^2 \cdot g^{-1}$) as nucleation sites leaded to the reduction of particle size of $LiFePO_4$ (Figure 1-14c).

Based on these observations, they divided hydrothermal synthesis process into three main parts: precursor dissolution, nucleation, and nuclei growth.

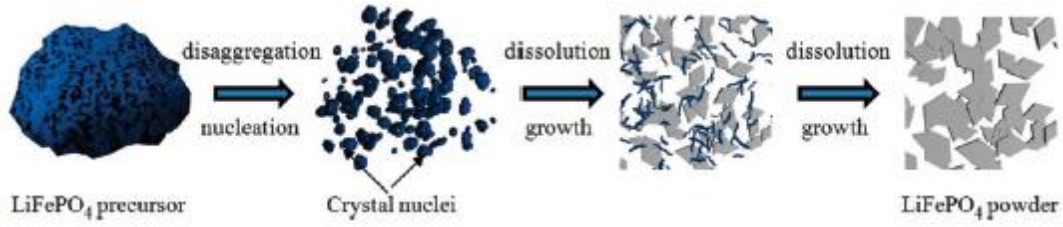

Figure 1-15 Hydrothermal process and mechanism of $LiFePO_4$ (Qin *et al*., 2010).

Precursor dissolution step: the starting materials are dissolved and hydrolyzed with the increasing temperature during the hydrothermal process, and leading to a decreasing pH value of solution. This dissolution and hydrolytic process disaggregate agglomerated precursor into smaller aggregation.

Nucleation step: As Gibbs free energy which changing for the formation of crystalline nucleation on any surface that interacts with nuclei is lower than that of the homogeneous nucleation mechanism, surface free energies of the nucleation will be minimized and lower barrier for nucleation. In this heterogeneous nucleation mechanism, the required critical nucleation concentration is lower than homogeneous nucleation. When the required heterogeneous nucleation concentration is reached, the aquo-metal ions in solution transformed into few nuclei at the surface or edge of nucleation agent, which is undissolved precursor. Nuclei growth step: partial nuclei begin crystal growth step, and leading to inhomogeneity of particle size. Therefore, the hydrothermal prepared particles formed through a dissolution-precipitation mechanism have a wide particle size distribution. As anisotropy of nuclei surface energy determines crystal morphology, the higher surface energy on nuclei surfaces, the greater ion adsorbing energy they have. Hence, $LiFePO_4$ crystalline grows faster along the vertical directions, and undissolved precursors are dissolved into nanoleaflets. When the concentrations of aquo-metal ions are lower than critical supersaturation concentration, the particle growth process is stopped.

1.5.2 Ferrous iron (Fe^{2+}) salt used as iron source

Ferrous iron (Fe^{2+}) salt has been widely used as iron source to generate $LiFePO_4$ particle by hydrothermal synthesis method. The advantage is that, $LiFePO_4$ can be generated by one-step when Fe^{2+} salt is used in hydrothermal synthesis.

Dokko *et al*. (2007) investigated how the concentration of Li source and pH value of solution affected the morphology of $LiFePO_4$ particles which synthesized by hydrothermal method at 170°C. In this work, $FeSO_4 \cdot 7H_2O$, $LiOH \cdot H_2O$ and

Li_2SO_4 (Li source), $(NH_4)_2HPO_4$ and H_3PO_4 (P source) are used as raw materials. Li source and P source are mixed firstly, and then $FeSO_4$ is added subsequently. As the increasing concentration of Li source, the particle size is decreased, which demonstrated that excess lithium in the precursor can reduce particle size significantly. Additionally, the solution pH value influences crystal growth orientation significantly.

Based on SEM images, it is considered that plate-like crystals (L3-5.1 and L2-6.5) had large facets in the ac-plane, as well as needle-like particles (L3-3.5) had a large facet in the bc-place. And the deposition rates of $LiFePO_4$ on the crystal planes under acidic conditions are: ab-plane>ac-plane>bc-plane. Therefore, needle-like particles can be generated from acidic solution (pH=3.5), plate-like crystals can be obtained from weak acidic solution (4<pH<6.5) and shows the highest electrochemical reactivity (163 mA hg^{-1} at 17 mA g^{-1}), and random shaped crystals can be produced from solution with higher pH value (pH>7.2).

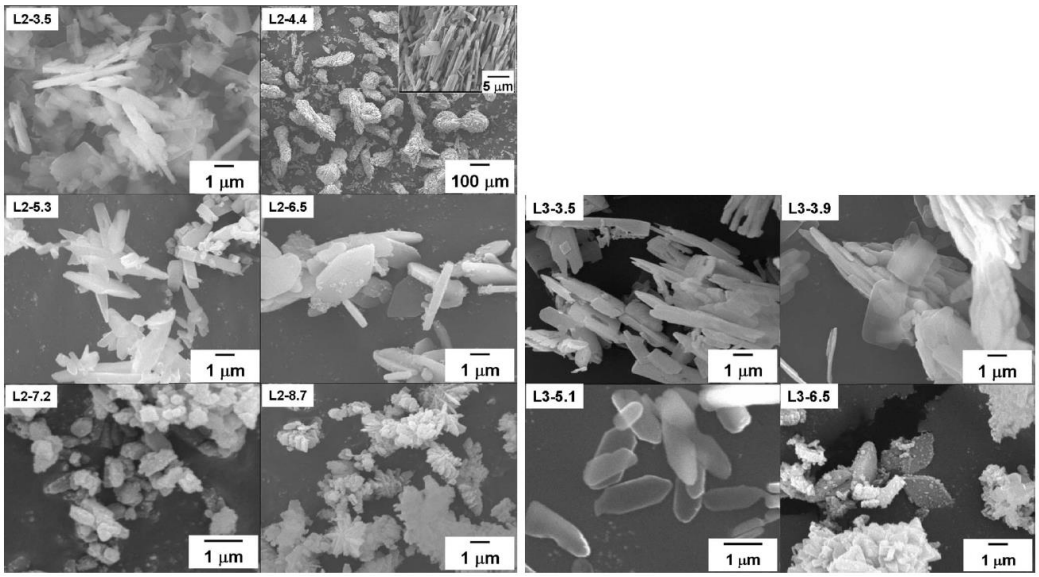

Figure 1-16 SEM images of the samples prepared by the hydrothermal method. L2 and L3 mean the samples were prepared from solutions containing 2 and 3 mol dm^{-3} respectively. 3.5, 4.4 *et al* mean the pH value of solutions (Dokko *et al.*, 2007).

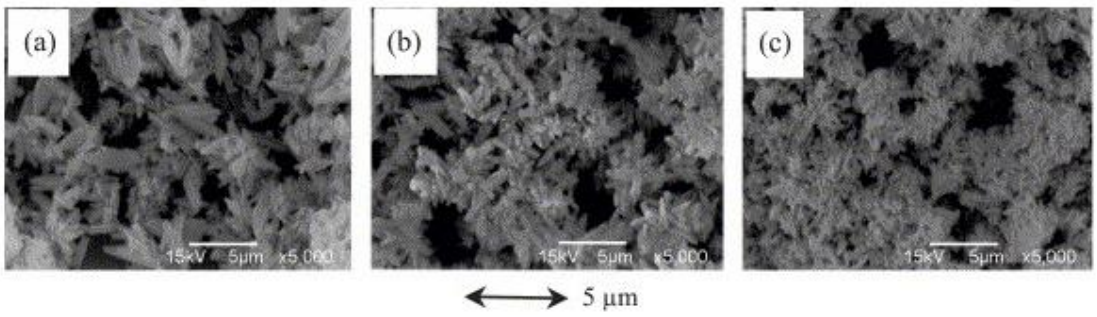

Figure 1-17 Particle morphology of $LiFePO_4$ prepared by hydrothermal reaction (a) without PEG, (b) with PEG/LiOH (1:1) solution, and (c) with PEG/LiOH (2:1) solution (Tajimi *et al*., 2004).

In 2004, Tajimi *et al.* reported hydrothermal synthesis method which can produce $LiFePO_4$ nanocrystalline particles with size from 500 to 1500 nm. $FeSO_4 \cdot 7H_2O$, H_3PO_4 and $LiOH \cdot H_2O$ are used as starting materials in a molar ratio of 1:1:3. The hydrothermal reaction condition is 150-220℃ for several reaction hours. Various amounts of polyethylene glycol (PEG) are used to generate fine particles because it has high viscosity and low solubility, which can help to inhibit crystal growth by capping crystal faces and reduce particle diameter.

Figure 1-17 shows how PEG influences particle morphology. The $LiFePO_4$ particles synthesized in solution with LiOH:PEG=1:2 show fine and needle-like particles with sizes of $1.0 \times 0.5 \times 0.5$ um^3. Because PEG can provide high viscosity due to the strong hydrogen bonds between hydroxyl groups of PEG, which can improve nuclear generation and suppress crystal growth of $LiFePO_4$. And this optimized $LiFePO_4$ sample can achieve a high discharge capacity of 143 mAh g^{-1} 0.5 mA cm^{-2} in initial cycle, which is higher the samples synthesized without PEG.

In 2006, Meligrana *et al*. synthesized $LiFePO_4$ powders with hydrothermal method. $FeSO_4 \cdot 7H_2O$, H_3PO_4, LiOH in the stoichiometric ratio 1:1:3 are used as raw materials. Hexadecyltrimethylammonium bromide (CTAB) with different amount is used as surfactant.

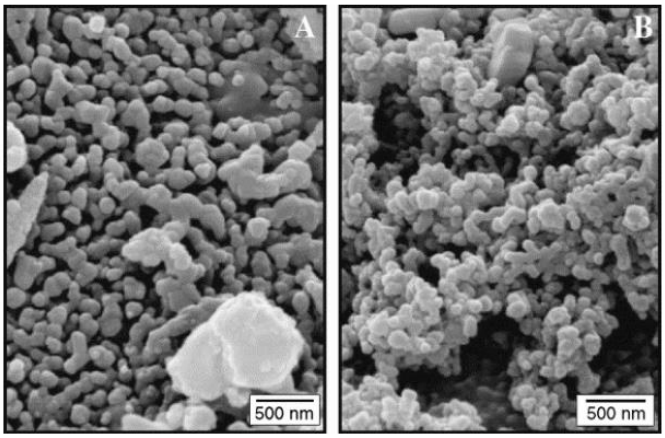

Figure 1-18 SEM images of (A) $LiFePO_4$ with addition of 4.11 mmol CTAB, (B) $LiFePO_4$ with addition of 13.70 mmol CTAB (Meligrana *et al.*, 2006).

Based on the analysis of SEM images and specific surface area, a higher molar amount of CTAB can enhance the specific surface area of $LiFePO_4$ particles, and lead to improved charge –discharge property. This result demonstrates fine particles with larger surface area are important for the increasing of charge-discharge performance.

Liu *et al.* (2015) synthesized $LiFePO_4$ via high shear mixer (HSM) without involving any environmentally toxic surfactants by hydrothermal method. $FeSO_4 \cdot 7H_2O$, H_3PO_4, $LiOH \cdot H_2O$ and glucose are used as starting materials and mixed and stirred in conventional impeller (CI) or HSM for 30 min under nitrogen atmosphere. Then the mixture is transferred to autoclave and experience hydrothermal reaction at 180℃ for 3 hours.

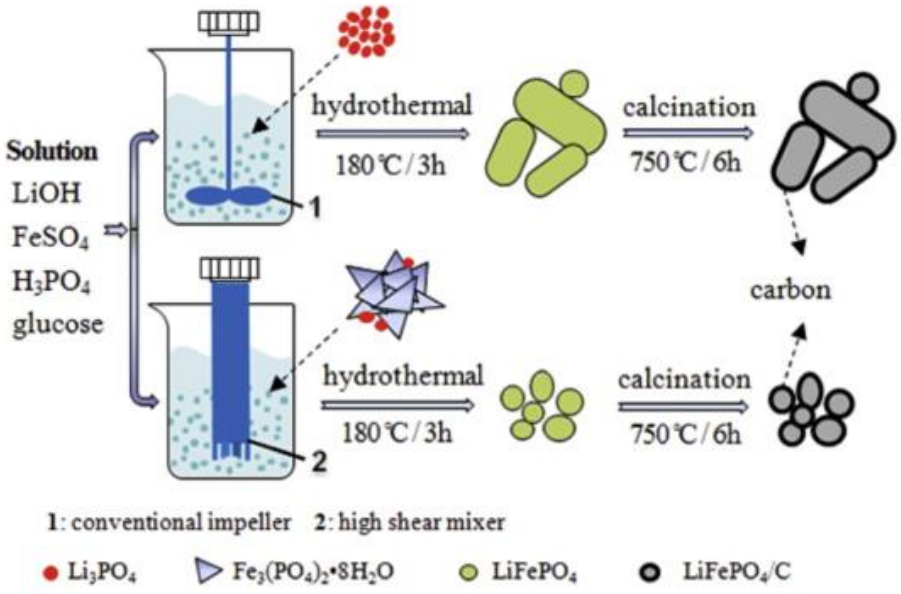

Figure 1-19 Synthesis procedure of $LiFePO_4$/C (Liu *et al*., 2015)

SEM images show that the particles synthesized in CI have micro-sized agglomerate structure, which is composed by aggregated nanoparticle with spherical-like shape. The samples synthesized in HSM have micro-sized show particles with over-lapping laminated structure. XRD and EDS analysis demonstrate laminated particles is $Fe_3(PO_4)_2 \cdot 8H_2O$ and spherical particles is Li_3PO_4. The samples synthesized with HSM at 1.3×10^4 rpm have the minimum particle size (around 220 nm with an enlarged surface area of 15.6 $m2 \cdot g^{-1}$) and exhibit the best electrochemical performances (160.1 mA hg^{-1} at 0.1 C and 90.8 mA hg^{-1} at 20 C). The reason is that, HSM can improve the generation of $Fe_3(PO_4)_2 \cdot 8H_2O$ as well as increase dissolution rate, which leading to the formation of more $LiFePO_4$ nuclei. Therefore, nucleation and crystal growth is accelerated and particle size is reduced.

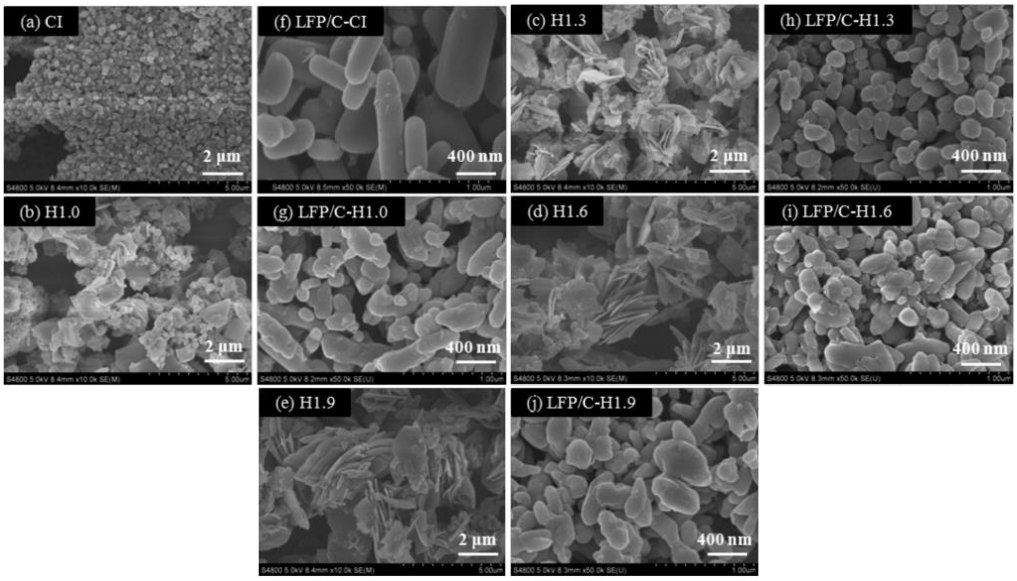

Figure 1-20 SEM images of (a-e) show the as-synthesized precursor precipitates prepared by the conventional impeller at the stirring rate of 1000 rpm (CI) or the high shear mixer at the stirring rate of 1.0×10^4 rpm (H1.0), 1.3×10^4 rpm (H1.3), 1.6×10^4 rpm (H1.6) and 1.9×10^4 rpm (H1.9), respectively. The SEM images of (f-j) show the $LiFePO_4$/C particles synthesized from the corresponding precursors. (Liu *et al*., 2015)

1.5.3 Ferric iron (Fe^{3+}) salt used as iron source

Comparing with Fe^{2+} salt, ferric iron (Fe^{3+}) salt is more stable, less-toxic and inexpensive. The $FePO_4$ particles generated with Fe^{3+} salt can show better spherical shape. Therefore, ferric iron (Fe^{3+}) salt is becoming more and more popular as iron source in hydrothermal synthesis.

Lou and Zhang (2011) used Fe^{3+} salt to synthesize $LiFePO_4$ microspheres which had both excellent high-rate performance and high tap density. In this research, H_3PO_4 and $Fe(NO_3)_3$ were mixed in sodium dodecylsulfate (SDS, 0.5 wt%) solution, then sealed in a teflon-lined stainless steel autoclave and heated at 170℃ for 4 hours. After that,

LiOH and polyethylene glycol (PEG-1000) were mixed with the $FePO_4 \cdot 2H_2O$ precursor, and calcined at 650°C for 10 hours in Ar flow to generate $LiFePO_4$ powders.

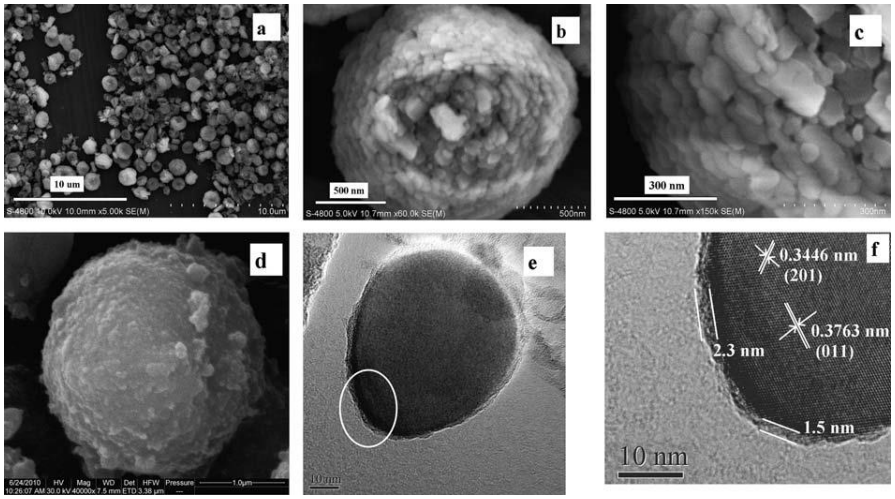

Figure 1-21 SEM (a, b, c, and d) and TEM (e and f) images for synthesized $FePO_4 \cdot 2H_2O$ precursors and the as-synthesized $LiFePO_4$/C. The SEM images a, b and c are for panorama, individual and partial $FePO_4 \cdot 2H_2O$ quasi-spheres, respectively. SEM image d shows a microsphere of $LiFePO_4$/C. High resolution TEM images e and f show the whole (e) and a part (f) of a $LiFePO_4$/C nanoplate; image f is the area circled with an ellipse in image e. (Lou and Zhang, 2011)

Figure 1-21 shows the size of $LiFePO_4$ particles is range from 0.5 to 2 um, and they have are quasi-spheres and composed of many densely compact nanoplates which is about 100nm size and 30 nm thickness. The $LiFePO_4$ particles have higher tap density (1.4 g cm^{-3}) as well as high discharge capacities, which can reach 116, 96, and 75 mAh g^{-1} at 10 C, 20 C and 30 C current respectively.

Shu *et al*. (2012) investigated how ammonia concentration affected the morphologies and electrochemical properties of $LiFePO_4$ in hydrothermal reaction. $LiOH \cdot H_2O$,

$Fe(NO_3)_3 \cdot 9H_2O$, $NH_4H_2PO_4$ and citric acid (mole ratio is 1:1:1:1) are used as raw materials. Ammonia solution with different concentration (0, 0.2, 0.4, 0.6 and 1.6 mol L^{-1}) is added into the mixture and stirred for 30 mins. Then the mixture solution is sealed in Teflon-lined stainless autoclave and maintained at 180 ℃ for 6 hours.

Figure 1-22 shows the morphology of precursors synthesized with different ammonia concentration. In this work, both citric and auxiliary ligand control the morphology of particles. Citric acid can help to prevent the agglomeration process and limit particle growth. Ammonia can affect the orientation and rate crystal growth; because it has chelating ability for some transition-metal ions, results in the releasing of free iron ions in this synthetic system (Bindu, Kingston and Sudheendra, 2004). Therefore, the $LiFePO_4$/C synthesized by 0.4 mol L^{-1} ammonia shows the most homogeneous spherical morphology, the least average particles size (2 um), and the best electrochemical performance (discharge capacities are 168.7, 165.0, 160.7, 155.8, 144.4, 125.0 mAh g^{-1} at 0.1 C, 0.2 C, 0.5 C, 1 C, 2 C and 5 C).

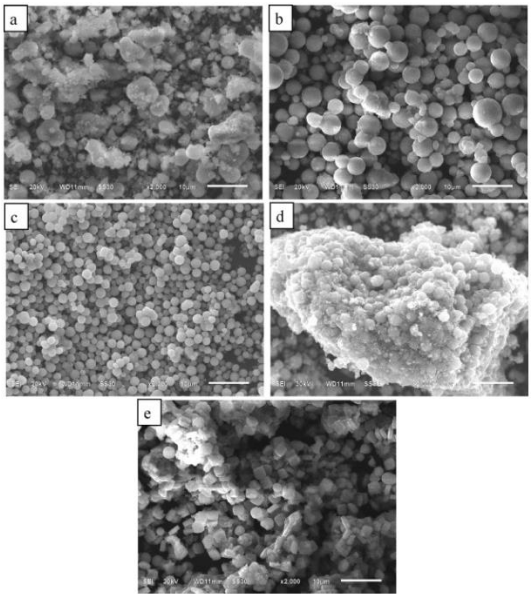

Figure 1-22 SEM photographs of the precursors of $LiFePO_4$/C synthesised with different ammonia concentrations of (a) 0 mol L^{-1}, (b) 0.2 mol L^{-1}, (c) 0.4 mol L^{-1}, (d) 0.6 mol L^{-1} and (e) 1.6 mol L^{-1} (Shu *et al.*, 2012).

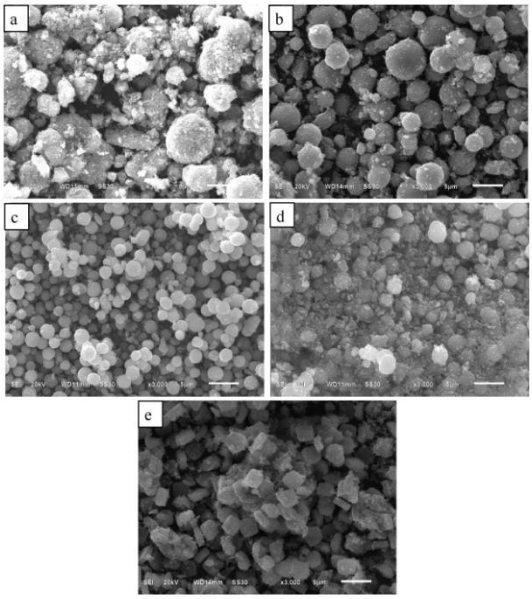

Figure 1-23 SEM photographs of $LiFePO_4$/C synthesized with different ammonia concentrations of (a) 0 mol L^{-1}, (b) 0.2 mol L^{-1}, (c) 0.4 mol L^{-1}, (d) 0.6 mol L^{-1} and (e) 1.6 mol L^{-1} (Shu *et al.*, 2012).

Lu *et al*. (2012) developed a membrane dispersion microreactor with microfiltration membrane to synthesize $LiFePO_4$ with hydrothermal treatment. The experimental setup is shown in Figure 1-24. In this work, $(NH_4)_3PO_4$ and $Fe(NO_3)_3 \cdot 9H_2O$ are used as starting materials and H_3PO_4 is used to adjust pH value and suppress the formation of $Fe(OH)_3$. The starting materials are mixed in the membrane dispersion microreactor continuously. Then the mixture is stirred for 1 hour before hydrothermal treatment. This method can produce $LiFePO_4$ with high purity, well dispersion and narrow size distribution around 59 nm.

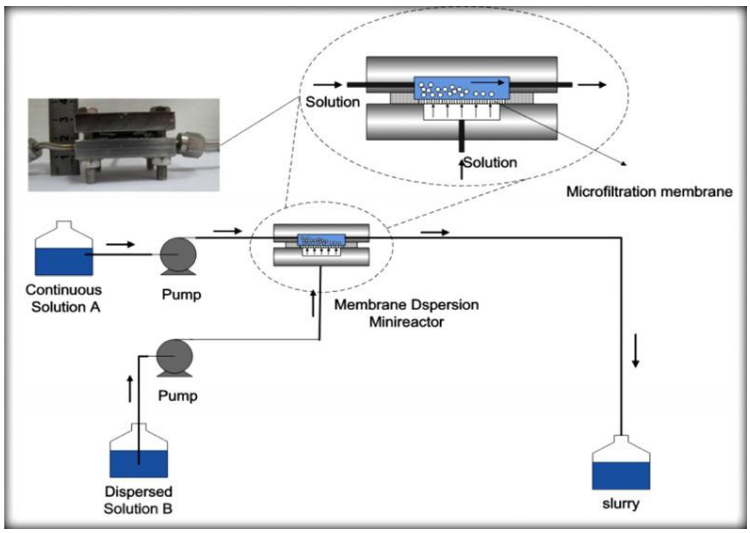

Figure 1-24 Experimental setup of fast precipitation using microcontactor. (Lu *et al*., 2012)

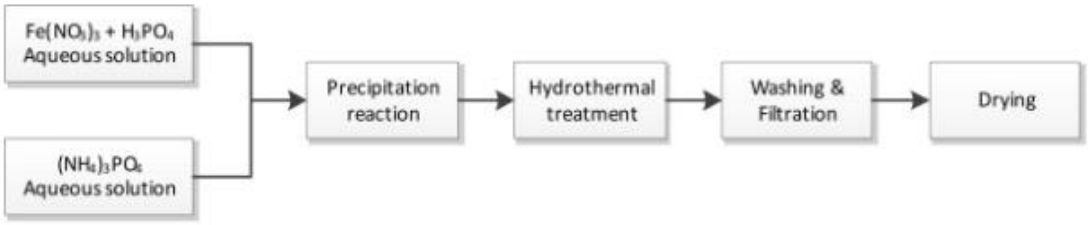

Figure 1-25 Experimental procedures of iron phosphate preparation. (Lu *et al*., 2012)

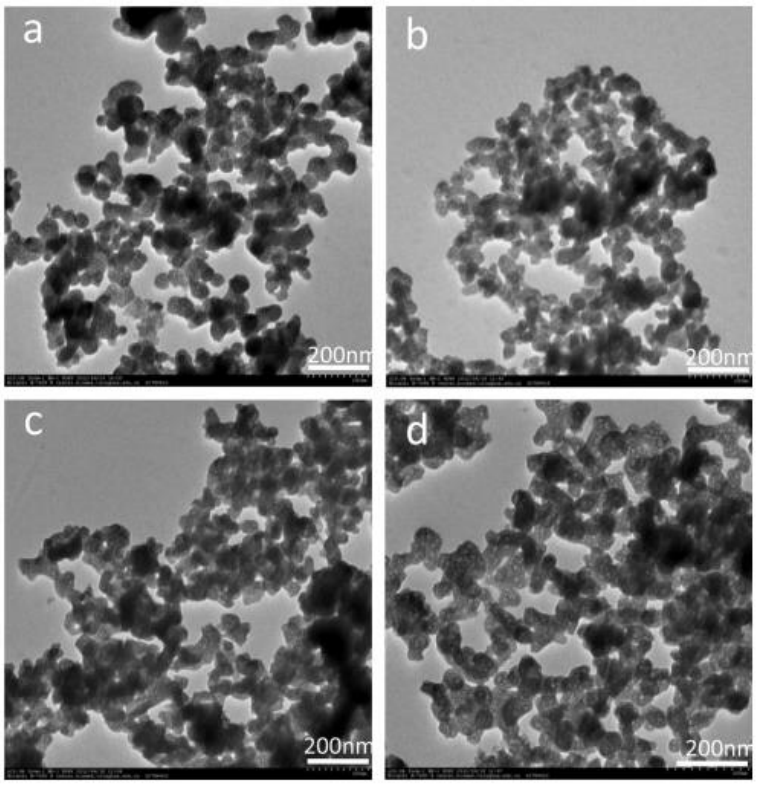

Figure 1-26 TEM photographs of $FePO_4$ nanomaterials without hydrothermal treatment (a) and with hydrothermal treatment for 10 min (b), 20 min (c) and 1 h (d), respectively. (Lu *et al*., 2012)

The kinetics of Li^+ insertion and extraction process is the primary mechanism to determine the battery delivery rate capability of a LFP-based electrode. This kinetics

involved consists of three main steps: (i) electron and Li^+ diffusion to/from the bulk material within the bulk material (solid phase); (ii) charge transfer reactions (electrochemical reactions) at the interface of the electrode/electrolyte; and (iii) Li^+ diffusion from/to the interface in electrolyte phase (Liu *et al*., 2011; Liu and Manthiram, 2011). Significant amount of efforts have been made on developing new methods to facilitate the kinetics of Li^+ insertion and extraction process, and improving the rate performance of $LiFePO_4$. Reducing the particle size and preparing nano-scale positive electrode materials have been proved to be one of the effective ways to shorten the Li^+ diffusion path and facilitate the kinetics of steps. Additionally, fabrication of positive electrode material possessing the porous structures can also increase electrode/electrolyte interface area and ensure effective electrolyte permeation (Wang, Li and Chen, 2015; Vu, Qian and Stein, 2012). The porous structures would be beneficial to the improvement on the rate performance of $LiFePO_4$. It should be emphasized here, however, that only meso- and macroporous structure is desirable, since the smaller size of micropores can hinder the reversibility of Li^+ insertion process and reduce the active interfaces of the electrode/electrolyte by an increased potential of blockage from residual carbon (Doherty, Caruso and Drummond, 2010; Adelhelm *et al*., 2007). Micropores may also cause the formation of an extensive solid electrolyte interface (SEI) layer and inhibit charge transfer across the interfaces, resulting in a decrease in conductivity (Wang *et al*., 2006). The application of $LiFePO_4$ in lithium ion battery requires an optimal combination of high porosity and surface area to provide excellent electrochemical properties.

References

1. Shu H., Wang X., Wen W. , Liang Q. , Yang X., Wei Q., Hu B., Liu L., Xue X., Song Y., Zho M., Bai Y., Jiang L. , Chen M., Yang S., Tan J., Liao Y., and Jiang H., 2013, Effective enhancement of electrochemical properties for $LiFePO_4$/C cathode materials by Na and Ti co-doping, Eletrochimica Acta, 89, 479-487

2. Gibot P., Casas-Cabanas M., Laffont L., Levasseur S., Carlach P., Hamelet S., Tarascon J.M., and Masquelier C., 2008, Room-temperature single-phase Li insertion/extraction in nanoscale $LixFePO_4$, Nature Materials, 7, 741-747

3. Ding Y., Jiang Y., Xu F., Yin J., Ren H., Zhuo Q., Long Z., and Zhang P., 2010, Preparation of nano-structured $LiFePO_4$/graphene composites by co-precipitation method, Eletrochemistry Communication, 12, 10-13

4. Park K.S., Son J.T., Chung H.T., Kim S.J., Lee C.H., and Kim H.G., 2003, Synthesis of $LiFePO_4$ by co-precipitation and microwave heating, Eletrochemistry Communication, 5, 839-842

5. Padhi K., Nanjundaswamy K. S., Masquelier C., Okada S., and Goodenough J. B., 1997, Effect of structure on the Fe^{3+} /Fe^{2+} redox couple in iron phosphates., Journal of the Electrochemistry Society, 144, 1609-1613

6. Dai C., Chen Z., Jin H., and Hu X., 2010, Synthesis and performance of $Li_3(V_{1-x}Mg_x)_2(PO_4)_3$ cathode materials. Journal of Power Sources, **195**, 5775-5779.

7. Shin H.C., Park S.B., Jang H., Chung K.Y., Cho W., Kim C.S., and Cho B.W., 2008, Rate performance and structural change of Cr-doped $LiFePO_4$/C during cycling, Eletrochimica Acta, 53, 7946-7951

8. Chung S.Y., Bloking J.T., and Chiang Y.M., 2002, Electronically conductive phospho-olivines as lithium storage electrodes, Nature Material, 1, 123-128

9. Guo L., Zhang Y., Ma L., Zhang Y., Wang E., Bi Y., Wang D., McKee W.C., Xu Y., Chen J., Zhang Q., Nan C., Gu L., Bruce P.G., and Peng Z.G., 2015, Unlocking the energy capabilities of micron-sized $LiFePO_4$, Nature Communication, 6, 7898-7905

10. Shin H.C., Chung K.Y., Min W.S., Byun D.J., Jang H., and Cho B.W., 2008, Asymmetry between charge and discharge during high rate cycling in $LiFePO_4$ – In Situ X-ray diffraction study. Electrochemistry Communications, **10**, 536-540.

11. Wang C.W., Sastry A.M., Striebel K.A., and Zaghib K., 2005, Extraction of Layerwise Conductivities in Carbon-Enhanced, Multilayered $LiFePO_4$ Cathodes. Journal of The Electrochemical Society, **152**, A1001-A1010.

12. Saravanan K., Reddy M.V., Balaya P., Gong H., Chowdari B.V.R., and Vittal J.J., 2009, Storage performance of $LiFePO_4$nanoplates. Journal of Materials Chemistry, **19**, 605-610.

13. Choi D. and P.N. Kumta, 2007, Surfactant based sol–gel approach to nanostructured $LiFePO_4$ for high rate Li-ion batteries. Journal of Power Sources, **163**, 1064-1069.

14. Wang K.X., Li X.H., and Chen J.S., 2015, Surface and interface engineering of electrode materials for lithium-ion batteries, Advanced Materials, 27, 527-545

15. Shi Y., Chou S.L., Wang J.Z., Wexler D., Li H.J., Liu H.K. and Wu Y.P., 2012, Graphene wrapped $LiFePO_4$/C composites as cathode materials for Li-ion batteries with enhanced rate capability, Journal of Materials Chemistry, 22, 16465-16470

16. Zhang J., Zhuo L., Zhang L., Wu C., Zhang X., and Wang L., 2011, Synthesis and electrochemical properties of $LiFePO_4$/C composite cathode material prepared by a new route using supercritical carbon dioxide as a solvent, Journal of Materials Chemistry, **21**, 6975-6980.
17. Park K.S., Son J.T., Chung H.T., Kim S.J., Lee C.H., Kang K.T., and Kim H.G., 2004, Surface modification by silver coating for improving electrochemical properties of $LiFePO_4$. Solid State Communications, **129**, 311-314.
18. Hu Y.S., Guo Y.G., Dominko R., Gaberscek M., Jamnik., and Maier J., 2007, Improved Electrode Performance of Porous $LiFePO_4$ Using RuO2 as an Oxidic Nanoscale Interconnect. Advanced Materials, **19**, 1963-1966.
19. Bilecka I., Hintennach A., Rossell M.D., Xie D., Novak P., and Niederberger M., 2011, Microwave-assisted solution synthesis of doped $LiFePO_4$ with high specific charge and outstanding cycling performance. Journal of Materials Chemistry, **21**, 5881-5890.
20. Wang Z., Sun S., Xia D., Chu W., Zhang S., and Wu Z., 2008, Investigation of electronic conductivity and occupancy sites of mo doped into $LiFePO_4$ by ab Initio calculation and X-ray absorption spectroscopy. The Journal of Physical Chemistry C, **112**, 17450-17455.

21. Ge Y., Yan X., Liu J., Zhang X., Wang J., He X., Wang R., and Xie H., 2010, An optimized Ni doped $LiFePO_4$/C nanocomposite with excellent rate performance. Electrochimica Acta, **55**, 5886-5890.
22. Zhou H., Li D., Hibino M., and Honma I., 2005, A self-ordered, crystalline-glass, mesoporous nanocomposite for use as a lithium-based storage device with both high power and high energy densities. Angewandte Chemie Interational Edition, **44**, 797-802.
23. Wang Y., Li H., He P., Hosono E., and Zhou H., 2010, Nano active materials for lithium-ion batteries. Nanoscale, **2**, 1294-1305.
24. Gaberscek M., Dominko R., and Jamnik J., 2007, Is small particle size more important than carbon coating? An example study on $LiFePO_4$ cathodes. Electrochemistry Communications, **9**, 2778-2783.
25. Schüth F., 2005, Engineered Porous Catalytic Materials. Annual Review of Materials Research, **35**, 209-238.
26. Vu A., Qian Y., and Stein A., 2012, Porous electrode materials for lithium-ion batteries - how to prepare them and what makes them special, Advanced Energy Materials, 2, 1056-1085.
27. Wan Y., Shi Y., and Zhao D., 2007, Designed synthesis of mesoporous solids via nonionic-surfactant-templating approach. Chemical Communication (Cambridge England), 9, 897-926.
28. Hatton B., Landskron K., Whitnall W., Perovic D., and Ozin G.A., 2005, Past, Present, and Future of Periodic Mesoporous Organosilicas-The PMOs. Accounts of Chemical Research, **38**, 305-312.

29. Lu A.H. and Schüth F., 2006，Nanocasting: A Versatile Strategy for Creating Nanostructured Porous Materials. Advanced Materials, **18**，1793-1805.

30. Stein A., Li F., and Denny N.R., 2008，Morphological Control in Colloidal Crystal Templating of Inverse Opals, Hierarchical Structures, and Shaped Particles. Chemistry of Materials, **20**, 649-666.

31. Jeffryes C., Campbell J., Li H., Jiao J., and Rorrer G., 2011, The potential of diatom nanobiotechnology for applications in solar cells, batteries, and electroluminescent devices. Energy & Environmental Science, **4**(10), 3930-3941.

32. Doherty M., Caruso R.A., and Drummond C.J., 2010, High performance $LiFePO_4$ electrode materials: influence of colloidal particle morphology and porosity on lithium-ion battery power capability, Energy & Environmental Science, 3, 813-823

33. Lee T.J., Cheng T.T., Juang H.K., and Chen S.Y., 1993, Relationship of cathode pore-size distribution and rated capacity in Li MnO2 cells. Journal of Power Sources, **44**(1-3), 709-712.

34. Jiao F., Bao J., Hill A.H., and Bruce P.G., 2008, Synthesis of ordered mesoporous Li-Mn-O spinel as a positive electrode for rechargeable lithium batteries. Angewandte Chemie International Edition, 47, 9711-9716.

35. Lakes R., 1993, Materials with structural hierarchy. Nature, **361**(11), 511-515.

36. Chen H.Y., Kuang D.B., and Su C.Y., 2012, Hierarchically micro/nanostructured photoanode materials for dye-sensitized solar cells. Journal of Materials Chemistry, **22**(31), 15475-15489.

37. Uchiyama H., Hosono E., Zhou H., and Imai H., 2009, Three-dimensional architectures of spinel-type LiMn2O4 prepared from biomimetic porous carbonates and their application to a cathode for lithium-ion batteries. Journal of Materials Chemistry, **19**(23), 4012-4016.
38. Wu Y., Wen Z., and Li J., 2011, Hierarchical carbon-coated $LiFePO_4$ nanoplate microspheres with high electrochemical performance for Li-ion batteries. Advanced Materials, **23**(9), 1126-1129.
39. Sun C., Rajasekhara S., Goodenough J.B., and Zhou F., 2011, Monodisperse porous $LiFePO_4$ microspheres for a high power Li-ion battery cathode. Journal of American Chemical Society, **133**(7), 2132-2135.
40. Jin S., Deng H., Long D., Liu X., Zhan L., Liang X., Qiao W., and Ling L., 2011, Facile synthesis of hierarchically structured Fe3O4/carbon micro-flowers and their application to lithium-ion battery anodes. Journal of Power Sources, **196**(8), 3887-3893.
41. Saravanan K., Balaya P., Reddy M.V., Chowdari B.V.R., and Vittal J.J., 2010, Morphology controlled synthesis of $LiFePO_4$/C nanoplates for Li-ion batteries. Energy & Environmental Science, **3**(4), 457-464.
42. Yuan C.Z., Gao B., Shen L.F., Yang S.D., Hao L., Lu X.J., Zhang F., Zhang L.J., and Zhang X.G., 2011, Hierarchically structured carbon-based composites: Design, synthesis and their application in electrochemical capacitors. Nanoscale, **3**(2), 529-545.
43. Li Y., Fu Z.Y., and Su B.L., 2012, Hierarchically Structured Porous Materials for Energy Conversion and Storage. Advanced Functional Materials, **22**(22), 4634-4667.

44. Fang B., Kim J.H., Kim M.S., and Yu J.S., 2013, Hierarchical Nanostructured Carbons with Meso–Macroporosity Design, Characterization, and Applications. Accounts of Chemical Research, **46**(7), 1397-1406.
45. Edström K., Gustafsson T., and Thomas J.O., 2004, The cathode–electrolyte interface in the Li-ion battery. Electrochimica Acta, **50**(2-3), 397-403.
46. Goodenough J.B. and Kim Y., 2010, Challenges for Rechargeable Li Batteries. Chemistry of Materials, **22**(3), 587-603.
47. Lee S.H., You H.G., Han K.S., Kim J., Jung I.H., and Song J.H., 2014, A new approach to surface properties of solid electrolyte interphase on a graphite negative electrode. Journal of Power Sources, **247**, 307-313.
48. Myung S.T., Amine K., and Sun Y.K., 2010, Surface modification of cathode materials from nano- to microscale for rechargeable lithium-ion batteries. Journal of Materials Chemistry, **20**(34), 7074-7095.
49. Meng X., Yang X.Q., and Sun X., 2012, Emerging applications of atomic layer deposition for lithium-ion battery studies. Advanced Materials, **24**(27), 3589-3615.
50. Zhao J. and Wang Y., 2013, Atomic layer deposition of epitaxial ZrO2 coating on LiMn2O4 nanoparticles for high-rate lithium ion batteries at elevated temperature. Nano Energy, **2**(5), 882-889.
51. Kulmala M., 2003, How particles nucleate and grow. Science, **302**, 1000-1001.
52. Dirksen J.A. and Ring T.a., 1991, Fundamentals of crystallization Kinetic effects on particle size distributions and morphology. Chemical Engineering Science, **46**(10), 2389-2427.
53. Baldyga J., Bourne J.R., and Hearn S.J., 1997, Interaction between chemical reactions and mixing on various scales. Chemical Engineering Science, **52**(4), 457-466.

54. Bhattacharya S. and Kresta S.M., 2004, Surface Feed with Minimum by-Product Formation for Competitive Reactions. Chemical Engineering Research and Design, **82**(9), 1153-1160.

55. Zhang Q.C., Liu Z.W., Zhu X.H., Wen L.X., Zhu Q.f., Guo K., and Chen J.F., 2015, Application of Microimpinging Stream Reactors in the Preparation of $CuO/ZnO/Al_2O_3$ Catalysts for Methanol Synthesis. Industrial Engineering Chemistry Research, 54, 8874-8882.

56. Zhang Q.C., Cheng K.P., Wen L.X., Guo K., and Chen J.F., 2016, A study on the precipitating and aging processes of $CuO/ZnO/Al_2O_3$ catalysts synthesized in micro-impinging stream reactors. RSC Advances. 6, 33611-33621.

57. Huang Y., Wang P., Yuan Y., and Yang F., 2015, Synergistic degradation of chitosan by impinging stream and jet cavitation. Ultrasonics Sonochemistry, 27, 592-601

58. Zhou Z., Liu S., and Liu Y., 2012, Synthesis of $Y_3Al_5O_{12}:Ce^{3+}$ phosphors by a modified impinging stream method: a crystal growth and luminescent properties study. Journal of Physics *D-Applied* Physics. 45, 195105-195112.

59. Valente I., Celasco E., Marchisio D.L., and Barresi A.A., 2012, Nanoprecipitation in confined impinging jets mixers: Production, characterization and scale-up of pegylated nanospheres and nanocapsules for pharmaceutical use. Chemical Engineering Science. 77, 217-227.

60. Xiao Y., Pu W., Wan W., and Cui Y., 2013, Preparation and Performance of the Cathode Precursor Ferric Phosphate for Li-ion Battery Facilitated by Impinging Stream. International Journal of Electrochemical Science. 8, 938-948.

61. Yan P., Lu L., Liu X. M., Cao Y., Zhang Z. P., Yang H., and Shen X.D., 2013, An economic and scalable approach to synthesize high power $LiFePO_4$/C nanocomposites from nano-$FePO_4$ precipitated from an impinging jet reactor, Journal of Materials Chemistry *A, 35, 10429-10435*

62. Andreussi T., Galletti C., Mauri R., Camarri S., and Salvetti M. V., 2015, Flow regimes in T-shaped micro-mixers. *Computers* & *Chemical* Engineering, 76, 150-159.

63. Krupa K., Nunes M.I., Santos R.J., and Bourne J.R., 2014, Characterization of micromixing in T-jet mixers. Chemical Engineering Science, 111, 48-55.

64. Siddiqui S.W., Unwin P.J., Xu Z., and Kresta S.M., 2009, The effect of stabilizer addition and sonication on nanoparticle agglomeration in a confined impinging jet reactor. Colloid and Surface A: Physicochemical and Engineering Aspects, 350, 38-50.

65. Simson G., Prasetyo E., Reiner S., and Hinrichsen O., 2013, Continuous precipitation of Cu/ZnO/Al_2O_3 catalysts for methanol synthesis in microstructured reactors with alternative precipitating agents. *Applied* Catalysis A: General. 450, 1-12.

66. Kaluza S., Behrens M., Schiefenhovel N., Kniep B., Fischer R., Schlogl R., and Muhler M., 2011, A Novel Synthesis Route for Cu/ZnO/Al_2O_3 Catalysts used in Methanol Synthesis: Combining Continuous Consecutive Precipitation with Continuous Aging of the Precipitate. ChemCatChem, 3, 189-199.

67. Jiang M., Li Y.D., Tung H.H., and Braatz R. D., 2015, Effect of jet velocity on crystal size distribution from antisolvent and cooling crystallizations in a dual

impinging jet mixer. *Chemical* Engineering and *Processing*: *Process* Intensification. 97, 242-247.

68. Casanova H. and Higuita L.P., 2011, Synthesis of calcium carbonate nanoparticles by reactive precipitation using a high pressure jet homogenizer. Chemical Engineering Journal. 175, 569-578.
69. Tari T., Fekete Z., Revesz P. S., Aigner Z., 2015, Reduction of glycine particle size by impinging jet crystallization. International Journal of Pharmaceutics. 478, 96-102.
70. Wu G., Zhou H., and Zhu S., 2007, Precipitation of barium sulfate nanoparticles via impinging streams. Materials Letter. 61, 168-170.
71. Li Z., Zhang F., Meng A., Xie C., and Xing J., 2015, ZnO/Ag micro/nanospheres with enhanced photocatalytic and antibacterial properties synthesized by a novel continuous synthesis method. RSC Advances. 5, 612-620.
72. Kumar D. V. R., Prasad B.L.V., and Kulkarni A.A., 2013, Impinging Jet Micromixer for Flow Synthesis of Nanocrystalline MgO: Role of Mixing/Impingement Zone. Industrial Engineering Chemistry & Reserach. 52, 17376-17382.
73. Liu Z., Guo L., Huang T., Wen L., and Chen J., 2014, Experimental and CFD studies on the intensified micromixing performance of micro-impinging stream reactors built from commercial T-junctions. Chemical Engineering Science. 119, 124-133.
74. Siddiqui S.W., Zhao Y., Kukukova A., and Kresta S.M., 2009, Characteristics of a Confined Impinging Jet Reactor Energy Dissipation Homogeneous and Heterogeneous Reaction Products and Effect of Unequal Flow. Industrial Engineering Chemistry & Reserach. 48, 7945-7958.

75. Liu Y. and Fox R.O., 2006, CFD predictions for chemical processing in a confined impinging-jets reactor. AIChE Journal, 52, 731-744
76. Fonte C.P., Sultan M.A., Santos R.J., Dias M.M., and Lopes J.C.B., 2015, Flow imbalance and Reynolds number impact on mixing in Confined Impinging Jet. Chemical Engineering Journal. 260, 316-330.
77. Shi Z.H., Li W.F., Du K.J., Liu H.F., and Wang F.C., 2015, Experimental study of mixing enhancement of viscous liquids in confined impinging jets reactor at low jet Reynolds numbers. Chemical Engineering Science, 138, 216-226.
78. Borukhova, S., Noel T., and Hessel V., 2016, Continuous-Flow Multistep Synthesis of Cinnarizine, Cyclizine, and a Buclizine Derivative from Bulk Alcohols. ChemSusChem. 9, 67-74
79. Polyzoidis A., Altenburg T., Schwarzer M., Loebbecke S., and Kaskel S., 2016, Continuous microreactor synthesis of ZIF-8 with high space–time-yield and tunable particle size. Chemical Engineering Journal, 283, 971-977.
80. Kolmykov O., Commenge J.M., Alem H., Girot E., Mozet K., Medjahdi G., and Schneider R., 2017, Microfluidic reactors for the size-controlled synthesis of ZIF-8 crystals in aqueous phase. Materials & Design. 122, 31-41.
81. Wong S., Ward M., and Wharton C., 2004, Micro T-mixer as a rapid mixing micromixer. Sensors and Actuators B: Chemical. 2004, 100, 359-379.
82. Soleymani A., Kolehmainen E., and Turunen I., 2008, Numerical and experimental investigations of liquid mixing in T-type micromixers. Chemical Engineering Journal, 2008, 135, S219-S228.
83. Gobby D., Angeli P., and Gavriilidis A., 2001, Mixing characteristics of T-type microfluidic mixers. Journal of Micromechanics and Microengineering, 2001, 126-132.

84. Gradl J., Schwarzer H.C., Schwertfirm F., Manhart M., Peukert W., 2006, Precipitation of nanoparticles in a T-mixer: Coupling the particle population dynamics with hydrodynamics through direct numerical simulation. Chemical Engineering and Processing: Process Intensification, 2006, 45, 908-916.

85. Asgharzadehahmadi S., Raman A.A.A., Parthasarathy R., and Sajjadi B., 2016, Sonochemical reactors: Review on features, advantages and limitations. Renewable and Sustainable Energy Reviews, 63, 302-314.

86. Monnier H., Wilhelm A.M., and Delmas H., 1999, Influence of ultrasound on mixing on the molecular scale for water and viscous liquids. Ultrasonics Sonochemistry, 6, 67-74.

87. McNamara W. B., Didenko Y. T., and Suslick K. S., 1999, Sonoluminescence temperatures during multi-bubble cavitation. Nature, 401, 772-775.

88. Mason, T.J. and Cordemans E.D., 1996, Ultrasonic intensification of chemical processing and related operations. Chemical Engineering Research and Design, 74, 511-516.

89. Noël T., Naber J.R., Hartman R.L., McMullen J.P., Hensen K.F., and Buchwald S.L., 2011, Palladium-catalyzed amination reactions in flow: overcoming the challenges of clogging via acoustic irradiation. Chemical Science, 2, 287-290.

90. Rivas D.F. and Kuhn S., 2016, Synergy of Microfluidics and Ultrasound : Process Intensification Challenges and Opportunities. Topic in Current Chemistry, 374, 70-99.

91. Sedelmeier J., Ley S.V., Baxendale I.R., and Baumann M., 2010, KMnO4-Mediated Oxidation as a Continuous Flow Process. Organic Letters, 12, 3618-3621.

92. Horie T., Sumino M., Tanaka T., Matsushita Y., Ichimura T., and Yoshida J., 2010, Photodimerization of Maleic Anhydride in a Microreactor Without Clogging. Organic Process Research & Development, 14, 405-410.

93. Zhang L., Geng M., Teng P., Zhao D., Lu X., and Li J.X., 2012, Ultrasound-promoted intramolecular direct arylation in a capillary flow microreactor. Ultrasonics Sonochemistry, 19, 250-256.

94. Sancheti S.V. and Gogate P.R., 2017, A review of engineering aspects of intensification of chemical synthesis using ultrasound. Ultrasonics Sonochemistry, **36**, 527-543.

95. Gutierrez M. and Henglein A., 1990, Chemical action of pulsed ultrasound observation of an unprecedented intensity effect. The journal of Physical Chemistry, **94**(9), 3625-3628.

96. Bansode S.R. and Rathod V.K., 2014, Ultrasound assisted lipase catalysed synthesis of isoamyl butyrate. Process Biochemistry, **49**(8), 1297-1303.

97. Khan N.R., Jadhav S.V., and Rathod V.K., 2015, Lipase catalysed synthesis of cetyl oleate using ultrasound: Optimisation and kinetic studies. Ultrasonics Sonochemistry, **27**, 522-529.

98. Waghmare G.V., Vetal M.D., and Rathod V.K., 2015, Ultrasound assisted enzyme catalyzed synthesis of glycerol carbonate from glycerol and dimethyl carbonate. Ultrasonics Sonochemistry, **22**, 311-316.

99. Ammar H.B., Chtourou M., Frikha M.H., and Trabelsi M., 2015, Green condensation reaction of aromatic aldehydes with active methylene compounds catalyzed by anion-exchange resin under ultrasound irradiation. Ultrasonics Sonochemistry, **22**, 559-564.

100. Safari J. and Javadian L., 2015, Ultrasound assisted the green synthesis of 2-amino-4H-chromene derivatives catalyzed by Fe_3O_4-functionalized nanoparticles with chitosan as a novel and reusable magnetic catalyst. Ultrasonics Sonochemistry,. **22**, 341-348.

101. Li D.J., Song J., Xu A., and Liu C., 2014, Optimization of the ultrasound-assisted synthesis of lutein disuccinate using uniform design. Ultrasonics Sonochemistry, **21**(1), 98-103.

102. Rabiei K. and Naeimi H., 2015, Ultrasonic assisted synthesis of gem-dichloroaziridine derivatives using Mg/CCl4 under neutral conditions. Ultrasonics Sonochemistry, **24**, 150-154.

103. Dange P.N., Kulkarni A.V., and Rathod V.K., 2015, Ultrasound assisted synthesis of methyl butyrate using heterogeneous catalyst. Ultrasonics Sonochemistry, **26**, 257-264.

104. Thompson L.H. and Doraiswamy L.K., 1999, Sonochemistry Science and Engineering. Industrial & Engineering Chemistry Research, **38**(4), 1215-1249.

105. Gogate P.R., 2008, Cavitational reactors for process intensification of chemical processing applications: A critical review. Chemical Engineering and Processing: Process Intensification, **47**(4), 515-527.

106. Son Y., Lim M., and Khim J., 2009, Investigation of acoustic cavitation energy in a large-scale sonoreactor. Ultrasonics Sonochemistry, **16**(4), 552-556.

107. Vivekanand P.A. and Wang M.L., 2011, Sonocatalyzed synthesis of 2-phenylvaleronitrile under controlled reaction conditions--a kinetic study. Ultrasonics Sonochemistry, **18**(5), 1241-1248.

108. Francony A. and Pétrier C., 1996, Sonochemical degradation of carbon tetrachloride in aqueous solution at two frequencies 20 kHz and 500 kHz. Ultrasonics Sonochemistry, **3**(2), S77-S82.

109. Entezari M.H., Heshmati A., and Sarafraz-Yazdi A., 2005, A combination of ultrasound and inorganic catalyst: removal of 2-chlorophenol from aqueous solution. Ultrasonics Sonochemistry, **12**(1-2), 137-141.

110. Kruusa P., Burk R.C., Entezari M.H., and Otson R., 1997, Sonication of aqueous solutions of chlorobenzene. Ultrasonics Sonochemistry, **4**(3), 229-233.

111. Vichare N.P., Senthilkumar P., Moholkar V.S., Gogate P.R., and A.B. Pandit., 2000, Energy Analysis in Acoustic Cavitation. Industrial & Engineering Chemistry Research, **39**(5), 1480-1486.

112. Raskar H.D., Avhad D.N., and Rathod V.K., 2014, Ultrasound assisted production of daunorubicin: Process intensification approach. Chemical Engineering and Processing: Process Intensification, **77**, 7-12.

113. Avhad D.N., Niphadkar S.S., and Rathod V.K., 2014, Ultrasound assisted three phase partitioning of a fibrinolytic enzyme. Ultrasonics Sonochemistry, **21**(2), 628-633.

114. Delgado-Povedano M.M. and Luque de Castro M.D., 2015, A review on enzyme and ultrasound: A controversial but fruitful relationship. Analytical Chimica Acta, **889**, 1-21.

115. Ilievsk D. and White E.T., 1994, Agglomeration during precipitation agglomeration mechanism identification for $Al(OH)_3$ crystals in stirred caustic aluminate solutions. Chemical Engineering Science, **49**, 3227-3239.

116. Ilievski D. and Hounslow M.J., 1995, Agglomeration during precipitation II. Mechanism deduction from tracer data. AIChE Journal, **41**, 525-535.

117. Brunsteiner, M., jones A.G., Pratola F., Price S.L., and Simons S.J.R., 2005, Toward a Molecular Understanding of Crystal Agglomeration. Crystal Growth & Design, **5**, 3-16.

118. Wu G., Zhou H., and Zhu S., 2007, Precipitation of barium sulfate nanoparticles via impinging streams. Materials Letter. 61, 168-170.

119. Ilievski D. and Hounslow M.J., 1995, Agglomeration during precipitation II. Mechanism deduction from tracer data. AIChE Journal, **41**, 525-535.

120. W.S. Kim., Kim W.S., Kim K.S., Kim J.S., and Ward M.D., 2004, Crystal agglomeration of europium oxalate in reaction crystallization using double-jet semi-batch reactor. Materials Research Bulletin, **39**(2), 283-296.

121. Sung M.H., Choi I.S., Kim J.S., Kim W.S., 2000, Agglomeration of Yttrium Oxalate Particles Produced by Reaction Precipitation in Semi-Batch Reactor. Chemical Engineering Science, 55, 2173-2184

122. AWójcika J. and GJonesa A., 1998, Particle disruption of precipitated $CaCO_3$ crystal agglomerates in turbulently agitated suspensions. Chemical Engineering Science, **53**, 1097-1101.

123. Wójcik J.A. and Jones A.G., 1997, Experimental Investigation into Dynamics and Stability of Continuous MSMPR Agglomerative Precipitation of CaCO3 Crystals. Chemical Engineering Research and Design, **75**(2), 113-118.

124. Jung W.M., Kang S.H., Kim W.S., and Choi C.K., 2000, Particle morphology of calcium carbonate precipitated by gas–liquid reaction in a Couette–Taylor reactor. Chemical Engineering Science, **55**, 733-747.

125. Ålander E.M., Uusi-Penttila M.S., and Rasmuson Å.C., 2004, Agglomeration of Paracetamol during Crystallization in Pure and Mixed Solvents. Industrial & Engineering Chemistry Research, **43**, 629-637.

126. Ålander E.M. and Rasmuson Å.C., 2007, Agglomeration and adhesion free energy of paracetamol crystals in organic solvents. AIChE Journal, **53**(10) 2590-2605.

127. Arnold G., Garche J., Hemmer R., Strobele S., Vogler C., Wohlfahrt-Mehrens M., 2003, Fine-particle lithium iron phosphate $LiFePO_4$ synthesized by a new low-cost aqueous precipitation technique. Journal of Power Sources, 119-121, 247-251

128. Zheng J., Li X., Wang Z., Guo H., and Zhou S., 2008, $LiFePO_4$ with enhanced performance synthesized by a novel synthetic route. Journal of Power Sources, **184**(2), 574-577.

129. Jugovic D., Mitric M., Cvjeticanin N., Jancar., Mentus S., and Uskokovic D., 2008, Synthesis and characterization of $LiFePO_4$/C composite obtained by sonochemical method. Solid State Ionics, **179**(11-12), 415-419

130. Hench L.L. and West J.K., 1990, The Sol-Gel Process. Chemical Review, **90**, 33-72

131. Iltchev N., Chen Y., Okada S., and Yamaki J., 2003, $LiFePO_4$ storage at room and elevated temperatures. Journal of Power Sources, **119-121**, 749-754.

132. Hsu K.F., Tsay S.Y., and Hwang B.J., 2005, Physical and electrochemical properties of $LiFePO_4$/carbon composite synthesized at various pyrolysis periods. Journal of Power Sources, **146**(1-2), 529-533.

133. Dominko R., Bele M., Gaberscek M., Remskar M., Hanzel D., Goupil J.M., Pejovnik S., and Jamnik J., 2006, Porous olivine composites synthesized by sol–gel technique. Journal of Power Sources, **153**(2), 274-280.

134. Padhi K., Nanjundaswamy K. S., Masquelier C., Okada S., and Goodenough J. B., 1997, Effect of structure on the Fe^{3+} /Fe^{2+} redox couple in iron phosphates., Journal of the Electrochemistry Society, 144, 1609-1613

135. Franger S., Cras F.L., Bourbon C., and Rousault H., 2003, Comparison between different $LiFePO_4$ synthesis routes and their influence on its physico-chemical properties. Journal of Power Sources, **119-121**, 252-257.

136. Yamada A., Chung S.C., and Hinokuma K., 2001, Optimized $LiFePO_4$ for Lithium Battery Cathodes. Journal of The Electrochemical Society, **148**(3), A224-A229.

137. Wang D., Wu X., Wang Z., and Chen L., 2005, Cracking causing cyclic instability of $LiFePO_4$ cathode material. Journal of Power Sources, **140**(1), 125-128.

138. Koltypin M., Aurbach D., Nazar L., and Ellis B., 2007, More on the performance of $LiFePO_4$ electrodes—The effect of synthesis route, solution composition, aging, and temperature. Journal of Power Sources, **174**(2), 1241-1250.

139. Yun N.J., Ha H.W.,Jeong K.H., Park H.Y., and Kim K., 2006, Synthesis and electrochemical properties of olivine-type $LiFePO_4$/C composite cathode material

prepared from a poly(vinyl alcohol)-containing precursor. Journal of Power Sources, **160**(2), 1361-1368.

140. Takahashi M., Tobishima S., Takei K., and Sakurai Y., 2001, Characterization of $LiFePO_4$ as the cathode material for rechargeable lithium batteries. Journal of Power Sources, **97-98**, 508-511.

141. Yang S., Zavalij P.Y., and Whittingham M.S., 2001, Hydrothermal synthesis of lithium iron phosphate cathodes. Electrochemistry Communications, **3**(9), 505-508.

142. Yang S., Song Y., Zavalij P.Y., Whittngham S.S., 2002, Reactivity, stability, and electrochemical behaviour of lithium iron phosphates. Electrochemistry Communications, **4**, 239-244.

143. Yang S., Song Y., Ngala K., Zavalij P.Y., and Whittngham S.S., 2003, Performance of $LiFePO_4$ as lithium battery cathode and comparison with manganese and vanadium oxides. Journal of Power Sources, **119-121**, 239-246.

144. Xu C., Lee J., and Teja A.S., 2008, Continuous hydrothermal synthesis of lithium iron phosphate particles in subcritical and supercritical water. The Journal of Supercritical Fluids, **44**(1), 92-97.

145. Chen J., Wang S., and Whittingham M.S., 2007, Hydrothermal synthesis of cathode materials. Journal of Power Sources, **174**(2), 442-448.

146. Zhang C., Huang X., Yin Y., Dai J., and Zhu Z., 2009, Hydrothermal synthesis of monodispersed $LiFePO_4$ cathode materials in alcohol–water mixed solutions. Ceramics International, **35**(7), 2979-2982.

147. Wang M., Yang Y., and Zhang Y., 2011, Synthesis of micro-nano hierarchical structured $LiFePO_4$/C composite with both superior high-rate performance and high tap density. Nanoscale, 3, 4434-4439.

148. Yang M.R., Teng T.H., and Wu S.H., 2006, $LiFePO_4$/carbon cathode materials prepared by ultrasonic spray pyrolysis. Journal of Power Sources, **159**(1), 307-311.

149. Konarova M. and Taniguchi I., 2008, Preparation of $LiFePO_4$/C composite powders by ultrasonic spray pyrolysis followed by heat treatment and their electrochemical properties. Materials Research Bulletin, **43**(12), 3305-3317.

150. Bewlay S.L., Konstantinov K., Wang G.X., Dou S.X., and Liu H.K., 2004, Conductivity improvements to spray-produced $LiFePO_4$ by addition of a carbon source. Materials Letters, **58**(11), 1788-1791.

151. Lou X., Hu B., Huang J., and Li T., 2006, Hydrothermal Process Synthesizing of $LiFePO_4$ with high rate capability and high tap density. Journal of Power Sources, 2015 AASRI International Conference on Industrial Electronics and Applications (IEA 2015), 15-17.

152. Wang Y., Wang Y., Hosono E., Wang K., and Zhou H., 2008, The design of a $LiFePO_4$/carbon nanocomposite with a core-shell structure and its synthesis by an in situ polymerization restriction method. Angewandte Chemie International Edition, 47, 7461-7465

153. Sun C.S., Zhang Y., Zhang X.J. and Zhou Z., 2010, Structural and electrochemical properties of Cl-doped $LiFePO_4$/C. Journal of Power Sources, 195, 3680-3683

154. Hong J., Wang Y., He G., and He M., 2012, A new approach to $LiFePO_4$/C synthesis: The use of complex carbon source without ball milling. Materials Chemistry and Physics, 133, 573-577

155. Hsieh C., Chen I., Chen W., and Wang J., 2012, Synthesis of iron phosphate powders by chemical precipitation route for high-power lithium iron phosphate cathodes. Electrochimica Acta, 83, 202-208

156. Zhu Y., Tang S., Shi H., and Hu H., 2014, Synthesis of $FePO_4 \cdot xH_2O$ for fabricating submicrometer structured $LiFePO_4$/C by a co-precipitation method. Ceramics International, 40, 2685-2690

157. Qian L., Xia Y., Zhang W., Huang H., Gan Y., Zeng H., and Tao X., 2012, Electrochemical synthesis of mesoporous $FePO_4$ nanoparticles for fabricating high performance $LiFePO_4$/C cathode materials. Microporous and Mesoporous Materials, 152, 128-133

158. Ni J.F., Zhou H.H., Chen J.T., and Zhang X.X., 2005, $LiFePO_4$ doped with ions prepared by co-precipitation method. Materials Letters, 59, 2361-2365

159. Liu H., Miao C., Meng Y., Xu Q., Zhang X. and Tang Z., 2014, Effect of graphene nanosheets content on the morphology and electrochemical performance of $LiFePO_4$ particles in lithium ion batteries, Eletrochimica Acta, 135, 311-318

160. Bai N., Chen H., Zhou W., Xiang K., Zhang Y., Li C., and Lu H., 2015, Preparation and electrochemical performance of $LiFePO_4$/C microspheres by a facile and novel co-precipitation. Electrochimica Acta, 167, 172-178

161. Han D., Ryu W., Kim W., Lim S., Kim Y., Eom J., and Kwon H., 2013, Tailoring crystal structure and morphology of $LiFePO_4$/C cathode materials synthesized by heterogeneous growth on nanostructured $LiFePO_4$ seed crystals. ACS Applied Materials & Interfaces, 5, 1342-1347

162. Zhu B.Q., Li X.H., Wang Z.X., and Guo H.J., 2006, Novel synthesis of $LiFePO_4$ by aqueous precipitation and carbothermal reduction. Materials Chemistry and Physics, **98**(2-3), 373-376.

163. Yang S., Song Y., Zavalij P.Y., and Whittingham M.S., 2002, Reactivity, stability and electrochemical behavior of lithium iron phosphates. Electrochemistry Communications, **4**(3), 239-244.

164. Jin B. and Gu H., 2008, Preparation and characterization of $LiFePO_4$ cathode materials by hydrothermal method. Solid State Ionics, **178**(37-38), 1907-1914.

165. Chen J., Vacchio M.J., Wang S., Chernova., Zavalij P.Y., and Whittingham M.S., 2008, The hydrothermal synthesis and characterization of olivines and related compounds for electrochemical applications. Solid State Ionics, **178**(31-32), 1676-1693.

166. Qin X., Wang X.H., Xiang H.M., Xie J., Li J.J., and Zhou Y.C., 2010, Mechanism for Hydrothermal Synthesis of $LiFePO_4$ Platelets as Cathode Material for Lithium-Ion Batteries, Journal of *Physical* Chemistry *C*, 114, 16806-16812.

167. Pinceloupa P., Courtois C., Vicens J., Leriche A., and Thierry B., 1999, Evidence of a dissolution–precipitation mechanism in hydrothermal synthesis of barium titanate powders. Journal of European Ceramic Society, **19**, 973-977.

168. Dokko K., Koizumi S., Nakano H., and Kanamura K., 2007, Particle morphology, crystal orientation, and electrochemical reactivity of $LiFePO_4$

synthesized by the hydrothermal method at 443 K. Journal of Materials Chemistry, **17**(45), 4803-4810.

169. Dokko K., Koizumi S., Sharaishi K., and Kanamura K., 2007, Electrochemical properties of $LiFePO_4$ prepared via hydrothermal route. Journal of Power Sources, **165**(2), 656-659.

170. Tajimi S., Ikeda Y., Uematsu K., Toda K., and Sato M., 2004, Enhanced electrochemical performance of $LiFePO_4$ prepared by hydrothermal reaction. Solid State Ionics, **175**(1-4), 287-290.

171. Meligrana G., Gerbaldi C., Tuel A., Bodaardo S., and Penazzi N., 2006, Hydrothermal synthesis of high surface $LiFePO_4$ powders as cathode for Li-ion cells. Journal of Power Sources, **160**(1), 516-522.

172. Liu Y., Gu J., Zhang J., Wang J., Nie N., Fu Y., Li W., and Yu F., 2015, Controllable synthesis of nano-sized $LiFePO_4$/C via a high shear mixer facilitated hydrothermal method for high rate Li-ion batteries. Electrochimica Acta, 173, 448-457.

173. Lou X. and Zhang Y., 2011, Synthesis of $LiFePO_4$/C cathode materials with both high-rate capability and high tap density for lithium-ion batteries. Journal of Materials Chemistry, **21**(12), 4156-4160.

174. Shu H., Wang X., Wu Q., Liu L., Liang Q., Yang S., Ju B., Yang X., Zhang X., Wang Y., Wei Q., Hu B., Liao Y., and Jiang H., 2012, The effect of ammonia concentration on the morphology and electrochemical properties of $LiFePO_4$ synthesized by ammonia assisted hydrothermal route. Electrochimica Acta, **76**, 120-129.

175. Xu Z., Xu L., Lai Q., and Ji X., 2007, A PEG assisted sol–gel synthesis of $LiFePO_4$ as cathodic material for lithium ion cells. Materials Research Bulletin, **42**(5), 883-891.

176. Bindu P., Kingston J.V., and Sudheendra Rao M.N., 2004, Dianionic silicate derivatives of transition metals: synthesis by a facile ion exchange route, characterization and thermolysis studies. Polyhedron, **23**(4), 679-686.

177. Lu Y., Zhang T., Liu Y., and Luo G., 2012, Preparation of $FePO_4$ nano-particles by coupling fast precipitation in membrane dispersion microcontactor and hydrothermal treatment. Chemical Engineering Journal, **210**, 18-25.

178. Liu J., Conry T. E., Song X., Doeff M. M., and Richardson T. J., 2011, Nanoporous spherical $LiFePO_4$ for high performance cathodes, Energy & Environmental Science, 4, 885-888

179. Liu J. and Manthiram A., 2011, Understanding the improvement in the electrochemical properties of surface modified 5 V $LiMn_{1.42}Ni_{0.42}Co_{0.16}O_4$ Spinel Cathodes in Lithium-ion Cells, Chemistry of Materials, 21, 1698-1707

180. Adelhelm P., Hu Y.S., Chuenchom L., Antonietti M., Smarsly B. M., and Maier J., 2007, Generation of hierarchical meso- and macroporous carbon from mesophase pitch by spinodal decomposition using polymer templates, Advanced Materials, 19, 4012-4017

181. Wang Z., Li F., Ergang N. S., Stein A., 2006, Effects of hierarchical architecture on electronic and mechanical properties of nanocast monolithic porous carbons and carbon−carbon nanocomposites, Chemistry of Materials, 18, 5543-5553

CHAPTER 2: Rapid Preparation of High Electrochemical Performance $LiFePO_4$/C Positive Electrode Material with an Ultrasonic-intensified Micro-impinging Jetting Reactor

SUMMARY

Following the literature review, nanoscale $LiFePO_4$ can shorten the diffusion distance of Li ions, and provide relatively large specific surface area on the interface between electrolyte and electrode materials. In this chapter, three methods which used to prepare nanoscale $LiFePO_4$ particles are compared. A joint chemical reactor system referred to as an ultrasonic-intensified micro-impinging stream reactor (UISR), which possesses the feature of fast micro-mixing, was proposed and has been employed for rapid preparation of $FePO_4$ particles that are amalgamated by nanoscale primary crystals. As one of the important precursors for the fabrication of lithium iron phosphate cathode, the properties of $FePO_4$ nano particles significantly affect the performance of the lithium iron phosphate cathode. Thus, the effects of joint use of impinging stream and ultrasonic irradiation on the formation of mesoporous structure of $FePO_4$ nano precursor particles and the electrochemical properties of amalgamated $LiFePO_4$/C have been investigated. Additionally, the effects of the reactant concentration (C = 0.5, 1.0 and 1.5 mol L^{-1}), and volumetric flow rate (V = 17.15, 51.44, and 85.74 mL min^{-1}) on synthesis of $FePO_4 \cdot 2H_2O$ nucleus have been studied when the impinging stream reactor (ISR) and UISR are to operate in nonsubmerged mode. It was affirmed from the experiments that the $FePO_4$ nano precursor particles prepared using UIJR have well-formed mesoporous structures with the primary

crystal size of 44.6 nm, an average pore size of 15.2 nm, and a specific surface area of 134.54 m^2g^{-1} when the reactant concentration and volumetric flow rate are 1.0 mol L^{-1} and 85.74 mL min^{-1} respectively. The amalgamated $LiFePO_4$/C nanoparticles can deliver good electrochemical performance with discharge capacities of 156.7 $mAhg^{-1}$ at 0.1 C, and exhibit 138.0 $mAhg^{-1}$ after 100 cycles at 0.5 C, which is 95.3% of the initial discharge capacity.

2.1 Introduction

Increasingly global warming and air pollution caused by the consumption of fossil fuels have imposed the priority of using green energy. As a result, the use of rechargeable lithium-ion batteries (LIBs) has increased rapidly (Shu *et al*., 2013; Gibot *et al*., 2008). Compared with other commercial cathode materials, such as $LiCoO_2$, $LiNiO_2$, $LiMn_2O_4$ and their derivatives, olivine-structured $LiFePO_4$ is considered as one of the most promising cathode material owing to its significant advantages of nontoxicity, low cost of raw materials, good structural stability at high temperature, excellent safety performance, and relatively high theoretical specific capacity (170 $mAhg^{-1}$) with a flat discharge-charge potential (3.45V vs. Li^+/Li) (Ding *et al*., 2010; Park *et al*., 2003; Padhi *et al*., 1997). However, the poor rate performance of $LiFePO_4$, resulting from its intrinsic low Li^+ diffusivity (10^{-17} to 10^{-14} cm^2s^{-1}) and low electronic conductivity (10^{-9} to 10^{-8} S cm^{-1}) , has become a technical bottleneck to confine its widely practical applications before these drawbacks being overcome fundamentally(Shin *et al*., 2008; Chung *et al*., 2002; Guo *et al*., 2015).

The kinetics of Li^+ insertion and extraction process is the primary mechanism to determine the battery delivery rate capability of a LFP-based electrode. This kinetics involved consists of three main steps: (i) electron and Li^+ diffusion to/from the bulk material within the bulk material (solid phase); (ii) charge transfer reactions (electrochemical reactions) at the interface of the electrode/electrolyte; and (iii) Li^+ diffusion from/to the interface in electrolyte phase (Liu *et al*., 2011; Liu and Manthiram, 2011). Significant amount of efforts have been made on developing new methods to facilitate the kinetics of Li^+ insertion and extraction process, and improving the rate performance of $LiFePO_4$. Reducing the particle size and preparing nano-scale cathode materials have been proved to be one of the effective ways to shorten the Li^+ diffusion path and facilitate the kinetics of steps. Additionally, fabrication of cathode material possessing the porous structures can also increase electrode/electrolyte interface area and ensure effective electrolyte permeation (Vu *et al*., 2012; Wang *et al*., 2015). The porous structures would be beneficial to the improvement on the rate performance of $LiFePO_4$. It should be emphasized here, however, that only meso- and macroporous structure is desirable, since the smaller size of micropores can hinder the reversibility of Li^+ insertion process and reduce the active interfaces of the electrode/electrolyte by an increased potential of blockage from residual carbon (Adelhelm *et al*., 2007; Doherty *et al*., 2010). Micropores may also cause the formation of an extensive solid electrolyte interface (SEI) layer and inhibit charge transfer across the interfaces, resulting in a decrease in conductivity (Wang *et al*., 2006). The application of $LiFePO_4$ in lithium ion battery requires an optimal combination of high porosity and surface area to provide excellent electrochemical properties.

There are several different preparation routes that have been attempted to develop the electrode materials for LIBs with high porosity structures. Sono-chemical synthesis is a well-known, simple and scalable technique to produce nanomaterials and the synthesized particles can have high porosities. The use of ultrasonic treatment is the other feasible way. By using ultrasonic treatment, acoustically created cavitation can be induced by ultrasonic wave while instantaneous collapse of the cavitation bubbles can create extreme conditions such as extremely high temperature up to 5000K, pressures up to 1000 atm, and the heating and cooling rate greater than 10^{10} Ks^{-1} inside the cavitation zone. When ultrasonic treatment is applied for synthesis of the particles, the synthesised particles usually present porous structures (Suslick and Price., 1999; Xu *et al*., 2013).

Adoption of impinging stream (IS) is the other promising technology for materials synthesis and it has been widely used in industry for various applications. Liquid-continuous impinging streams are where two high speed impinging streams collide each other to form a local intensive micro-mixing have two major features: strong pressure fluctuation and many highly turbulent eddies. When this impinge streams are used for synthesis of particles, the generated turbulent micro-mixing can effectively increase local mass transfer rate and enhance the reaction rate, significantly boosting the probability of engulfed molecular diffusion by eddy collision. Meanwhile, the pressure fluctuation can also influence the energy and mass transfer in the solution (Huang *et al*., 2015). Comparing to conventional stirred tanks, an impinging stream reactor (ISR) has fixed and confined volume, which lead to several orders of magnitude higher mixing intensity as well as uniform residence time when the feeding rate is kept unchanged. This kind of hydrodynamic reaction environment can enhance

the control of the mixing conditions and local reactant concentrations (Siddiqui *et al*., 2009).

This paper proposes three different synthesis routes, aiming to synthesis $FePO_4$ nano precursor particles that can have mesoporous structures. These obtained precursor micro or nano particles will be used to synthesize $LiFePO_4$/C composites. The effects of impinging jet stream and ultrasonic irradiation on the morphology of $FePO_4$ precursor and electrochemical properties of $LiFePO_4$/C will be investigated and the findings will be discussed. The paper is organised as follows. Section 2 will describe the experimental details for synthesis of $FePO_4$ nanocomposites. The properties of $FePO_4$ and $LiFePO_4$ synthesised by using different synthesis methods are discussed in Section 3. Finally, some important conclusions drawn from the present work are given in Section 4.

2.2 Materials and experimental methods

2.2.1 Synthesis of $FePO_4$ nanoparticles

The $Fe(NO_3)_3$ (1 mol L^{-1}) and $(NH_4)_2HPO_4$ (1 mol L^{-1}) aqueous solutions were prepared by dissolving $Fe(NO_3)_3 \cdot 9H_2O$ (Sinopharm Chemical Reagent Co., Ltd, 99%) and $(NH_4)_2HPO_4$ (Sinopharm Chemical Reagent Co., Ltd, 99%) into deionized water. A certain amount of ammonia solution was used to adjust the pH value of $(NH_4)_2HPO_4$ to maintain the desired value.

Three different methods were designed to synthesis the nanoparticles of $FePO_4$. The first type of $FePO_4$ nanoparticles were synthesized via an ultrasonic-assisted impinging stream reaction at room temperature. The two reaction solutions were

added continuously into an impinging jet reactor which was irradiated by a FS-600pv horn type ultrasonic wave piezoelectric vibrator (600 W, 13 mm in diameter) with 20 kHz (as shown in Figure 2-1). The inlet of impinging jetting reactor had an inner diameter of 4 mm, while the inner diameter of outlet was 15 mm. The volumetric feeding rate of solutions was maintained at 85.74 ml/min (100 rpm). The pH value of solution was maintained at 1.70 by adding the ammonia solution using a pH automatic controller. Temperature was maintained at 60 ℃. The obtained products were then subsequently washed with deionized water several times, filtrated and then dried in air at 100 ℃ for 12 h. Then the sample was calcined in air at 600 ℃ for 10 h to obtain anhydrous crystalline $FePO_4$ samples. This nano $FePO_4 \cdot xH_2O$ sample was denoted as FP-UltraImp.

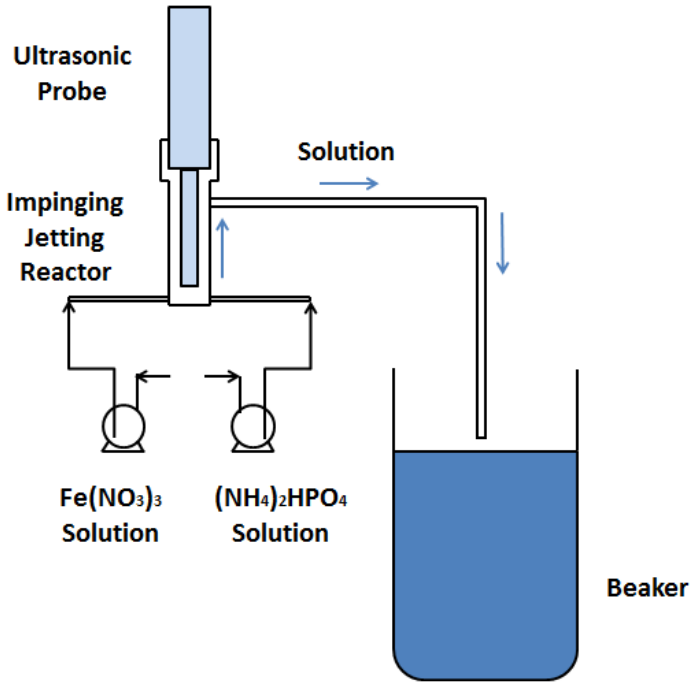

Figure 2-1 Schematic diagrams of experimental setup for combined ultrasonic-assisted impinging jetting reaction method.

The second type of $FePO_4$ nanoparticles were synthesized by applying a similar impinging jet reaction to the described first method. The only difference between the first and second type of synthesis methods is only the ultrasonic irradiation step. The second type of $FePO_4 \cdot xH_2O$ sample is not irradiated with ultrasonic waves. The obtained nano $FePO_4$ sample was referred to as FP-Imp.

The third type of $FePO_4 \cdot xH_2O$ nanoparticles were prepared for comparison purpose by a conventional co-precipitation method. The two reaction solutions were added continuously into a stirring reactor at a constant volumetric feeding rate of 85.74 ml/min (100 rpm). The pH value of solution was also maintained at 1.70 by adding ammonia solution via pH automatic controller. After adopting the same filtration, drying and calcination procedures, the $FePO_4$ nanoparticles were obtained, named by FP-Copre.

In addition, to investigate the effect of reagent concentration and volumetric flow rate, FP-UltraImp and FP-Imp nanoparticles were also synthesized under precisely controlled reagent concentration (C = 0.5 and 1.5 mol L^{-1}) and volumetric flow rate (V = 17.15 and 51.44 ml min^{-1}).

2.2.2 Synthesis of $LiFePO_4$/C nanoparticles

Three types of anhydrous $FePO_4$ samples were mixed with Li_2CO_3 (Sinopharm Chemical Reagent Co., Ltd, 99%) and glucose (Sinopharm Chemical Reagent Co., Ltd, 99%) at a desired ratio and ball-milled at 300 rpm for 6 h by a planetary ball mill, respectively. Then the mixtures were calcined in nitrogen atmosphere at 650 ℃ for 10 h. The obtained $LiFePO_4$/C samples were designated as LFP- UltraImp, LFP-Imp, and LFP-Copre, respectively.

2.2.3 Characterization of $FePO_4$ and $LiFePO_4/C$

Thermalgravimetric was measured by simultaneous thermal analyser (TG, NETZSCH STA 449 F3 Jupiter, Germany) at a heating rate of 10 ℃ min^{-1} in air. The n_{Fe}/ n_P ratio of $FePO_4 \cdot 2H_2O$ precursors was analysed by ICP. The crystal structure of $FePO_4$ and $LiFePO_4/C$ samples were analysed by a Bruker D8 series X-ray diffraction using Cu Kα radiation (λ=1.5406Å) operated at 40kV and 40 mA. The 2Θ was scanned from 10 degree to 70 degree (with a resolution of 0.01 degree). The surface morphology of $FePO_4 \cdot xH_2O$ particles were observed by scanning electron microscope (Sigma VP, ZEISS, Germany) and transmission electron microscope (Tecnai F20, FEI, U.S). Surface area, porosity and particle size are analysed by Brunauer Emmett Teller (BET, Micromeritics ASAP 2020, U.S.A). In terms of tap density measurement, a simple method described by Wang *et al.* (2011) was employed. In this work, about 5 g of the samples were stored in 10 ml plastic centrifugal tube and tapped on the lab bench for 10 min by hand. The measured mass and volume of samples were then recorded to calculate the tap density.

2.2.4 Electrode and coin cell battery preparation

The electrochemical performance was tested using a CR2032 coin-type cell. The cathode material was consisted of as-synthesized $LiFePO_4/C$ composite, acetylene black and polytetrafluoroethylene (PTFE) binder in a weight ratio of 80:10:10. The mixture was coating on an aluminium foil. After rolling and drying at 80 ℃ for 8 h. The coated aluminium was cut into circular plates. The thickness and diameter of these circular plates were 0.06 and 12 mm respectively. The loading density of $LiFePO_4$ active material was around 5.0 mg cm^{-2}. 0.1 M $LiPF_6$ dissolved in ethylene carbonate (EC)/diethyl carbonate (DEC) (1:1 volume ratio) was used as the

electrolyte. Celguard 2300 microporous film was adopted as the separator. The assembly of the cells was carried out in a dry Ar-filled glove box. The cells were galvanostatically charged and discharged at various rates within the voltage range of 2.5 V and 4.2 V (versus Li/Li+) on an electrochemical test workstation (CT2001A, Wuhan LAND Electronic Co.Ltd., China). All the electrochemical tests were carried out at room temperature. Cyclic voltammetry (CV) measurement was performed on an electrochemical workstation (Shanghai Chenhua Instrument Co. Ltd., China) over the potential range of 2.5–4.2 V (vs. Li/Li^+) at a scanning rate of 0.1 mVs^{-1}.

2.3 Results and Discussion

2.3.1 Effect of impinging jetting reaction and ultrasonic assisted impinging jetting reaction

To determine the water containing content of $FePO_4 \cdot xH_2O$ precursors, TG-DTA examination of the FP-UltraImp precursor particles was carried out by variation of the temperature from room temperature to 600 ℃ in air. The variations of the moisture are shown in Figure 2-2. The TGA curve shows that the mass loss of $FePO_4 \cdot xH_2O$ samples was found to be 22.5 wt%, indicating there are two molecules in one as-synthesized iron phosphate molecule. After 500 ℃, the sample has no weight loss, indicating the dehydration of $FePO_4 \cdot 2H_2O$ occurs in the range between 178 and 500 ℃.

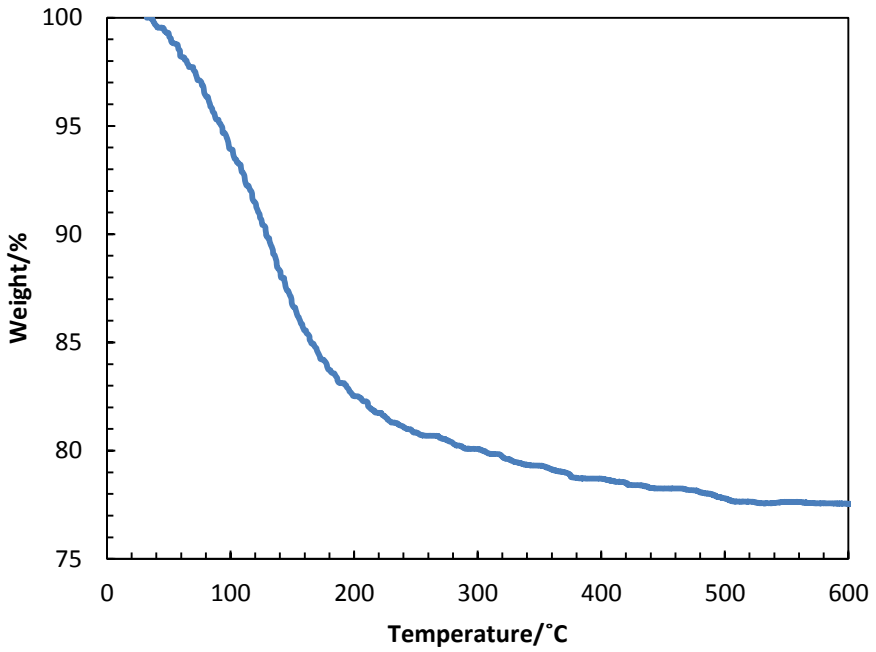

Figure 2-2 TG/DTA curves of FP-UltraImp precursors at a heating rate of 10 ˚C min^{-1} in the air.

It has been reported in the literature that the n_{Fe}/ n_P ratio of $FePO_4 \cdot 2H_2O$ precursors is sensitive to the pH value of the working solution (Pan *et al*., 2013). To investigate the effect of impinging stream and ultrasonic irradiation on the atom ratios between Fe ion and P ion, the $FePO_4 \cdot 2H_2O$ precursors prepared with different synthesis methods are measured by inductively coupling the use of a plasma mass spectrometry (ICP-MS). The test results are shown in Table 2-1. The n_{Fe}/ n_P ratio of all $FePO_4 \cdot 2H_2O$ samples obtained in this work is less than 1. The n_{Fe}/ n_P ratio of FP-UltraImp precursor is 0.97, which is higher than the n_{Fe}/ n_P ratio of FP-Imp precursor (0.95) and FP-Copre precursor (0.92). The ICP-MS result indicates that the n_{Fe}/ n_P ratio of $FePO_4 \cdot 2H_2O$ precursors is sensitive to the synthesis method when the pH of working solution is maintained at the same value. When water is irradiated by ultrasound, large

amount of H· and OH· are generated (Bang and Suslick., 2010). The main reactions are summarized below:

$$H_2O \rightarrow H\cdot + OH\cdot$$

$$H\cdot + H\cdot \rightarrow H_2$$

$$OH\cdot + OH\cdot \rightarrow H_2O_2$$

$$H\cdot + OH\cdot \rightarrow H_2O$$

For the synthesis of FePO4 precursor, the main reactions are as follows:

$$Fe^{3+} + PO_4^{3-} \rightarrow FePO_4 \downarrow$$

$$Fe^{3+} + 3OH\text{-} \rightarrow Fe(OH)_3 \downarrow$$

The generation of $FePO_4$ and $Fe(OH)_3$ is a homogeneous competitive-consecutive (series-parallel) reaction. Comparing with impinging jetting stream, ultrasonic irradiation can further improve micromixing effect and reduce micromixing time (Mahajan and Donald, 1996). Therefore, with the help of ultrasound irradiation, the chemical reactions tend to produce $FePO_4$ and leading to an increased nFe/ nP ratio.

Table 2- 1 The n_{Fe}/ n_P ratio of $FePO_4 \cdot 2H_2O$ precursors prepared by different methods

Samples	FP-UltraImp precursor	FP-Imp precursor	FP-Copre precursor
n_{Fe}/ n_P	0.97	0.95	0.92

The X-ray powder diffraction (XRD) patterns of different $FePO_4$ samples, which are pre-heated at 600 ℃ for 10 h, are shown in Figure 2-3. The calculated cell parameters and mean crystalline size of these samples are listed in Table 2-2. All the calculated lattice constants match well with anhydrous hexagonal structured $FePO_4$ (JCPDS card no. 29-0715, a = 5.035 Å, b = 5.035 Å, c = 11.245 Å), suggesting the formation of perfect crystalline $FePO_4$ nanoparticles after the thermal treatment. Simultaneously, it can be clearly observed that the intensities of the diffraction peaks decrease with the use of impinging jet reactor and ultrasonic irradiation, which may suggest that the adoption of impinging jet stream and ultrasonic irradiation have remarkable effect on the crystallinity of the products. The highest intensities of FP-Copre, FP-Imp and FP-UltraImp nanoparticles around 25.83 degree are 4184, 3218 and 2949, respectively. The reason of lower intensities of FP-Imp and FP-UltraImp samples may be attributed to their smaller mean crystalline size (Liu *et al*., 2014).

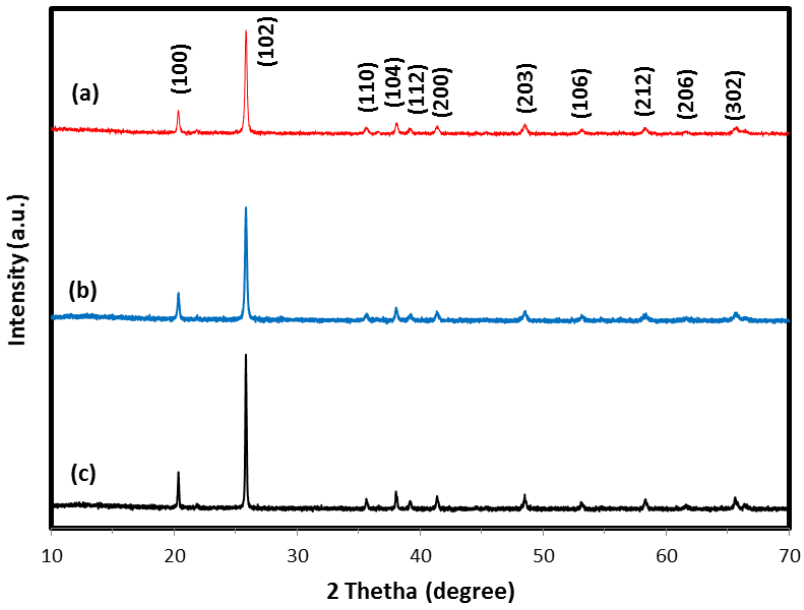

Figure 2-3 X-ray diffraction patterns of different $FePO_4$ nanoparticles (a) FP-UltraImp, (b) FP-Imp, and (c) FP-Copre.

Table 2-2 Calculated lattice parameters and nuclei size of as-synthesized $FePO_4$ samples

	a(Å)	b(Å)	c(Å)	V($Å^3$)	Mean crystalline size(nm)
FP-UltraImp	5.0412	5.0412	11.2462	285.8075	42.9
FP-Imp	5.0365	5.0365	11.2445	285.2317	48.5
FP-Copre	5.0362	5.0362	11.2482	285.2916	82.7

The BET specific surface area and pore size distribution of the $FePO_4 \cdot 2H_2O$ precursors have been characterized by nitrogen adsorption-desorption analysis. It can be seen that the N_2 sorption isotherm of all $FePO_4 \cdot 2H_2O$ precursors (Figure 2-4a) were Type IV. Their big hysteresis loops can be evidenced by the presence of meso-pores (>2nm and <50nm) and large surface areas. Table 2-3 shows the effect of impinging stream and ultrasonic irradiation has had on the surface area, porosity and average nuclei size of the $FePO_4 \cdot 2H_2O$ samples. The average nuclei size of three $FePO_4 \cdot 2H_2O$ precursors confirms the same trend obtained from XRD analysis. The average nuclei sizes of FP-UltraImp and FP-Imp precursors are 44.60 and 54.80 nm, respectively, which is smaller than the average nuclei size of FP-Copre precursor (77.92 nm). In addition, it can be seen that the FP-Copre precursor shows the largest average pore diameter of 23.2 nm, and exhibits the smallest BET surface area and total pore volume, corresponding to 77 m^2g^{-1} and 0.446 cm^3g^{-1} respectively. In contrast, the precursor of FP-UltraImp sample shows the highest BET surface area of

134.54 m^2 g^{-1} and the smallest average pore size of 15.2 nm. For the FP-Imp precursor, it has the highest pore volume of 0.663 cm^3 g^{-1}. The analytical results of pore size distribution based on desorption of the $FePO_4 \cdot 2H_2O$ precursors synthesized using different methods are shown in Fig.4b and c. It becomes clear as can be seen from the figure that the FP-Imp precursor has a significant amount of large-mesopores in the range of 20 to 50 nm, leading to its highest pore volume. The reason that FP-UltraImp precursors have the highest specific surface area of porosity is mainly ascribed to the small-mesopores that fall into the range from 4 to 20 nm. Obviously, both FP-UltraImp and FP-Imp precursors feature pores in mesoporous (>2nm and <50nm) range, indicating that the acquirement of large surface areas of FP-UltraImp and FP-Imp precursors are caused by not only the reduction in the average nuclei size but also the increase in the numbers of mesopores rather than micropores (<2nm) or macropores (>50nm). Generally speaking, a larger specific surface area can effectively increase the interface between electrode and electrolyte, thus enhancing an effective charge transfer across the interface. A reduced nuclei size is beneficial to shortening the diffusion distance of lithium ion, giving rise to an improved electrochemical performance for $LiFePO_4$. Meanwhile, mesoporous structure can facilitate the penetration of electrolyte and improve the electronic conductivity. However, it has been proved that large surface area and high pore volume of electrode materials also limits its application in industry due to the reduced tap density and volumetric energy density (Tan *et al.*, 2014). For FP-Ultra Imp precursor, its small-mesoporous structure is thus to play roles in facilitation of the electrolyte penetration, improvement of the electronic conductivity and maintenance of an average tap density and volumetric density of the resulting LFP-UltraImp sample.

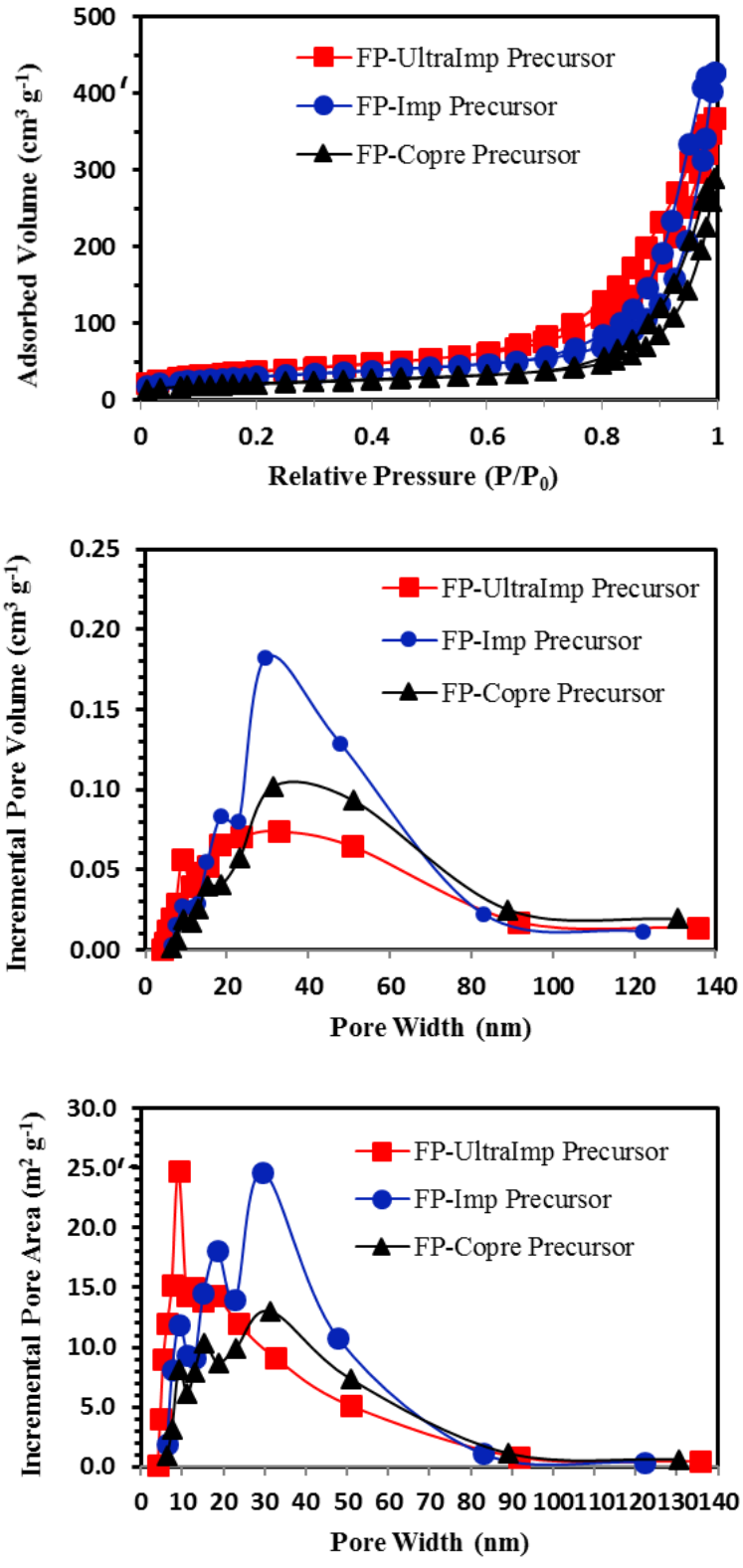

Figure 2-4 The BJH desorption pore size distribution of $FePO_4 \cdot 2H_2O$ samples prepared with different synthesis methods.

Table 2-3 N_2 adsorption-desorption analysis results of $FePO_4 \cdot 2H_2O$ precursors prepared with different synthesis methods.

Samples	Surface area ($m^2 g^{-1}$)	Average Pore Width (nm)	Total pore volume ($cm^3 g^{-1}$)	Average nuclei size (nm)
FP-UltraImp precursor	134.54	15.2	0.570	44.60
FP-Imp precursor	109.49	21.4	0.663	54.80
FP-Copre precursor	77.00	23.2	0.446	77.92

Figure 2-5 shows the TEM images of different $FePO_4$ samples after heat treatment at 600 ℃ for 10 h. The FP-UltraImp primary nuclei (Figure 2-5a) exhibits near-spherical shape with a primary crystallite size of 20-50 nm. In Figure 2-5b, the FP-Imp nanoparticles have a larger nuclei size (around 50 nm) and similar near-spherical shape with FP-UltraImp. Moreover, the pore size of FP-Imp is also larger than that of FP-UltraImp. In contrast, FP-Copre sample exhibits irregular nuclei shape and the nuclei size is increased to 50-100 nm. It can be seen clearly from the figure that all three $FePO_4$ samples still possess nano-sized nuclei and porous structure after heat treatment, which may provide high quality precursors for synthesising $LiFePO_4$/C nanoparticles.

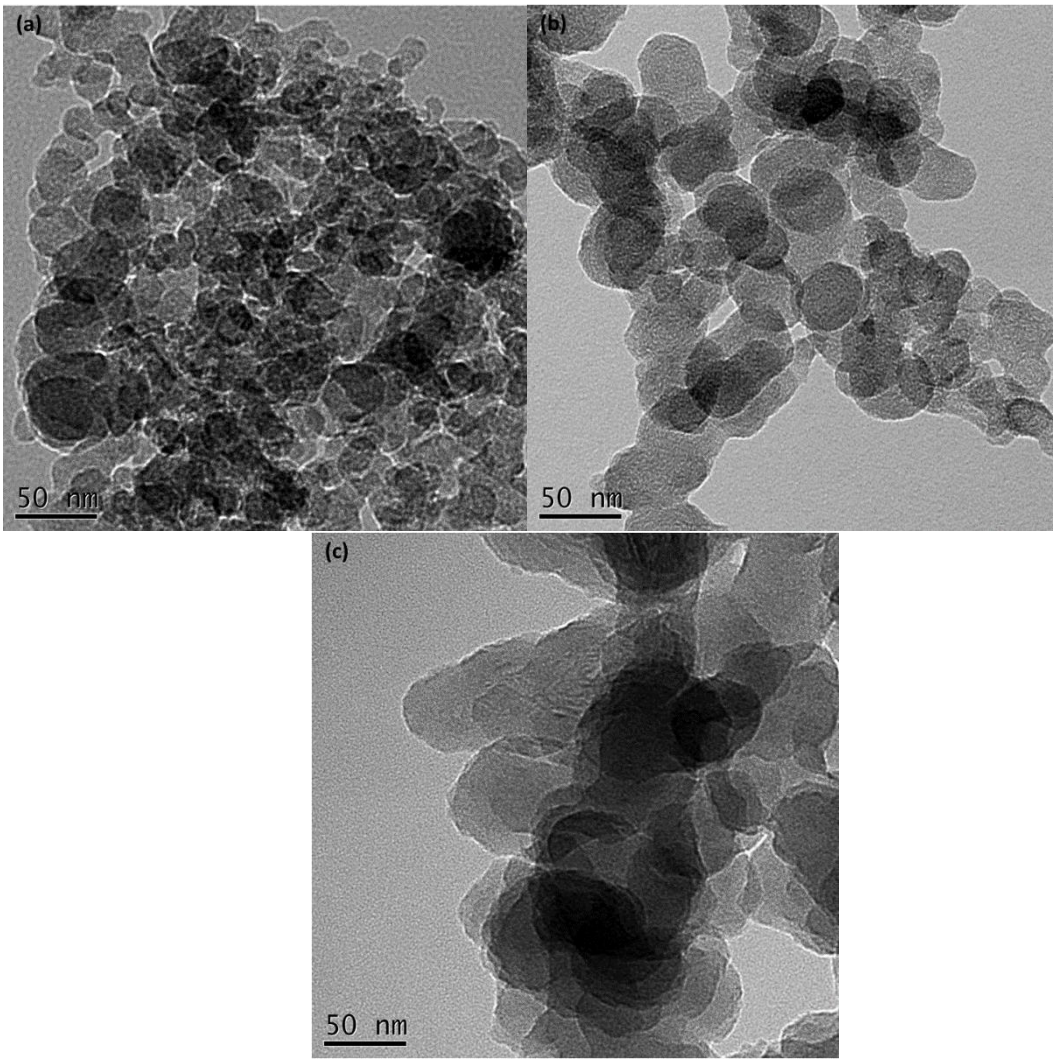

Figure 2-5 TEM images of different $FePO_4$ samples (a) FP-UltraImp, (b) FP-Imp, and (c) FP-Copre.

According to the XRD, BET and TEM results, there exists a clear tendency that the use of both ultrasonic irradiation and impinging jet reaction can have a significant effect on increasing surface area, and reducing primary grain size and pore diameter of $FePO_4 \cdot 2H_2O$ precursors. To understand the effect of ultrasonic irradiation and impinging jet stream on the formation of porous $FePO_4 \cdot 2H_2O$ precursor, a schematic illustration is presented in Figure 2-6. In the impinging stream reaction, the streams of Fe^{3+} and PO_4^{3-} solutions impinge on each other directly, which can deliver a high

level of supersaturation and sufficient mixing of the raw materials in an extremely short time (~10^{-7} s). The initial high supersaturation level can enhance the micromixing in the solution, thus facilitating nucleation rate and generating large amount of iron phosphate nuclei. The level of supersaturation level will decrease because the rapid nucleation process also consumes large amount of raw materials. Thus, particle growth process is confined, which results in a smaller average nuclei size. Additionally, it is conjectured that the improved molecular collision rate gives rise to the generation of large amount of large-mesopores as can be seen from BET analysis.

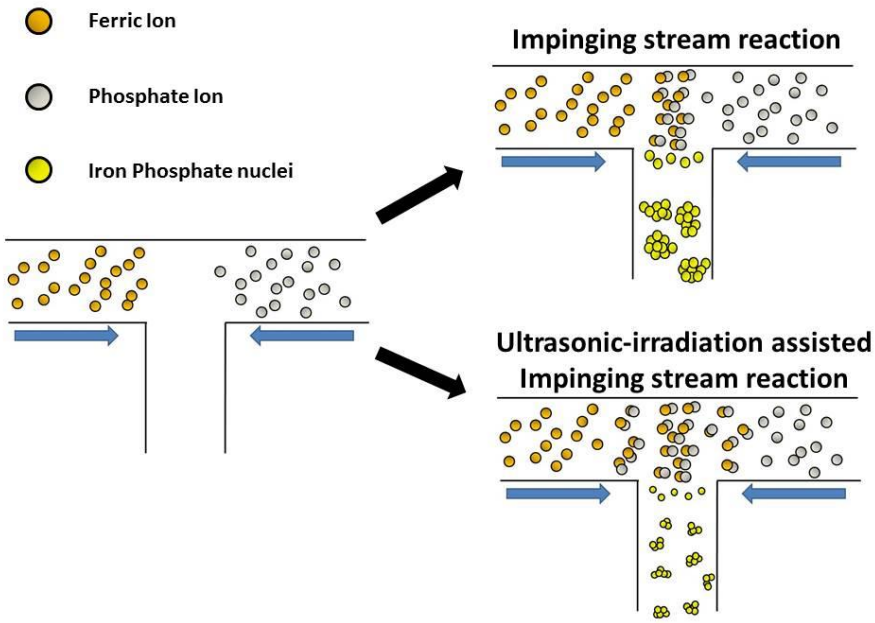

Figure 2-6 Schematic illustration of the synthesis processes of impinging stream reaction and ultrasonic-assisted impinging stream reaction.

The higher BET surface area, smaller average pore width and nuclei size of FP-UltraImp precursor might be the result of joint effect of ultrasonic irradiation and high speed impinging jet streams. In joint ultrasonic-irradiation impinging stream reaction,

ultrasonic irradiation can further improve the diffusion, promoting the reaction and nucleation. Therefore, the average nuclei size of FP-UltraImp precursors is smaller than FP-Imp precursors. In addition, the function of ultrasonic irradiation can prevent the agglomeration and break large agglomerated particles into smaller particles to increase surface area. The formed small-mesopores of FP-UltraImp may be attributed to the breakup of the surface film at liquid-solid interfaces which is caused by shock waves and microjets (Suslick and Price, 1999). This may explain why FP-UltraImp precursor can attain the smallest average nuclei size, largest specific surface area, and small-mesopores among three preparation routes.

2.3.2 Effect of reagent concentration

To further understand the optimal concentration of initial reagents, $FePO_4 \cdot 2H_2O$ precursors were synthesized with three different reagent concentration (C = 0.5, 1.0 and 1.5 mol L^{-1}) by using UIJR and IJR methods and the volumetric feeding rate was maintained at 85.74 ml/min.

The BET specific surface area, total pore adsorption volume and pore size distribution of the $FePO_4 \cdot 2H_2O$ precursors synthesized under different conditions have been characterized by nitrogen adsorption-desorption analysis. As shown in Table 2-4 and Figure 2-7, increasing the reagent concentration had significant influence on the surface area, porosity and average nuclei size of the $FePO_4$ precursor samples.

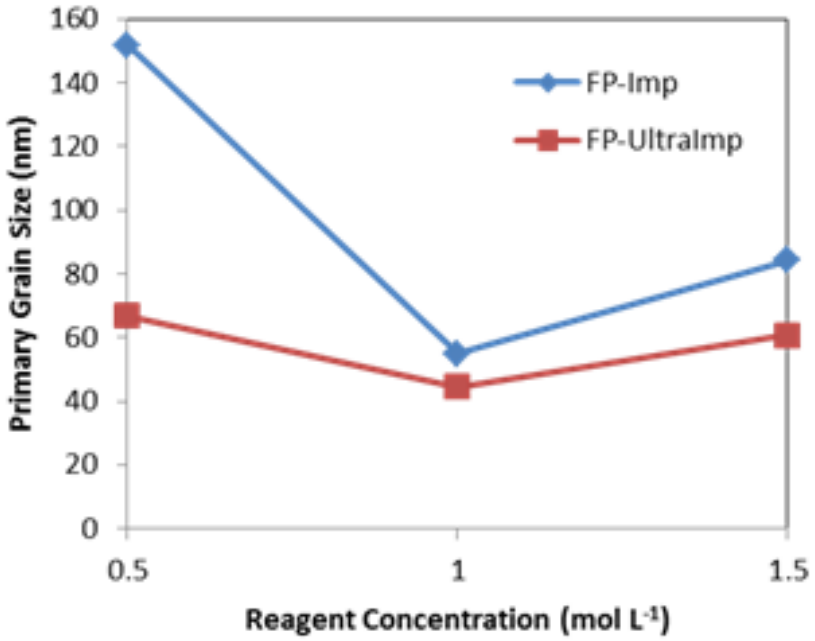

(a)

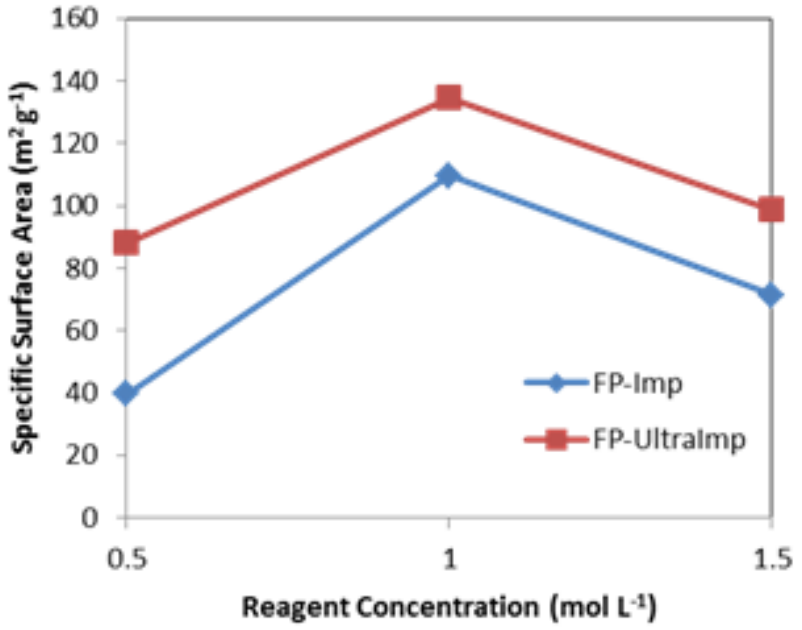

(b)

Figure 2-7 The relationship between reagent concentration and (a) primary grain size; (b) specific surface area.

When the reagent concentration is 1.0 mol/L, the $FePO_4$ precursor sample (FP-UltraImp-1.0) synthesized by UIJR method features largest surface area (134.54 m^2 g^{-1}) and smallest average nuclei size (44.60 nm). The measured BET surface area for FP-UltraImp-0.5 and FP-UltraImp-1.5 precursors is 87.94 and 98.69 m^2 g^{-1}, respectively. Meanwhile, the average nuclei size of these two samples is 66.67 and 60.79 nm respectively. When $FePO_4$ precursor samples are synthesized by IJR method, similar tendency can be observed and FP-Imp-1.0 relative large surface area (109.49 m^2 g^{-1}) and adsorption pore volume (0.663 cm^3 g^{-1}), as well as a smaller average primary grain size (54.80 nm).

Generally, a higher initial reactant concertation can increase supersaturation level and nucleation rate in ISR and UISR reaction. However, as the volumetric feeding rate is not changed. Therefore, large amount of nanoscale $FePO_4$ nucleus will be synthesized in a short time. Some of the nucleus might be attached to the impinging stream reactor and blocked the chamber slightly. Then heterogeneous nucleation happens on the attached nuclei. Thus, these nuclei might be agglomerated and grown up in impinging stream reactor, leading to an enlarged nuclei size, and reduced surface area and pore adsorption volume. In comparison, ultrasonic irradiation can further increase micromixing effect and prevent agglomeration in impinging jetting reactor, leading to a reduced primary grain size and enlarged surface area.

Table 2-4 N_2 adsorption-desorption analysis results of $FePO_4 \cdot 2H_2O$ precursors prepared with different reagent concertation by ISR and UISR methods (Volumetric feeding rate = 85.74 ml/min)

Precursors	Reactant concetration (mol L^{-1})	Specific surface area (m^2 g^{-1})	Total pore adsorption volume (cm^3 g^{-1})	Average primary grain size (nm)
FP-Imp-0.5	0.5	39.53	0.203	151.78
FP-Imp-1.0	1.0	109.49	0.663	54.80
FP-Imp-1.5	1.5	71.24	0.315	84.22
FP-UltraImp-0.5	0.5	87.94	0.580	66.67
FP-UltraImp-1.0	1.0	134.54	0.570	44.60
FP-UltraImp-1.5	1.5	98.69	0.477	60.79

2.3.3 Effect of volumetric feeding rate

To evaluate the effect of volumetric feeding rate, $FePO_4 \cdot 2H_2O$ precursors were prepared at three different level (V = 17.15, 51.44 and 85.75 ml/min). It has been found that the increasing of volumetric feeding rate result in reduction of average primary grain size and improvement of specific surface area of $FePO_4 \cdot 2H_2O$ precursors, especially when the samples are prepared by ISR.

Table 2-5 and Figure 2-8 show the BET analysis results of the $FePO_4 \cdot 2H_2O$ samples prepared with 3 different volumetric feeding rate by IJR and UIJR methods. When using IJR method, the surface area and total adsorption volume increase with increasing the volumetric feeding rate. The maximum specific surface area (109.49 $m^2\ g^{-1}$) and total adsorption volume (0.663 $cm^3\ g^{-1}$) were obtained when the volumetric feeding rate is 85.74 ml/min. On the contrary, it was found that the average primary grain size of $FePO_4 \cdot 2H_2O$ samples decrease significantly as the increasing of volumetric feeding rate. Therefore, the sample FP-Imp-100 precursor has the best abundant mesoporous structure. This is mainly ascribed to the reduced micromixing time and increased mass transfer rate and collision rate. When ultrasonic irradiation is applied in impinging jetting reaction, the specific surface area, total pore adsorption volume and average primary grain size changed slightly with the increasing of volumetric feeding rate, especially at a relatively lower rate (V = 17.15 and 51.44 ml/min). This indicates that the application of ultrasonic irradiation can enhance micromixing more significantly than increasing of volumetric feeding rate.

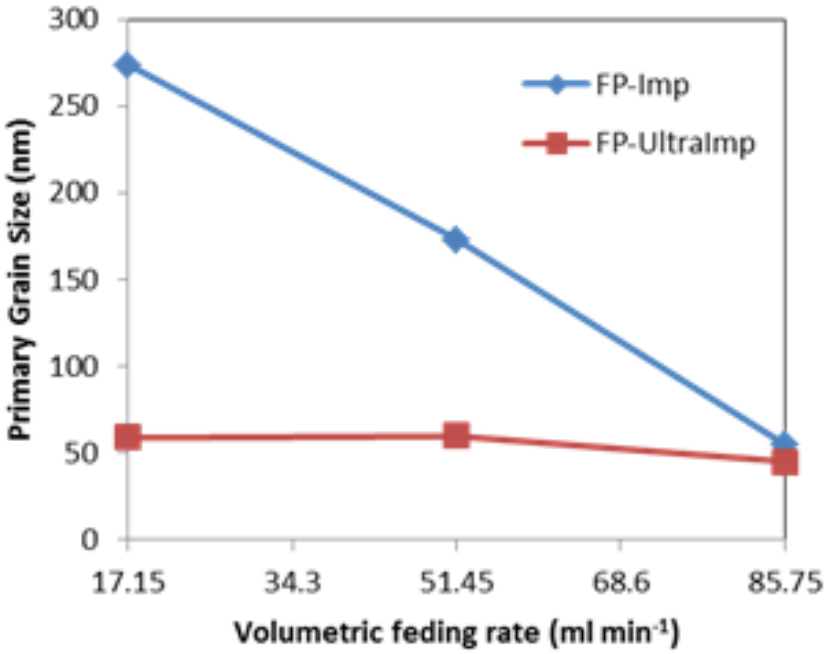

(a)

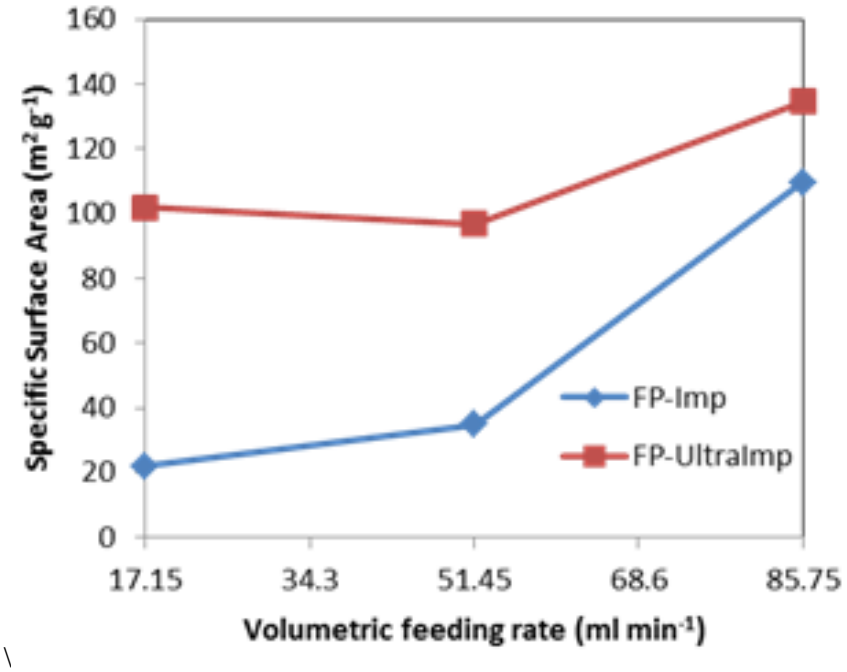

\

(b)

Figure 2-8 The relationship between volumetric feeding rate and (a) primary grain size; (b) specific surface area.

Table 2-5 N_2 adsorption-desorption analysis results of $FePO_4 \cdot 2H_2O$ precursors prepared with different volumetric feeding rate by ISR and UISR methods (Reagent concentration = 1.0 mol L^{-1})

Precursors	Volumetric feeding rate (ml/min)	Specific surface area ($m^2 g^{-1}$)	Total pore adsorption volume ($cm^3 g^{-1}$)	Average primary grain size (nm)
FP-Imp-20	17.15 (20 rpm)	21.94	0.087	273.48
FP-Imp-60	51.44 (60 rpm)	34.75	0.263	172.69
FP-Imp-100	85.74 (100 rpm)	109.49	0.663	54.80
FP-UltraImp-20	17.15 (20 rpm)	101.89	0.652	58.89
FP-UltraImp-60	51.44 (60 rpm)	96.88	0.576	59.60
FP-UltraImp-100	85.74 (100 rpm)	134.54	0.570	44.60

2.3.4 Properties of $LiFePO_4$/C

Those as-synthesized $FePO_4$ precursors by using different preparation routes as discussed in the preceding section were used for further synthesizing $LiFePO_4$/C positive electrode particles. The XRD patterns and calculated lattice parameters of the three as-synthesized $LiFePO_4$/C samples are shown in Figure 2-9 and listed in Table 2-6. All diffraction peaks seen from XRD patterns and crystal lattice parameters are also well indexed to accord with $LiFePO_4$ which has the orthorhombic structure

(JCPDS card no.40-1499, a = 10.347 Å, b = 6.019 Å, c = 4.704 Å), suggesting all the three $LiFePO_4$/C nanoparticles were synthesized without any appreciable impurity phases.

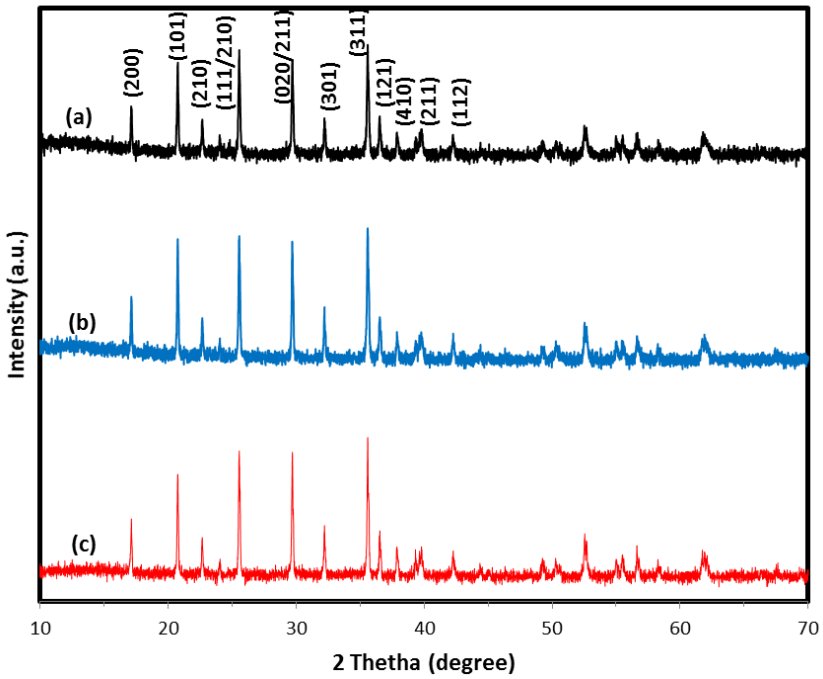

Figure 2-9 X-ray diffraction patterns of as-synthesized $LiFePO_4$/C nanoparticles: (a) LFP-UltraImp, (b) LFP-Imp, and (c) LFP-Copre.

Table 2-6 Lattice parameters of as-synthesized $LiFePO_4$/C samples

	a(Å)	b(Å)	c(Å)	V(Å^3)
LFP-UltraImp	10.3254	6.0078	4.6916	291.0337
LFP-Imp	10.3322	6.0071	4.6896	291.0673
LFP-Copre	10.3276	6.0069	4.6906	290.9901

The morphology of $LiFePO_4$/C nanoparticles prepared by different methods was also examined by scanning electron microscopy (SEM). It can be seen from Figures 2-10a and b that both LFP-UltraImp and LFP-Imp samples present a similar particle morphology consisting of nanospheres with sizes in the range of 80 nm to 300 nm. These nanospheres interweave together and form high porosity structure. By comparison, Figure 2-10c shows the LFP-Copre composite has a structure with lower porosity while the corresponding particle size becomes larger than those of LFP-UltraImp and LFP-Imp samples.

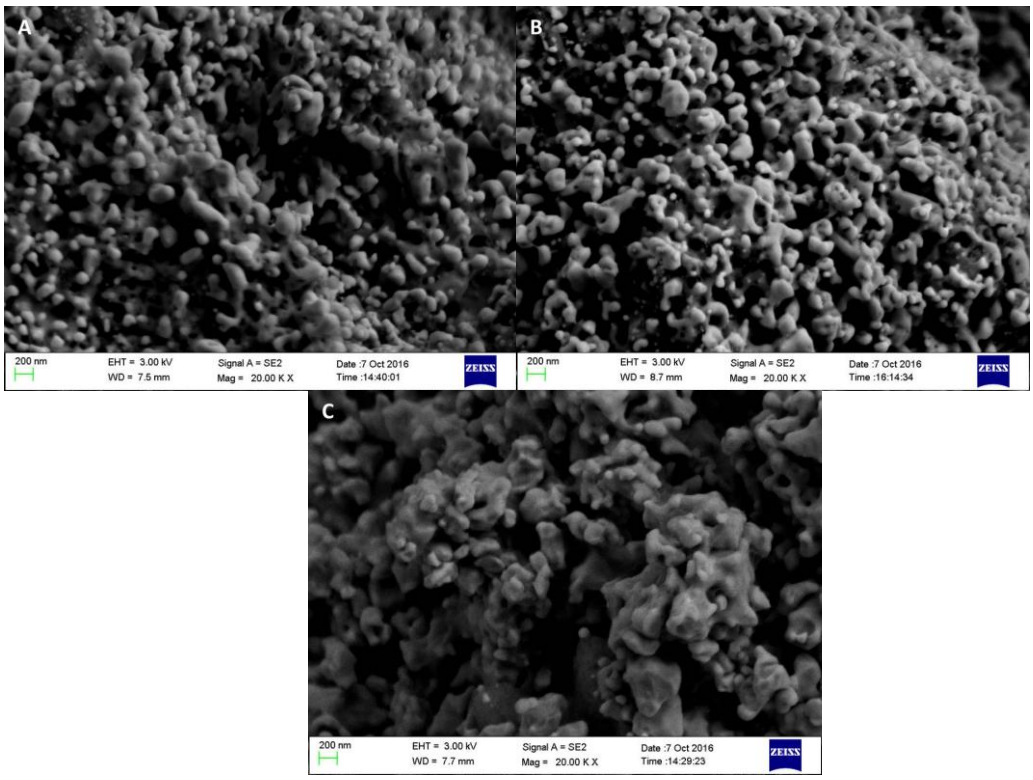

Figure 2-10 SEM images of $LiFePO_4$/C composites from the precursors prepared with different methods (a) LFP-UltraImp, (b) LFP-Imp, and (c) LFP-Copre.

The electrochemical properties of all $LiFePO_4$/C samples were tested in 2032-type coin half-cells batteries. Figure 2-11a shows charge/discharge capacities for the LFP-Copre, LFP-Imp and LFP-UltraImp nanoparticles within the voltage range of 2.5 V and 4.2 V (versus Li/Li+) at 0.1 C (17 mA g^{-1}). The charge and discharge plateaus of all three $LiFePO_4$/C samples are 3.45 V and 3.40 V respectively. At low charge/discharge rates, both LFP-UltraImp and LFP-Imp samples exhibit comparable performance. The discharge capacities of LFP-UltraImp and LFP-Imp can reach 156.7 mA h g^{-1} and 150.9 mA h g^{-1} respectively, which is higher than the discharge capacity of LFP-Copre (141.3 mA h g^{-1}). As shown in Figure 2-11b, the discharge capacities of LFP-Ultra Imp at 0.5, 1, and 2C rate can reach up to 140.7, 126.5 and 105.4 mA h g^{-1} respectively. The LFP-Imp composite delivers a discharge capacity of 135.3, 118.5 and 99.1 mA h g^{-1} at 0.5, 1 and 2C. The LFP-UltraImp sample behaves poorly and exhibits the lowest discharge capacity, 125.8, 110.2 and 93.4 mA h g^{-1} at 0.5, 1, and 2 C. To investigate the recyclability of the as-synthesized $LiFePO_4$/C samples, the coin cells were cycled at 0.5 C for 100 cycles. As can be seen from Figure 2-11c, it was found that LFP-Imp and LFP-Copre can exhibit discharge capacities of 119.1 and 108.0 mA h g^{-1} at 0.5C after 100 cycles, which are about 90.2 and 85.0 % of the initial discharge capacity respectively. In contrast, LFP-UltraImp sample delivers the best cycling stability. The LFP-UltraImp sample can show a discharge capacity of 138.0 mA h g^{-1}, with less than 4.7 % loss of discharge capacity after 100 cycles at 0.5C.

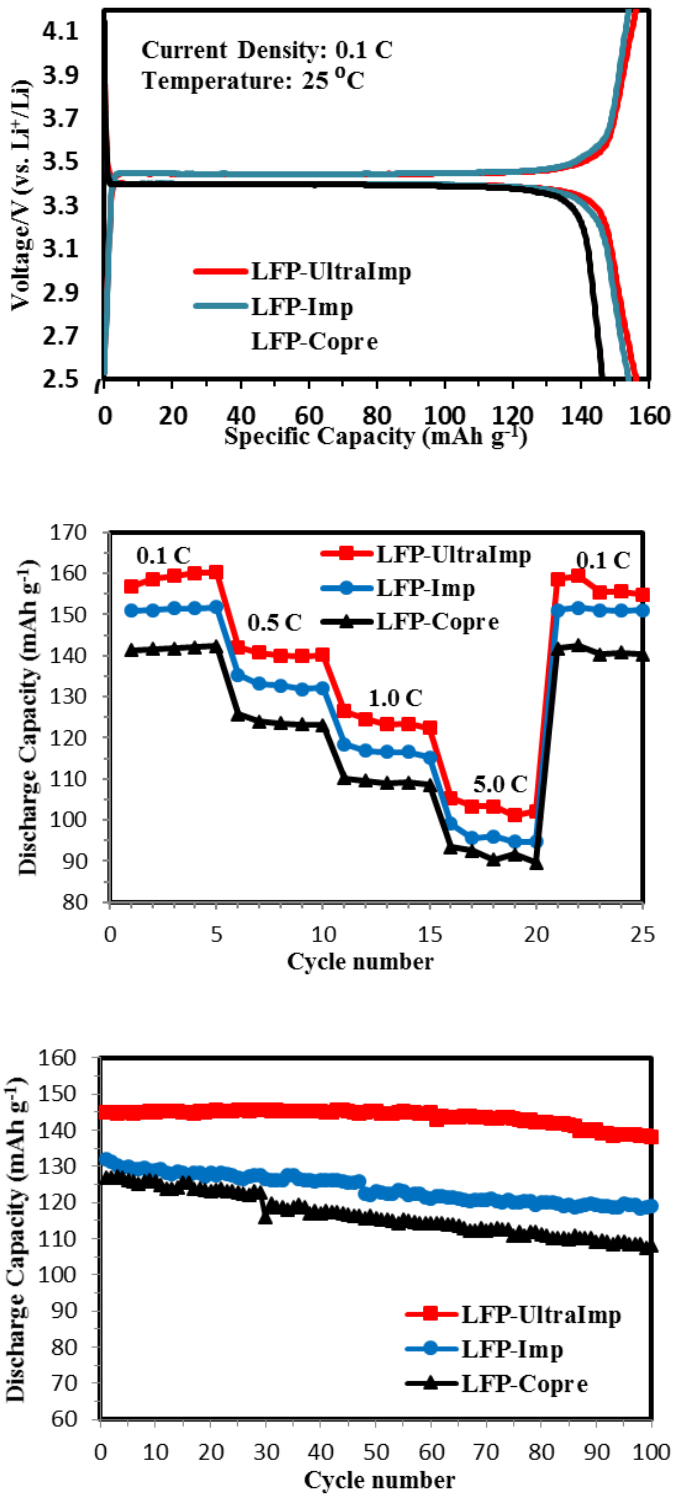

Figure 2-11 Electrochemical performance of LFP-UltraImp, LFP-Imp and LFP-Copre nanoparticles (a) The initial charge/discharge curves at 0.1 C, (b) Rate performance at various rates, (c) Cycling performance at 0.5 C for 100 cycles.

The cyclic voltammogram curves of LFP-UltraImp composite for the first two cycles are shown in Figure 2-12a. During the first cycle, the oxidation and reduction peaks, which are corresponding to the charge/discharge reactions of the Fe^{3+}/Fe^{2+} redox couple, appear at 3.569 and 3.319 V. During the second cycle, the oxidation and reduction peaks take place at 3.541 and 3.326 V respectively. The voltage peak difference between oxidation and reduction is decreased from 0.25 V to 0.181 V. Meanwhile, the current/mass peaks are increased from 0.447 to 0.669 A g^{-1}. The difference of voltage and current/mass peaks indicate that electrode material is activated, and the electrochemical reversibility has been established after the first cycle (Wang *et al*., 2006). In contrast, the potential difference for both LFP-Imp and LFP-Copre is only 0.215 and 0.326 V respectively (Figure 2-12b). The larger and narrower current/mass peaks implicitly confirm that LFP-UltraImp nanoparticles have an improved reversibility and better kinetics of electrochemical reaction (Sun *et al*., 2010; Shi *et al*., 2012).

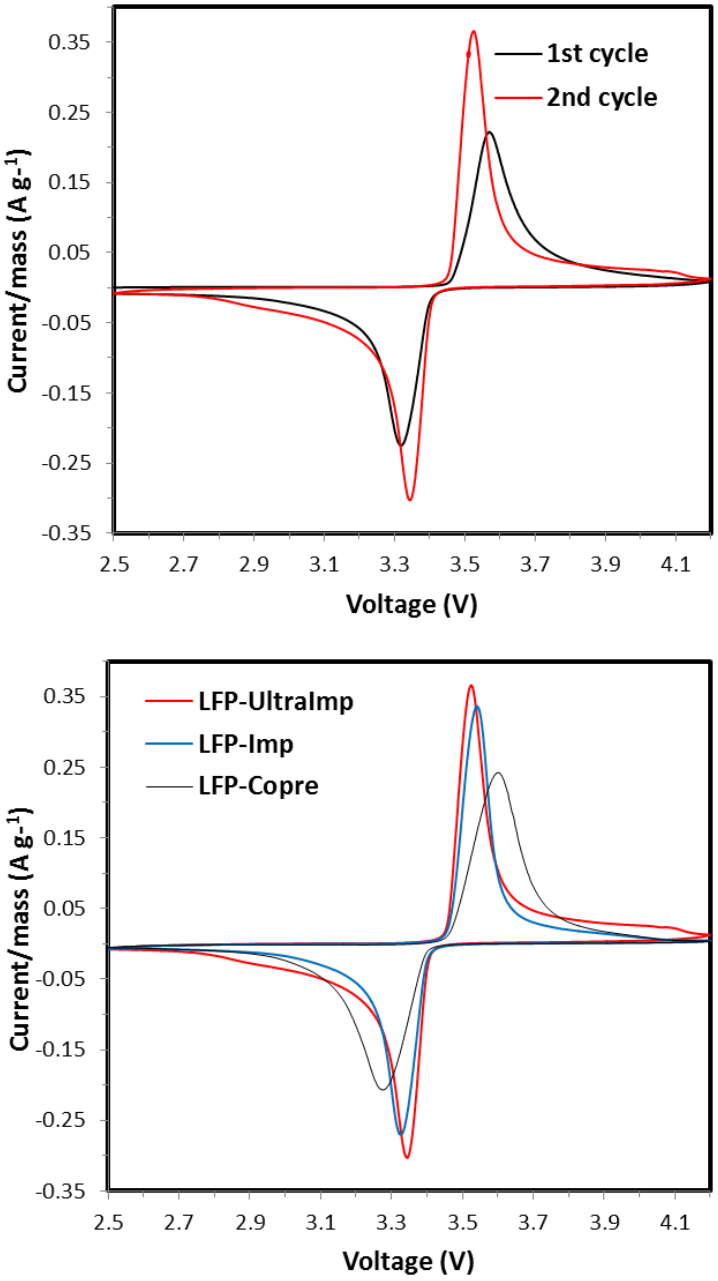

Figure 2-12 Cyclic voltammogram curves of $LiFePO_4$/C samples at a scan rate of 0.1 mV s^{-1} (a) the first and second cycle of LFP-UltraImp sample, (b) the second cycle of three $LiFePO_4$/C samples.

The better electrochemical performance of LFP-UltraImp sample can be attributed to reduced particle size, mesoporous structure and large specific surface area, as well as a higher n_{Fe}/ n_P ratio. It is believed that this structure can shorten the diffusion distance of lithium ion, increase electrolyte/electrode interface area and ensure effective electrolyte permeation into electrode materials, which lead to a relatively high utilization of the active $LiFePO_4$ material. The relatively high n_{Fe}/ n_P ratio of FP-UltraImp also contribute to the better electrochemical properties of LFP-UltraImp. In the lithiation/delithiation process, Li^+ moves through 1D channels which are parallel to b axis. However, 1D channel is easy to be blocked by impurities (Yan *et al*., 2013). The relatively high n_{Fe}/ n_P ratio of FP-UltraImp indicates that LFP-UltraImp composite has higher purity and few blocked 1D channel. Furthermore, besides good electrochemical properties, LFP-UltraImp composite also possesses higher tap density than LFP-Imp due to the smaller pore width and smaller pore volume. The tap density of LFP-UltraImp nanoparticles can reach 1.33 g cm^{-3} in contrast to 1.17 g cm^{-3} for LFP-Imp nanoparticles. All of results obtained have clearly indicated that LFP-UltraImp samples have better electrochemical properties and higher volumetric energy density, thus demonstrating that the adoption of LFP-UltraImp route is an effective way to synthesise the high performance positive electrode precursor particle materials.

2.4 Conclusions

Three different routes were designed for synthesis of $FePO_4$ positive electrode precursor particles, which have been used for amalgamating lithium iron phosphate cathode particles to fabricate the lithium cell battery. It has been demonstrated that the adoption of ultrasonic-assisted impinging stream reaction is an effective approach to

produce high electrochemical performance positive electrode precursor particles. The LFP-UltraImp samples obtained from the experiments have shown an initial discharge capacity of 156.7 mA h g^{-1} at 0.1 C, and exhibited 138.0 mA h g^{-1} after 100 cycles at 0.5 C, which is 95.3% of the initial discharge capacity. The conclusions reached from the current study, in terms of synthesis of mesoporous $FePO_4$ precursors for improving the electrochemical performance of $LiFePO_4$/C, can be summarised:

1) The adoption of impinging stream reaction can be beneficial to generation of $FePO_4$ nanoparticles that have smaller primary grain size, large-mesoporous structures and higher specific surface areas.

2) Application of ultrasonic irradiation can lead to synthesis of small-mesoporous $FePO_4$ precursors that have nanoscale primary nuclei size and high specific surface areas. It can also remarkably improve the purity of $FePO_4$ precursors due to the increased mass diffusion rate between $FePO_4$ and Li_2CO_3.

3) The formation of small-mesopores contributes to an improved electrochemical property and relatively high volumetric energy density of LFP-UltraImp.

References

1. Shu H., Wang X., Wen W. , Liang Q. , Yang X., Wei Q., Hu B., Liu L., Xue X., Song Y., Zho M., Bai Y., Jiang L. , Chen M., Yang S., Tan J., Liao Y., and Jiang H., 2013, Effective enhancement of electrochemical properties for $LiFePO_4$/C cathode materials by Na and Ti co-doping, Eletrochimica Acta, 89, 479-487

2. Gibot P., Casas-Cabanas M., Laffont L., Levasseur S., Carlach P., Hamelet S., Tarascon J.M., and Masquelier C., 2008, Room-temperature single-phase Li insertion/extraction in nanoscale $LixFePO_4$, Nature Materials, 7, 741-747

3. Ding Y., Jiang Y., Xu F., Yin J., Ren H., Zhuo Q., Long Z., and Zhang P., 2010, Preparation of nano-structured LiFePO4/graphene composites by co-precipitation method, Eletrochemistry Communication, 12, 10-13

4. Park K.S., Son J.T., Chung H.T., Kim S.J., Lee C.H., and Kim H.G., 2003, Synthesis of $LiFePO_4$ by co-precipitation and microwave heating, Eletrochemistry Communication, 5, 839-842

5. Padhi K., Nanjundaswamy K. S., Masquelier C., Okada S., and Goodenough J. B., 1997, Effect of structure on the Fe^{3+} /Fe^{2+} redox couple in iron phosphates., Journal of the Electrochemistry Society, 144, 1609-1613

6. Shin H.C., Park S.B., Jang H., Chung K.Y., Cho W., Kim C.S., and Cho B.W., 2008, Rate performance and structural change of Cr-doped $LiFePO_4$/C during cycling, Eletrochimica Acta, 53, 7946-7951

7. Chung S.Y., Bloking J.T., and Chiang Y.M., 2002, Electronically conductive phospho-olivines as lithium storage electrodes, Nature Material, 1, 123-128

8. Guo L., Zhang Y., Ma L., Zhang Y., Wang E., Bi Y., Wang D., McKee W.C., Xu Y., Chen J., Zhang Q., Nan C., Gu L., Bruce P.G., and Peng Z.G., 2015, Unlocking the energy capabilities of micron-sized $LiFePO_4$, Nature Communication, 6, 7898-7905

9. Liu J., Conry T. E., Song X., Doeff M. M., and Richardson T. J., 2011, Nanoporous spherical $LiFePO_4$ for high performance cathodes, Energy & Environmental Science, 4, 885-888

10. Liu J. and Manthiram A., 2011, Understanding the improvement in the electrochemical properties of surface modified 5 V $LiMn_{1.42}Ni_{0.42}Co_{0.16}O_4$ Spinel Cathodes in Lithium-ion Cells, Chemistry of Materials, 21, 1698-1707

11. Vu A., Qian Y., and Stein A., 2012, Porous electrode materials for lithium-ion batteries - how to prepare them and what makes them special, Advanced Energy Materials, 2, 1056-1085

12. Wang K.X., Li X.H., and Chen J.S., 2015, Surface and interface engineering of electrode materials for lithium-ion batteries, Advanced Materials, 27, 527-545

13. Adelhelm P., Hu Y.S., Chuenchom L., Antonietti M., Smarsly B. M., and Maier J., 2007, Generation of hierarchical meso- and macroporous carbon from mesophase pitch by spinodal decomposition using polymer templates, Advanced Materials, 19, 4012-4017

14. Doherty M., Caruso R.A., and Drummond C.J., 2010, High performance $LiFePO_4$ electrode materials: influence of colloidal particle morphology and porosity on

lithium-ion battery power capability, Energy & Environmental Science, 3, 813-823

15. Wang Z., Li F., Ergang N. S., Stein A., 2006, Effects of hierarchical architecture on electronic and mechanical properties of nanocast monolithic porous carbons and carbon−carbon nanocomposites, Chemistry of Materials, 18, 5543-5553

16. Suslick K.S. and Price G.J., 1999, Applications of ultrasound to materials chemistry, Annual Review of Materials Science, 29, 295-326

17. Xu H., Zeiger B.W., and Suslick K.S., 2013, Sonochemical synthesis of nanomaterials. Chemical Society Review, 42, 2555-2567

18. Huang Y., Wang P., Yuan Y., Ren X., and Yang F., 2015, Synergistic degradation of chitosan by impinging stream and jet cavitation, Ultrasonics Sonochemistry, 27, 592-601

19. Siddiqui S.W., Unwin P.J., Xu Z., and Kresta S.M., 2009, The effect of stabilizer addition and sonication on nanoparticle agglomeration in a confined impinging jet reactor, Colloids and Surfaces A: Physicochemical and Engineering Aspects, 350, 38-50

20. Yan P., Lu L., Liu X. M., Cao Y., Zhang Z. P., Yang H., and Shen X.D., 2013, An economic and scalable approach to synthesize high power $LiFePO_4$/C nanocomposites from nano-$FePO_4$ precipitated from an impinging jet reactor, Journal of Materials Chem*istry* A, *35, 10429-10435*

21. Bang J.H. and Suslick K.S., 2010, Applications of ultrasound to the synthesis of nanostructured materials, Advanced Materials, 22, 1039-1059.

22. Mahajan J. and Donald J.K., 1996, Micromixing effects in a two impinging jets precipitator, AIChE Journal, 42, 1801-1814

23. Liu H., Miao C., Meng Y., Xu Q., Zhang X. and Tang Z., 2014, Effect of graphene nanosheets content on the morphology and electrochemical performance of $LiFePO_4$ particles in lithium ion batteries, Eletrochimica Acta, 135, 311-318

24. Tan L., Tang Q., Chen X., Hu A., Deng W., Yang Y., and Xu L., 2014, Mesoporous $LiFePO_4$ microspheres embedded homogeneously with 3D CNT conductive networks for enhanced electrochemical performance, Eletrochimica Acta, 137 344-351

25. Wang Y., Wang J., Yang J. and Nuli Y., 2006, High-Rate $LiFePO_4$ Electrode Material Synthesized by a Novel Route from $FePO_4 \cdot 4H_2O$. Advanced Functional Materials, 16, 2135-2140

26. Sun C.S., Zhang Y., Zhang X.J. and Zhou Z., 2010, Structural and electrochemical properties of Cl-doped $LiFePO_4$/C. Journal of Power Sources, 195, 3680-3683

27. Shi Y., Chou S.L., Wang J.Z., Wexler D., Li H.J., Liu H.K. and Wu Y.P., 2012, Graphene wrapped $LiFePO_4$/C composites as cathode materials for Li-ion batteries with enhanced rate capability, Journal of Materials Chemistry, 22, 16465-16470

CHAPTER 3: Synthesis of $FePO_4 \cdot 2H_2O$ Nanoparticles Using T-type micromixer

SUMMARY

A T-type micromixer was adopted for synthesis of nanoscale $FePO_4 \cdot 2H_2O$ particles. The experiments clearly demonstrate that the application of the impinging streams in T-mixer is able to significantly enhance the mass transfer rate of the reactant solutions through strong turbulent eddy mixing due to the impingement of two narrow reactant streams at high velocity. In this work, the $FePO_4 \cdot 2H_2O$ nanocomposites were synthesized under precisely controlled pH value (pH = 1.2, 1.4, 1.6, 1.8 and 2.0), reagent concentration (C = 0.5, 1.0 and 1.5 mol L^{-1}), and volumetric flow rate (Q = 17.15, 34.30, 51.44, 68.59, 85.74, 128.61, 171.48, 214.35 and 257.22 mL min^{-1}). Effects of the pH value, reactant concentration (C), and volumetric flow rate Q on synthesis of $FePO_4 \cdot 2H_2O$ nucleus have been studied when the T-mixer operates in nonsubmerged mode. The as-synthesized $FePO_4 \cdot 2H_2O$, $FePO_4$ and its corresponding $LiFePO_4$/C product was characterised by XRD, SEM, BET and electrochemical charge-discharge tests. Under the optimized operation conditions (pH = 1.6, C = 1.0 mol L^{-1}, Q = 85.74 mL min^{-1}), it was revealed that the $LiFePO_4$/C possesses the best charge-discharge performance while the discharge capacities can reach 152.6, 146.9, 139.1, 130.4 and 118.2 mAh g^{-1} at 0.1 C, 0.5 C, 1 C 2 C and 5 C current rates, respectively.

3.1 Introduction

Rechargeable lithium-ion batteries (LIBs) have been demonstrated to be a reliable and predominant power sources and energy storage devices for various usages. Typical examples of applying LIBs are electric vehicles, hybrid electric vehicles and other devices that require sustainable energies (Shu *et al*., 2013; Gibot *et al*., 2008). Compared with the other commercially available positive electrode materials such as $LiCoO_2$, $LiNiO_2$, $LiMn_2O_4$ and their derivatives, olivine-structured $LiFePO_4$ can be considered as one of the highly promising positive electrode material due to its significant advantages of nontoxicity, low cost of the raw materials, good structural stability at high temperature, excellent safety performance, and relatively high theoretical specific capacity (170 mA h g^{-1}) with flat discharge-charge potential (3.45 V vs. Li^+/Li) (Ding *et al*., 2010; Park *et al*., 2003; Padhi *et al*., 1997). In spite of the numerous merits of the performance of $LiFePO_4$, however, the low Li^+ diffusivity (10^{-17} to 10^{-14} cm^2 s^{-1}) and intrinsic low electronic conductivity (10^{-9} to 10^{-8} S cm^{-1}) have confined the electrochemical performance of $LiFePO_4$ and constrained its practical application (Shin *et al*., 2008; Chung *et al*., 2002; Guo *et al*., 2015). The reported approaches to improve charge transport of $LiFePO_4$ for high rate applications are mainly based on conductive carbon coating, particle morphology optimization and metal doping. Among these, particle morphology optimization, especially for reduction of particle size and fabrication of electrode materials with integrated porosity, can remarkably enhance electrochemical properties of positive electrode because reduction in particle size can shorten the Li^+ diffusion path and facilitate the kinetics of Li^+ insertion and extraction process. Meanwhile, fabrication of positive

electrode material with porous structure can increase electrode/electrolyte interface area and ensure effective electrolyte permeation (Vu *et al*., 2012; Wang *et al*., 2015).

It has been recognised that rapid and homogeneous micromixing of feeding streams would be beneficial to the preparation of nanoparticles. However, a rapid micromixing is very difficult to be realised when employing the traditional stirring reactor due to the poor mixing and mass transfer performance (Baldyga *et al*., 1997; Bhattacharya and Kresta, 2004). Some micromixers, such as impinging jet stream reactor and T-type micromixer, however, has been proved to be able to significantly intensify the mixing, especially micromixing, within extremely short time. Thus it has been applied for the preparation or synthesis of catalysts (Zhang *et al*., 2015; Zhang *et al*., 2016), chitosan (Huang *et al*., 2015), light conversion materials (Zhou *et al*., 2012), drugs (Valente *et al*., 2012), and energy storage materials (Xiao *et al*., 2013; Yan *et al*., 2013). Generally, impinging jet stream reactor and T-mixer are simplest component that two inlet tubes and one outlet tube join the main channel (Andreussi *et al*., 2015; Krupa *et al*., 2014). The difference between impinging jet stream reactor and T-mixer is that, impinging jet stream reactor has sufficient space in outlet so that pressure energy can be released and translated in kinetic energy. In these components, a local intensive micro-mixing can be generated by the collision between two high speed impinging streams. The existing understanding to the impinging streams has revealed the adoption of liquid-continuous impinging streams (LIS) to have two major features: local pressure fluctuations and homogeneous micromixing. In a synthesis process, efficient micromixing due to turbulent eddy motion can remarkably improve the mass transfer rate between the mixed solutions and increase the reaction rate. As a result, the probability of crystal nucleus collision increases significantly. The local

pressure fluctuations can also influence the energy and mass transfer in the solution (Huang *et al*., 2015). Comparing with conventional stirred tanks, an impinging stream reactor or T-type micromixer has fixed and confined volume, leading to several orders of magnitude higher mixing intensity and uniform residence time when the feeding rate is kept to be steady. This kind of hydrodynamic reaction environment will be beneficial to the control of the mixing conditions and local reactant concentrations (Siddiqui *et al*., 2009).

The use of impinging stream in micromixer for material synthesis has been documented in many previous researches for various applications. $CuO/ZnO/Al_2O_3$ catalysts used for methanol synthesis, prepared by impinging steam reactor, has shown superior physicochemical properties and higher catalytic activity compared with the preparation method of conventional batch processing (Kaluza *et al.,* 2011; Simson *et al*., 2013). Zhang *et al* (2015) prepared $CuO/ZnO/Al_2O_3$ catalysts by using a similar method and have investigated the effects of reagent concentration, volumetric flow rates and aging time on the catalyst structure and catalytic performance. Jiang *et al* (2015) applied a dual impinging jet mixer to investigate the effect of jet velocity on crystal size distribution of pharmaceutical ingredients. Yan *et al.* (2013) have found that the use of impinging stream reaction with the pH of the working solution being 1.3 can achieve the molar ratio of nFe to nP to be equal 1 in the obtained amorphous FP and uniform particle size in the range of 40-60 nm. They considered the hexagonal FP to be the preferred form for synthesising the LFP/C with good electrochemical performance. They also attribute the use of the impinging stream to give rise to the low possibility of ionic disorder and stacking faults in LFP nanoparticles, and the capability of the highly pure LFP. Casanova and Higuita

adopted a specially designed high pressure jet homogenizer to investigate the effect of total pressure drop, pH value, temperature, and protein concentration on the formation of calcium carbonate nanoparticles. Tari *et al* (2015) have revealed that the crystal size of glycine can be reduced by using impinging stream. Wu *et al* (2006) also demonstrated that the function of the impinging stream reaction is to assist to gain homogeneous mixing and to reduce the particle size of barium sulfate. Li *et al* (2015) synthesized ZnO/Ag micro/nanospheres using microwave-assisted impinging stream microreactor and found that the photocatalytic and antibacterial properties of ZnO/Ag can be enhanced. Kumar *et al* (2013) synthesized nanocrystalline MgO by impinging stream micromixing, and investigated the effect of jet impingement angle and jet velocity (Reynolds number). Additionally, the use of computational fluid dynamics (CFD) modelling approach has been applied to study the micromixing efficiency of impinging stream by adopting Villermaux-Dushman parallel competing reaction system as indicators (Liu *et al*., 2014; Siddiqui *et al*., 2009; Liu and Fox, 2006). Planar Laser Induced Fluorescence (PLIF) technique is also used to investigate the impact of Reynolds number on mixing (Fonte *et al*., 2015; Shi *et al*., 2015). For T-mixer, Svetlana Borukhova *et al* (2016) used T-mixer to convert bulk alcohols into the corresponding chlorides. Polyzoidis *et al* (2016) developed a microreaction technology (MRT) with T-mixer to prepared metal-organic framework ZIF-8. Due to the highly controlled mas and heat transport conditions provided by MRT, the productivity and repeatability in the preparation of ZIF-8 can be enhanced significantly. Oleksii Kolmykov *et al* (2017) also synthesize ZIF-8 crystals via microfluidic technology by using T-micromixer. Seck Hoe Wong *et al* (2004) demonstrated that, in a micro T-mixer, rapid mixing can be achieved when the Reynolds number is between 400 and 500, because liquid streams can break up into

striations and then these striations will disappear into uniform concentration across the mixing channel. Moreover, the mixing characteristics of T-type mixer are also investigated with gas phase (Soleymani *et al*., 2008), liquid phase (Gobby *et al*., 2001), and for the generation of nanoparticles (Gradl *et al*., 2006).

Though there are many studies on applying the impinging stream in T-type micromixer for different materials synthesis, the studies on synthesis of $LiFePO_4$ nanocomposites using impinging stream are still limited and the factors that afftect the synthesis process are required further investigations.

The aim of this paper is to report synthesis of $FePO_4 \cdot 2H_2O$ nanocomposites using the impinging streams in T-type micromixer at various operating conditions, focusing on (1) effect of different pH values, reagent concentrations (*C*) and volumetric flow rates (*Q*); (2) effect of the synthesis conditions on the morphology and structures of samples; and (3) the electrochemical properties of the corresponding $LiFePO_4$/C samples. The paper will be organised in such a way. Section 2 will present the experimental details including materials preparation, characterisation of $FePO_4$ and $LiFePO_4$/C and cell preparation for electrochemistry test while section 3 will present the results and discussion, focusing on the effects of various conditions on synthesis of $FePO_4 \cdot 2H_2O$ nanocomposites when applying impinging stream in T-type micromixer. Section 4 will present the conclusions derived from the study.

3.2 Experimental

3.2.1 Materials preparation

The $FePO_4 \cdot 2H_2O$ nanocomposites were synthesized through the T-type micromixer. Iron nitrate solution and diammonium phosphate solution (C = 0.5, 1.0 and 1.5 mol L^-

^{1}, respectively) were injected continuously into aT-type micromixer by using two peristaltic pumps (BT100FJ, Baoding Chuangrui, China) to precisely control flow rates. The experimental set-up and internal structure of T-type micromixer were shown in Figure 3-1. The inlet ports of T-type micromixer were connected to two stainless steel tubes with an inner diameter of 2.5 mm. The inner diameter and length of internal chamber in T-type micromixer were 3.5 mm and 17 mm, respectively. The outlet of the T-type micromixer which has the same diameter as the impinging stream inlets and an enlarged channel (with an inner diameter of 4 mm) was interconnected to the inner chamber of the T-type micromixer.

The volumetric flow ratio of the two reagent solutions was kept at 1, with varying volumetric flow rate (Q) ranging from 17.15 to 257.22 mL min^{-1}. The mixed solution was then transfered into a 1 L glass beaker and vigorously stirred for 10 mins after impinging and precipitating within T-type micromixer under room temperature of 20 °C. Meanwhile, the pH value of solution was maintained at the given value (pH=1.2, 1.4, 1.6, 1.8 and 2.0, respectively) but was added the ammonia solution (1.5 mol L^{-1}) carefully through a pH automatic controller. The conditions of different experiments are shown in Table 3-1. The obtained products were subsequently washed with deionized water for 3 times, filtrated and then dried in air at 100 ℃ for 12 h. Then the synthesised particles were calcined in air at 600 °C for 10 hours to obtain anhydrous crystalline $FePO_4$ samples.

To synthesize $LiFePO_4$/C composites, the nano-sized crystalline $FePO_4$ samples were mixed with Li_2CO_3 and glucose at a desired molar ratio of 1:1.05:0.1 and ball-milled at 300 rpm for 2 hours by a planetary ball mill to obtain a homogeneous mixture. The

mixtures were then dried and calcined at 650 ℃ for 10 h in nitrogen atmosphere to obtain $LiFePO_4$/C samples.

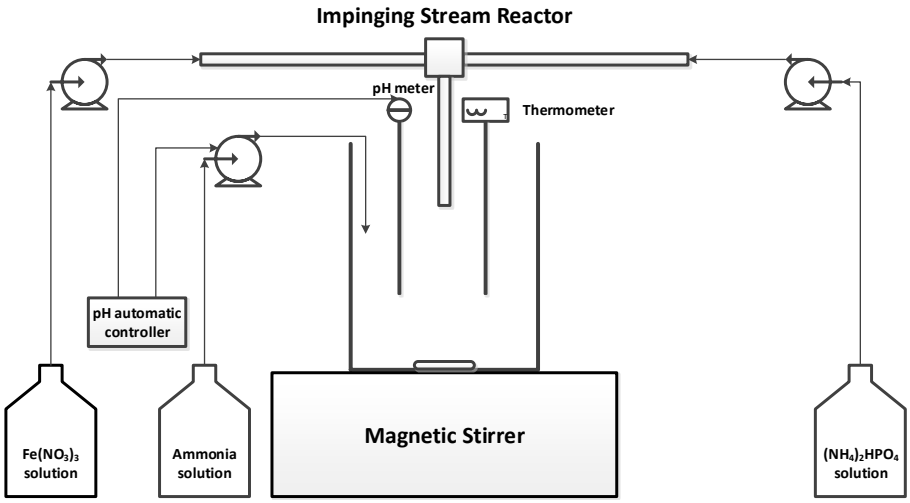

(a)

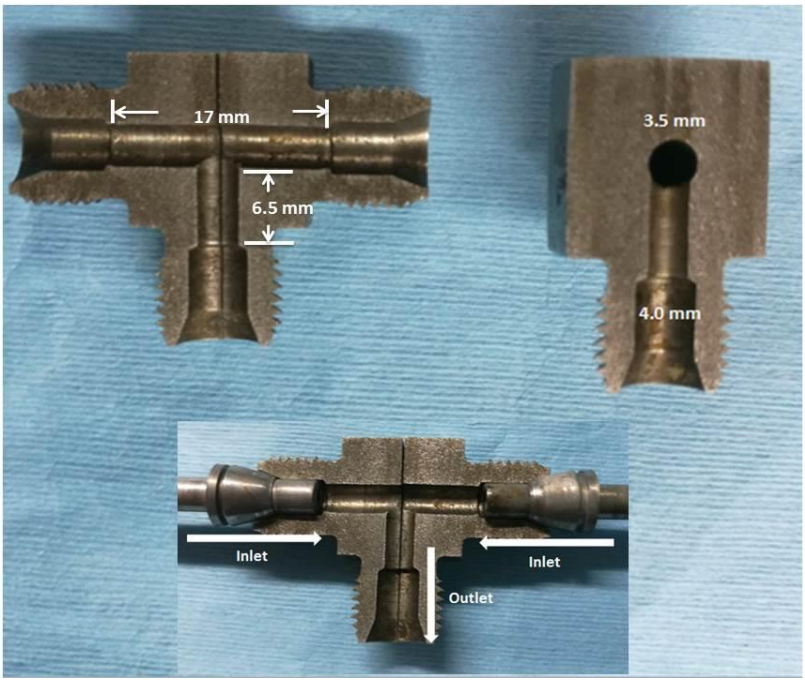

(b)

Figure 3-1 (a) T-mixer system used for synthesis of $LiFePO_4$ nanocomposites; (b) Photographic views of the internal structure of T-mixer.

Table 3-1 Dimensions of experiments for the systhesis of $FePO_4 \cdot 2H_2O$ particles

Experiments	pH value	Reagent concentration (C, mol L^{-1})	Volumetric feeding rate (V, ml min^{-1})
S1	1.2	1.0	85.74
S2	1.4	1.0	85.74
S3	1.6	1.0	85.74
S4	1.8	1.0	85.74
S5	2.0	1.0	85.74
S6	1.6	0.5	85.74
S7	1.6	1.5	85.74
S8	1.6	1.0	17.15
S9	1.6	1.0	34.30
S10	1.6	1.0	51.44
S11	1.6	1.0	68.59
S12	1.6	1.0	128.61
S13	1.6	1.0	171.48
S14	1.6	1.0	214.35
S15	1.6	1.0	257.22

3.2.2 Characterization of $FePO_4$ and $LiFePO_4$/C

The crystal structure of $FePO_4$ and $LiFePO_4$/C samples were subjected to the analysis using a Bruker D8 series X-ray diffraction with Cu Kα radiation (λ=1.5406Å) operated at 40kV and 40 mA. The scanning range of diffraction angle (2Θ) was set

$10^0 \leq 2\Theta \leq 70^0$. The sample morphology was also observed by scanning electron microscope (Sigma VP, ZEISS, Germany). Pore size/volume and specific surface area were acquired and analysed by using Brunauer Emmett Teller (BET, Micromeritics ASAP 2020, U.S.A).

3.2.3 Cell fabrication and electrochemical analysis

To test electrochemical performance, as-synthesized $LiFePO_4$/C active material, acetylene black and polytetrafluoroethylene (PTFE) binder were mixed in a weight ratio of 80 : 15 : 5. Then 1 g mixture was vigorous magnetically stirred in 3 ml N-methyl-2-pyrrolidene (NMP) solvent to prepare homogeneous slurry. An appropriate amount of slurry was then spread on Al foils and dried at 80 ℃ for 6 h in a vacuum oven. The dried samples were punched to form disc shape with a diameter of 1.3 cm and weighted in a high-precision analytical balance. The obtained Al foils coated with active materials were used as positive electrode. The electrolyte was 1 M $LiPF_6$ which dissolved in ethylene carbonate (EC)/diethyl carbonate (DEC) (50:50 vol%). Celguard 2300 microporous film was applied as separator. The coin cell assembling process was carried out in a dry Ar-filled glove box. The charge-discharge performance of the fabricated coin cells was measured on a battery system (LAND,CT2001A, China) between 2.5 V and 4.2 V versus Li/Li^+ for given cycles.

3.3 Results and discussion

3.3.1 Effect of pH value on the morphology and electrochemical performance of $FePO_4$ precursor and $LiFePO_4$/C composites

To determine the optimal pH value of solution for the best electrochemical properties, samples were prepared with reactant concentration (*C*) of 1.0 mol L^{-1} and volumetric

flow rate (Q) of 85.74 ml min^{-1}. The XRD patterns of $FePO_4$ composites prepared at different pH value by T-type micromixer are shown in Figures 3-2a. All the XRD patterns of $FePO_4$ composites match well with anhydrous hexagonal structure $FePO_4$ (JCPDS card no. 29-0715, a=5.035Å, b=5.035Å, c= 11.245Å). It can be seen clearly from the figure that when $FePO_4$ composites were synthesized at pH=1.6, the diffraction peaks at $2\Theta = 20.3^0$ and 25.8^0 were higher and sharper than those for other samples. This can be ascribed to the high degree of crystallinity of the samples when keeping pH=1.6. The calculated cell parameters, nuclei size and yield of FP samples synthesized at different pH value are listed in Table 3-2. All the calculated lattice constants match well with anhydrous hexagonal structured $FePO_4$ (JCPDS card no. 29-0715, a = 5.035 Å, b = 5.035 Å, c = 11.245 Å), suggesting the formation of perfect crystalline $FePO_4$ composites at all pH value. Simultaneously, it can be clearly observed that the S3-FP sample shows a relatively smaller nuclei size (246.77 $Å^3$), and the highest yield (86.8 %), which may suggest that the pH = 1.6 is the optimal pH value for the synthesis of FP sample in this study.

Table 3-2 Calculated lattice parameters, nuclei size and yield of FP samples synthesized at different pH value

Samples	a(Å)	b(Å)	c(Å)	V(Å^3)	Yield (%)
S1-FP	5.0359	5.0359	11.2524	247.13	46.0
S2-FP	5.0330	5.0330	11.2567	246.94	57.1
S3-FP	5.0335	5.0335	11.2467	246.77	86.8
S4-FP	5.0327	5.0327	11.2432	246.62	78.3
S5-FP	5.0341	5.0341	11.2434	246.76	84.1

The diffraction of corresponding $LiFePO_4$/C composites as shown in Figure 3-2b is well indexed with $LiFePO_4$ with the orthorhombic structure (JCPDS card no.40-1499, a=10.347 Å, b=6.019 Å, c=4.704 Å), indicating that the crystallinity of the precursor has no effect on the structure and crystallinity of the resulting $LiFePO_4$/C. The calculated lattice parameters and nuclei size of the five as-synthesized $LiFePO_4$/C samples are listed in Table 3-3. All crystal lattice parameters are also well indexed to accord with $LiFePO_4$ which has the orthorhombic structure (JCPDS card no.40-1499, a = 10.347 Å, b = 6.019 Å, c = 4.704 Å), suggesting all the five $LiFePO_4$/C nanocomposites were synthesized without any appreciable impurity phases.

Table 3-3 Calculated lattice parameters and nuclei size of LFP samples samples synthesized at different pH value

Samples	a(Å)	b(Å)	c(Å)	V(Å^3)
S1-LFP	6.0020	10.3243	4.7133	292.06
S2-LFP	6.0034	10.3288	4.6892	290.77
S3-LFP	6.0083	10.3239	4.6923	291.06
S4-LFP	6.0061	10.3286	4.6883	290.83
S5-LFP	6.0064	10.3286	4.6902	290.97

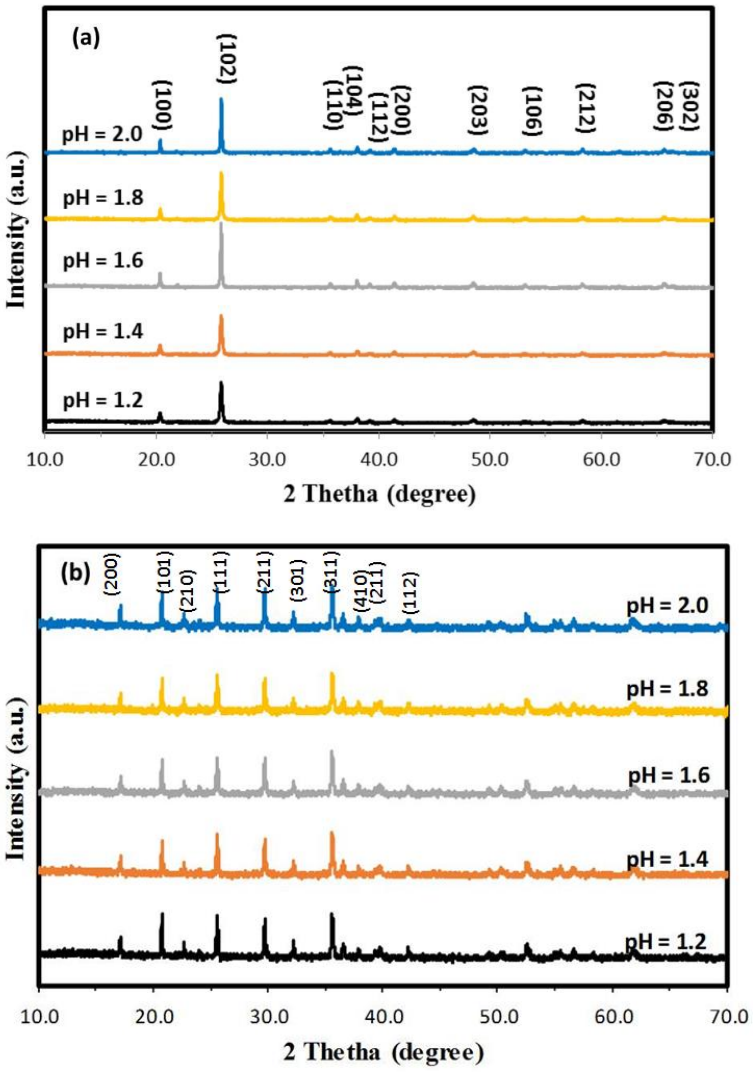

Figure 3-2 X-ray diffraction patterns of (a) $FePO_4$ composites and (b) $LiFePO_4$/C composites synthesized at different pH values.

The morphology of $LiFePO_4$/C composites prepared by the T-type micromixer at different pH values was examined by scanning electron microscopy (SEM). As the morphology of $LiFePO_4$/C samples is significantly affected by $FePO_4$ precursor, the reagent concentration and volumetric flow rate were maintained at same level for the synthesis of $FePO_4$ precursor by varying the pH values. It is noticed that the difference of $LiFePO_4$/C prepared when adopting the pH values greater than 1.6 is not remarkable as can be seen from the SEM images shown in Figure 3-3. For the cases of pH=1.6, 1.8 and 2.0, $LiFePO_4$/C were well synthesised, exhibiting apparent characteristics of nano-porosity and nanocrystals. The nanocrystals formed for these three pH conditions present very similar morphological structures that can be judged as nanospheres with sizes ranging from 80 nm to 300 nm. These nanospheres interweave to accumulate and form the high porosity structures. However, the $LiFePO_4$/C composites synthesized at the conditions pH=1.2 and 1.4, as shown in Figures 3-3a and 3-3b, have structures of lower porosity with those nanospheres to accumulate disorderly and non-uniformly distribute.

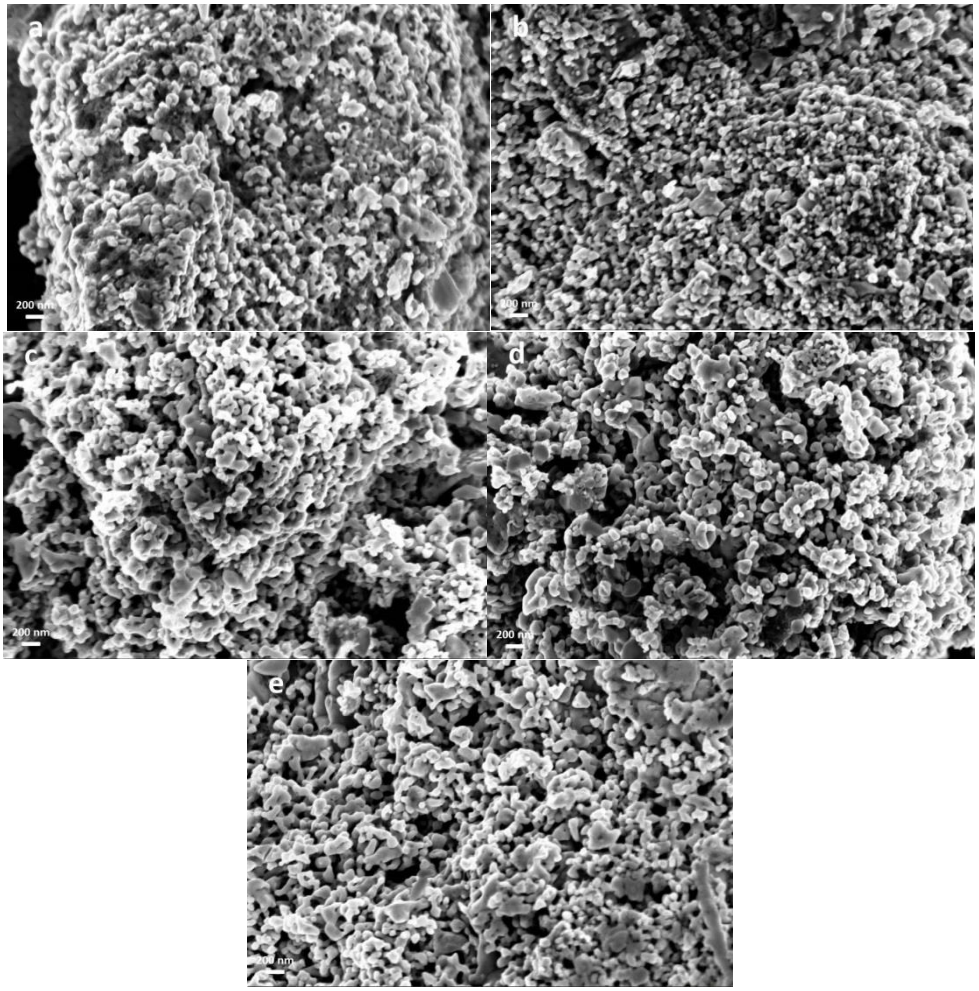

Figure 3-3 SEM images of $LiFePO_4$/C composites synthesized at different pH values: (a) pH=1.2, (b) pH=1.4, (c) pH=1.6, (d) pH=1.8 and (e) pH=2.0.

The coin cell batteries assembled using the synthesised $LiFePO_4$/C composites were charged and discharged at various rates varying from 0.1 C to 5 C and finally returned to 0.1 C in cycle. The test results of the electrochemical performance characterised by the current capacity, as shown in Figure 3-4 and listed Table 3-4, indicate that the pH value used during synthesis process has an important impact on the rate and cycle performance of the samples. This can be seen clearly from the figure that $LiFePO_4$/C samples synthesized at relatively higher pH value (1.6, 1.8 and 2.0) exhibit better rate and cycle performance. The $LiFePO_4$/C obtained at pH=1.6 shows the best rate

capability among all the samples. Its average discharge capacities can reach 150.5, 143.9, 138.6, 130.4 and 117.8 mAh g^{-1} at 0.1 C, 0.5 C, 1 C, 2 C and 5 C, respectively. It is noticed that the discharge capacity of $LiFePO_4$/C composites synthesized at pH=2.0 is higher than the $LiFePO_4$/C obtained at pH=1.6 at a high rate of 5 C (118.2 mAh g^{-1}), indicating that Li^+ insertion/extraction process is kinetically facilitated at a relatively high rate. The migration pathway of Li^+ in $LiFePO_4$ is one-dimensional channel orienting along [010] direction which is blocked by impurities easily. Therefore, the relatively higher electrochemical performance of $LiFePO_4$/C samples might reveal that less undesirable impurities are produced at relatively higher pH value (1.6, 1.8 and 2.0) in this study (Islam *et al*., 2005) . The cycle performances of $LiFePO_4$/C synthesized at different pH values are shown in Figure 3-4b and listed in Table 3-4. The $LiFePO_4$/C composite obtained at pH=2.0 achieves the most stable cycle performance. The discharge capacity at 1^{st} and 100^{th} cycle was 140.6 and 141.8 mAh g^{-1}, respectively, and the capacity retention after 100 cycles is 100.8%.

Table 3-4 The comparison of electrochemical performance of the $LiFePO_4$/C synthesized by T-type micromixer with different pH value (pH=1.2, 1.4, 1.6, 1.8, and 2.0).

pH value	Cycle performance at 0.5 C ($mAh\ g^{-1}$)			Average Rate Performance ($mAh\ g^{-1}$)				
	1st cycle	100th cycle	R_1[a](%)	0.1 C	0.5 C	1 C	2 C	5 C
pH=1.2	116.5	116.9	100.3	129.8	117.6	112.6	101.9	86.0
pH=1.4	121.3	119.1	98.2	134.5	124.4	117.2	106.0	92.5
pH=1.6	144.7	136.4	94.3	150.5	143.9	138.6	130.4	117.8
pH=1.8	138.3	139.3	100.7	143.0	137.7	133.1	129.0	118.0
pH=2.0	140.6	141.8	100.8	146.7	141.2	135.9	130.0	118.2

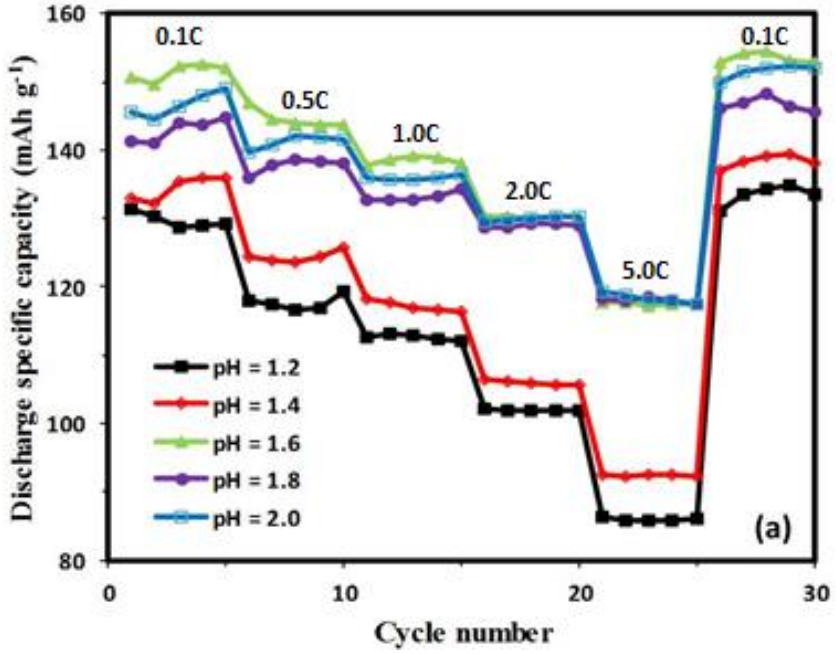
0.1C
0.5C
1.0C
2.0C
5.0C
0.1C
pH = 1.2
pH = 1.4
pH = 1.6
pH = 1.8
pH = 2.0
(a)
Discharge specific capacity (mAh g-1)
Cycle number
160
140
120
100
80
0
10
20
30

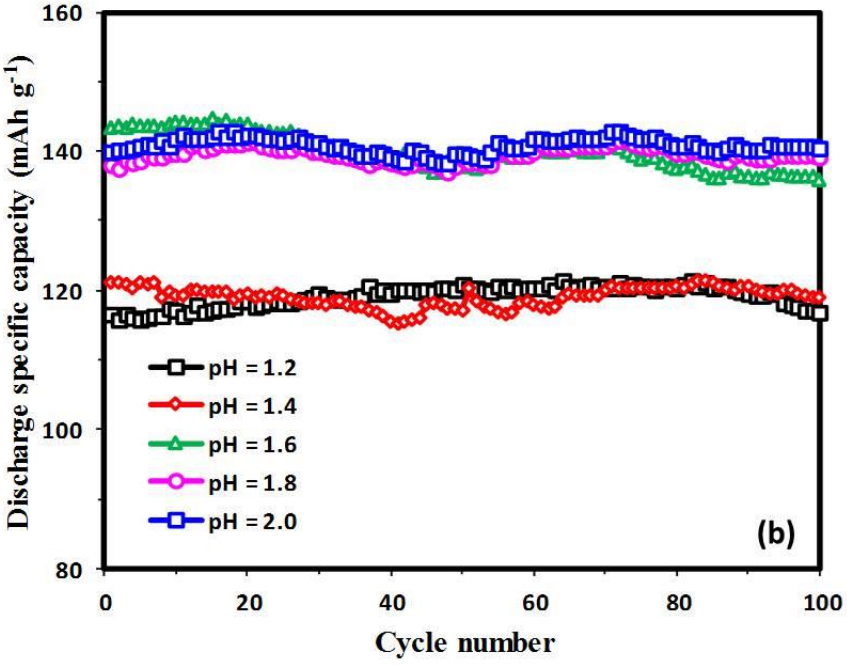
pH = 1.2
pH = 1.4
pH = 1.6
pH = 1.8
pH = 2.0
(b)
Discharge specific capacity (mAh g-1)
Cycle number
160
140
120
100
80
0
20
40
60
80
100

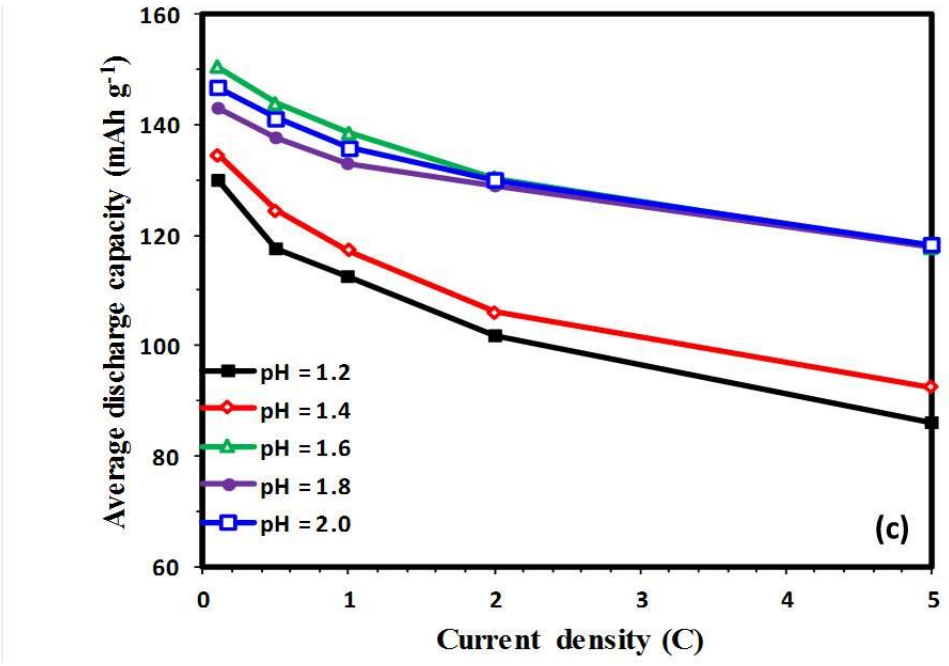

Figure 3-4 Electrochemical performance of $LiFePO_4$/C composites synthesized at different pH values: (a) Rate performance at various rates; (b) Cycling performance at 0.5 C for 100 cycles; (c) Average rate capability.

3.3.2 Effect of reactant concentration on the morphology and electrochemical performance of $FePO_4$ and $LiFePO_4$/C

To seek the optimal value of the initial reagent concentration, $FePO_4 \cdot 2H_2O$ precursors were synthesized using the T-type micromixer but with three different reagent concentrations (C = 0.5, 1.0 and 1.5 mol L^{-1}) while the pH value and volumetric feeding rate were maintained at 1.6 and 85.74 ml min^{-1}, respectively. The BET specific surface area, pore size distribution and primary grain size of the $FePO_4$ precursors prepared with 3 different reagent concentrations were characterised by applying the nitrogen adsorption-desorption analysis. The N_2 sorption isotherm of all $FePO_4 \cdot 2H_2O$ precursors (see Figure 3-5a) was Type IV (Alothman, 2005). Their big

hysteresis loops have provided the evidence for the presence of mesopores (>2nm and <50nm) and large surface area. The analysis results of the pore size distribution of these three samples are shown in Figure 3-5b. All of these three samples presented the features of multi scales, the pores change from the mesopores (pores between 2 and 50 nm) to small macropores (pores between 50 and 90 nm). Table 3-5 and Figure 3-5c clearly demonstrate the influence that increase in the reagent concentration has on the surface area, porosity and average primary grain size of the $FePO_4$ precursor samples. The S3-FP precursor prepared with a reagent concentration of 1.0 mol L^{-1} presents the largest surface area (84.19 m^2 g^{-1}) and adsorption pore volume (0.463 cm^3 g^{-1}) but the smallest average primary grain size (71.27 nm) among all the samples. The measured BET surface areas for S7-FP and S6-FP precursors are 39.53 and 71.24 m^2 g^{-1}, respectively. Meanwhile, the average primary grain sizes of these two samples are 151.78 and 84.22 nm, respectively.

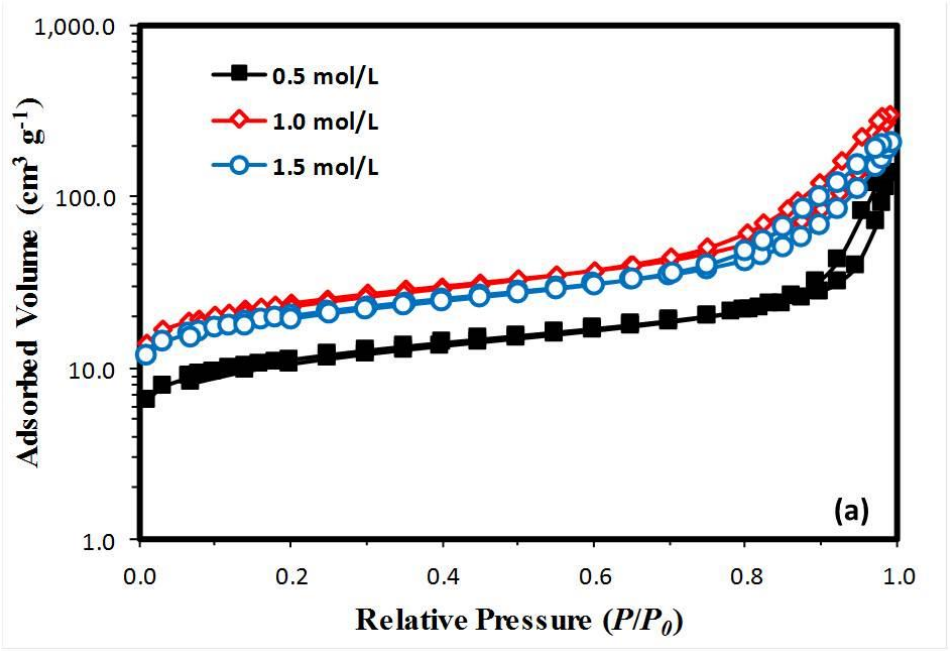
1,000.0
100.0
10.0
1.0
0.5 mol/L
1.0 mol/L
1.5 mol/L
(a)
Adsorbed Volume (cm^3 g^{-1})
0.0
0.2
0.4
0.6
0.8
1.0
Relative Pressure (P/P_0)

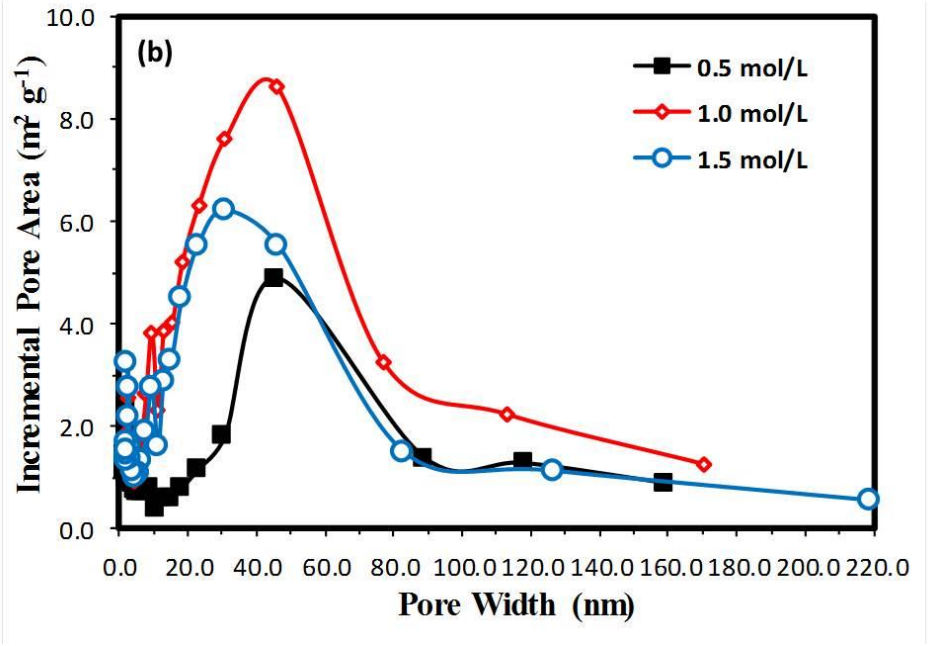
10.0
8.0
6.0
4.0
2.0
0.0
(b)
0.5 mol/L
1.0 mol/L
1.5 mol/L
Incremental Pore Area (m^2 g^{-1})
0.0 20.0 40.0 60.0 80.0 100.0 120.0 140.0 160.0 180.0 200.0 220.0
Pore Width (nm)

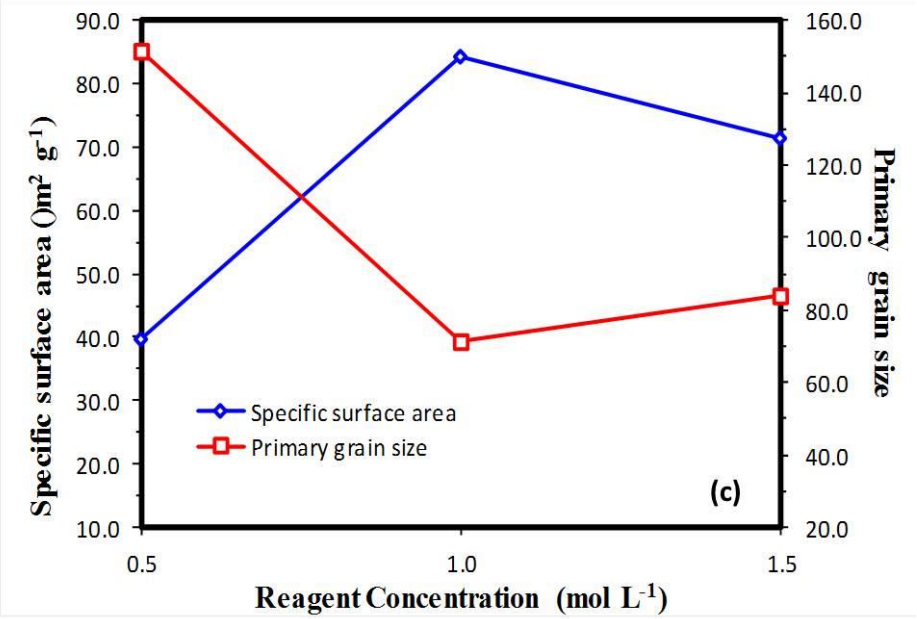

Figure 3-5 (a) N_2 adsorption-desorption isotherms of $FePO_4 \cdot 2H_2O$ composites prepared by T-mixer with different reactant concentration; (b) the corresponding pore-size distribution obtained from the adsorption branch using the BJH method of $FePO_4 \cdot 2H_2O$ composites; (c) the relationships among reagent concentration, average primary grain size and specific surface area of $FePO_4 \cdot 2H_2O$ composites.

Generally speaking, the higher reactant concentration can increase the supersaturation level and nucleation rate in the impinging stream reaction. This can be seen from the following chemical reaction relation:

$$Fe^{3+}(aq) + PO_4^{3-}(aq) = FePO_4(s)$$

where the chemical reaction rate can be evaluated by

$$r = k\left[Fe^{3+}\right]\left[PO_4^{3-}\right] \qquad (3\text{-}1)$$

with *k* being the specific rate constant. It can be seen from the relation that when the initial reagent concentration is doubled, from 0.5 to 1.0 mol L^{-1}, the chemical reaction rate will increase four times. This gives rise to a significant increase in the number of $FePO_4 \cdot 2H_2O$ precursors within the given time and is much beneficial to the generation of the pore structures. As the result, both surface area and total pore adsorption volume are increased but the average primary grain size is reduced, likely due to the confinement of the reaction chamber size of the T-type micromixer. When the reagent concentration is further increased to 1.5 mol L^{-1}, the surface area and total pore adsorption volume decrease and the average primary grain size increases, indicating that with significant increase in chemical reaction rate and nucleation rate, the formation of $FePO_4 \cdot 2H_2O$ nuclei is going more rapidly at a higher reagent concentration when maintaining the volumetric feeding velocity unchanged. The other likely mechanism is that some of the nanoscale nuclei might be stuck to the internal surface of the inlets of the reaction chamber of the T-type micromixer, slightly causing the partial blockage of the inlets to the chamber. The heterogeneous nucleation then occurs on these attached nuclei, resulting in these nuclei to be agglomerated and growing up before they are fed into the turbulent eddies due to the impinging streams. These agglomerated nuclei are trapped by the smallest Kolmogorov scale eddies to form nanoparticles with the pore structures that possess the features of enlarged primary grain size, reduced surface area and pore adsorption volume.

Table 3-5 N_2 adsorption-desorption analysis results of $FePO_4$ precursors prepared by T-type micromixer with different reactant concentration (*C*)

Precursors	Reactant concentration (mol L^{-1})	Surface area (m^2 g^{-1})	Total pore adsorption volume (cm^3 g^{-1})	Primary grain size (nm)
S6-FP	0.5	39.53	0.203	151.78
S3-FP	1.0	84.19	0.463	71.27
S7-FP	1.5	71.24	0.315	84.22

The XRD patterns of a series of $FePO_4$ and $LiFePO_4$/C samples prepared at three different reagent concentrations are shown in Figure 3-6. As shown in Figure 3-6a, all the XRD patterns of $FePO_4$ composites fit the ideally crystallized hexagonal structure $FePO_4$ (JCPDS card no. 29-0715, a = 5.035 Å, b = 5.035 Å, c = 11.245 Å). When *C* = 1.0 mol L^{-1}, the diffraction peak at $2\Theta = 20.3^0$ and 25.8^0 is stronger than other samples, indicating a relatively higher degree of crystallinity. Figure 3-6b shows the XRD patterns of $LiFePO_4$/C synthesized with different reagent concentrations. All the diffraction peaks of $LiFePO_4$/C products match well with standard $LiFePO_4$ with orthorhombic structure (JCPDS card no.40-1499, a = 10.347 Å, b = 6.019 Å, c = 4.704 Å) and no impurity phases was detected, suggesting a perfect crystallinity of the as-synthesized samples. In addition, unlike its $FePO_4$ samples, the diffraction peaks of S3-LFP at $2\Theta = 17^0$, 22^0, 26^0, 29^0, 32^0 and 26^0 are weaker than other samples. The reason might be that S3-FP samples have higher degree of crystallinity. Therefore,

highly crystallized hexagonal structured $FePO_4$ composites are not easy to transfer to orthorhombic structured $LiFePO_4$ when they are culminated in a nitrogen atmosphere, leading to weaker diffraction peaks.

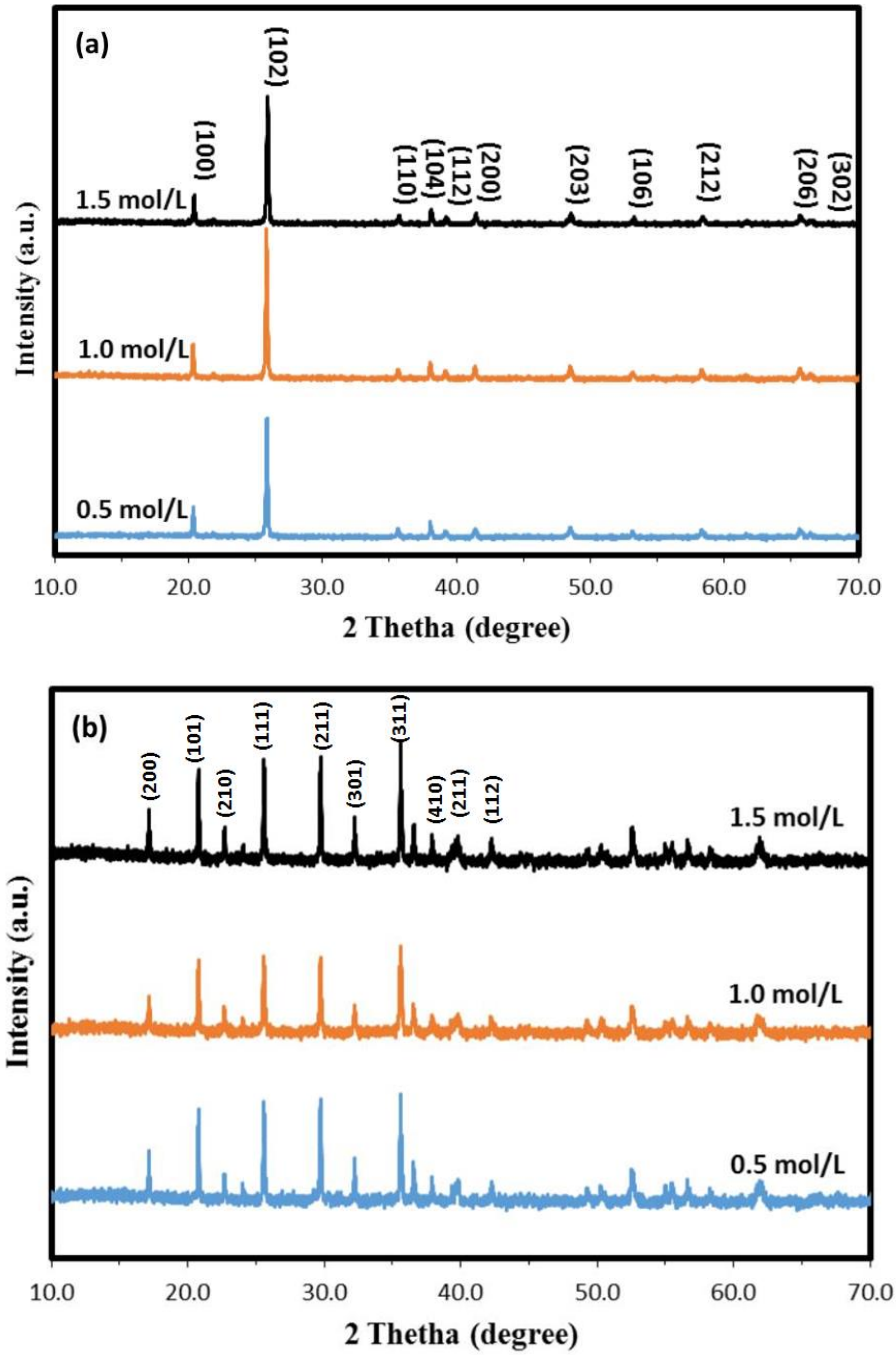

Figure 3-6 X-ray diffraction patterns of (a) $FePO_4$ composites and (b) $LiFePO_4$/C composites synthesized at different reagent concentration.

The SEM images of $LiFePO_4$/C composites prepared at different reactant concentrations by T-type micromixer are shown in Figure 3-7. The sample prepared at C = 0.5 mol L^{-1} shows irregular particle shape with typical diameter of 200-600 nm. When C was increased to 1.0 mol L^{-1}, the $LiFePO_4$/C samples present near spherically shaped grains in the size ranging from 50-300 nm in diameter. Further increasing reagent concentration to 1.5 mol L^{-1}, the $LiFePO_4$/C composites exhibit irregularly shaped crystal with the diameter of 100-600 nm. It should be noted here that some previous studies have shown the reactant concentration to remarkably influence the supersaturation level, nucleation and particle growth rate during the particle formation process. It can be claimed that the feeding concentration confines the minimal nanoparticle size. In general, smaller nanoparticles can be obtained at higher concentrations due to the higher level of supersaturation (Schwarzer amd Peukert, 2004). It is noticed that in this work, the smallest particle size of $LiFePO_4$/C samples was obtained when C = 1.0 mol L^{-1}, consistent with the findings based on the BET results of $FePO_4 \cdot 2H_2O$ precursors. These agglomerated $FePO_4$ crystals may be merged together at high temperature during calcination and $LiFePO_4$/C preparation process, yielding relatively larger $LiFePO_4$/C particles.

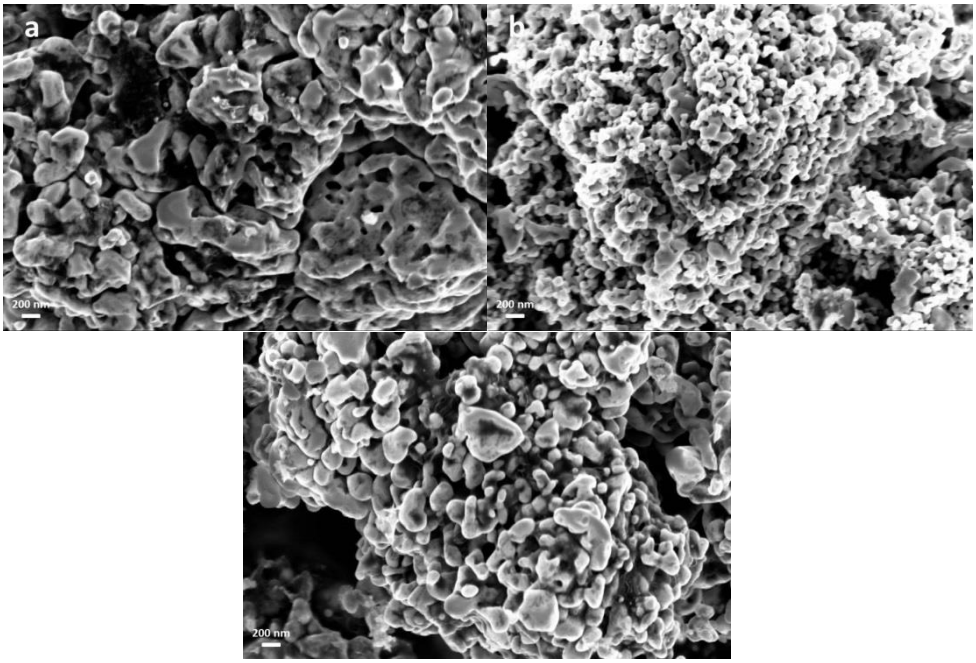

Figure 3- 7 SEM images of $LiFePO_4$/C composites synthesized at different reagent concentration: (a) C = 0.5 mol L^{-1}, (b) C = 1.0 mol L^{-1}, (c) C = 1.5 mol L^{-1}.

The results of electrochemical characterization of $LiFePO_4$/C prepared at different reagent concentrations are shown in Figure 3-8 and listed in Table 3-6. A larger specific surface area is beneficial to increase the interface between electrode and electrolyte, thus providing an effective charge transfer across the interface. A reduced primary grain size helps to shorten the diffusion distance of lithium ion, resulting in an improved electrochemical performance for $LiFePO_4$. Meanwhile, the mesoporous structure can facilitate the penetration of electrolyte and improve the electronic conductivity. The $LiFePO_4$/C prepared at C = 1.0 mol L^{-1} possess the above mentioned conditions, thus showing the best discharge capacities from 0.1 to 5 C. When C = 0.5 mol L^{-1}, the as-synthesised $LiFePO_4$/C nanocomposites present an average discharge capacity of 125.3, 112.8, 103.9, 94.8 and 83.6 mAh g^{-1} at a rate of 0.1 C, 0.5 C, 1 C, 2 C and 5 C, respectively. At higher reactant concentration (C = 1.5 mol L^{-1}), the average discharge capacity can reach 136.9, 121.5, 112.0, 101.9, and

87.5 mAh g^{-1} at a rate of 0.1 C, 0.5 C, 1 C, 2 C and 5 C, respectively. Though the cycling capability of S3-LFP sample, which is shown in Figure 8b, is poorer than other samples, the capacity loss of the S3-LFP is only 5.7 % after 100 cycles at 0.5 C, a favourable property for practical applications This is likely attributed to the larger interface area between nano-sized particles while the electrolyte may lead to undesired side reactions so as to cause poor cycling performance.

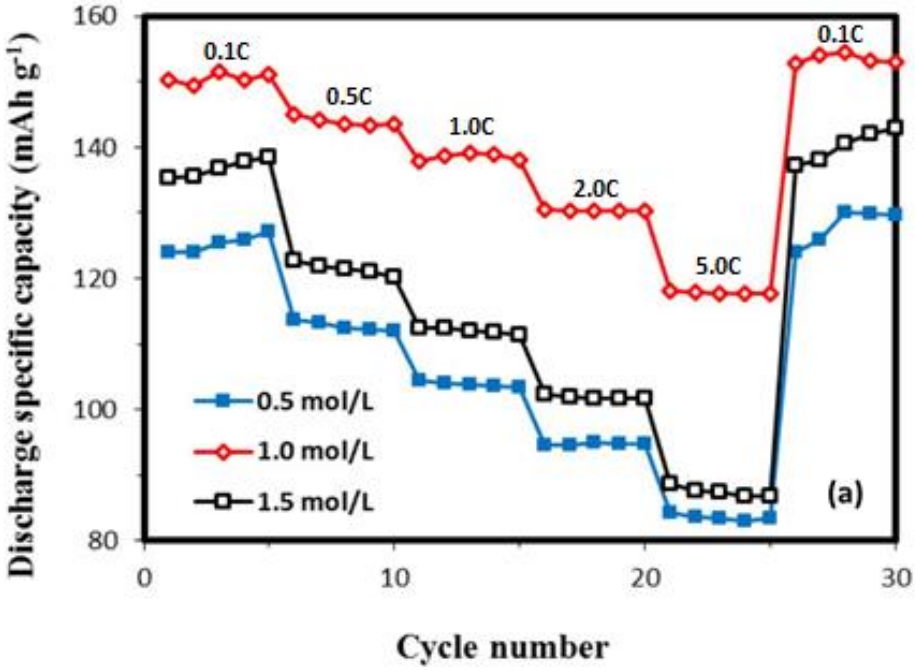
Discharge specific capacity (mAh g-1)
Cycle number
0.1C
0.5C
1.0C
2.0C
5.0C
0.1C
0.5 mol/L
1.0 mol/L
1.5 mol/L
(a)

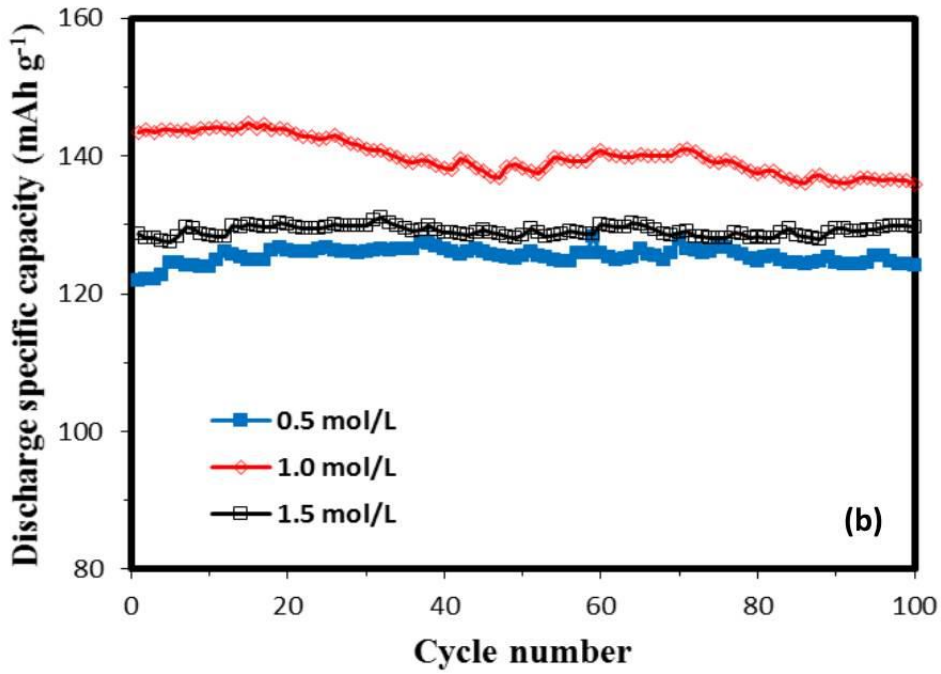
Discharge specific capacity (mAh g-1)
Cycle number
0.5 mol/L
1.0 mol/L
1.5 mol/L
(b)

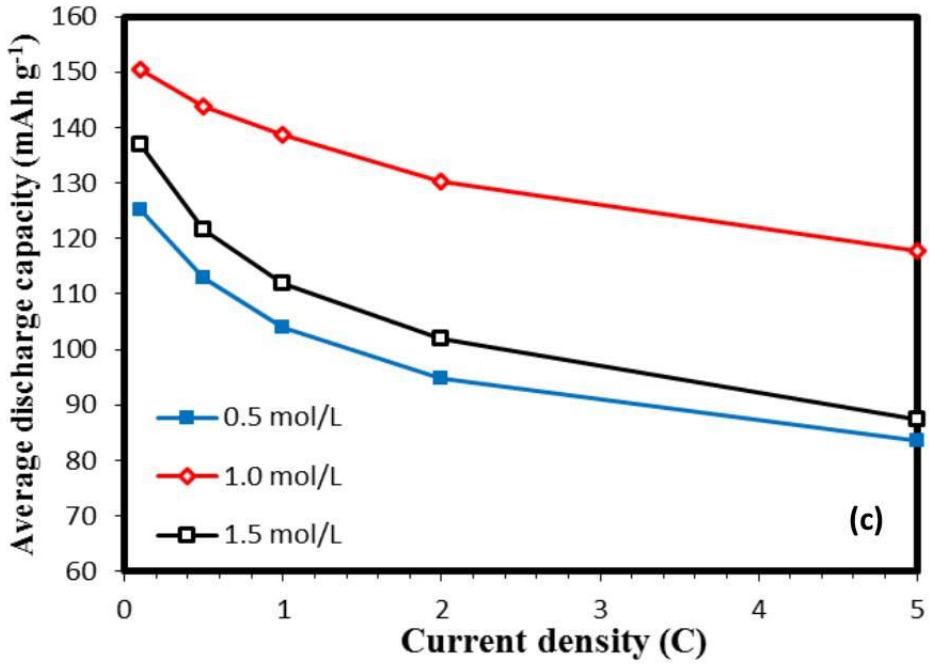

Figure 3-8 Electrochemical performance of $LiFePO_4$/C composites synthesized at different reagent concentrations: (a) Rate performance at various rates, (b) Cycling performance at 0.5 C for 100 cycles, (c) Average rate capability,

Table 3-6 Electrochemical performance of the $LiFePO_4$/C synthesized by employing T-type micromixer with different reagent concentrations

Concentration (C, mol L^{-1})	Cycle performance at 0.5 C (mAh g^{-1})			Average Rate Performance (mAh g^{-1})				
	1^{st} cycle	100^{th} cycle	R_1[a](%)	0.1 C	0.5 C	1 C	2 C	5 C
0.5	122.0	124.1	101.7	125.3	112.8	103.9	94.8	83.6
1.0	144.7	136.4	94.3	150.5	143.9	138.6	130.4	117.8
1.5	128.6	129.6	100.8	136.9	121.5	112.0	101.9	87.5

3.3.3 Effect of Volumetric Flow Rate on the morphology and electrochemical performance of $FePO_4$ and $LiFePO_4$/C

To investigate the effect of volumetric feeding rate, $FePO_4 \cdot 2H_2O$ precursors were prepared at different volumetric feeding rates ranging from 17.15 to 257.22 mL min^{-1}. As the internal volume of fluid interconnectors in T-mixer is about 178 μL, the mean residence time is between 5.19 ms and 0.35 ms. Table 3-7 and Figure 3-9 show the BET analysis results of the $FePO_4$ precursor samples prepared with 9 different volumetric feeding rates. It can be seen from the figure that when the volumetric feeding rate is relatively small (Q < 85.74 ml min^{-1}), the average primary grain size of $FePO_4 \cdot 2H_2O$ samples decreases remarkably with the increase in the volumetric feeding rate. In contrast to the grain size, the specific surface area increases with the increase in the volumetric feeding rate. It is noted that the minimum average primary grain size (71.27 nm), maximum specific surface area (84.19 m^2 g^{-1}) and total

adsorption volume (0.463 cm^3 g^{-1}) were obtained when the volumetric feeding rate of 85.74 ml min^{-1} was used. Also, the sample S3-FP precursor has presented a mesoporosity dominatant structure. This is likely attributed to the reduced micromixing time and increased mass transfer rate due to the enhanced collision rate among the turbulent eddies, promoting the nucleation. However, further increasing the volumetric feeding rate (taking Q > 85.74 ml min^{-1}) does not show the noticeable influence on the primary grain size reduction and specific surface area increase.

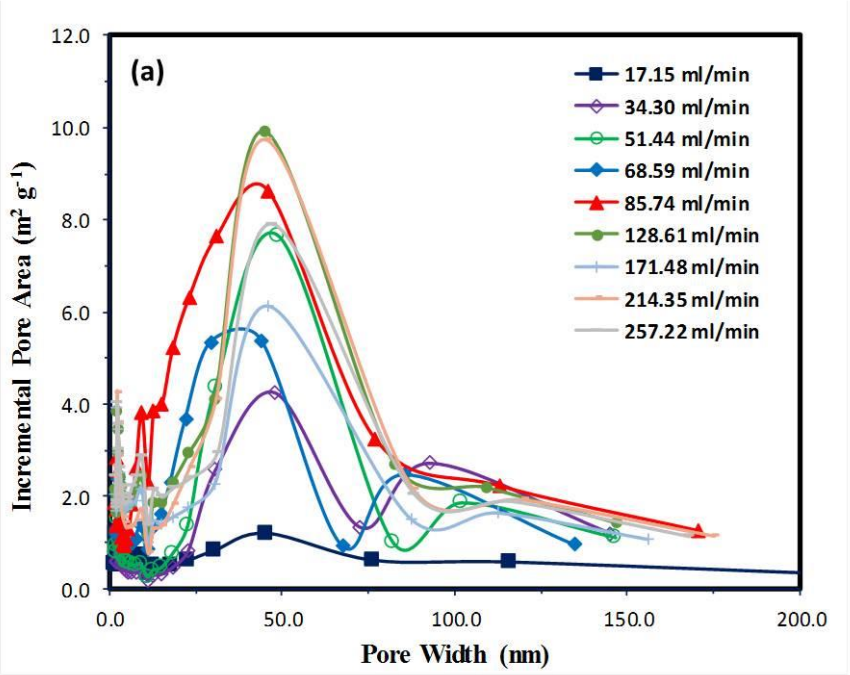
(a)
17.15 ml/min
34.30 ml/min
51.44 ml/min
68.59 ml/min
85.74 ml/min
128.61 ml/min
171.48 ml/min
214.35 ml/min
257.22 ml/min
Incremental Pore Area (m² g⁻¹)
Pore Width (nm)
12.0
10.0
8.0
6.0
4.0
2.0
0.0
0.0
50.0
100.0
150.0
200.0

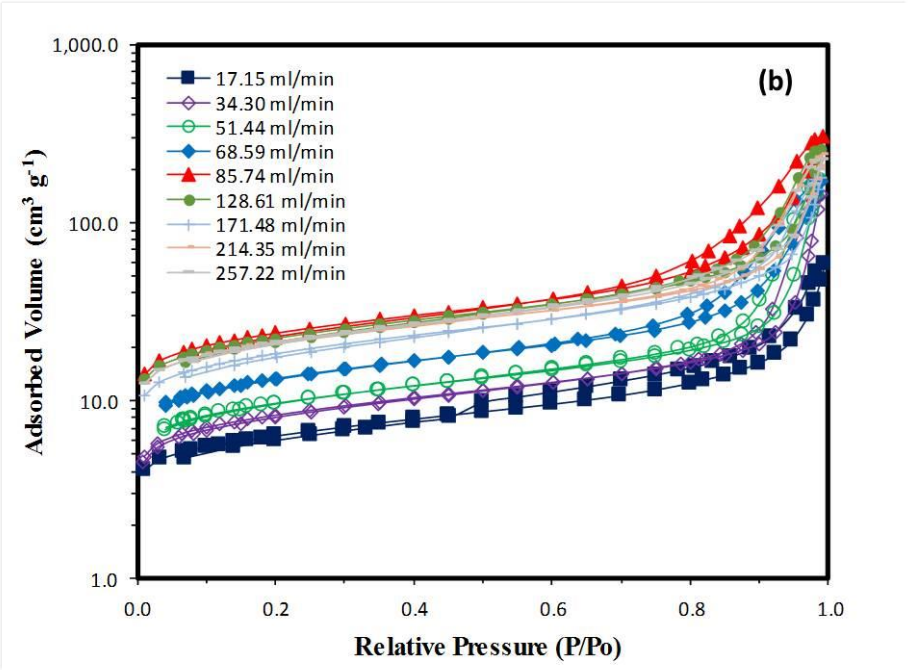
(b)
17.15 ml/min
34.30 ml/min
51.44 ml/min
68.59 ml/min
85.74 ml/min
128.61 ml/min
171.48 ml/min
214.35 ml/min
257.22 ml/min
Adsorbed Volume (cm³ g⁻¹)
Relative Pressure (P/Po)
1,000.0
100.0
10.0
1.0
0.0
0.2
0.4
0.6
0.8
1.0

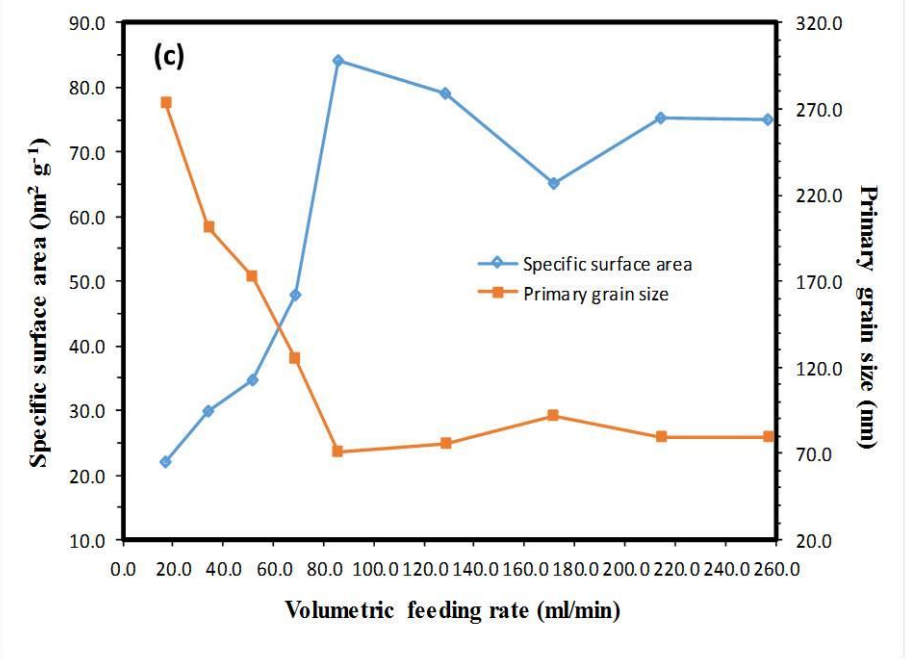

Figure 3-9 (a) N_2 adsorption-desorption isotherms of $FePO_4 \cdot 2H_2O$ composites prepared by T-mixer with different feeding rate; (b) the corresponding pore-size distribution obtained from the adsorption branch using the BJH method of $FePO_4 \cdot 2H_2O$ composites; (c) the relationships among volumetric feeding rate, average primary grain size and specific surface area.

To explain this observed phenomenon, a scaling model is used to estimate the characteristic time t_M for micromixing, which can be interpreted as the time for the diffusion to take place across a turbulence eddy slab with the thickness equal to the Kolmogorov length λ (Mahajan and Donald, 1996; Johnson and Prud'homme, 2003).

$$t_M = \frac{(0.5\lambda)^2}{D_{eddy}} \tag{3-2}$$

where D_{eddy} is the eddy diffusivity of the reactant solutions. The Kolmogorov length λ can be estimated based on the micromixing turbulent energy dissipation rate ε [J/s·kg] and the kinematic viscosity of the mixed solution, ν_{ms}, at the point of mixing, given by

$$\lambda = \left(\frac{\nu_{ms}^3}{\varepsilon} \right)^{1/4} \tag{3-3}$$

where ν_{ms} is assumed to be calculated using the following expression:

$$\nu_{ms} = \alpha \nu_1 + (1-\alpha)\nu_2 = \frac{Q_1 \nu_1 + Q_2 \nu_2}{Q_1 + Q_2} \tag{3-4}$$

where $\alpha = Q_1/(Q_1+Q_2)$ is defined as the ratio of the volumetric flow rate at inlet 1 to the total volumetric flow rates. The turbulent energy dissipation rate should be equal to the energy change associated with the pressure drop in the T-mixer reactor, i.e. the input power P divided by the mixed solution mass in the reactor. For the configuration of the T-type micromixer used in this work, one has

$$\varepsilon = \frac{P}{\rho_{ms} V_T} \tag{3-5}$$

$$\rho_{ms} = \alpha \rho_1 + (1-\alpha)\rho_2 = \frac{Q_1 \rho_1 + Q_2 \rho_2}{Q_1 + Q_2} \tag{3-6}$$

where V_T is the mixing volume of the T-type micromixer. The impinging streams have been assumed to be incompressible and the flow rate at the outlet is equal to the sum of the flow rates of two inlets. ρ_1 and ρ_2 are the densities of the impinging stream solutions. The energy input to the system is contributed from each stream with velocities, u_1 and u_2. Since the impinging streams have a small diameter and the

velocity distribution across the cross-sections of the inlets of the T-type micromixer can be assumed to be uniform, the net rate of kinetic energy input into the system can be considered as the pressure drop taking place in the T-type micromixer. Because both the two inlets and outlet have the same cross-sectional area, the impinging streams can be treated as the combining flow in a T-junction and the results of Idel'cik (1979) can be used. Thus, the pressure drop across the reactor can be estimated by

$$\Delta p = \xi_T \frac{U_3^2}{2} = \xi_T \frac{8Q_3^2}{\pi^2 d^2} = \xi_T \frac{8(Q_1 + Q_2)^2}{\pi^2 d^2} \tag{3-7}$$

where ξ_T is the local loss coefficient which can be estimated using the following empirical relation

$$\xi_T = 1 + \varphi^2 + 3\varphi^2 \left(q_T^2 - q_T \right) \tag{3-8}$$

where $q_T = Q_1/(Q_1+Q_2)$ is the discharge ratio and $\varphi = A_1/A_3$ the ratio of the cross-sectional areas of the inlet 1 to outlet. For the experimental condition used in the current study, $q_T = 0.5$ and $\varphi = 1$, $\xi_T = 1.25$. The energy change associated with the pressure drop in the impinging stream reactor P is calcualetd with $Q_1=Q_2=Q$ and $A_1=A_2=\pi/4d^2$, which yields

$$P = \Delta p Q_3 = \xi_T \frac{8(Q_1 + Q_2)^3}{\pi^2 d^2} = 1.25 \frac{64 Q^3}{\pi^2 d^2} \tag{3-9}$$

The turbulent energy dissipation rate in the T-type micromixer and the Kolmogorov length λ, when substituting equation (9) into (5), are thus estimated, respectively, by

$$\varepsilon = \frac{1.25}{\rho_{ms} V_T} \frac{64 Q^3}{\pi^2 d^2} \tag{3-10}$$

$$\lambda = \left(\frac{\nu_{ms}^3 \rho_{ms} V_T \pi^2 d^2}{80 Q^3} \right)^{1/4} \tag{3-11}$$

and the micromixing time can be estimated by

$$t_M = \frac{(0.5\lambda)^2}{D_{eddy}} = \frac{0.25}{D_{eddy}} \left(\frac{\nu_{ms}^3 \rho_{ms} V_T \pi^2 d^2}{80 Q^3} \right)^{1/2} \tag{3-12}$$

The Reynolds numbers based on the two inlet diameters are calculated according to

$$\mathrm{Re}_i = \frac{4 \rho_i Q_i}{\mu_i \pi d_i} \tag{3-13}$$

As the density and viscosity of $Fe(NO_3)_3$ and $(NH_4)_2HPO_4$ solutions are different, the Reynolds number used to characterise the mixing in the T-type micromixer can be defined by

$$\mathrm{Re}_T = \frac{4 \rho_{ms} \sum_{i=1}^{2} Q_i}{\mu_{ms} \pi d} \tag{3-14}$$

The values of these parameters are listed Table 3-8. The increase in the volumetric feeding rate leads to the enhancement of the mass transfer due to intensified diffusion through the engulfment of two solutions among the Kolmogorov length scale eddies

and improved collision rate. In addition, the turbulent energy dissipation rate ε will increase as the result of increasing volumetric flow rates. It should be pointed out here that the Kolmogorov length λ would decrease with increasing Reynolds number so that the micromixing time t_M is decreased. In addition, mean residence time (t_R) is also decreased with the increasing of volumetric feeding rate. These can be seen from Table 3-9, while the relationship among volumetric feeding rate, Reynolds number and mean residence time is shown in Figure 3-10. The mean residence time decreases dramatically when the volumetric feeding rate range from 17.14 ml min^{-1} to 85.74 ml min^{-1}. As high level of supersaturation can be achieved in T-type micromixer, homogeneous nucleation will occur and large amount of $FePO_4$ nuclei are generated. The heterogeneous nucleation will then start due to the presence of $FePO_4$ nucleus and reduced supersaturation level of solution. When these $FePO_4$ nuclei are transported by the jet stream to enter the self-sustained chaotic eddies, particles start to grow in size. As the volumetric feeding rate is lower than 85.74 ml min^{-1} ($Re_s \leq$ 572), an increase in the feeding velocity may give rise to an increased mass transfer rate and nucleation rate, a shortened mean residence time and micromixing time. This is helpful to achieve smaller primary grain size, and larger specific surface area and total adsorption pore volume. When further increasing the volumetric flow rate to exceed 85.74 ml min^{-1}, the average primary grain size and specific surface area are less to response to the volumetric feeding rate. This may be attributed to equilibrium between the mass transfer and chemical reaction, or the rough equivalence between micromixing homogenization time (t_M) and nucleation time (t_N). Due to the same initial reagent concentration and temperature, the chemical reaction rate and nucleation time (t_N) were maintained at the same level. Further increase in the

volumetric feeding velocity can enhance mass transfer while reduce the micromixing homogenization time t_M and mean residence time within T-type micromixer (t_R). Thus, the desirable mixing of reactant can be achieved through shortening the micromixing homogenization time t_N. However, when t_M and t_R are much less than t_N nucleation of $FePO_4$ nuclei will be mainly confined in the beaker but not T-type micromixer. Due to the same experimental condition being applied in the beaker, the $FePO_4$ precursor grains tend to grow in a very similar way. Furthermore, Seck Hoe Wong *et al* (2004) reported that liquid streams can break up into striations and then these striations disappeared into uniform concentration across the mixing chann bel when Reynolds number was between 400 and 500, so that rapid mixing can be achieved in T-mixer (Wong et al., 2004) . The optimum Reynolds number is similar with the result in this study (Re = 572), which might indicates that a flow regime transition occurs when Re number is 572.

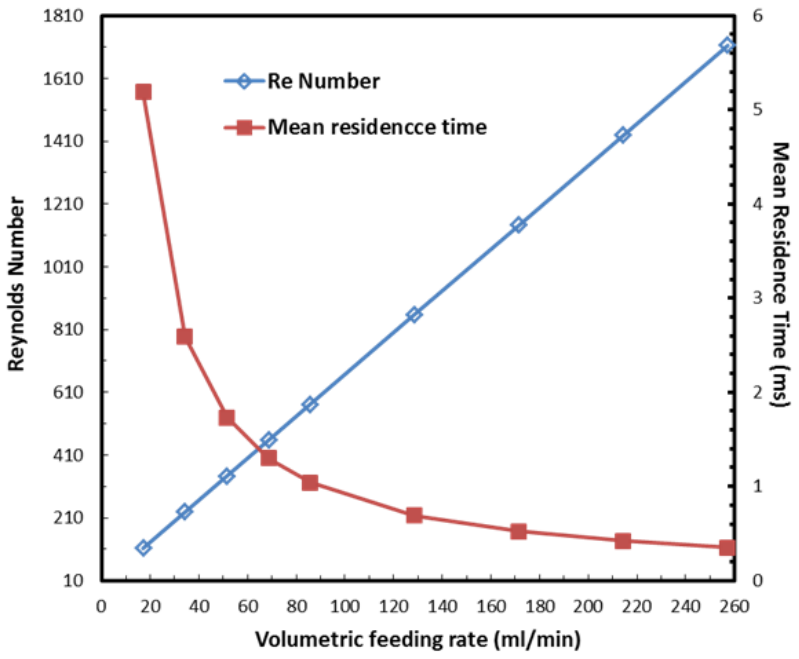

Figure 3-10 The relationships among volumetric feeding rate, Reynolds number and mean residence time.

Figure 3-11 shows significant changes in the XRD results when the $FePO_4$ and $LiFePO_4$/C composites were prepared with increasing volumetric flow rate (*Q*) from 17.15 to 85.74 mL min^{-1} (feeding velocity range from 0.040 – 0.202 m s^{-1}). All the XRD patterns of $FePO_4$ composites fit the ideally crystallized hexagonal structure $FePO_4$ (JCPDS card no. 29-0715, a = 5.035 Å, b = 5.035 Å, c = 11.245 Å). It can be seen clearly from the figure that the diffraction peak at $2\Theta = 20.3^0$ and 25.8^0 becomes higher and sharper as the volumetric flow rate is increased, indicating that the use of higher volumetric flow rate is able to produce higher crystallized $FePO_4$ composites. The XRD patterns of the as-prepared $LiFePO_4$/C samples are presented in Figure 3-11b. The presented XRD patterns have demonstrated that though the $LiFePO_4$/C products do show a similar trend to those with $FePO_4$ precursors, while the diffraction peak at $2\Theta = 22^0$, 26^0, 29^0 and 36^0 become weaker with increasing the volumetric flow rate.

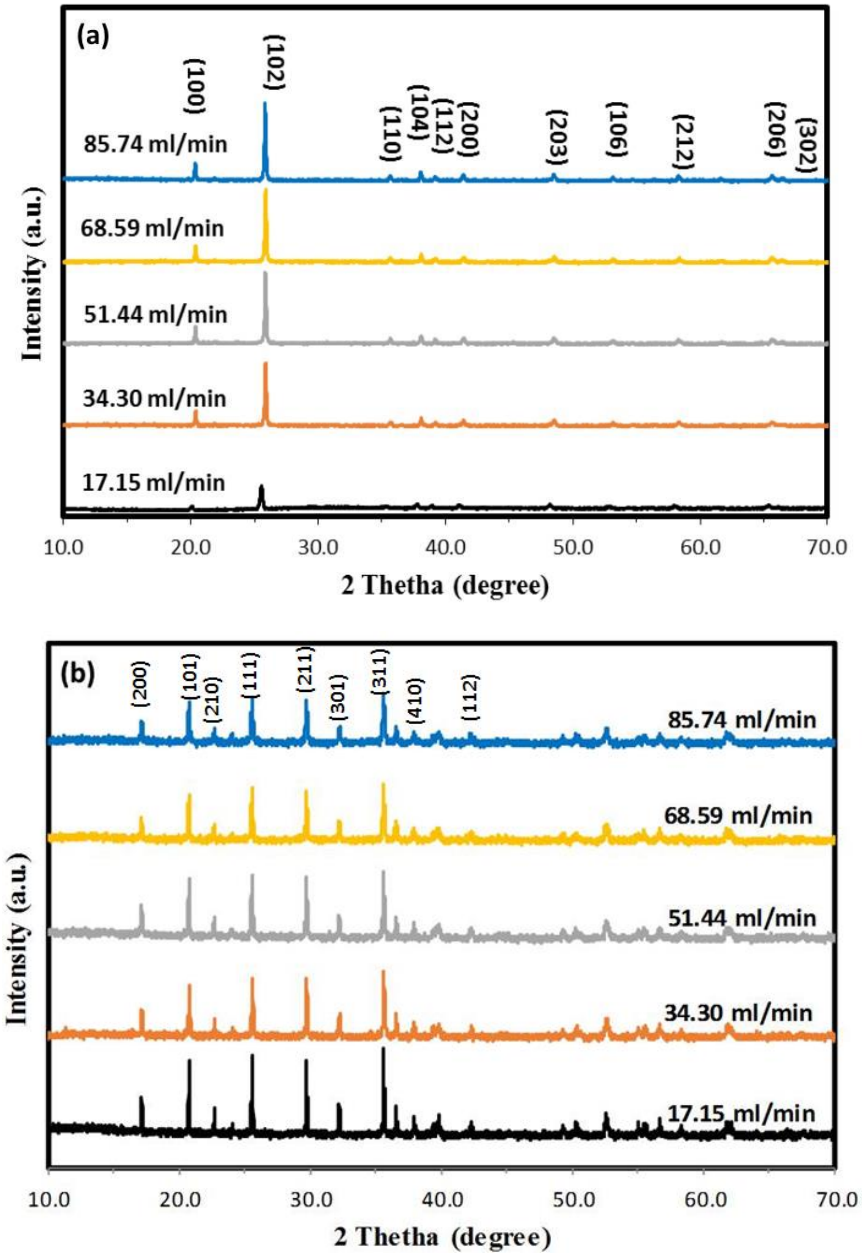

Figure 3-11 X-ray diffraction patterns of (a) $FePO_4$ composites and (b) $LiFePO_4$/C composites synthesized at different volumetric feeding rates.

Table 3-7 N_2 adsorption-desorption analysis results of $FePO_4 \cdot 2H_2O$ precursors prepared by impinging jet reaction with different feeding rates.

Samples	Feeding rate (ml min^{-1})	Feeding velocity (u, m s^{-1})	Surface area (m^2 g^{-1})	Total pore adsorption volume (cm^3 g^{-1})	Primary grain size (nm)
S8-FP	17.15	0.03	21.94	0.087	273.48
S9-FP	34.30	0.06	29.82	0.219	201.24
S10-FP	51.44	0.09	34.75	0.263	172.69
S11-FP	68.59	0.12	47.96	0.263	125.11
S3-FP	85.74	0.15	84.19	0.463	71.27
S12-FP	128.61	0.22	78.94	0.398	76.01
S13-FP	171.48	0.30	65.06	0.278	92.22
S14-FP	214.35	0.37	75.14	0.371	79.86
S15-FP	257.22	0.45	75.11	0.352	79.88

Table 3-8 Experimental parameters for calculation of the Reynolds numbers

Solutions	Density (ρ, kg m^3)	Viscosity (μ, Pa·s)	Tube diameter (d, m)
$Fe(NO_3)_3$	1177	0.001008	0.0035
$(NH_4)_2HPO_4$	1075	0.001003	0.0035
$FePO_4$ precursor solution	1144.4	0.001005	0.0035

Figure 3-12 shows the SEM images of $LiFePO_4$/C samples prepared at the volumetric flow rates ranging from 17.15 to 85.74 ml min^{-1}. As expected, the SEM analysis indicates that an increase in the volumetric flow rate can result in an increase of porosity and a reduction of particle size of as-prepared $LiFePO_4$/C samples. At low volumetric flow rate (Q = 17.15 ml min^{-1}), the as-prepared $LiFePO_4$/C samples shows irregular particle shape with typical diameter of more than 400 nm. As the volumetric flow rate is increased to 85.74 mL min^{-1}, the particle size of $LiFePO_4$/C decreases to 50-200 nm, showing a similar trend to $FePO_4 \cdot 2H_2O$ composites.

Table 3-9 Calculated Reynolds numbers for different experimental conditions

Samples	Feeding rate (ml min^{-1})	Mean residence time (t_R, ms)	$Fe(NO_3)_3$ solution Re (Re_{Fe})	$(NH_4)_2HPO_4$ solution Re (Re_{PO4})	Overall Re number (Re_s)
S8-FP	17.15	5.19	117	112	114
S9-FP	34.3	2.59	234	223	229
S10-FP	51.44	1.73	350	335	343
S11-FP	68.59	1.30	467	447	457
S3-FP	85.74	1.04	584	558	572
S12-FP	128.61	0.69	876	838	858
S13-FP	171.48	0.52	1168	1117	1143
S14-FP	214.35	0.42	1460	1396	1429
S15-FP	257.22	0.35	1752	1675	1715

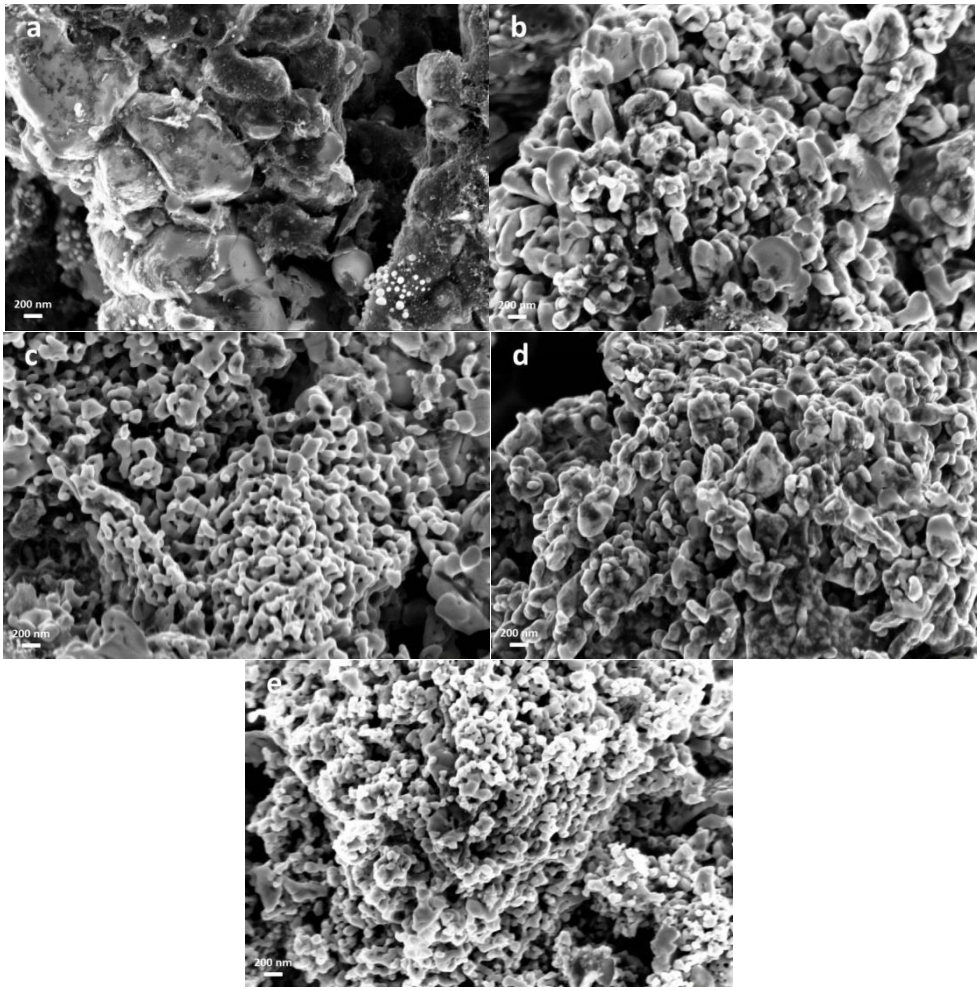

Figure 3-12 SEM images of $LiFePO_4$/C composites synthesized at different volumetric feeding rate: (a) 17.15 ml min^{-1}; (b) 34.30 ml min^{-1}; (c) 51.44 ml min^{-1}; (d) 68.59 ml min^{-1}; (e) 85.74 ml min^{-1}.

Figure 3-13 also the data listed in Table 3-10 show the comparisons of the electrochemical performance for the $LiFePO_4$/C samples prepared with the volumetric flow rates from 17.15 to 85.74 ml min^{-1}. There exists an apparent trend that increasing the volumetric flow rate in the synthesis process has a positive impact on the electrochemical performance of the $LiFePO_4$/C products. As can be seen from Figure 3-13a, the higher the discharge rate, the greater the relative difference in rate capacities among the samples. It is noticed that the $LiFePO_4$/C prepared at Q= 34.30

mL min^{-1} presents higher discharge capacity at a low discharge rate of 0.1 C but the electrochemical performance decays remarkably at high rates from 0.5 to 5 C. This may imply that the transfer of electrons in $LiFePO_4$/C becomes constrained and the $LiFePO_4$/C samples cannot sustain high discharge current because the insertion/extraction process of Li^+ is kinetically limited. As a result, the discharge capacity decreases rapidly. To investigate the cycling stability of the $LiFePO_4$/C prepared at various volumetric flow rates, the coin cell batteries were cycled at 0.5 C for 100 cycles. As shown in Figure 3-13b, the S3-LFP exhibits a high discharge capacity of 136.4 mAh g^{-1}, corresponding to 94.3% of its initial discharge capacity (144.7 mAh g^{-1}).

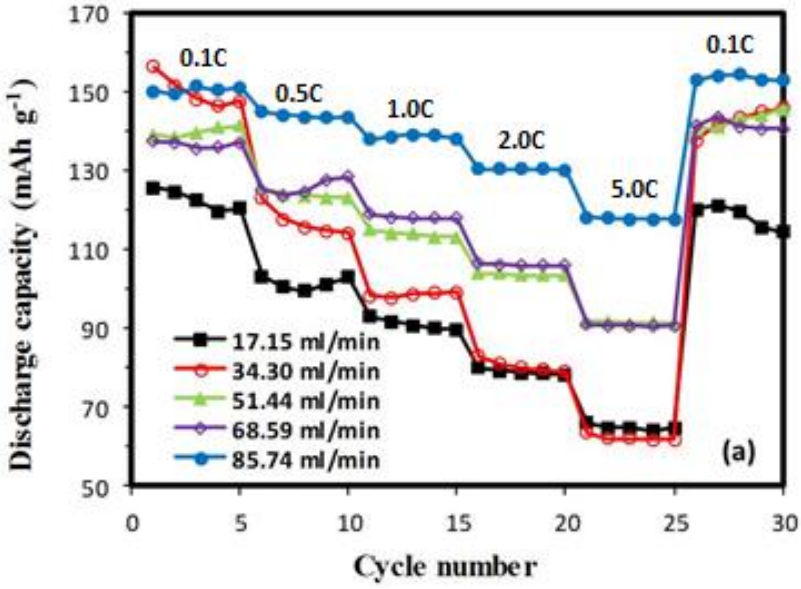

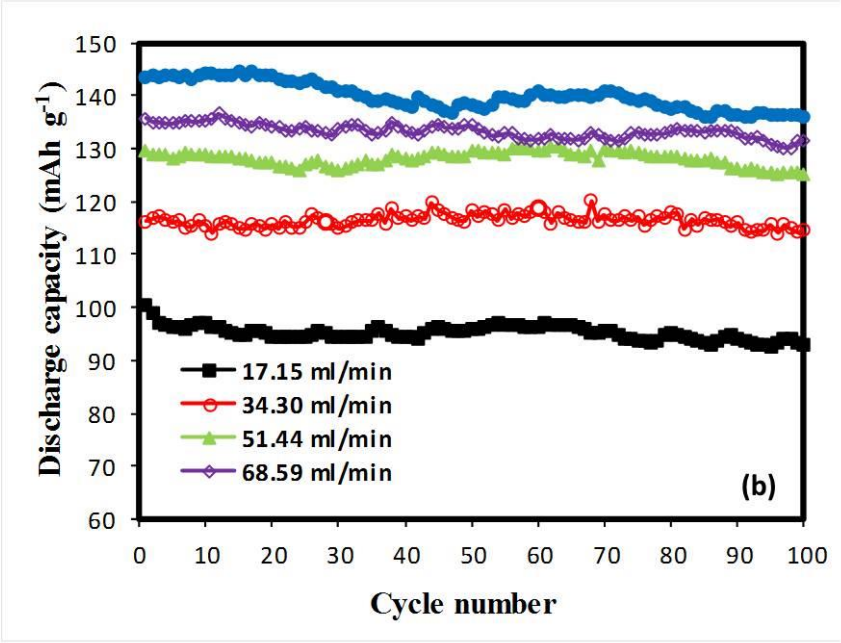

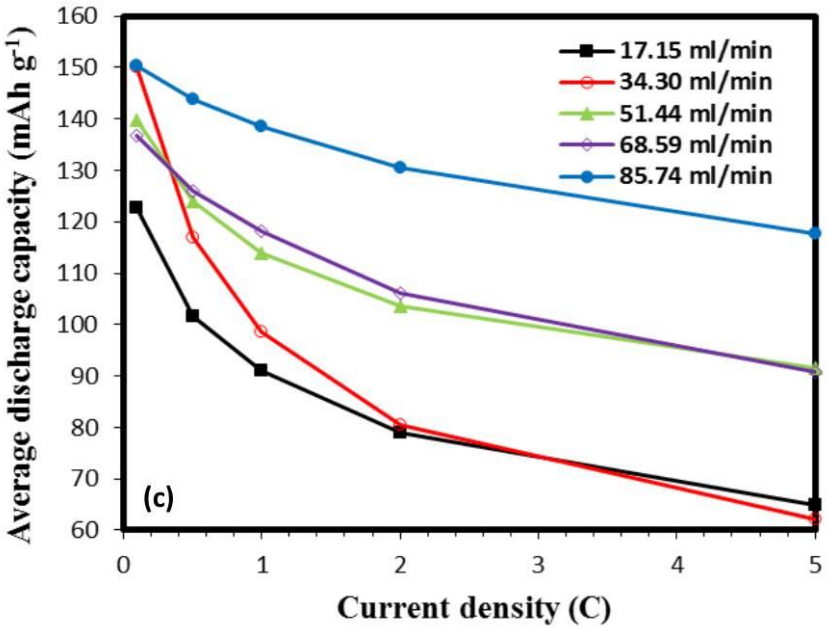

Figure 3-13 Electrochemical performance of $LiFePO_4$/C composites synthesized at different reagent concentrations: (a) Rate performance at various rates, (b) Cycling performance at 0.5 C for 100 cycles, (c) Average rate capability.

Table 3-10 Electrochemical performance of the $LiFePO_4$/C synthesized by impinging stream reaction with different volumetric feeding rates

Feeding rate ($ml\ min^{-1}$)	Cycle performance at 0.5 C ($mAh\ g^{1}$)			Average Rate Performance ($mAh\ g^{-1}$)				
	1^{st} cycle	100^{th} cycle	R_1[a](%)	0.1 C	0.5 C	1 C	2 C	5 C
17.15	100.4	93.1	92.7	122.6	101.5	91.1	78.9	64.9
34.30	116.2	114.7	98.7	150.1	117.0	98.6	80.5	62.2
51.44	129.6	125.2	96.6	139.9	124	113.9	103.7	91.5
68.59	135.7	131.7	97.1	136.7	125.9	118.3	106.1	90.7
85.74	143.4	135.9	94.8	150.5	143.9	138.6	130.4	117.8

3.4 Conclusions

In this work, $LiFePO_4$/C nanocomposites were synthesized by utilising the T-type micromixer under precisely controlled pH value, reactant concentration, and volumetric flow rate. Due to the high micromixing efficiency of impinging stream, it has been demonstrated that the adoption of the T-type micromixer can produce $FePO_4$ with nano-scale particle size with higher specific surface area and pore volume, eventually leading to superior electrochemical performance of $LiFePO_4$/C in the designed charge-discharge tests. When applying the optimized operation conditions (C = 1.0 $molL^{-1}$, pH = 1.6, Q = 85.74 $mlmin^{-1}$), it was revealed that the fabricated $LiFePO_4$/C coin cell sample presents the best rate performance compared with other

$LiFePO_4$/C samples. It is thus concluded that the use of impinging stream reaction technology within T-type micromixer is a very promising synthesis method for the rapid preparation of $FePO_4$ nanocomposites for energy storage. The conclusions reached as the results of the current study are as follows:

(1) The pH value of solution slightly influences the particle size and morphology of $FePO_4$ precursor but significantly affects the electrochemical properties of $LiFePO_4$ nanocomposites.

(2) For a T-type micromixer, increase in the reactant concentration can promote chemical reaction, yielding the reduced average primary grain size, increased specific surface area and total adsorption pore volume so that the electrochemical performance can be improved. However, over-increase in the reactant concentration would have negative impact on these properties of $LiFePO_4$ nanocomposites.

(3) Increased specific surface area and total adsorption pore volume, and reduced average primary grain size can be obtained through increasing the volumetric flow rate of the reactant solutions fed into the T-type micromixer. An increase in the volumetric flow rate will reduce the size of Kolmogorov dissipation eddies (characterised by enhanced Reynolds number based on the diameter of the impinging streams), effectively reducing the micromixing time and promoting the mass transfer between the reactant solutions due to an enhanced collision rate among the turbulent eddies. However, when the volumetric feeding rate is increased to exceed a certain value, it has little impact on the reduction of primary grain size of $LiFePO_4$ nanocomposites.

References

1. Shu H., Wang X., Wen W. , Liang Q. , Yang X., Wei Q., Hu B., Liu L., Xue X., Song Y., Zho M., Bai Y., Jiang L. , Chen M., Yang S., Tan J., Liao Y., and Jiang H., 2013, Effective enhancement of electrochemical properties for $LiFePO_4$/C cathode materials by Na and Ti co-doping, Eletrochimica Acta, 89, 479-487

2. Gibot P., Casas-Cabanas M., Laffont L., Levasseur S., Carlach P., Hamelet S., Tarascon J.M., and Masquelier C., 2008, Room-temperature single-phase Li insertion/extraction in nanoscale $LixFePO_4$, Nature Materials, 7, 741-747

3. Ding Y., Jiang Y., Xu F., Yin J., Ren H., Zhuo Q., Long Z., and Zhang P., 2010, Preparation of nano-structured $LiFePO_4$/graphene composites by co-precipitation method, Eletrochemistry Communication, 12, 10-13

4. Park K.S., Son J.T., Chung H.T., Kim S.J., Lee C.H., and Kim H.G., 2003, Synthesis of $LiFePO_4$ by co-precipitation and microwave heating, Eletrochemistry Communication, 5, 839-842

5. Padhi K., Nanjundaswamy K. S., Masquelier C., Okada S., and Goodenough J. B., 1997, Effect of structure on the Fe^{3+} /Fe^{2+} redox couple in iron phosphates., Journal of the Electrochemistry Society, 144, 1609-1613

6. Shin H.C., Park S.B., Jang H., Chung K.Y., Cho W., Kim C.S., and Cho B.W., 2008, Rate performance and structural change of Cr-doped $LiFePO_4$/C during cycling, Eletrochimica Acta, 53, 7946-7951

7. Chung S.Y., Bloking J.T., and Chiang Y.M., 2002, Electronically conductive phospho-olivines as lithium storage electrodes, Nature Material, 1, 123-128

8. Guo L., Zhang Y., Ma L., Zhang Y., Wang E., Bi Y., Wang D., McKee W.C., Xu Y., Chen J., Zhang Q., Nan C., Gu L., Bruce P.G., and Peng Z.G., 2015, Unlocking the energy capabilities of micron-sized $LiFePO_4$, Nature Communication, 6, 7898-7905

9. Vu A., Qian Y., and Stein A., 2012, Porous electrode materials for lithium-ion batteries - how to prepare them and what makes them special, Advanced Energy Materials, 2, 1056-1085.

10. Wang K.X., Li X.H., and Chen J.S., 2015, Surface and interface engineering of electrode materials for lithium-ion batteries, Advanced Materials. 27, 527-545.

11. Baldyga J., Bourne J.R., and Hearn S.J., 1997, Interaction between chemical reactions and mixing on various scales. Chemical Engineering Science, 52, 457-466.

12. Bhattacharya S. and Kresta S.M., 2004, Surface Feed with Minimum by-Product Formation for Competitive Reactions. Chemical Engineering Research & Design. 82, 1153-1160.

13. Zhang Q.C., Liu Z.W., Zhu X.H., Wen L.X., Zhu Q.f., Guo K., and Chen J.F., 2015, Application of Microimpinging Stream Reactors in the Preparation of $CuO/ZnO/Al_2O_3$ Catalysts for Methanol Synthesis. Industrial Engineering Chemistry Research, 54, 8874-8882.

14. Zhang Q.C., Cheng K.P., Wen L.X., Guo K., and Chen J.F., 2016, A study on the precipitating and aging processes of $CuO/ZnO/Al_2O_3$ catalysts synthesized in micro-impinging stream reactors. RSC Advances. 6, 33611-33621.
15. Huang Y., Wang P., Yuan Y., and Yang F., 2015, Synergistic degradation of chitosan by impinging stream and jet cavitation. Ultrasonics Sonochemistry, 27, 592-601
16. Zhou Z., Liu S., and Liu Y., 2012, Synthesis of Y3Al5O12 : Ce3+phosphors by a modified impinging stream method: a crystal growth and luminescent properties study. Journal Of Physics D-Applied Physics. 45, 195105-195112.
17. Valente I., Celasco E., Marchisio D.L., and Barresi A.A., 2012, Nanoprecipitation in confined impinging jets mixers: Production, characterization and scale-up of pegylated nanospheres and nanocapsules for pharmaceutical use. Chemical Engineering Science. 77, 217-227.
18. Xiao Y., Pu W., Wan W., and Cui Y., 2013, Preparation and Performance of the Cathode Precursor Ferric Phosphate for Li-ion Battery Facilitated by Impinging Stream. International Journal of Electrochemical Science. 8, 938-948.
19. Yan P., Lu L., Liu X. M., Cao Y., Zhang Z. P., Yang H., and Shen X.D., 2013, An economic and scalable approach to synthesize high power $LiFePO_4/C$ nanocomposites from nano-$FePO_4$ precipitated from an impinging jet reactor, Journal of Materials Chemistry *A, 35, 10429-10435*
20. Siddiqui S.W., Unwin P.J., Xu Z., and Kresta S.M., 2009, The effect of stabilizer addition and sonication on nanoparticle agglomeration in a confined

impinging jet reactor, Colloids and Surfaces A: Physicochemical and Engineering Aspects, 350, 38-50

21. Kaluza S., Behrens M., Schiefenhovel N., Kniep B., Fischer R., Schlogl R., and Muhler M., 2011, A Novel Synthesis Route for $Cu/ZnO/Al_2O_3$ Catalysts used in Methanol Synthesis: Combining Continuous Consecutive Precipitation with Continuous Aging of the Precipitate. ChemCatChem, 3, 189-199.
22. Simson G., Prasetyo E., Reiner S., and Hinrichsen O., 2013, Continuous precipitation of $Cu/ZnO/Al_2O_3$ catalysts for methanol synthesis in microstructured reactors with alternative precipitating agents. Applied Catalysis A: General. 450, 1-12.
23. Jiang M., Li Y.D., Tung H.H., and Braatz R. D., 2015, Effect of jet velocity on crystal size distribution from antisolvent and cooling crystallizations in a dual impinging jet mixer. Chemical Engineering and Processing: Process Intensification. 97, 242-247.
24. Vatta L.L., Sanderson R.D., and Koch K.R., 2007, An investigation into the potential large-scale continuous magnetite nanoparticle synthesis by high-pressure impinging stream reactors. Journal of Magnetism and Magnetic Materials. 311, 114-119.
25. Casanova H. and Higuita L.P., 2011, Synthesis of calcium carbonate nanoparticles by reactive precipitation using a high pressure jet homogenizer. Chemical Engineering Journal. 175, 569-578.
26. Tari T., Fekete Z., Revesz P. S., Aigner Z., 2015, Reduction of glycine particle size by impinging jet crystallization. International Journal of Pharmaceutics. 478, 96-102.

27. Wu G., Zhou H., and Zhu S., 2007, Precipitation of barium sulfate nanoparticles via impinging streams. Materials Letter. 61, 168-170.
28. Li Z., Zhang F., Meng A., Xie C., and Xing J., 2015, ZnO/Ag micro/nanospheres with enhanced photocatalytic and antibacterial properties synthesized by a novel continuous synthesis method. RSC Advances. 5, 612-620.
29. Kumar D. V. R., Prasad B.L.V., and Kulkarni A.A., 2013, Impinging Jet Micromixer for Flow Synthesis of Nanocrystalline MgO: Role of Mixing/Impingement Zone. Industrial Engineering Chemistry & Reserach. 52, 17376-17382.
30. Liu Z., Guo L., Huang T., Wen L., and Chen J., 2014, Experimental and CFD studies on the intensified micromixing performance of micro-impinging stream reactors built from commercial T-junctions. Chemical Engineering Science. 119, 124-133.
31. Siddiqui S.W., Zhao Y., Kukukova A., and Kresta S.M., 2009, Characteristics of a Confined Impinging Jet Reactor Energy Dissipation Homogeneous and Heterogeneous Reaction Products and Effect of Unequal Flow. Industrial Engineering Chemistry & Reserach. 48, 7945-7958.
32. Liu Y. and Fox R.O., 2006, CFD predictions for chemical processing in a confined impinging-jets reactor. AIChE Journal, 52, 731-744
33. Fonte C.P., Sultan M.A., Santos R.J., Dias M.M., and Lopes J.C.B., 2015, Flow imbalance and Reynolds number impact on mixing in Confined Impinging Jet. Chemical Engineering Journal. 260, 316-330.
34. Shi Z.H., Li W.F., Du K.J., Liu H.F., and Wang F.C., 2015, Experimental study of mixing enhancement of viscous liquids in confined impinging jets

reactor at low jet Reynolds numbers. Chemical Engineering Science, 138, 216-226.

35. Schwarzer H.C. and Peukert W., 2004, Combined experimental/numerical study on the precipitation of nanoparticles. AIChE Journal, 50, 3234-3247.
36. Mahajan A.J. and Donald J.K., 1996, Micromixing effects in a two impinging jets precipitator. AIChE Journal, 42, 1801-1814.
37. Johnson B.K. and Prud'homme R. K., 2003, Chemical Processing and Micromixing in Confined Impinging Jets. AIChE Journal. 49, 2264-2282
38. Andreussi T., Galletti C., Mauri R., Camarri S., and Salvetti M. V., 2015, Flow regimes in T-shaped micro-mixers. Computers & Chemical Engineering, 76, 150-159.
39. Krupa K., Nunes M.I., Santos R.J., and Bourne J.R., 2014, Characterization of micromixing in T-jet mixers. Chemical Engineering Science, 111, 48-55.
40. Borukhova, S., Noel T., and Hessel V., 2016, *Continuous-Flow Multistep Synthesis of Cinnarizine, Cyclizine, and a Buclizine Derivative from Bulk Alcohols.* ChemSusChem. 9, 67-74
41. Polyzoidis A., Altenburg T., Schwarzer M., Loebbecke S., and Kaskel S., 2016, *Continuous microreactor synthesis of ZIF-8 with high space–time-yield and tunable particle size.* Chemical Engineering Journal, 283, 971-977.
42. Kolmykov O., Commenge J.M., Alem H., Girot E., Mozet K., Medjahdi G., and Schneider R., 2017, *Microfluidic reactors for the size-controlled synthesis of ZIF-8 crystals in aqueous phase.* Materials & Design. 122, 31-41.
43. Wong S., Ward M., and Wharton C., 2004, *Micro T-mixer as a rapid mixing micromixer.* Sensors and Actuators B: Chemical. 2004, 100, 359-379.

44. Soleymani A., Kolehmainen E., and Turunen I., 2008, *Numerical and experimental investigations of liquid mixing in T-type micromixers.* Chemical Engineering Journal, 2008, 135, S219-S228.
45. Gobby D., Angeli P., and Gavriilidis A., 2001, *Mixing characteristics of T-type microfluidic mixers.* Journal of Micromechanics and Microengineering, 2001, 126-132.
46. Gradl J., Schwarzer H.C., Schwertfirm F., Manhart M., Peukert *W., 2006, Precipitation of nanoparticles in a T-mixer: Coupling the particle population dynamics with hydrodynamics through direct numerical simulation.* Chemical Engineering and Processing: Process Intensification, 2006, 45, 908-916.
47. Islam M. S., Driscoll D. J., Fisher C.A.J., and Slater P.R., 2005, *Atomic Scale Investigation of Defects, Dopants, and Lithium Transport in the $LiFePO_4$ Olivine Type Battery Material.* Chemistry of Materials, 17, 5085-5092.
48. Alothman Z.A., 2012, *A Review: Fundamental Aspects of Silicate Mesoporous Materials.* Materials. 5, 2874-2902.

CHAPTER 4: Synthesis of FexMn1-xPO4 (x = 1.00, 0.96, 0.93, and 0.90) nanocomposites by Ultrasound-intensified Impinging Stream Microreactor

SUMMARY

In Chapter 3, ISR method has been systematically investigated. This chapter will discuss the effects of ultrasound intensity, pulse, and volumetric feeding rate on the particle size and porosity of $FePO_4$. In addition, the impact of Mn doping on electrochemical performance of $LiFe_xMn_{1-x}PO_4/C$ (x=1.00, 0.96, 0.93 and 0.90) is also discussed in this chapter. $Fe_xMn_{1-x}PO_4$ (x = 1, 0.96, 0.93, and 0.90) precursor particles which amalgamated by nanoscale primary crystals were prepared rapidly using a combination of ultrasound and impinging stream microreactor (UISR). This joint chemical reactor system can provide the feature of fast micro-mixing, leading to an improvement of mass transfer rate and chemical reaction rate. As one of the important precursors for the fabrication of lithium ion battery positive electrode, the properties of $Fe_xMn_{1-x}PO_4$ nanocomposites significantly affect the electrochemical performance of the active positive electrode material in lithium ion battery. Thus, the effects of combination of impinging stream and ultrasonic irradiation on the formation of mesoporous structure of $Fe_xMn_{1-x}PO_4$ nano precursor particles and the electrochemical properties of amalgamated $LiFe_xMn_{1-x}PO_4/C$ have been investigated. In this work, firstly, the $FePO_4$ precursor nanoparticles were synthesized under precisely controlled operation parameters, such as ultrasound intensity (0-900 W), ultrasound pulse (continuous, 1/2 s, and 1/5 s), and volumetric flow rate (Q = 17.15,

34.30, 51.44, 68.59, and 85.74 mL min^{-1}), to investigate how these operation factors influence synthesis process when the UISR operates in nonsubmerged mode. It was affirmed from the experiments that, comparing with the samples synthesized without ultrasound, application of ultrasonic irradiation can lead to the reduction of nuclei size and improvement of specific surface area on $FePO_4$ precursor nanoparticles. When the optimum condition was determined, $Fe_xMn_{1-x}PO_4$ and $LiFe_xMn_{1-x}PO_4/C$ composites were prepared with optimum condition. The as-synthesized samples were characterised by XRD, SEM, FTIR and electrochemical charge-discharge tests to investigate the effect of Mn ion on the properties $Fe_xMn_{1-x}PO_4$ and $LiFe_xMn_{1-x}PO_4/C$ which prepared by UISR method.

4.1 Introduction

As a predominant and reliable power sources and energy storage equipment, rechargeable lithium-ion batteries (LIBs) have been widely used in hybrid electric vehicles (HEV), electric vehicles (EV) and other devices that require sustainable energies (Shu *et al*., 2013; Gibot *et al*., 2008). Olivine-structured $LiMPO_4$ (M=Fe, Mn) has been considered as one of the highly promising positive electrode material and extensively studied owing to its significant advantages of nontoxicity, low cost of the raw materials, good structural stability at high temperature, excellent safety performance, and relatively high theoretical specific capacity ($LiFePO_4$: 170 mA h g^{-1}; $LiMnPO_4$: 171 mA h g^{-1}) with flat discharge-charge potential (Ding *et al*., 2010; Park *et al*., 2003). The redox potential of Fe^{2+}/Fe^{3+} and Mn^{2+}/Mn^{3+} are 3.5 V and 4.1 V, respectively (Padhi *et al*., 1997; Yao *et al*., 2006). The increasing of Mn content in $LiFe_xMn_{1-x}PO_4$ results in an apparent plateau with increasing width at 4.1 V. In addition, the oxidation of Mn^{2+} occurs after the oxidation of Fe^{2+} (Padhi *et al*., 1997).

In spite of the numerous merits of the performance of $LiMPO_4$ (M=Fe, Mn), however, the low electronic conductivity ($LiMnPO_4$: less than 10^{-12} S cm^{-1}; $LiFePO_4$: 1.8×10^{-8} S cm^{-1}) and low Li^+ diffusity have confined the electrochemical performance of $LiFePO_4$ and constrained its practical application (Oh *et al*., 2011; Shin *et al*., 2008; Guo *et al*., 2015). Particle morphology optimization, including fabricating positive electrode materials with nanostructure and integrated porosity, can significantly increase electrode/electrolyte interface area and ensure effective electrolyte permeation (Vu *et al*., 2012; Wang *et al*., 2015). Therefore, the electrochemical properties of positive electrode materials can be remarkably enhance due to shortened Li^+ diffusion path and improved kinetics of Li^+ insertion/extraction process.

For industrial precipitation, the properties of final products, such as morphology, particle size distribution (PSD) and purity, can be significantly affected by mixing effects in precipitation (Mahajan and Donald, 1996). Therefore, a reactor which provides extremely rapid micromixing can achieve homogeneous supersaturation level before nucleation process, and leading to the generation of final products with uniform morphology, narrow PSD, and high purity. T-type impinging stream microreactor (ISR) is a simplest component which can provide rapid micromixing. Generally, in ISR, two inlet tubes and one outlet tube join the main channel with T-shaped branches. Two liquid/gas streams with high velocity impinge upon each other in a small mixing chamber. The collision between two high velocity impinging streams can generate intensive micromixing, so that reactants were homogeneously distributed, result in an effectively enhancement of mass transfer rate, energy dissipation rate and chemical reaction rate. Moreover, liquid impinging stream can also induce pressure fluctuation, which can change the energy and distribution of

molecules (Huang *et al*., 2015). However, rapid generation of solid products and/or by-products may result in irreversible clogging of microchannels, which is one of the biggest disadvantages in the using of ISR (Noël *et al*., 2011). Several methods have been applied to prevent the contacting of as-synthesized solid on reactor walls, including the using of segmented liquid flows (Nagasawa and Mae., 2006; Shestopalov *et al*., 2004; and Löb *et al*., 2004). However, the efficiency of chemical reaction may be reduced due to the existence of additional solvent may be incompatible with the reagents and detrimental to the main reactions (Noël *et al*., 2011; Naber and Buchwald, 2010). In addition, although the micromixing can be intensified in ISR, it is still very difficult to obtain turbulent flow in ISR, unless high feeding velocity which leads to an increased samples consumption (Shastry *et al*., 1998).

Ultrasound intensified synthesis methods has been applied in industrial manufacturing process and material synthesis due to its fast, cost-effective and environmentally-friendly. There are several types of ultrasonic-intensified reactors, and they can be divided into probe-horn (including vertical probe horn and longitudinal horn) reactor and cup-horn (ultrasonic bath) reactor (Asgharzadehahmadi *et al*., 2016). Comparing with cup-horn reactor, probe-horn reactor requires less energy cost during synthesis process (Monnier *et al*., 1999). When liquid medium is irradiated by ultrasound, ultrasonic wave can introduce acoustic cavitation and generate large amount of cavitation bubbles. Because the instantaneous collapse of the cavitation bubbles an create extremely high pressures (up to 1000 atm), temperature (up to 5000K), and the heating and cooling rate greater than 10^{10} Ks^{-1} inside the cavitation zone, the chemical and physical changes in solution are enhanced by the imploding of cavitation bubbles

significantly (MnNamara *et al*., 1999; Mason and Cordemans, 1996). In addition, ultrasound can help to prevent the agglomeration among particles and interaction between particles and reactor surface (Rivas and Kuhn, 2016). Therefore, high intensity ultrasonic-irradiation is a promising technology which can enhance micromixing, as well as overcome clogging and slurry transport difficulties problem in ISR (Noël *et al*., 2011; Rivas and Kuhn, 2016; Sedelmeier *et al*., 2010; Horie *et al*., 2010; Zhang *et al*., 2012). However, most of these research only treatment outlet tube (Noël *et al*., 2011; Zhang *et al*., 2012), or use extra gas (Horie *et al*., 2010), which increase the operation cost.

In this study, the aim is to report synthesis of $Fe_xMn_{1-x}PO_4$ (x = 1, 0.96, 0.93, and 0.90) precursor nanocomposites using the UISR technology, which can overcome clogging problem and enhance micromixing together, at various operating parameters. A schematic diagram of UISR technology is shown in Figure 4-1. The effects of ultrasound intensity, pulse, and volumetric feeding rate, and Mn content are systematically investigated in this paper. The paper will be organised in such a way. Section 2 will present the experimental details including materials preparation, characterisation of $FePO_4$ and $LiFePO_4$/C and cell preparation for electrochemistry test. Section 3 focuses on (1) effects of ultrasound intensity, ultrasound impulse, and volumetric flow rates (Q); (2) effect of the operating parameters on the morphology, purity and structure of samples; and (3) the electrochemical properties of the corresponding $LiFe_xMn_{1-x}PO_4$/C samples. While section 4 will present the conclusions derived from the study.

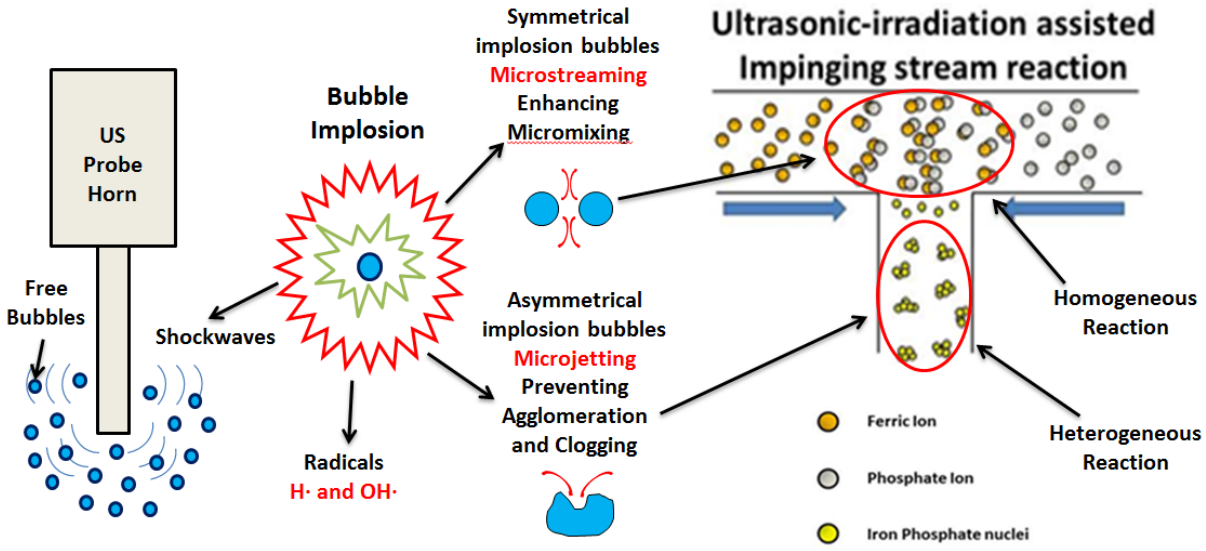

Figure 4- 1 Schematic diagram of ultrasonic-intensified impinging stream reaction (UISR).

4.2 Experimental

4.2.1 Sample synthesis

To investigate the effects of ultrasound intensity, pulse, and volumetric feeding rate, two methods were designed to synthesise $FePO_4$ precursor nanoparticles. The first type of $FePO_4$ precursor nanoparticles were synthesized via an ultrasonic-assisted impinging stream reaction (UISR). Iron nitrate solution and diammonium phosphate solution (reagent concentration = 1.0 mol L^{-1}) were injected continuously into a T-type impinging stream micromixer (T-mixer), which is shown in Figure 4-2, by using two peristaltic pumps (BT100FJ, Baoding Chuangrui, China) to precisely control volumetric feeding rate (Q) ranging from 17.15 to 85.74 ml min^{-1}. Meanwhile, the outlet of T-mixer was connected with a FS-600pv horn type ultrasonic wave piezoelectric vibrator, so that the solution can be irradiated by 20 kHz ultrasound with different intensity (0-900 W) and pulse. During the synthesis process, the pH value of

solution was kept at 1.70 by adding ammonia solution (1.5 mol L^{-1}) carefully through a pH automatic controller. The obtained products were subsequently washed with deionized water for 3 times, filtrated and then dried in air at 100 ℃ for 12 h.

For comparison purpose, the second type of $FePO_4$ precursor nanoparticles were synthesized via only impinging stream reaction (ISR) with precisely control volumetric feeding rate (Q= 17.15, 34.30, 51.44, 68.59, and 85.74 ml min^{-1}) when pH value of the solution was maintained at 1.70.

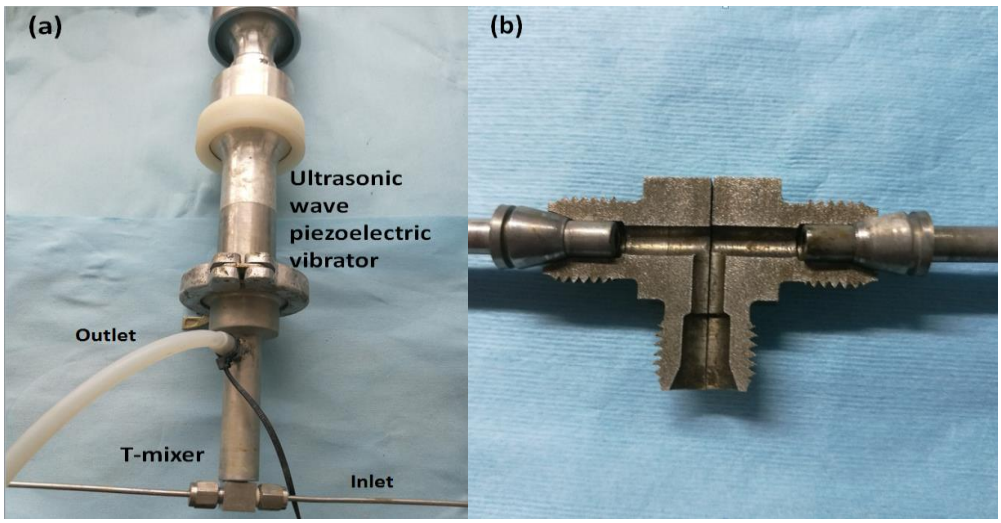

Figure 4-2 (a) Experimental set-up of ultrasonic-intensified T-mixer and (b) internal structure of T-mixer

When the optimum ultrasound intensity, ultrasound pulse and volumetric feeding rate were determined, $Fe_xMn_{1-x}PO_4$ (x = 1, 0.96, 0.93, and 0.90) nanocomposites were prepared by UISR method under optimum condition by UISR method. The $Fe(NO_3)_3{\cdot}9H_2O$ and $Mn(NO_3)_2{\cdot}6H_2O$ were mixed and dissolved in de-ionised water based on the desirable molar ratio. Then the mixture solution and diammonium phosphate solution were injected to UISR reaction system with optimal Q, which is 85.74 ml min^{-1}. The obtained samples were washed, filtrated and then dried in air at

100 ℃ for 12 h. After that, the samples were calcined in air at 600 °C for 10 hours to obtain anhydrous crystalline $Fe_xMn_{1-x}PO_4$ samples. The conditions of different experiments are shown in Table 4-1.

To synthesize $LiFe_xMn_{1-x}PO_4/C$ composites, the nano-sized crystalline $Fe_xMn_{1-x}PO_4$ nanocomposites were mixed with Li_2CO_3 and glucose at a desired molar ratio of 1:1.05:0.1 and ball-milled at 300 rpm for 2 hours by a planetary ball mill to obtain a homogeneous mixture. The mixtures were then dried and calcined at 650 ℃ for 10 h in nitrogen atmosphere to obtain $LiFe_xMn_{1-x}PO_4/C$ samples.

Table 4- 1 Dimensions of experiments for the synthesis of samples

Experiments	Samples	Method	Ultrasound Intensity (W)	Pulse	Volumetric Feeding Rate (ml/min)
S1	FP-U0W	UISR	0	Continuous	85.74
S2	FP-U300W	UISR	300	Continuous	85.74
S3	FP-U600W	UISR	600	Continuous	85.74
S4	FP-U900W	UISR	900	Continuous	85.74
S5	FP-P1/2	UISR	600	1/2	85.74
S6	FP-P1/5	UISR	600	1/5	85.74
S7	FP-U20rpm	UISR	600	Continuous	17.15
S8	FP-U40rpm	UISR	600	Continuous	34.30
S9	FP-U60rpm	UISR	600	Continuous	51.44
S10	FP-U80rpm	UISR	600	Continuous	68.59
S11	FP-20rpm	ISR	/	/	17.15
S12	FP-40rpm	ISR	/	/	34.30
S13	FP-60rpm	ISR	/	/	51.44
S14	FP-80rpm	ISR	/	/	68.59
S15	FP-100rpm	ISR	/	/	85.74

4.2.2 Characterization of FexMn1-xPO4 and LiFexMn1-xPO4 (x = 1.00, 0.96, 0.93, and 0.90)

Specific surface area, average primary grain size and porous distribution were analysed by Brunauer Emmett Teller (BET, Micromeritics ASAP 2020, U.S.A). The crystal structure of samples was analysed by a Bruker D8 series X-ray diffraction using Cu Kα radiation (λ=1.5406Å). The scanning range of diffraction angle (2Θ) was set $10^0 \leq 2\Theta \leq 70^0$. The surface morphology of the obtained particles was observed by scanning electron microscope (Sigma VP, ZEISS, Germany). The infrared spectra was recorded on a Fourier transform infrared spectroscopy (FTIR, Bruker V70, U.S.A) using the KBr disk technique.

4.2.3 Cell Fabrication and Electrochemical Analysis

To test electrochemical performance, as-synthesized $LiFe_xMn_{1-x}PO_4/C$ active material, acetylene black and polytetrafluoroethylene (PTFE) binder were mixed in a weight ratio of 80: 15: 5 and vigorous magnetically stirred in N-methyl-2-pyrrolidene (NMP) solvent to prepare homogeneous slurry. An appropriate amount of slurry was then spread on Al foils and dried at 80 ℃ for 6 h in a vacuum oven. The dried samples were punched to form disc shape with a diameter of 1.3 cm and weighted in a high-precision analytical balance. The obtained Al foils coated with active materials were used as positive electrode. The electrolyte was 1 M $LiPF_6$ which dissolved in ethylene carbonate (EC)/diethyl carbonate (DEC) (50:50 vol%). Celguard 2300 microporous film was applied as separator. The coin cell assembling process was carried out in a dry Ar-filled glove box. The charge-discharge performance of the fabricated coin cells was measured on a battery system (LAND,CT2001A, China) between 2.5 V and 4.2 V versus Li/Li^+ for given cycles.

4.3 Results and discussion

4.3.1 Effect of ultrasonic intensity

To investigate the effect of ultrasonic power, $FePO_4 \cdot 2H_2O$ precursors were prepared at different ultrasound power ranging from 0 W to 900 W. The BET specific surface area, pore size distribution and primary grain size of the as-synthesized precursor particles prepared with 4 different ultrasound power were characterised by applying the nitrogen adsorption-desorption analysis. The N_2 sorption isotherm of all precursor particles (see Figure 4-3a) was Type IV (Alothman, 2012). Their big hysteresis loops have provided the evidence for the presence of mesopores (>2nm and <50nm) and large surface area. The analytical results of pore size distribution based on desorption of the $FePO_4 \cdot 2H_2O$ precursors synthesized at different ultrasound intensity are shown in Figure 4-3b. It becomes clear as can be seen from the figure that all the $FePO_4 \cdot 2H_2O$ precursor samples feature pores in mesoporous (>2nm and <50nm) and small-marcoporous (>50nm and <85nm) range. In addition, the increasing of ultrasound power leads to the changing of surface area, porosity and average nuclei size of $FePO_4$ precursor samples, which is shown in Figure 4-3c and Table 4-2. It can be seen from the figure that a significant decline of average primary grain size (from 71.27 nm to 53.74 nm), and an increasing of specific surface area (from 84.19 m^2g^{-1} to 114.97 m^2g^{-1}**)** and total pore adsorption volume (from 0.463 cm^3g^{-1} to 0.570 cm^3g^{-1}) can be obtained with the increasing of ultrasonic power from 0 W to 600 W. However, the further increasing of ultrasound power from 600 W to 900 W results in an increasing of average primary grain size and reduction of specific surface area, indicates that keep increasing the ultrasound power might not always lead to the reduction of average primary grain size and increase of specific surface area.

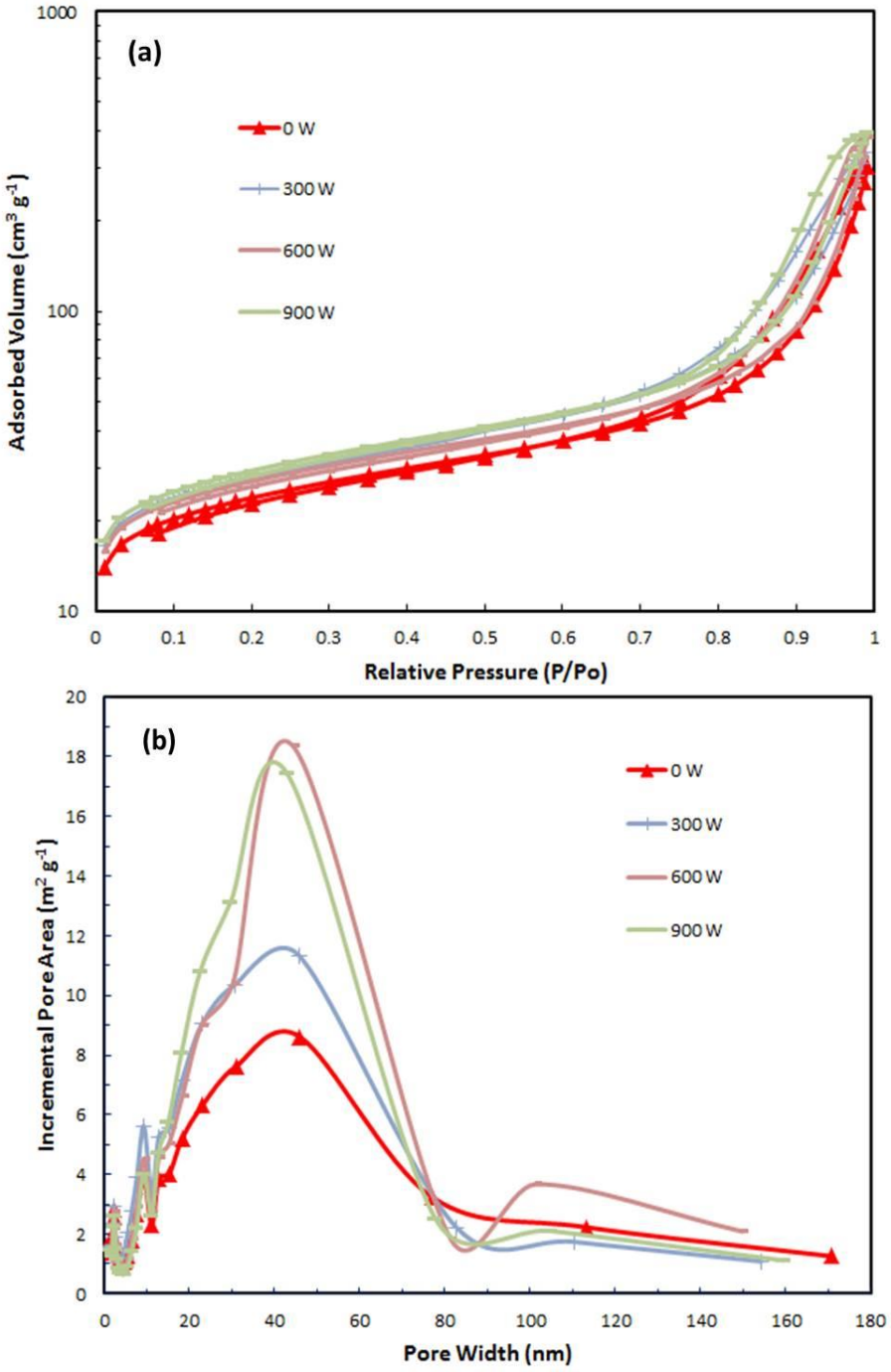
(a)
0 W
300 W
600 W
900 W
Adsorbed Volume (cm3 g-1)
Relative Pressure (P/Po)
(b)
0 W
300 W
600 W
900 W
Incremental Pore Area (m2 g-1)
Pore Width (nm)

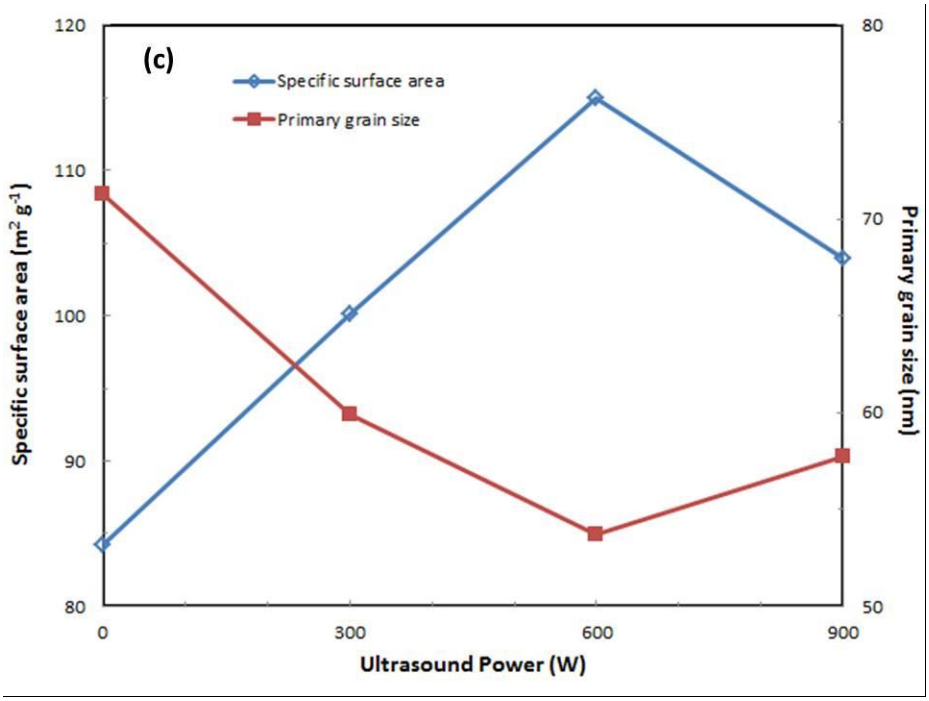

Figure 4-3 The BET analysis results of $FePO_4 \cdot 2H_2O$ samples prepared with different ultrasound power: (a) N_2 adsorption-desorption isotherms; (b) the corresponding pore-size distribution obtained from the adsorption branch using the BJH method; (c) the relationships among ultrasound power, average primary grain size and specific surface.

Table 4-2 N_2 adsorption-desorption analysis results of $FePO_4 \cdot 2H_2O$ precursors prepared with different ultrasound power.

Ultrasound power (W)	Specific surface area ($m^2 g^{-1}$)	Total pore adsorption volume ($cm^3 g^{-1}$)	Average primary grain size (nm)
0	84.19	0.463	71.27
300	100.12	0.524	59.93
600	114.97	0.570	53.74
900	103.89	0.608	57.75

Due to the same UISR chamber volume and volumetric feeding rate, the mean residence time of the samples synthesised with different ultrasound intensity were kept the same. However, the ultrasound intensity affected the micromixing time and chemical reaction rate significantly. Previous study has proposed a scaling model is used to estimate the characteristic time t_M for micromixing, which can be interpreted as the time for the diffusion to take place across a turbulence eddy slab with the thickness equal to the Kolmogorov length λ (Mahajan and Donald, 1996; Johnson and Prud'homme, 2003):

$$t_M = \frac{(0.5\lambda)^2}{D_{eddy}} \tag{4-1}$$

where D_{eddy} is the eddy diffusivity of the reactant solutions. The Kolmogorov length λ can be estimated based on the micromixing turbulent energy dissipation rate ε [J/s·kg] and the kinematic viscosity of the mixed solution, ν_{ms}, at the point of mixing, given by

$$\lambda = \left(\frac{\nu_{ms}^3}{\varepsilon} \right)^{1/4} \tag{4-2}$$

The turbulent energy dissipation rate should be equal to the energy change associated with the pressure drop in ISR, i.e. the input power P divided by the mixed solution mass in the reactor. For the configuration of ISR used in this work, one has

$$\varepsilon = \frac{P}{\rho_{ms} V_T} \tag{4-3}$$

where ρ_{ms} is the density of the fully mixed solution, V_T is the mixing volume of the ISR used in this study. For the present study, the input power P can be approximately assumed to be the superposition contributed from the input power for impinging stream P_{IS} and the ultrasonic irradiation P_{UI}:

$$P = P_{IS} + P_{UI} \tag{4-4}$$

The micromixing time can thus be estimated by:

$$t_M = \frac{\left[0.5 \left(\frac{\rho_{ms} V_T \nu_{ms}^3}{P_{IS} + P_{UI}} \right)^{1/4} \right]^2}{D_{eddy}} \tag{4-5}$$

In addition, Ratoarinoro *et al* (1995) evaluate the overall reaction rate r_o under sonication, which can be written as (Contanmine *et al*., 1995):

$$r_o = k_l C_o \frac{6}{d_{3\,2}} \frac{m_p}{\rho_p V_l} \tag{4-6}$$

Where k_l is mass transfer coefficient, C_o is reagent initial concentration, $d_{3\,2}$ is mean diameter over the surface distribution, also called Sauter mean diameter, V_l is the liquid volume, which assume to be equal to the volume of reactor chamber V_T, m_p and ρ_p are the mass and density of the solid particles respectively.

An empirical power correlation was proposed to evaluate the mass transfer coefficient k_l, which is:

$$k_l = \frac{D}{d_{4\,3}} [2 + 0.4 \left(\frac{\varepsilon d_p^4 \rho_l^3}{\mu_l^3} \right)^{\frac{1}{4}} \left(\frac{\mu_l}{\rho_l D} \right)^{\frac{1}{3}}] F_c \tag{4-7}$$

Therefore, the mass transfer coefficient can thus be estimated by:

$$k_l = \frac{D}{d_{4\,3}} [2 + 0.4 \left(\frac{(P_{IS} + P_{UI}) d_p^4 \rho_l^3}{\rho_s V_T \mu_l^3} \right)^{\frac{1}{4}} \left(\frac{\mu_l}{\rho_l D} \right)^{\frac{1}{3}}] F_c \tag{4-8}$$

Where μ_l and ρ_l are the viscosity and density of the liquid respectively, ε is the energy dissipation rate [J/s·kg], D is the diffusivity of the reagent in the solvent, F_c is a shape factor, and $d_{4\,3}$ is mean diameter over the volume distribution, which is also called Herdan or De Brouckere diameter. Therefore, it is obviously to see that the increasing of ultrasound intensity leads to the increasing of energy dissipation rate, mass transfer coefficient, overall reaction rate, as well as the reduction of micromixing time. This virtue of ultrasound could be also explained by the symmetrical implosion of cavitation bubbles, which can generate localized turbulence, or micro-stream. The enhanced collision rate among the turbulent eddies results in the reduced micromixing time and increased mass transfer rate, which can promote the nucleation rate. The mass transfer rate is also improved by increasing the intrinsic

mass transfer coefficient, will lead to the high possibility for the particles to collide with each other and thus form the nuclei. The increase of ultrasound power, meanwhile, contributed more energy infusion into the solution and therefore enhanced the effect of cavitation. In addition, instantaneous high temperature is helpful to improve chemical reaction rate when the cavitation bubbles imploded.

The increasing of average primary grain size and reduction of specific surface area when the ultrasound power is further increased from 600 W to 900 W can be attributed to that, the implosion bubbles lead to violent collision between particles and the generation of extremely high temperatures. Therefore these nuclei may be merged together at extremely high instantaneous high temperature, results in reduced specific surface area, enlarged primary grain size of precursor samples, and a waste of energy, which implied that higher ultrasound power might have negative effects on the synthesis of $FePO_4$ precursor nanoparticles. Furthermore, FP-600W reveals highest pore area when the pore width is larger than 90 nm. This can be attributed to interparticle pores which are generated by the micro-jetting effect from asymmetrical implosion bubbles. Therefore, larger particles can be broke into small pieces, leading to the preventing of agglomeration and clogging. Based on the sample properties and energy saving, the more suitable ultrasonic in this study was 600 W.

4.3.2 Effect of pulsed ultrasound

Three different pulsed ultrasound are applied to investigate the effect of pulse on the synthesis of $FePO_4 \cdot 2H_2O$ nanoparticles. The cycle time of pulsed ultrasound is consisted of pulse duration time ("on") and interval time ("off") of the sonicator. For the pulsed ultrasound preparation of $FePO_4 \cdot 2H_2O$ nanoparticles, the pulse duration-interval time, and the atom ratio between Fe ion and P ion (n_{Fe}/ n_P ratio) are shown in

Table 4-3. Meanwhile, the photo of $FePO_4$ samples calcinated at 650 ℃ for 10 h in air is shown in Figure 4-4. As shown in Figure 4-4, after calcination process, FP-Cont sample show white-yellow colour. It is obviously to see that the colour of calcinated samples become red and deepen as the increasing of interval time, implies that Fe_2O_3 impurities which show red colour can be generated during calcination process.

Figure 4-4 Photo of calcined samples prepared with different pulse ultrasound.

The calcined $FePO_4$ samples prepared with different pulsed ultrasound are measured by inductively coupling the use of a plasma mass spectrometry (ICP-OES) to investigate how pulsed ultrasound influence the atom ratio between Fe ion and P ion (n_{Fe}/ n_P ratio). The n_{Fe}/ n_P ratio of FP-Cont sample obtained in this work is 0.99, which is lower than other samples. The n_{Fe}/ n_P ratio of FP-1/2 and FP-1/5 is 1.03 and 1.05 respectively, indicates that the n_{Fe}/ n_P ratio of as-synthesized $FePO_4$ sample is sensitive to the pulsed ultrasound when all the other operation parameters are maintained at the same level. The observed phenomenon can be explained from the following chemical reaction relations for the synthesis of $FePO_4$ precursor samples:

$$\text{Main Reaction: } Fe^{3+} + PO_4^{3-} \rightarrow FePO_4 \downarrow$$

Side Reaction: $Fe^{3+} + 3OH^- \rightarrow Fe(OH)_3 \downarrow$

In addition, large amount of H· and OH· are generated and rearranged to form H_2, H_2O_2, and H_2O when water molecules are irradiated by ultrasound. The main reactions are summarized below:

$$H_2O \rightarrow H\cdot + OH\cdot$$

$$H\cdot + H\cdot \rightarrow H_2$$

$$OH\cdot + OH\cdot \rightarrow H_2O_2$$

$$H\cdot + OH\cdot \rightarrow H_2O$$

Due to the acid reaction environment, H· and OH· radicals were combined rapidly and produce H_2O molecules under ultrasound irradiation. Therefore, there is less amount of OH· radicals in the solution which can combine with Fe^{3+} and produce $Fe(OH)_3$. As homogeneous competitive reactions, the distribution of these two products is affected by the micromixing level in this system significantly. It has been reported previously that, comparing with impinging jetting stream, ultrasonic irradiation can further improve micromixing effect and reduce micromixing time (Mahajan and Donald, 1996). Therefore, the formation of $FePO_4$, as well as the generation of OH· can be facilitated during the duration time. However, as the existing of large amount of OH· which generated by ultrasonic irradiation and weakened micromixing level during interval time, more $Fe(OH)_3$ product is produced as the increasing of interval time, resulting in the deepened red colour and increased nFe/ nP ratio of products.

Table 4-3 The n_{Fe}/ n_P ratio of $FePO_4 \cdot 2H_2O$ precursors prepared by different impulse

Samples	Pulsed ultrasound cycle time		n_{Fe}/ n_P ratio
	Duration (On)	Interval (Off)	
FP-1/5	1 s	4 s	1.05
FP-1/2	1 s	1 s	1.03
FP-Cont	Continuous ultrasound		0.99

4.3.3 Effect of volumetric flow rate

The effect of volumetric feeding rate is evaluated when samples are prepared at five different level (Q = 17.15, 34.30, 51.44, 68.59 and 85.75 ml min^{-1}) by both UISR and ISR methods. As shown in Figure 4-5a, all the ten samples reveal Type IV N_2 sorption isotherm, which provide evidence for the existence of mesopores (>2nm and <50nm) and large surface area by the big hysteresis. The desorption pore size distribution of as-synthesized samples is shown in Figure 4-5b. It can be seen clearly that the pore width of samples prepared by ISR is mainly ranging from 10 nm to 90 nm. In comparison, the applying of ultrasound can facilitate the generation of porous in three main diameters, which are: (1) small mesopores (5-10 nm), (2) mesopores and small macropores (20-80 nm), and (3) macropores (larger than 90 nm). Type 1 and 2 can be attributed to intraparticle pores, which are formed by the agglomeration of primary nano-grains and shockwave from bubble implosion. Meanwhile, type 3 can be attributed to interparticle pores, formed by breakup of larger particles. Generally, as the increasing of volumetric feeding rate, the FP samples prepared by

UISR reveal enhanced uniform and higher pore area when pore width range from 20 to 80 nm. While the electrode with uniform pore size can optimize the open volume and leading to better mass transport without wasted space (Jiao et al., 2008).

However, it is interesting to see that FP-UISR-20 shows higher pore area than FP-UISR-40. This might be caused by the reduced mean residence time (t_R). Furthermore, the specific surface area, total pore adsorption volume, and average primary grain size results of the $FePO_4$ precursor samples prepared with 5 different volumetric feeding rates using 2 synthesis methods are shown in Table 4-4 and Figure 4-5. It is noticeable that there is a significant increasing of specific surface area and total pore adsorption volume of $FePO_4$ precursor particles prepared by ISR method can be obtained with the increasing of volumetric feeding rate from 17.15 ml min^{-1} to 85.75 ml min^{-1}. When the volumetric feeding rate is 17.15 ml min^{-1}, the specific surface area and total pore adsorption volume of as-synthesized $FePO_4$ precursor sample are 21.94 m^2 g^{-1} and 0.087 cm^3 g^{-1} respectively, then increase dramatically to 84.19 m^2 g^{-1} and 0.463 cm^3 g^{-1} when volumetric feeding rate raise to 85.74 ml min^{-1}, corresponding to 3.8 times and 5.3 times respectively. Meanwhile, the average primary grain size decreases significantly from 273.48 nm (V = 17.15 ml min^{-1}) to 71.27 nm (V = 85.74 ml min^{-1}). By comparison, when the ultrasound power is maintained at 600 W, the specific surface area, pore adsorption volume, and average primary grain size of as-synthesized samples prepared by UISR change slightly with the increasing of volumetric feeding rate. When the volumetric feeding rate is 17.15 ml min^{-1}, the specific surface area, total pore adsorption volume, and average primary grain size are 95.41m^2 g^{-1}, 0.587 cm^3 g^{-1} and 58.89 nm respectively, which change to 114.97 m^2 g^{-1}, 0.570 cm^3 g^{-1} and 53.74 nm when volumetric feeding rate increases to 85.75 ml min^{-1}.

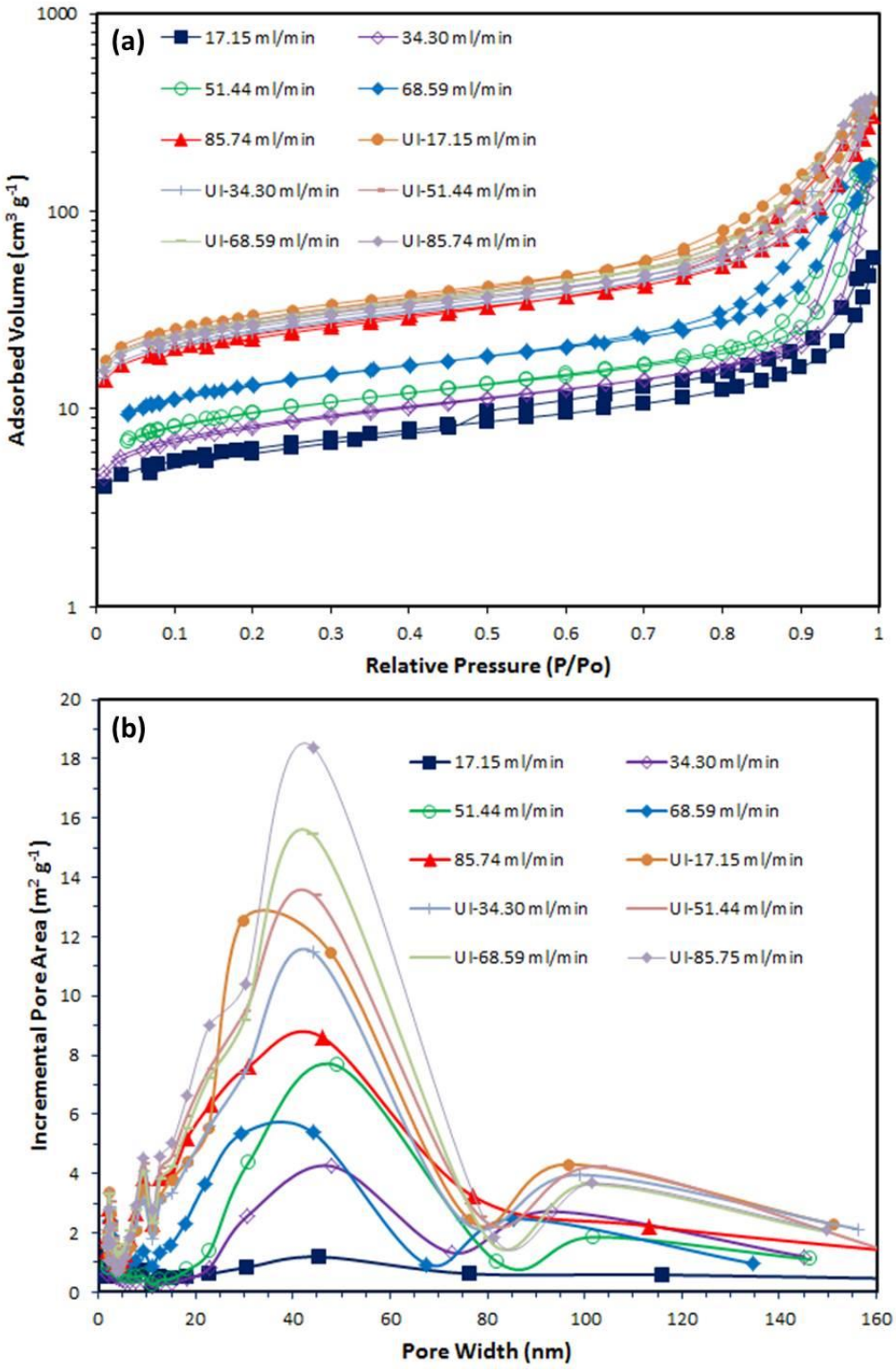
(a)
17.15 ml/min
34.30 ml/min
51.44 ml/min
68.59 ml/min
85.74 ml/min
UI-17.15 ml/min
UI-34.30 ml/min
UI-51.44 ml/min
UI-68.59 ml/min
UI-85.74 ml/min
Adsorbed Volume (cm3 g-1)
Relative Pressure (P/Po)
(b)
17.15 ml/min
34.30 ml/min
51.44 ml/min
68.59 ml/min
85.74 ml/min
UI-17.15 ml/min
UI-34.30 ml/min
UI-51.44 ml/min
UI-68.59 ml/min
UI-85.75 ml/min
Incremental Pore Area (m2 g-1)
Pore Width (nm)

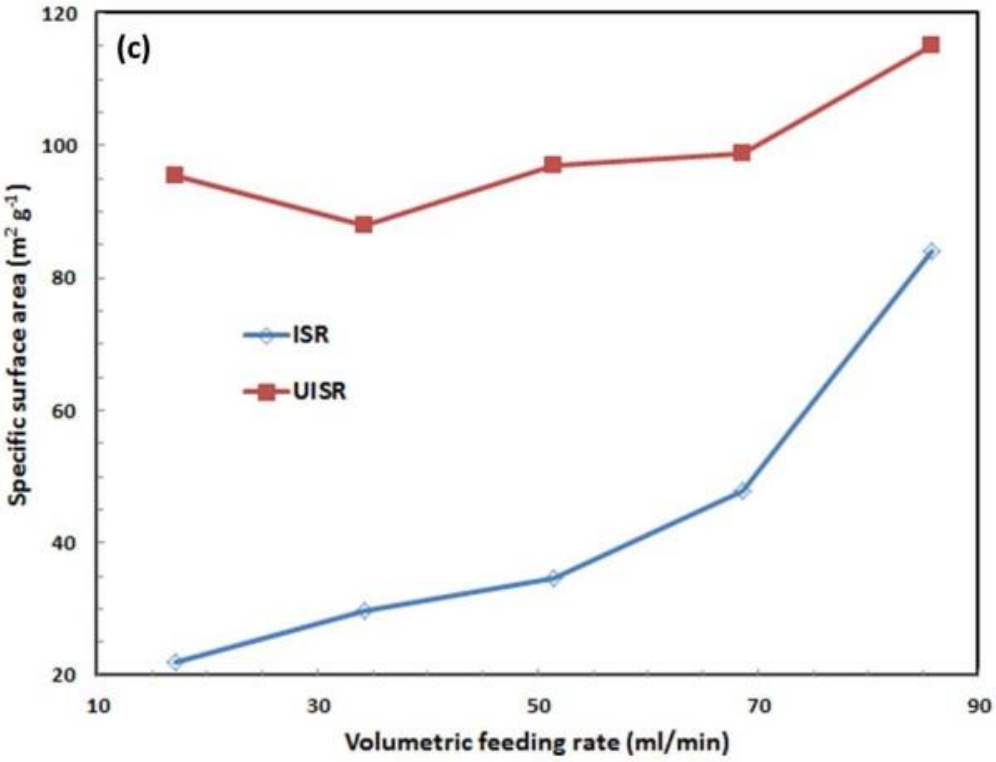
(c)
Specific surface area ($m^2 g^{-1}$)
120
100
80
60
40
20
ISR
UISR
10
30
50
70
90
Volumetric feeding rate (ml/min)

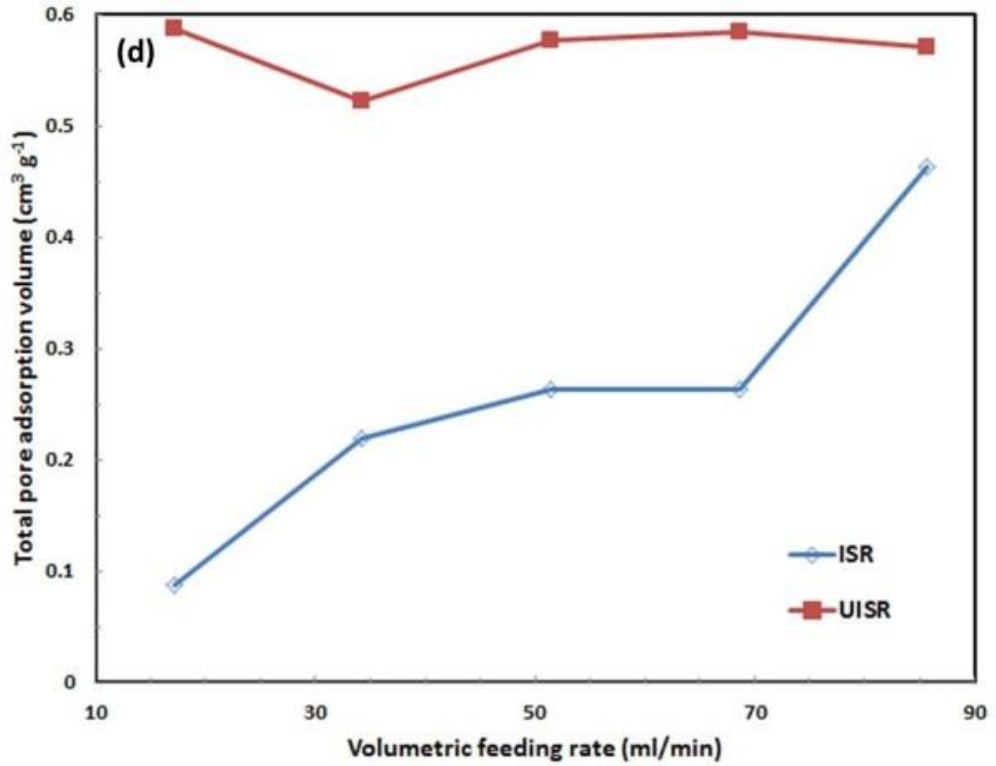
(d)
Total pore adsorption volume ($cm^3 g^{-1}$)
0.6
0.5
0.4
0.3
0.2
0.1
0
ISR
UISR
10
30
50
70
90
Volumetric feeding rate (ml/min)

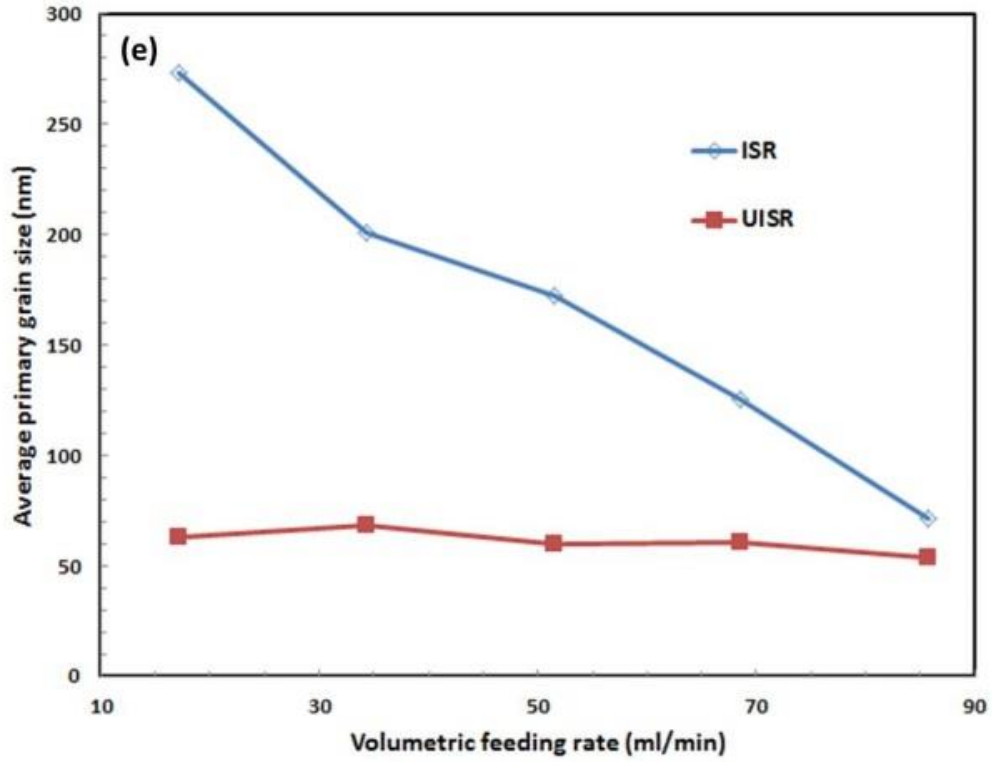

Figure 4-5 The BET analysis results of $FePO_4 \cdot 2H_2O$ samples prepared with different volumetric feeding rate: (a) N_2 adsorption-desorption isotherms; (b) the corresponding pore-size distribution obtained from the adsorption branch using the BJH method; (c-e) the relationship between volumetric feeding rate and specific surface area (c), total adsorption volume (d), and average primary size (e).

A scaling model is used to explain this observed phenomenon. The velocity distribution across the cross-sections of the inlets of impinging stream micromixer used in this work can be assumed to be uniform due to the small inlet diameter. The net rate of kinetic energy input into the system can be considered as the pressure drop taking place in the T-type micromixer. Because both the two inlets and outlet have the same cross-sectional area, the impinging streams can be treated as the combining flow

in a T-junction and the results of Idel'cik (1979) can be used. Thus, the pressure drop across the reactor can be estimated by

$$\Delta p = \xi_T \frac{U_3^2}{2} = \xi_T \frac{8Q_3^2}{\pi^2 d^2} = \xi_T \frac{8(Q_1+Q_2)^2}{\pi^2 d^2} \tag{4-9}$$

where ξ_T is the local loss coefficient which can be estimated using the following empirical relation

$$\xi_T = 1 + \varphi^2 + 3\varphi^2\left(q_T^2 - q_T\right) \tag{4-10}$$

where $q_T = Q_1/(Q_1+Q_2)$ is the discharge ratio and $\varphi = A_1/A_3$ the ratio of the cross-sectional areas of the inlet 1 to outlet. For the experimental condition used in the current study, $q_T = 0.5$ and $\varphi = 1$, $\xi_T = 1.25$. The energy change associated with the pressure drop in the impinging stream reactor P is calcualetd with $Q_1=Q_2=Q$ and $A_1=A_2=\pi/4d^2$, which yields

$$P = \Delta p Q_3 = \xi_T \frac{8(Q_1+Q_2)^3}{\pi^2 d^2} = 1.25\frac{64Q^3}{\pi^2 d^2} \tag{4-11}$$

The turbulent energy dissipation rate in the T-type micromixer and the Kolmogorov length λ, when substituting equation (9) into (5), are thus estimated, respectively, by

$$\varepsilon = \frac{1.25}{\rho_{ms} V_T}\frac{64Q^3}{\pi^2 d^2} \tag{4-12}$$

$$\lambda = \left(\frac{\nu_{ms}^3 \rho_{ms} V_T \pi^2 d^2}{80Q^3}\right)^{1/4} \tag{4-13}$$

and the micromixing time can be estimated by

$$t_M = \frac{(0.5\lambda)^2}{D_{eddy}} = \frac{0.25}{D_{eddy}}\left(\frac{\nu_{ms}^3 \rho_{ms} V_T \pi^2 d^2}{80Q^3}\right)^{1/2} \quad (4\text{-}14)$$

The Reynolds numbers based on the two inlet diameters are calculated according to

$$\mathrm{Re}_i = \frac{4\rho_i Q_i}{\mu_i \pi d_i} \quad (4\text{-}15)$$

As the density and viscosity of $Fe(NO_3)_3$ and $(NH_4)_2HPO_4$ solutions are different, the Reynolds number used to characterise the mixing in the T-type micromixer can be defined by

$$\mathrm{Re}_T = \frac{4\rho_{ms}\sum_{i=1}^{2} Q_i}{\mu_{ms}\pi d} \quad (4\text{-}16)$$

According to these equations, it is clear to see that the Reynolds number, micromixing time, and energy dissipation rate in ISR is only related to volumetric feeding rate *Q* when all the other factors are maintained at same level. The increasing of volumetric feeding rate results in an intensified diffusion through the engulfment of two solutions among the Kolmogorov length scale eddies, which leading to enhanced mass transfer rate and energy dissipation rate, as well as shortened mean residence time and micromixing time. The values of the parameters in this study are listed Table 4-5. The Reynolds number is 572 in both ISR and UISR system when the volumetric is 85.74 ml min^{-1}, which can be regarded as laminar flow.

However, in UISR system, the use of ultrasonic irradiation can produce a large number of micro bubbles. Such imploding bubbles can be considered as small microreactors which can generate powerful hydraulic shocks, and an environment with extremely high temperature and pressure. In the beginning of experiment, as

there is no solid in solution, the system can be considered as homogeneous reaction. The bursting of the microbubbles which caused by ultrasound induce hydraulic shocks in the solution. The symmetrical implosion bubbles induce micro-streaming and eddies that promote the regime transition from laminar to turbulent so that the turbulent energy dissipation can be enhanced. As a result, the diffusion rate or micro-mixing among these eddies are remarkably improved due to the application ultrasonic irradiation. In addition, chemical reaction rate and nucleation rate are increased due to the extremely high temperature and pressure created by imploding bubbles, which lead to the formation of large amount of nanoscale seeds. After the generation of nanoscale seeds, the system is changed to heterogeneous system. The asymmetrical implosion bubbles can produce micro-jetting, which can prevent agglomeration and clogging among particles or between particles and the internal surface of reactor. Therefore, during the nucleation of precursor particles in UISR, the enhanced micromixing effect and mass transfer coefficient (deriving from micro-streaming) is helpful for the nucleation of the crystals, and the effect caused by micro-jetting is helpful to prevent the agglomeration and avoid abnormal growth. Furthermore, ultrasound can induce turbulent vortex even when Reynolds number is relatively low. The micromixing effect can be improved by ultrasonic irradiation more significantly than the increasing of volumetric feeding rate. These effects lead to the generation of particles with smaller size, enlarged specific surface area, narrower and sharper particle size distribution.

Table 4-4 N_2 adsorption-desorption analysis results of $FePO_4 \cdot 2H_2O$ precursors prepared with different volumetric feeding rate by ISR and UISR methods (Reagent concentration = 1.0 mol L^{-1})

Samples	Specific surface area (m^2 g^{-1})	Total pore adsorption volume (cm^3 g^{-1})	Average primary grain size (nm)	Reynolds number (Re)
FP-20rpm	21.94	0.087	273.48	118
FP-40rpm	29.82	0.219	201.24	237
FP-60rpm	34.75	0.263	172.69	355
FP-80rpm	47.96	0.263	125.11	474
FP-100rpm	84.19	0.463	71.27	592
FP-U20rpm	95.41	0.587	62.89	118
FP-U40rpm	88.05	0.522	68.14	237
FP-U60rpm	96.88	0.576	59.60	355
FP-U80rpm	98.72	0.584	60.78	474
FP-U100rpm	114.97	0.570	53.74	592

Table 4-5 Experimental parameters for calculation of the Reynolds numbers

Solutions	Density (ρ, kg m^3)	Viscosity (μ, Pa·s)	Tube diameter (d, m)
$Fe(NO_3)_3$	1177	0.001008	0.0035
$(NH_4)_2HPO_4$	1075	0.001003	0.0035
$FePO_4$ precursor solution	1144.4	0.001005	0.0035

4.3.4 Synthesis of FexMn1-xPO4 and LiFexMn1-xPO4 (x = 0.90, 0.93, 0.96, 1.00) by UISR reaction

The XRD patterns of a series of $Fe_xMn_{1-x}PO_4$ and $LiFe_xMn_{1-x}PO_4$/C (x=0.90. 0.93, 0.96, 1.00) samples prepared by UISR are shown in Figure 4-6. And lattice parameters of $Fe_xMn_{1-x}PO_4$ samples are shown in Table 4-6. As shown in Figure 4-6a, all the XRD patterns of $Fe_xMn_{1-x}PO_4$ composites fit the ideally crystallized hexagonal structure $FePO_4$ (JCPDS card no. 29-0715, a = 5.035 Å, b = 5.035 Å, c = 11.245 Å. In addition, it is obviously to see that the cell parameters of $Fe_xMn_{1-x}PO_4$ samples changed slightly. The $Fe_{0.96}Mn_{0.04}PO_4$ sample has the smallest cell volume (246.85 Å^3), while $Fe_{0.93}Mn_{0.07}PO_4$ sample shows the largest cell volume (248.18 Å^3). As shown in Figure 4-6b, all the XRD patterns of $LiFe_xMn_{1-x}PO_4$/C products match well with standard $LiFePO_4$ with orthorhombic structure (JCPDS card no.40-1499, a = 10.347 Å, b = 6.019 Å, c = 4.704 Å), suggesting a perfect crystallinity of the as-synthesized samples.

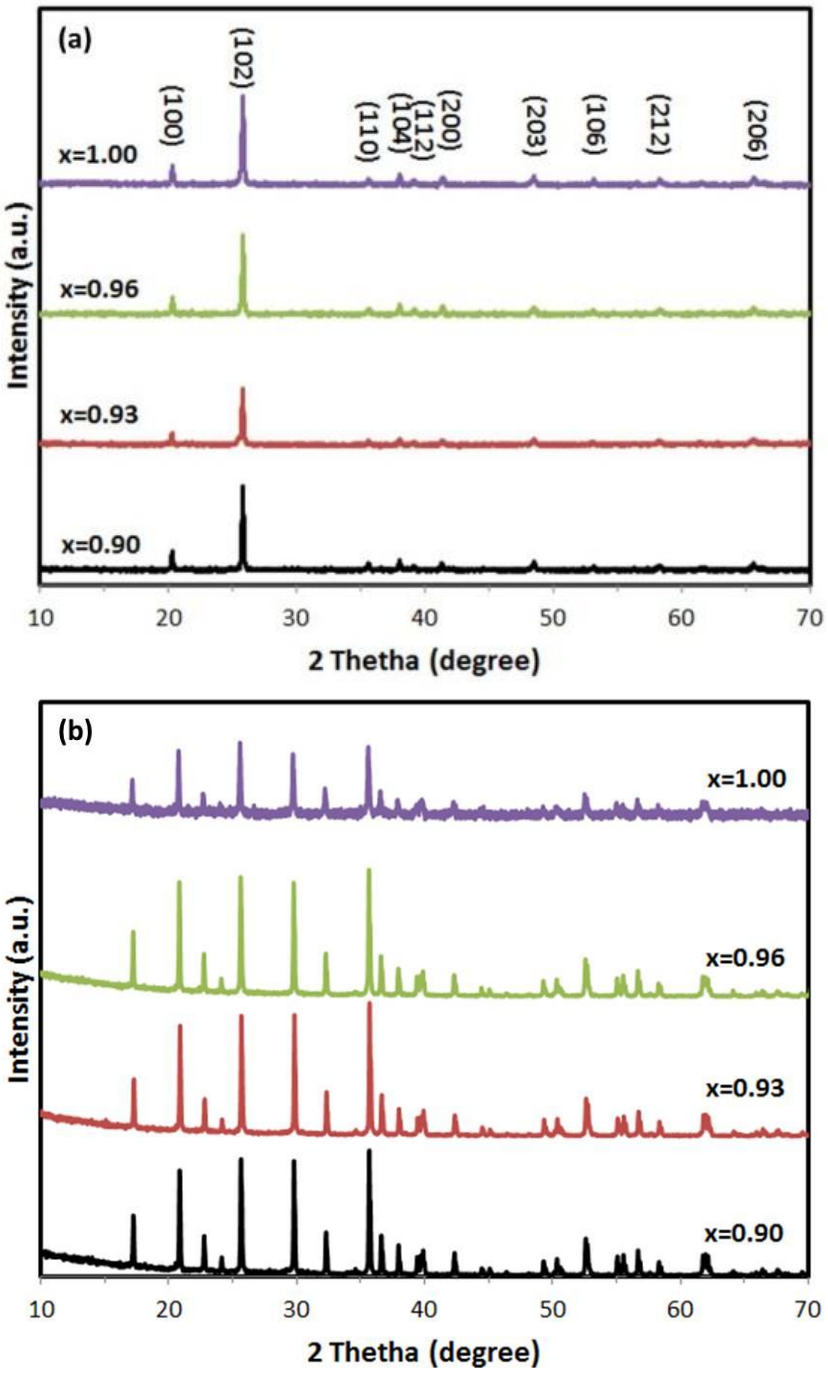

Figure 4-6 XRD results of $Fe_xMn_{1-x}PO_4$ and $LiFe_xMn_{1-x}PO_4/C$ samples synthesized with different Mn content (a) $Fe_xMn_{1-x}PO_4$; (b) $LiFe_xMn_{1-x}PO_4/C$

Table 4-7 Lattice parameters of as-synthesized $Fe_xMn_{1-x}PO_4$ samples

Samples	a(Å)	b(Å)	c(Å)	V(Å^3)
$Fe_{0.9}Mn_{0.1}PO_4$	5.034	5.034	11.258	247.12
$Fe_{0.93}Mn_{0.07}PO_4$	5.046	5.046	11.250	248.18
$Fe_{0.96}Mn_{0.04}PO_4$	5.035	5.035	11.245	246.85
$FePO_4$	5.037	5.037	11.257	247.38

To investigate the presence of all bands corresponding to as-synthesized samples, FTIR spectra is shown in Figure 4-7. For $Fe_xMn_{1-x}PO_4$ samples, the absorption peaks confirm the presence of PO_4^{3-} functional group, including v_4 (O-P-O) double band of 574 and 597 cm^{-1}, v_3 (P-O) band of 1042 cm^{-1}, v_2 (O-P-O) band of 456 cm^{-1}, and v_1 (P-O) band of 996 cm^{-1} (Wang *et al*., 2014; Zhang *et al*., 2015; Shen *et al*., 2016).

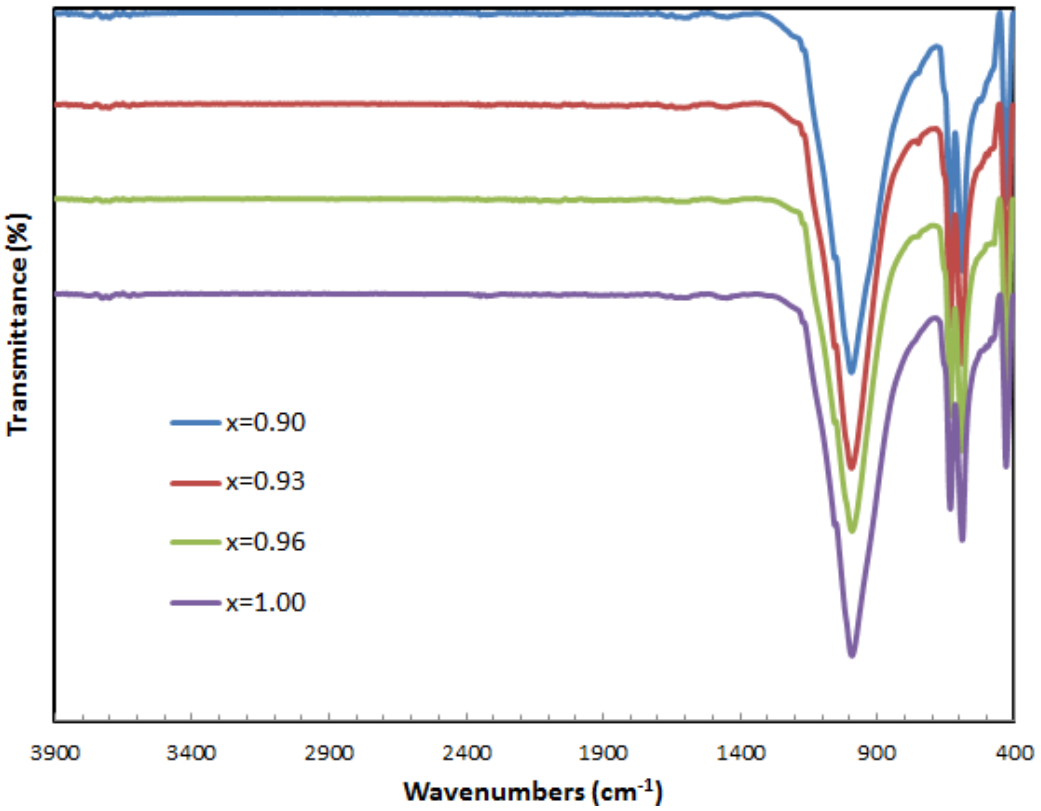

Figure 4-7 FTIR patterns of $Fe_xMn_{1-x}PO_4$ samples synthesized with different Mn content

The morphology of $Fe_xMn_{1-x}PO_4$ composites prepared by UISR was examined by scanning electron microscopy (SEM) and SEM images were shown in Figure 4-8. The reagent concentration and volumetric flow rate were maintained at same level for the synthesis of $FePO_4$ precursor by varying the Mn content. It is noticed that all the samples with Mn doping exhibit apparent characteristics of nanocrystals with sizes ranging from 50 nm to 300 nm. These nanospheres interweave to accumulate and form the high nanoporosity structures. However, the $FePO_4$ sample, as shown in Figures 4-8d, reveals smaller nanocrystal size and structures of higher porosity.

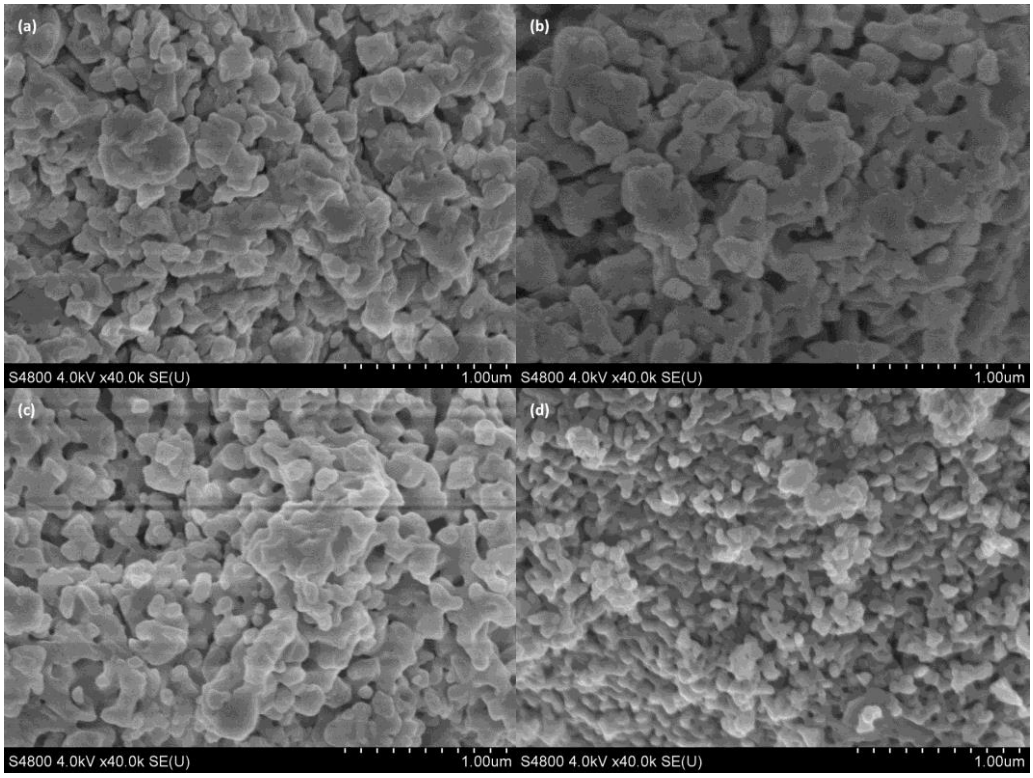

Figure 4-8 SEM images of $Fe_xMn_{1-x}PO_4$ composites synthesized with different Mn content: (a) x=0.90, (b) x=0.93, (c) x=0.96, (d) x=1.00.

The SEM images of $LiFe_xMn_{1-x}PO_4$/C composites are shown in Figure 4-9. The agglomerated nanocrystals prepared with Mn doping were merged together and yield larger particles at high temperature during calcination process.

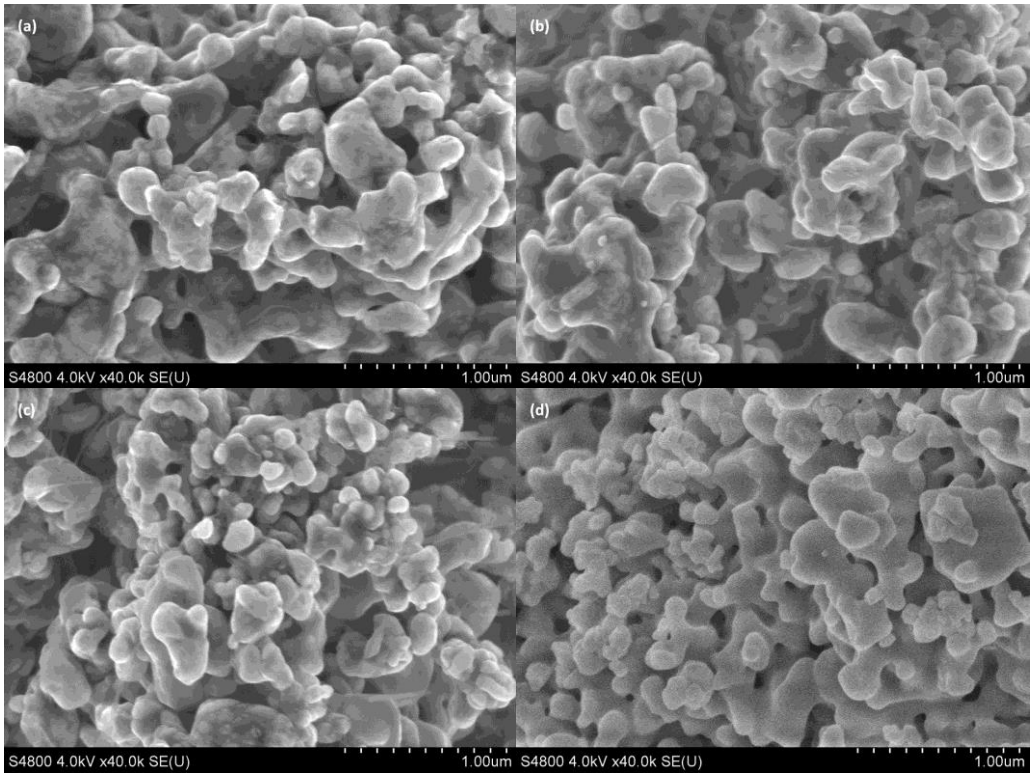

Figure 4-9 SEM images of $LiFe_xMn_{1-x}PO_4/C$ composites synthesized with different Mn content: (a) x=0.90, (b) x=0.93, (c) x=0.96, (d) x=1.00.

The coin cell batteries assembled using the synthesised $LiFe_xMn_{1-x}PO_4/C$ composites were charged and discharged at various rates varying from 0.1 C to 5 C and finally returned to 0.1 C in cycle. The test results of the electrochemical performance characterised by the current capacity, as shown in Figure 4-10 and listed Table 4-7, indicate that the important impact of Mn doping on the rate and cycle performance of the samples. This can be seen clearly from the figure that $LiFe_{0.93}Mn_{0.07}PO_4/C$ sample shows the best rate capability among all the samples. Its average discharge capacities can reach 156.8, 150.5, 140.0, 126.6 and 110.0 mAh g^{-1} at 0.1 C, 0.5 C, 1 C, 2 C and 5 C, respectively. The reason is that, $LiMnPO_4$ has similar theoretical capacity with $LiFePO_4$, but about 20 % higher energy density on account of the higher redox potential of Mn^{3+}/Mn^{2+} (4.1 V versus 3.5 V in Fe^{3+}/Fe^{2+}). Therefore, Mn doping can

improve the kinetic properties and electrochemical performance of $LiFePO_4$. For the cycle performances, $LiFePO_4$/C achieves the most stable cycle performance. The discharge capacity at 1^{st} and 100^{th} cycle was 144.9 and 138.0 mAh g^{-1}, respectively, and the capacity retention after 100 cycles is 95.2%.

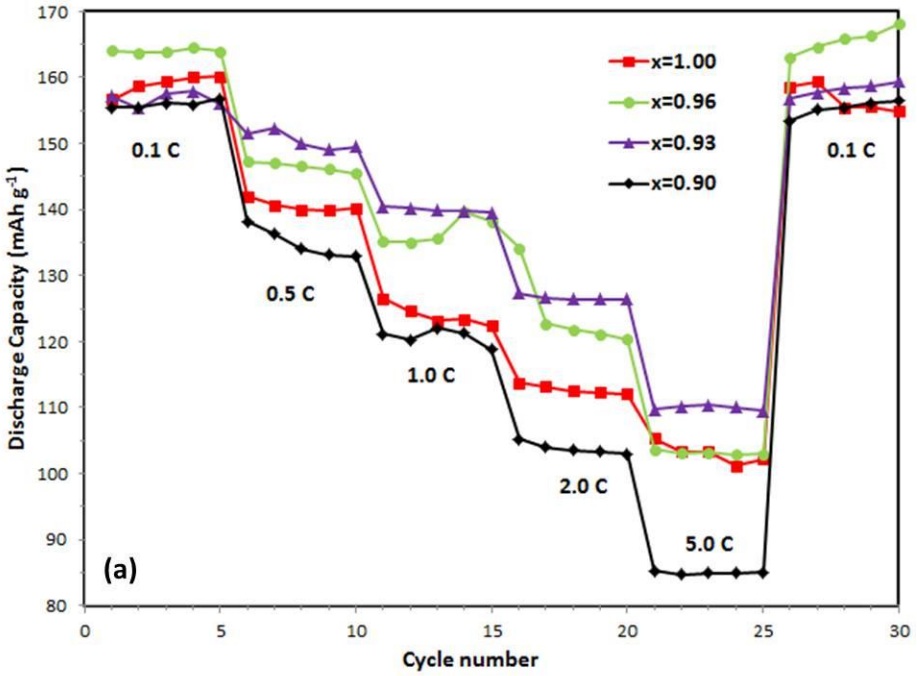
Discharge Capacity (mAh g-1)
Cycle number
x=1.00
x=0.96
x=0.93
x=0.90
0.1 C
0.5 C
1.0 C
2.0 C
5.0 C
0.1 C
(a)

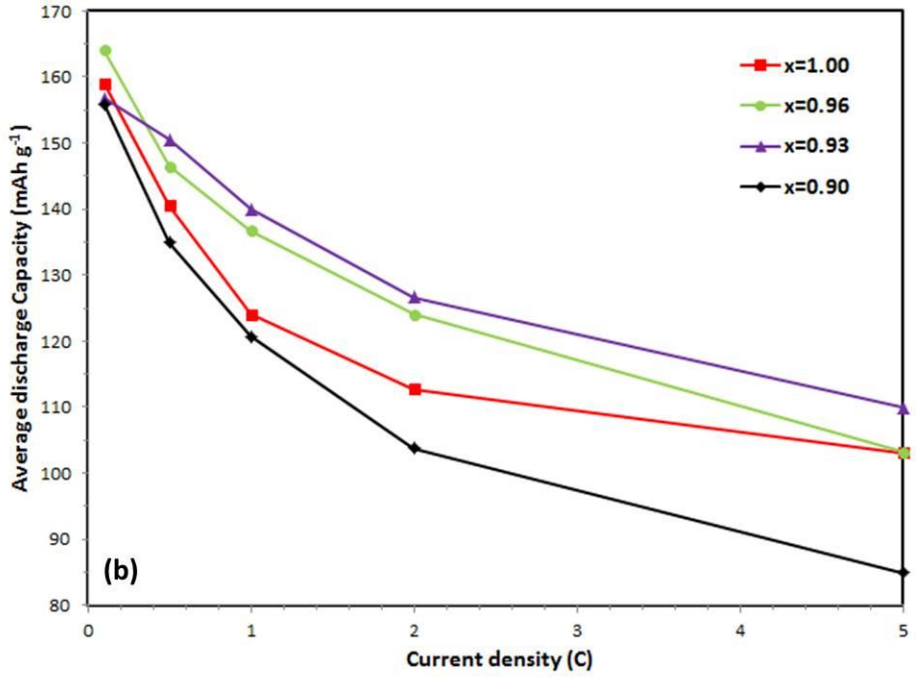
Average discharge Capacity (mAh g-1)
Current density (C)
x=1.00
x=0.96
x=0.93
x=0.90
(b)

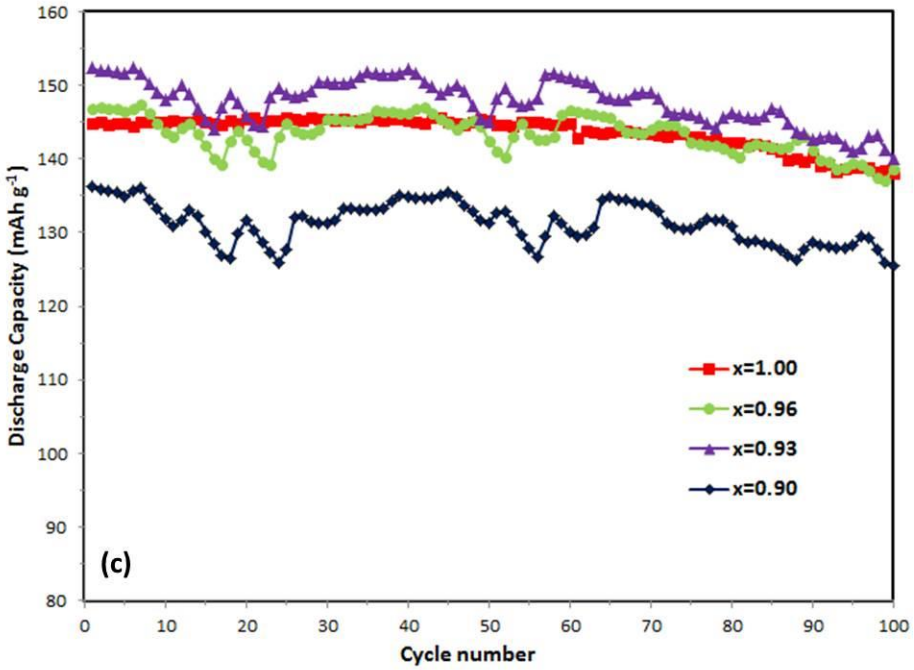

Figure 4-10 Electrochemical performance of $LiFe_xMn_{1-x}PO_4/C$ composites synthesized with different Mn doping: (a) Rate performance at various rates; (b) Average rate capability; (c) Cycling performance at 0.5 C for 100 cycles.

Table 4-7 The comparison of electrochemical performance of the $LiFe_xMn_{1-x}PO_4/C$ synthesized by UISR with different Mn doping.

Fe content	Cycle performance at 0.5 C (mAh g^{-1})			Average Rate Performance (mAh g^{-1})				
	1st cycle	100th cycle	R_1[a](%)	0.1 C	0.5 C	1 C	2 C	5 C
X=1.00	144.9	138.0	95.2	159.0	140.6	124.0	112.8	103.1
X=0.96	146.9	138.7	94.4	164.0	146.5	136.7	124.1	103.2
X=0.93	152.4	140.1	91.9	156.8	150.5	140.0	126.6	110.0
X=0.90	136.3	125.5	92.1	155.9	134.9	120.7	103.8	85.0

4.4 Conclusions

In this work, $Fe_xMn_{1-x}PO_4$ and $LiFe_xMn_{1-x}PO_4/C$ nanocomposites are prepared by ultrasound-intensified impinging streaming reaction (UISR). The effects of ultrasound intensity, pulse, volumetric feeding rate, and Mn doping on particle size, porosity, specific surface area, and electrochemical performance, are systematically investigated in the work. The conclusions reached as the results of the current study are as follows:

(1) The increasing of ultrasound intensity can reduce micromixing time, and improve both mass transfer coefficient and overall reaction rate, which result in smaller primary particle size, higher specific surface area, and narrower and

sharper pore size distribution. However, over-increase in the ultrasound intensity would have negative impact, results in the increasing of average grain size, and reduction of specific surface area due to the extremely high temperature caused by higher ultrasound intensity.

(2) The purity of $FePO_4$ is affected by ultrasound pulse significantly due to the homogeneous competitive reactions between $FePO_4$ and $Fe(OH)_3$. The increasing of interval time leads to the formation of more $Fe(OH)_3$ because of the weakened micromixing effect and reduced mass transfer coefficient.

(3) Increased specific surface area and total adsorption pore volume, and reduced average primary grain size can be obtained through increasing the volumetric flow rate, especially in ISR. The reasons are that, the energy dissipation rate and micromixing time in the T-type micromixer are only related to volumetric feeding rate *Q*. However, for UISR, the explosion of bubbles can cause hydraulic shocks and induce eddies which promote the regime transition from laminar to turbulent so that the turbulent energy dissipation can be enhanced. In addition, the micromixing effect can be improved by ultrasonic irradiation more significantly than the increasing of volumetric feeding rate.

(4) The Fe content in $LiFe_xMn_{1-x}PO_4/C$ has important impact on electrochemical performance. In this work, the optimum Fe content is 0.93.

Reference

1. Shu H., Wang X., Wen W. , Liang Q. , Yang X., Wei Q., Hu B., Liu L., Xue X., Song Y., Zho M., Bai Y., Jiang L., Chen M., Yang S., Tan J., Liao Y., and Jiang H., 2013, Effective enhancement of electrochemical properties for $LiFePO_4$/C cathode materials by Na and Ti co-doping, Eletrochimica Acta, 89, 479-487
2. Gibot P., Casas-Cabanas M., Laffont L., Levasseur S., Carlach P., Hamelet S., Tarascon J.M., and Masquelier C., 2008, Room-temperature single-phase Li insertion/extraction in nanoscale $LixFePO_4$, Nature Materials, 7, 741-747
3. Ding Y., Jiang Y., Xu F., Yin J., Ren H., Zhuo Q., Long Z., and Zhang P., 2010, Preparation of nano-structured $LiFePO_4$/graphene composites by co-precipitation method, Eletrochemistry Communication, 12, 10-13
4. Park K.S., Son J.T., Chung H.T., Kim S.J., Lee C.H., and Kim H.G., 2003, Synthesis of $LiFePO_4$ by co-precipitation and microwave heating. Electrochemistry Communications, 5, 839-842
5. Padhi K., Nanjundaswamy K. S., Masquelier C., Okada S., and Goodenough J. B., 1997, Effect of structure on the Fe^{3+}/Fe^{2+} redox couple in iron phosphates., Journal of the Electrochemistry Society, 144, 1609-1613
6. Yao, J., Bewlay S., Konstantionv K., Drozd V.A., Liu R.S., Wang X.L., Liu H.K., and Wang G.X., 2006, Characterisation of olivine-type LiMnxFe1−xPO4 cathode materials. Journal of Alloys and Compounds, 425, 362-366.
7. Padhi, A.K., Nanjundaswamy K.S., and Goodenough J.B., 1997, Phospho-olivines as Positive Electrode Materials for Rechargeable Lithium Batteries. Journal of Eletrochemical Society, 144, 1188-1194

8. Oh S.M., Myung S.T., Choi Y.S., Oh K.H., and Sun Y.K., 2011, Co-precipitation synthesis of micro-sized spherical LiMn0.5Fe0.5PO4 cathode material for lithium batteries, Journal of Materials Chemistry, 21, 19368-19374
9. Shin H.C., Park S.B., Jang H., Chung K.Y., Cho W., Kim C.S., and Cho B.W., 2008, Rate performance and structural change of Cr-doped $LiFePO_4$/C during cycling, Eletrochimica Acta, 53, 7946-7951
10. Chung S.Y., Bloking J.T., and Chiang Y.M., 2002, Electronically conductive phospho-olivines as lithium storage electrodes, Nature Material, 1, 123-128
11. Guo L., Zhang Y., Ma L., Zhang Y., Wang E., Bi Y., Wang D., McKee W.C., Xu Y., Chen J., Zhang Q., Nan C., Gu L., Bruce P.G., and Peng Z.G., 2015, Unlocking the energy capabilities of micron-sized $LiFePO_4$, Nature Communication, 6, 7898-7905
12. Vu A., Qian Y., and Stein A., 2012, Porous electrode materials for lithium-ion batteries - how to prepare them and what makes them special, Advanced Energy Materials, 2, 1056-1085.
13. Wang K.X., Li X.H., and Chen J.S., 2015, Surface and interface engineering of electrode materials for lithium-ion batteries, Advanced Materials. 27, 527-545.
14. Mahajan A.J. and Donald J.K., 1996, Micromixing effects in a two impinging jets precipitator. AIChE Journal, 42, 1801-1814.
15. Huang Y., Wang P., Yuan Y., and Yang F., 2015, Synergistic degradation of chitosan by impinging stream and jet cavitation. Ultrasonics Sonochemistry, 27, 592-601
16. Noël T., Naber J.R., Hartman R.L., McMullen J.P., Hensen K.F., and Buchwald S.L., 2011, Palladium-catalyzed amination reactions in flow: overcoming the challenges of clogging via acoustic irradiation. Chemical Science, 2, 287-290.

17. Nagasawa H. and Mae K., 2006, Development of a New Microreactor Based on Annular Microsegments for Fine Particle Production. Industrial & Engineering Chemistry Research, 45, 2179-2186.
18. Shestopalov I., Tice J.D., and Ismagilov R.F., 2004, Multi-step synthesis of nanoparticles performed on millisecond time scale in a microfluidic droplet-based system, Lab Chip, 2004. 4, 316-21.
19. Löb P., Drese K.S., Hessel V., Hardt S., Hofmann C., Lowe H., Schenk R., Schonfeld F., and Werner B., 2004, Steering of Liquid Mixing Speed in Interdigital Micro Mixerssfrom Very Fast to Deliberately Slow Mixing, Chemical Engineering & Technology, 27, 340-345.
20. Naber, J.R. and Buchwald S.L., 2010, Packed-bed reactors for continuous-flow C-N cross-coupling. Angewandte Chemie International Edition, 49, 9469-9474.
21. Shastry M.C.R., Luck S.D., and Roder H., 1998, A Continuous-Flow Capillary Mixing Method to Monitor Reactions on the Microsecond Time Scale. Biophysical Journal, 74, 2714-2721.
22. Asgharzadehahmadi S., Raman A.A.A., Parthasarathy R., and Sajjadi B., 2016, Sonochemical reactors: Review on features, advantages and limitations. Renewable and Sustainable Energy Reviews, 63, 302-314.
23. Monnier H., Wilhelm A.M., and Delmas H., 1999, Influence of ultrasound on mixing on the molecular scale for water and viscous liquids. Ultrasonics Sonochemistry, 6, 67-74.
24. McNamara W. B., Didenko Y. T., and Suslick K. S., 1999, Sonoluminescence temperatures during multi-bubble cavitation. Nature, 401, 772-775.

25. Mason, T.J. and Cordemans E.D., 1996, Ultrasonic intensification of chemical processing and related operations. Chemical Engineering Research and Design, 74, 511-516.
26. Rivas D.F. and Kuhn S., 2016, Synergy of Microfluidics and Ultrasound : Process Intensification Challenges and Opportunities. Topic in Current Chemistry, 374, 70-99.
27. Sedelmeier J., Ley S.V., Baxendale I.R., and Baumann M., 2010, KMnO4-Mediated Oxidation as a Continuous Flow Process. Organic Letters, 12, 3618-3621.
28. Horie T., Sumino M., Tanaka T., Matsushita Y., Ichimura T., and Yoshida J., 2010, Photodimerization of Maleic Anhydride in a Microreactor Without Clogging. Organic Process Research & Development, 14, 405-410.
29. Zhang L., Geng M., Teng P., Zhao D., Lu X., and Li J.X., 2012, Ultrasound-promoted intramolecular direct arylation in a capillary flow microreactor. Ultrasonics Sonochemistry, 19, 250-256.
30. Alothman Z.A., 2012, A Review: Fundamental Aspects of Silicate Mesoporous Materials. Materials. 5, 2874-2902.
31. Johnson B.K. and Prud'homme R. K., 2003, Chemical Processing and Micromixing in Confined Impinging Jets. AIChE Journal. 49, 2264-2282
32. Contanmine F., Wilhelm A.M., Berlan J., and Delmas H., 1995, Activation of a solid-liquid chemical reaction by ultrasound. Chemical Engineering Science, 50, 554-558.
33. Bang J.H. and Suslick K.S., 2010, Applications of ultrasound to the synthesis of nanostructured materials, Advanced Materials, 22, 1039-1059.

34. Jiao F., Bao J., Hill A.H., and Bruce P.G., 2008, Synthesis of ordered mesoporous Li-Mn-O spinel as a positive electrode for rechargeable lithium batteries. Angewandte Chemie International Edition, 47, 9711-9716.
35. Wang H. Q., Zhang X. H., Zheng F. H., Huang Y. G., and Li Q. Y., 2014, Surfactant effect on synthesis of core-shell $LiFePO_4$/C cathode materials for lithium-ion batteries. Journal of Solid State Electrochemistry, 19, 187-194.
36. Zhang L.L., Li H.J., Li K.Z., Fu Q.G., Zhang Y.L., and Liu S. J., 2015, Synthesis and characterization of nanobelt-shaped Na, F and carbonate multi-substituted hydroxyapatite, Materials Letters, 138, 48-51.
37. Shen J., Jin B., Jiang Q., Hu Y., and Wang X., 2016, Morphology-controlled synthesis of fluorapatite nano/microstructures via surfactant-assisted hydrothermal process. Material & Design, 97, 204-212.

CHAPTER 5: Synthesis of Hierarchical Micro/Nano-structured Porous $FePO_4$ for High Performance Lithium-Ion Batteries using a Two-step Co-Precipitation Method

SUMMARY

In Chapter 3 and 4, the ISR and UISR methods, which have important impacts on nucleation process, have been systematically investigated. To prepare $LiFePO_4$ particles with hierarchical structure, it is necessary to control particle growth process. In this chapter, a two-step co-precipitation method has been adopted for the synthesis of hierarchical micro/nano-structured mesoporous $FePO_4 \cdot 2H_2O$ particles. $FePO_4 \cdot 2H_2O$ seed nano-composites were firstly synthesized by impinging stream reaction (ISR). Then these nano-scale $FePO_4 \cdot 2H_2O$ seed crystals were transferred into a continuous stirring tank reactor (CSTR) and stirred for several hours. Hierarchical micro/nano-structured mesoporous $FePO_4 \cdot 2H_2O$ composites were generated after enough reaction time and stirring. The effects of mean residence time and rotation speed on the physical and chemical properties of $FePO_4 \cdot 2H_2O$ and $LiFePO_4$/C samples were systematically investigated in this work. The as-synthesized $FePO_4 \cdot 2H_2O$, $FePO_4$ and corresponding $LiFePO_4$/C products are characterized by XRD, SEM, BET, Mastersizer, and electrochemical charge-discharge test. Under optimum operating condition, the $FePO_4 \cdot 2H_2O$ composites have near-spherical hierarchical micro/nano-structure which is consisted of nanoscale primary grains, while the resulting $LiFePO_4$/C possesses the best electrochemical performance. Its discharge capacities can reach 145.6, 133.7, 118.0, 103.7, and 85.7 mAh g^{-1} at 0.1 C,

0.5 C, 1 C 2 C and 5 C current rates, respectively. For cycling capability, $LiFePO_4$/C exhibited 132.4 mAh g^{-1} after 100^{th} cycle at 0.5 C, corresponding to 103.7% of its initial discharge capacity (127.7 mAh g^{-1}). It has been clearly demonstrated that the as-synthesized $LiFePO_4$/C products prepared by this method can show excellent rate capacities, superior cycling performance, and a relatively high tap density.

5.1 Introduction

In recent years, serious climate issues coupled with the shortage of conventional energy have already become one of the biggest problems which is facing by the people around the world. To solve it, many kinds of sustainable energies, such as solar power, wind energy, and tidal energy have already been researched and investigated. As one of the most important equipment for the storage of regeneration energy, lithium ion battery (LIB) has attracted more attentions from public. Olivine structured lithium iron phosphate ($LiFePO_4$) has been recognized as one of the most appropriate and promising positive electrode material in Li-ion battery due to nontoxicity, low cost of raw materials, good structural stability at high temperature, excellent safety performance, and relatively high theoretical specific capacity (170 $mAhg^{-1}$) with a flat discharge-charge potential (3.45V vs. Li^+/Li) (Ding *et al*., 2010; Park *et al*., 1997; Padhi *et al*., 1997). However, the low energy density resulted by relatively low redox potential (3.45V vs. Li^+/Li) (Xiang *et al.*, 2016), and slow lithium ion diffusion through the $LiFePO_4$-$FePO_4$ interface which may lead to poor rate capability are the main disadvantages of the pure material (Naik *et al*., 2016; Shu *et al*., 2013). Meanwhile, essentially poor ionic and electronic conductivity has limited the insertion and extraction of lithium ions and charge transport rate seriously, which also hold back the large-scale application and the extensively use of $LiFePO_4$ to the

commercial market (Wang *et al*., 2011). Refining $LiFePO_4$ particles to nanoscale level is one of the most popular strategies to improve the $LiFePO_4$'s electrochemical property, because reduction of the $LiFePO_4$ particle size can lead to shortening the Li^+ diffusion path and facilitating the kinetics of Li^+ insertion and extraction process. However, both the volumetric and the gravimetric energy density are decreased.

The synthesis of $FePO_4$ precursor and $LiFePO_4$ composites has been documented in many previous researches. Ying *et al* (2006) prepared micro-scale spherical $FePO_4$ precursor and $Li_{0.97}Cr_{0.01}FePO_4/C$ with high tap density by co-precipitation method. Shin *et al.* (2008) also evaluated the effect of Cr-doping on LFP nanocomposites. Wang *et al.* (2008) reported an in situ polymerization restriction method to synthesise nanoscale $FePO_4$ and $LiFePO_4$/carbon composites. Sun *et al.* (2010) prepared nanoscale Cl-doped $LiFePO_4$ and found Cl-doping could facilitate the diffusion of Li ion and improve the high rate capability of positive electrode material. Hong *et al* (2012) synthesized $LiFePO_4/C$ nanocomposites and evaluated how sucrose amount influenced electrochemical performance of $LiFePO_4/C$. Hsieh *et al.* (2012) prepared nanoscale $FePO_4$ precursor at different pH value by co-precipitation method, and found that the optimum pH value was 3. Zhu *et al.* (2014) reported a facile co-precipitation method to prepare nanoscale $FePO_4$ precursor and revealed that reagent concentration would affected both of the morphology and electrochemical performance of positive electrode material. Qian *et al.* (2012) applied an electrochemical method to synthesise $FePO_4$ nanoparticles and found that electrochemical performance of $LiFePO_4/C$ can be improved if $FePO_4$ precursor had mesoporous structure. With the using of Fe(II) salts, Arnold *et al.* (2003) synthesized $LiFePO_4$ nanoflates by aqueous co-precipitation method. A microwave heating

assisted co-precipitation method was adopted by Park *et al.* (2003) to prepare $LiFePO_4$ nanocomposites. Ni *et al.* (2005) prepared $LiFePO_4$ nanocomposites by co-precipitation method, and the effects of ion doping (Mg^{2+}, Cu^{2+}, and Zn^{2+}) on physical and chemical properties of LFP were evaluated. Ding *et al.* (2010) reported a novel co-precipitation method to prepare nano-structured LFP/graphene composites, and found the electrochemical performance of LFP can be improved by adding graphene nanosheets. Liu *et al.* (2014) evaluated how the graphene nanosheet content affected the morphology and electrochemical performance of LFP. Shi *et al.* (2012) investigated the effect of graphene and found the rate capability can be enhanced by graphene wrapping. Bai *et al.* (2015) synthesized LFP/C microspheres by co-precipitation method. Han *et al.* (2013) have found that the use of two step heterogeneous growth technology could produce porous and coarse LFP/C composites with improved electrochemical performance.

To develop $LiFePO_4$ with good electrochemical performance and high tap density, four requirements have to be achieved: (1) reduce $LiFePO_4$ primary grains to nanoscale, so that the diffusion pathway of Li-ion can be shortened; (2) enlarge specific surface area of $LiFePO_4$ to increase the interface between electrode and electrolyte; (3) increase the secondary structure of $LiFePO_4$ to microscale to guarantee relatively high tap density; (4) make sure the uniform carbon coating on $LiFePO_4$ to improve the electronic conductivity of $LiFePO_4$ (Han *et al.*, 2013; Whittingham, 2004) . Therefore, fabricating $LiFePO_4$ positive electrode material with micro-nano hierarchical porous structure can, shorten diffusion length of Li-ion, increase electrode/electrolyte interface area and ensure effective electrolyte permeation, as well as guarantee relatively high volumetric and gravimetric energy density (Vu *et al*.,

2012; Wang *et al*., 2015; Wang *et al*., 2011) . Thus, though there are many studies on using co-precipitation method to synthesize FP and LFP nanocomposites or microspheres, the studies on synthesis of FP and LFP composites with hierarchical porous micro/nano structure using co-precipitation method are still limited and the factors that affect the synthesis process are required further investigations.

In this work, FP precursor composites with hierarchical porous micro/nano structure were prepared by two-step co-precipitation method at various operating conditions. Due to the application of impinging stream (IS) can significantly enhance the mixing, especially micro-mixing, within extremely short time, impinging stream reaction was employed as primary process to synthesize nano-scale $FePO_4 \cdot 2H_2O$ seed crystals. Then co-precipitation method was used as secondary step. The as-synthesized $FePO_4$ precursor composites revealed hierarchical micro/nano-structured mesoporous morphology. The effects of (1) mean residence time (*t*); (2) rotation speed (*r*); (3) two-step co-precipitation method on the physical and chemical properties of FP and LFP were systematically evaluated. The as-synthesized $LiFePO_4$/C products at optimum condition showed both excellent electrochemical performance and relatively high tap density. The paper will be organised in such a way. Section 2 will present the experimental details including materials preparation, characterisation of FP, LFP and cell preparation for electrochemistry test while section 3 will present the results and discussion, focusing on the effects of various conditions on synthesis of hierarchical micro/nano-structured porous FP and LFP by using two-step co-precipitation method and conventional method. Section 4 will present the conclusions derived from the study.

5.2 Synthesis and experimental methods

5.2.1 Synthesis of Hierarchical Micro/Nano-structured porous $FePO_4$

The schematic diagram of this experimental system used for synthesis of hierarchical micro/nano-structured porous $FePO_4$ particles was shown in Figure 5-1. In the first step, $Fe(NO_3)_3 \cdot 9H_2O$ (Sinopharm Chemical Reagent Co., Ltd, 99%) and $(NH_4)_2HPO_4$ (Sinopharm Chemical Reagent Co., Ltd, 99%) were dissolved into deionized water to prepare $Fe(NO_3)_3$ (1 mol L^{-1}) and $(NH_4)_2HPO_4$ (1.0 mol L^{-1}) aqueous solutions. The pH value of $(NH_4)_2HPO_4$ was maintained at desired value by adding certain amount of ammonia solution. Then $FePO_4 \cdot 2H_2O$ seed nano-composites were synthesized by impinging stream reaction. $Fe(NO_3)_3$ (1.0 mol L^{-1}) and $(NH_4)_2HPO_4$ (1.0 mol L^{-1}) solutions were added continuously into an impinging stream reactor (ISR). The pH value of solution was maintained at 1.80 by adding ammonia solution via pH automatic controller.

For the second step, nano-scale $FePO_4 \cdot 2H_2O$ seed crystals were transferred into a continuous stirring tank reactor (CSTR) and stirred for up to 48 hours. Meanwhile, The solutions of $Fe(NO_3)_3$ (1.0 mol L^{-1}) and $(NH_4)_2HPO_4$ (1.0 mol L^{-1}) were continuously added into the reactor at a ratio of 1:1. $NH_3 \cdot H_2O$ solution (1.5 mol L^{-1}) was also pumped into the reactor and maintained the pH value of solution at 1.80 carefully. Meanwhile, the temperature was kept at 60 °C. Then hierarchical micro/nano-structured mesoporous $FePO_4 \cdot 2H_2O$ composites were generated after enough reaction time and stirring. To investigate the effects of reaction time (t) and rotation speed (r), $FePO_4$ precursors were also synthesized under precisely controlled reaction time (t = 12, 24, 36, 48 h) and stirring rate (r = 400, 800, 1200 and 1600 rpm).

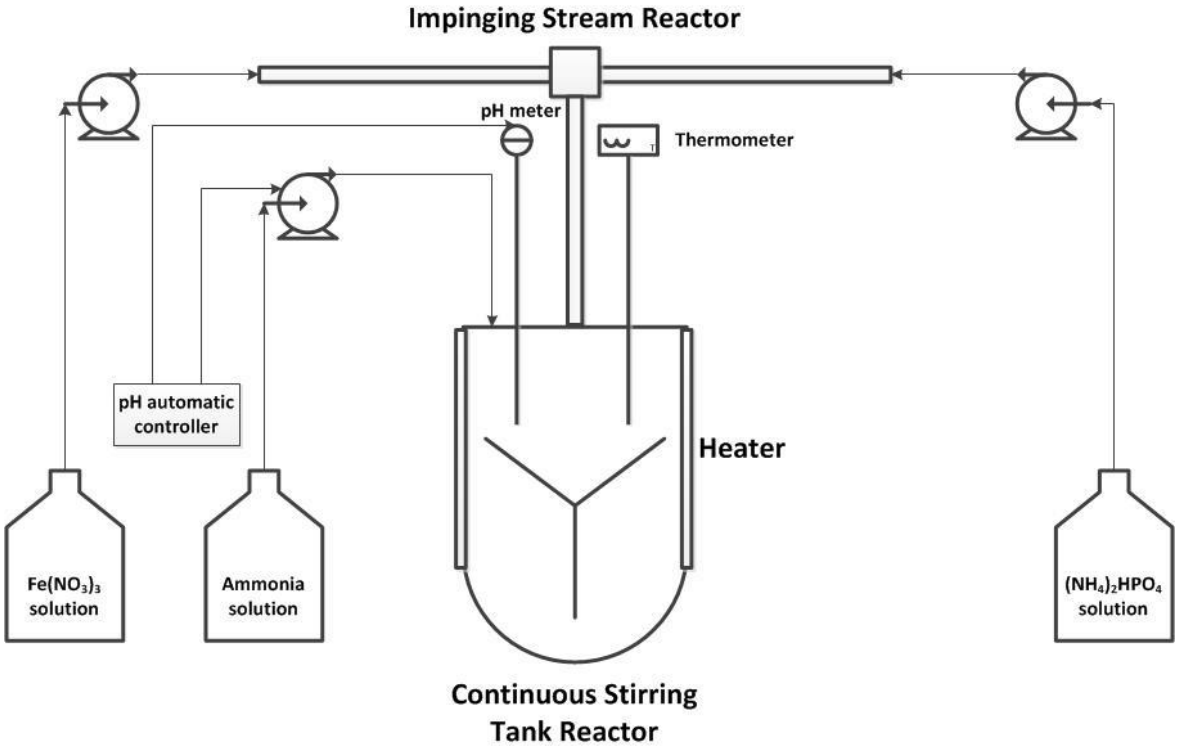

Figure 5- 1 Schematic diagram of two-step co-precipitation method.

Furthermore, $FePO_4$ precursor samples were prepared for comparison purpose by a conventional co-precipitation method. $Fe(NO_3)_3$ (1.0 mol L^{-1}) and $(NH_4)_2HPO_4$ (1.0 mol L^{-1}) solutions were added continuously into the same CSTR. The pH value of solution was also maintained at 1.80 by adding ammonia solution via pH automatic controller.

The obtained products by these two methods were subsequently washed with deionized water for three times, then filtrated and dried in air at 100 ℃ for 12 h. after that, the samples were calcined in air at 600 °C for 10 hours to obtain anhydrous crystalline $FePO_4$ samples.

5.2.2 Synthesis of $LiFePO_4$ composites

The as-synthesized $FePO_4$ samples were mixed with Li_2CO_3 (Sinopharm Chemical Reagent Co., Ltd, 99%) and glucose (Sinopharm Chemical Reagent Co., Ltd, 99%) at a desired ratio and ball-milled at 300 rpm for 6 h by a planetary ball mill, respectively. The mixtures were calcined in nitrogen atmosphere at 650 ℃ for 10 h. Then $LiFePO_4$/C composites were obtained.

The positive electrode material was consisted of as-synthesized $LiFePO_4$/C composite, acetylene black and polytetrafluoroethylene (PTFE) binder in a weight ratio of 80:10:10. The mixture was coating on an aluminum foil. After rolling and drying at 80 ℃ for 8 h. The coated aluminum was cut into circular plates. The thickness and diameter of these circular plates were 0.06 and 12 mm respectively. The loading density of $LiFePO_4$ active material was around 5.0 mg cm^{-2}. 0.1 M $LiPF_6$ dissolved in ethylene carbonate (EC)/diethyl carbonate (DEC) (1:1 volume ratio) was used as the electrolyte. Celguard 2300 microporous film was adopted as the separator. The assembly of the cells was carried out in a dry Ar-filled glove box.

5.2.3 Characterization of $FePO_4$ and $LiFePO_4$/C

The crystal structure of $FePO_4$ and $LiFePO_4$/C samples were analysed by a Bruker D8 series X-ray diffraction using Cu Kα radiation (λ=1.5406Å) operated at 40kV and 40 mA. The 2Θ was scanned from 10 degree to 70 degree (with a resolution of 0.01 degree). The surface morphology of $FePO_4$ precursor and corresponding $LiFePO_4$/C particles were observed by scanning electron microscope (Sigma VP, ZEISS, Germany). Surface area, porosity and particle size were analysed by Brunauer Emmett Teller (BET, Micromeritics ASAP 2020, U.S.A). The particle size and

distribution of $FePO_4$ precursors were measured by using laser diffraction method (Mastersizer 3000, Malvern Inc, UK). The average primary grain size of $FePO_4$ precursors were analysed by SEM images and Image J software. In terms of tap density measurement, a simple method described by Wang *et al* (2011) was employed. In this work, about 5 g of the samples were stored in 10 ml plastic centrifugal tube and tapped on the lab bench for 10 min by hand. The measured mass and volume of samples were then recorded to calculate the tap density (Wang et al., 2011). To investigate the electrochemical properties, the cells were galvanostatically charged and discharged at various rates within the voltage range of 2.5 V and 4.2 V (versus Li/Li^+) on an electrochemical test workstation (CT2001A, Wuhan LAND Electronic Co.Ltd., China). All the electrochemical tests were carried out at room temperature.

5.3 Results and Discussion

5.3.1 Effect of mean residence time

The TEM image of nanoscale $FePO_4$ precursor seeds obtained from ISR is shown in Figure 5-2. The average size of these $FePO_4$ precursor seeds were 71.27 nm. Using these nanoscale $FePO_4$ seeds, the hierarchical micro/nano-structured porous $FePO_4$ composites were synthesized in a continuous stirring tank reactor (CSTR).

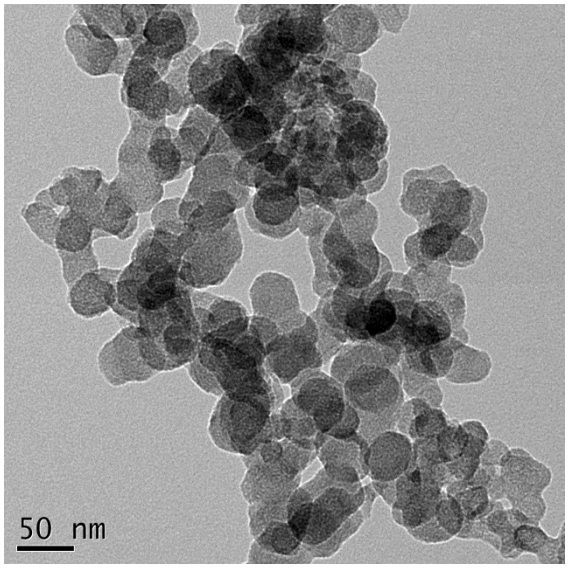

Figure 5-2 TEM image of $FePO_4$ precursor seeds synthesized by impinging stream reaction

To investigate the optimum mean residence time, the experiments were run varied from 12 to 48 hours with a rotation speed of 1600 rpm. The SEM images of $FePO_4$ precursor composites synthesized at different mean residence time were shown in Figure 5-3. While the particle size distribution results of $FePO_4$ precursor synthesized with different mean residence time are shown in Figure 5-4 and Table 5-1. There is a clear trend that the long mean residence time of particles exposure to hydrodynamic fluid shear stress leads to a more spherical shape and narrow particle size distribution (Thai et al., 2015). When the mean residence time is 12 h (as shown in Figure 5-3a), most of the $FePO_4$ precursor particles are not agglomerated together. As shown in Figure 5-4 and Table 5-2, the average particle size (Dx50) of FP-12 is 8.02 um. While the Dx10 and Dx90 of $FePO_4$ particles were 1.11 and 28.9 um respectively, indicating FP-12 precursor particles exhibit broad particle size distribution. The larger $FePO_4$ particles may be generated by the growth of initial nanoscale $FePO_4$ seeds. While the smaller $FePO_4$ particles were produced by the continuous precipitation in CSTR.

After 24 h, it is obvious to see that a large population of nanoscale $FePO_4$ precursor composites are agglomerated together and produce micro-scale $FePO_4$ particles. The average particle size reduced from 8.02 um to 2.19 um. However, FP-24 precursor particles are still broadly distributed. When increasing mean residence time to 36 h, as show in Figure 5-3c, more $FePO_4$ precursor composites with near-spherical shape and hierarchical micro/nano structure were produced. The average particle size of $FePO_4$ further decreased to 1.75 um, and the particle size distribution become much narrower. The values of Dx10 and Dx90 were 0.73 um and 10.5 um respectively. After 48 hours, the $FePO_4$ particles become larger and more spherical, the average particle size increased to 2.85 um. However, porous and hierarchical micro/nano structure cannot be observed. Thus, a longer exposure time to the hydrodynamic fluid shear flow contributed to the generation of near-spherical shape and narrow size distribution of the FP particles. But the mesoporous structure will be disappeared if the mean residence time was too long. Besides, there is a clear trend that the average primary grain size of $FePO_4$ precursor composites is increased as the increase of mean residence time. In the first 36 hours, the average primary grain size of $FePO_4$ precursor composites increase slightly, from 71.27 nm (FP-Seed) to 115.48 nm (FP-36). When the mean residence time is over 36 h, the primary grains grow rapidly and the average grain size improves to 427.94 nm after 48 h. This may be attributed to that, the new generated FP nuclei will be covered on the surface of FP particles in the continuous reaction. Thus, several primary grains may combine together and become a larger primary grain. As a result, 36 h is chosen as the optimum mean residence time because the FP-36 precursor particles exhibited the smallest average particle size, most narrow particle size distribution, and hierarchical porous micro/nano structure.

Table 5- 1 The particle size distribution and average primary grain size of $FePO_4$ precursor synthesized with different reaction time

Sample	Reaction time (hours)	Dx10 (um)	Average Particle Size (um, Dx50)	Dx90 (um)	Average Primary Grain Size (nm)
FP-Seed	0	1.79	8.33	29.1	71.27
FP-12	12	1.11	8.02	28.9	89.31
FP-24	24	0.61	2.19	13.7	95.49
FP-36	36	0.73	1.75	10.5	115.48
FP-48	48	0.62	2.85	10.0	427.94

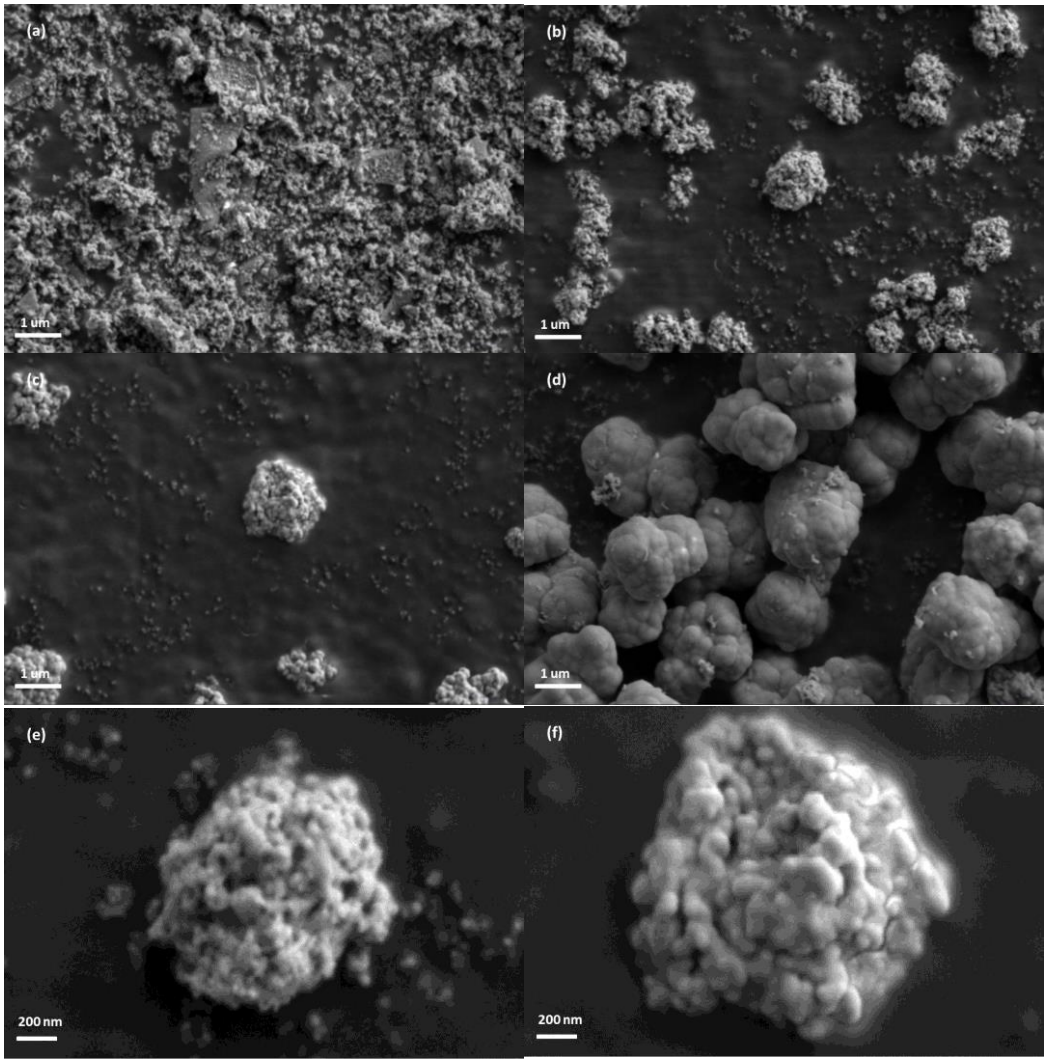

Figure 5-3 SEM images of $FePO_4 \cdot 2H_2O$ composites synthesized by different reaction time: (a) 12 h, (b) 24 h, (c) 36 h, (d) 48 h, (e) and (f) high magnification of FP-24 and FP-36.

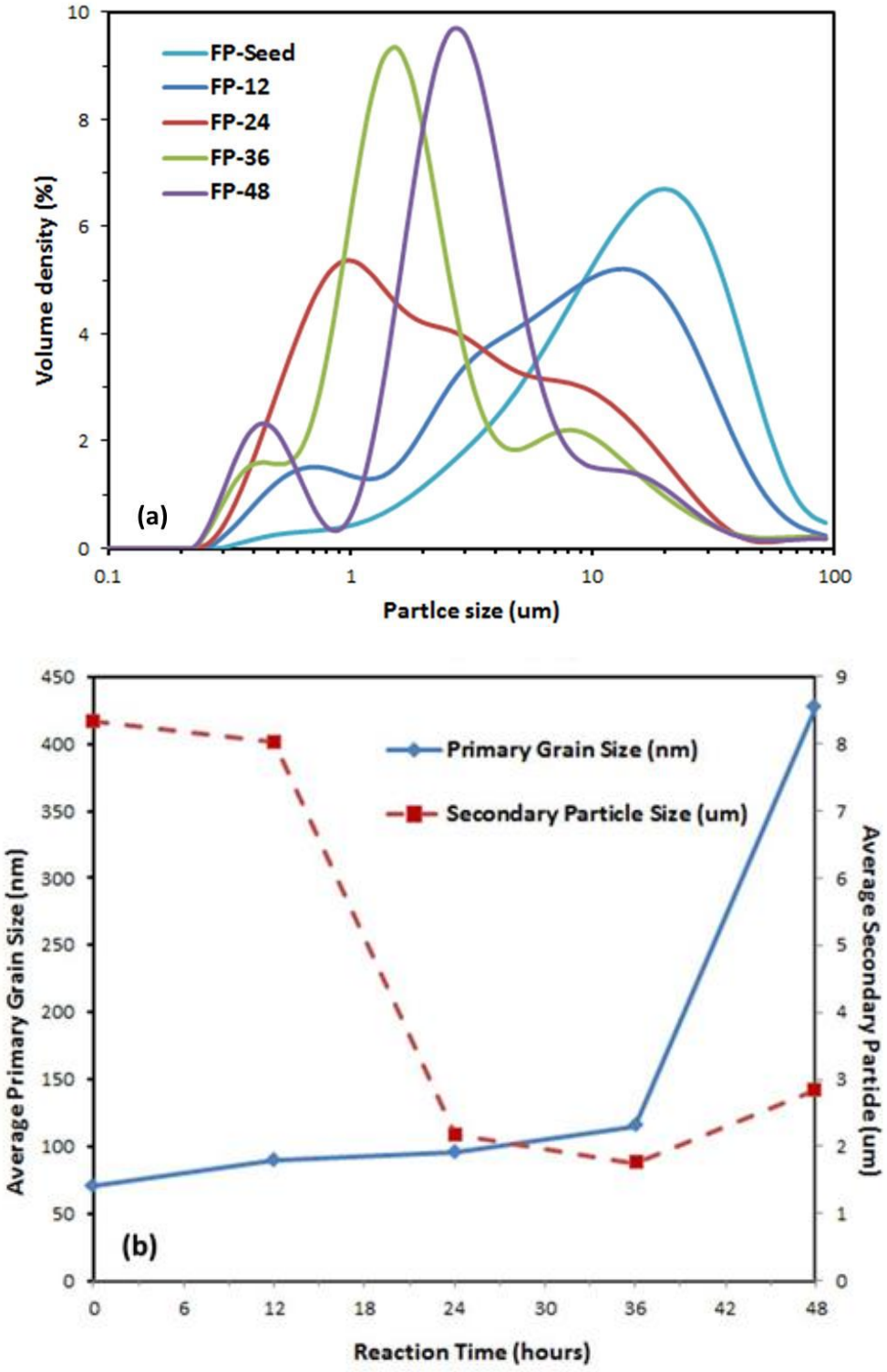

Figure 5-4 (a) Particle size distribution of $FePO_4$ precursor composites; (b) average primary grain size and secondary particle size of $FePO_4$ precursor synthesized by different reaction time

The co-precipitation process in CSTR can be divided into two main ways, including growth of core particles and homoagglomeration of new generated particles. Kim *et al* (2017) had found that particle surface charge was a critical factor to determine the interaction between particles, and the way reaction tended to happen was depended directly on the pH value of solution. The synthetic mechanism of hierarchical micro/nano-structured porous $FePO_4$ composites was shown in Figure 5-5. In this work, the objective is to synthesize $FePO_4$ precursor particles with hierarchical mesoporous micro/nano structure. Therefore, it is important to facilitate the homoagglomeration of $FePO_4$ precursor particles. Then these new generated $FePO_4$ precursor particles were used as "bridge", or "glue", and improved the interactive connection among nano-scale $FePO_4$ seeds.

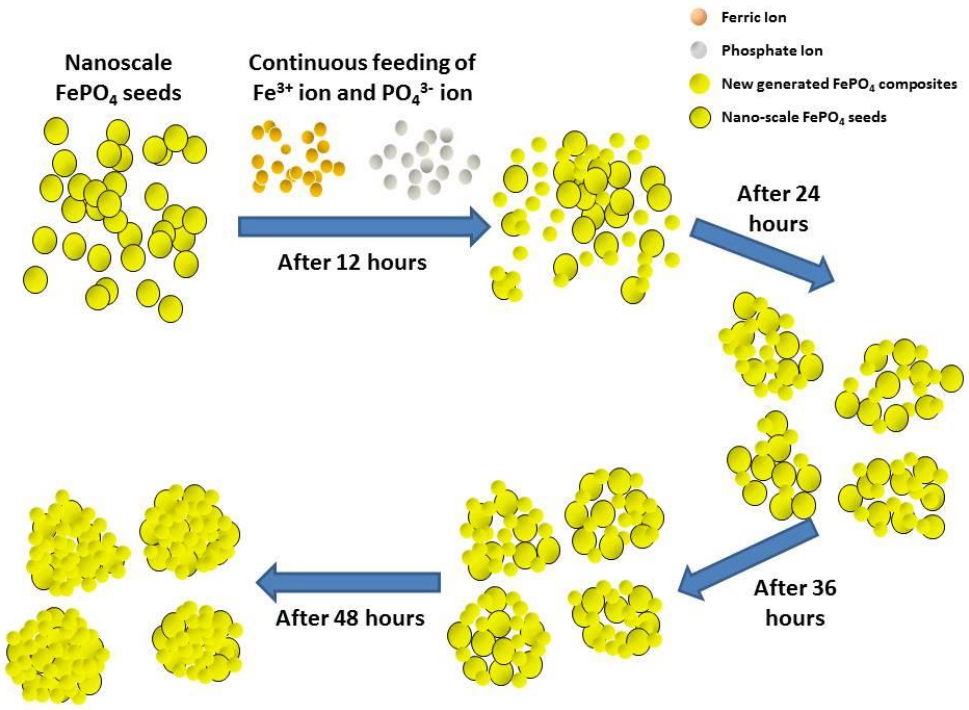

Figure 5-5 Schematic illustration of the two-step co-precipitation method

5.3.2 Effect of rotation speed

To investigate the effect of rotation speed, $FePO_4 \cdot 2H_2O$ precursors were prepared at four different rotation speed ranging from 400 to 1600 rpm. Table 5-2 and Figure 5-6 show the particle size distribution results of the $FePO_4$ precursor samples. The minimum average particle size (1.75 um) was obtained when the rotation speed of 1600 rpm was used. It is noticed that the average particle size of FP-800 and FP-1200 was almost same, but the Dx90 value of FP-1200 sample (13.3 um) is much smaller than FP-800 (16.5 um). All the results demonstrate that, as the stirring rate increased from 400 to 1600 rpm, the average particle size of $FePO_4$ precursor samples decreases remarkably, while the particle size distribution becomes narrow.

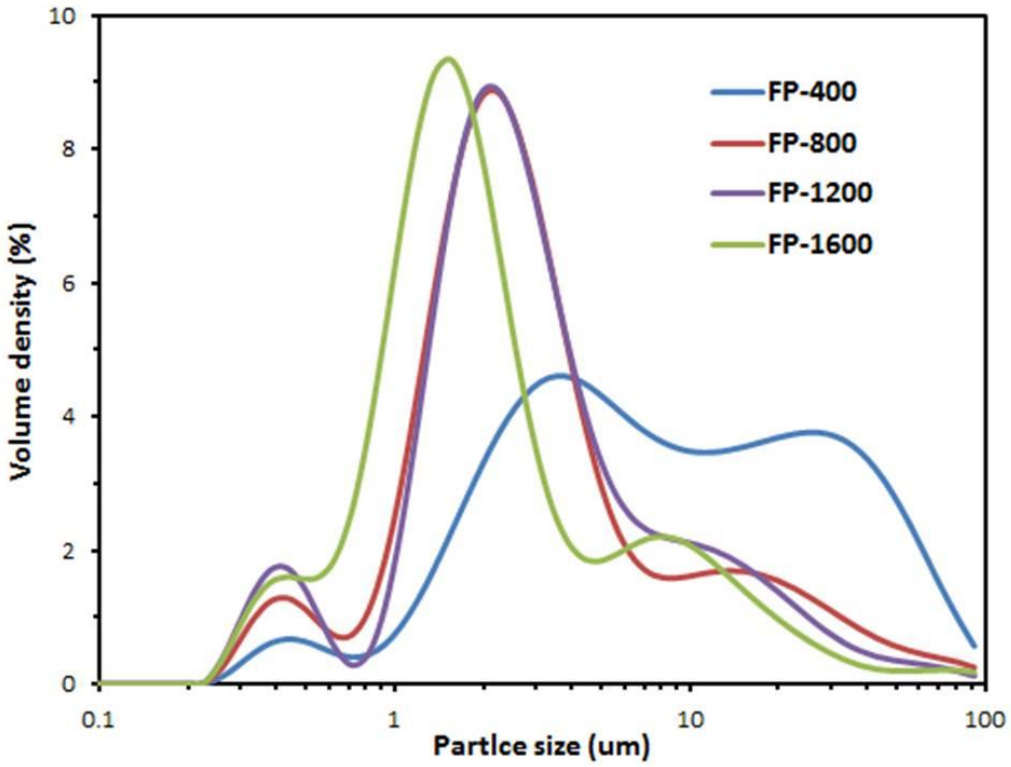

Figure 5-6 Particle size distribution of $FePO_4$ precursor composites synthesized at different stirring rate.

Table 5-2 Particle size distribution results of $FePO_4$ precursors prepared with different synthesis methods.

Samples	Dx10 (um)	Dx50 (um)	Dx90 (um)
FP-400	1.70	7.71	42.5
FP-800	1.04	2.52	16.5
FP-1200	1.05	2.57	13.3
FP-1600	0.73	1.75	10.5

Figure 5-7 shows the SEM images of $FePO_4$ precursor samples prepared at four different rotation speed. All the particles are composed of a larger number of densely appregated nanoscale primay grains with sphercal shape. As expected, the SEM analysis also indicates that an increase in the rotation speed can result in an increase of sphericity and a reduction of particle size of as-prepared $FePO_4$ precursor samples. At low rotation speed (r = 400 rpm), the as-prepared $FePO_4$ precursor sample shows irregular particle shape with broad particle size distribution. As the rotation speed is increased to 1600 rpm, uniformly near-spherical $FePO_4$ precursor particles are generated with a mean residence time of 36 h. Thus, it can be concluded that the particle shape became more spherical and the particle size distribution became narrower when increasing the rotation speed from 400 rpm to 1600 rpm. These results can be explained by the comparision among fluid shear stress, turbulent dissipation energy, and the physical interactive force between particles in CSTR.

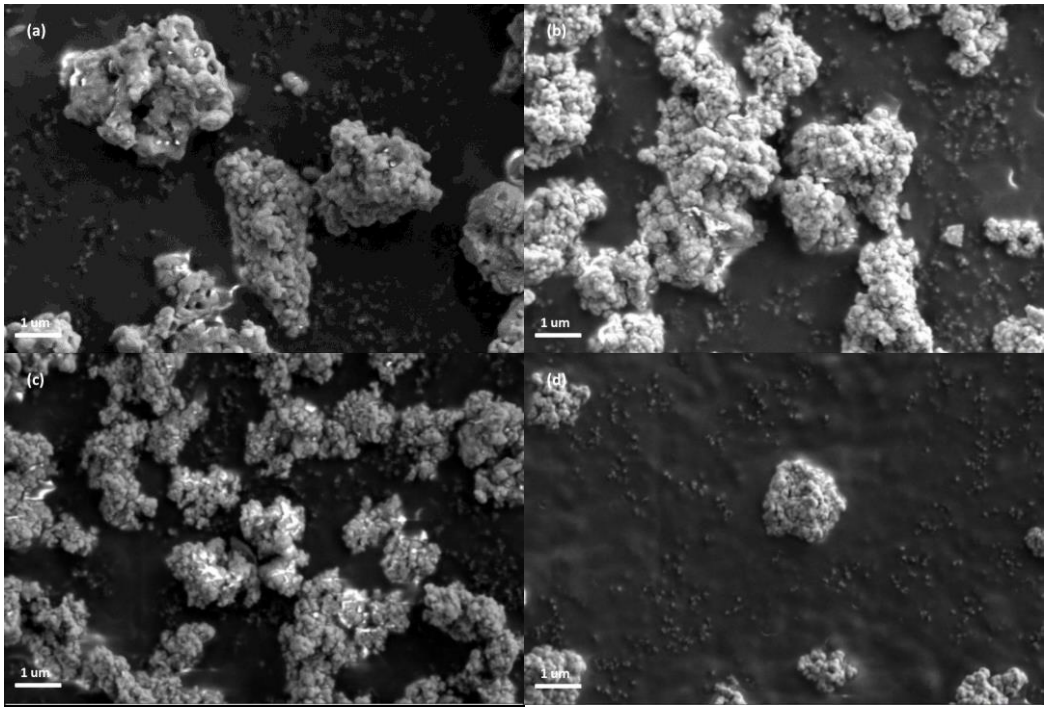

Figure 5-7 SEM images of $FePO_4 \cdot 2H_2O$ composites synthesized by different stirring rate: (a) 400 rpm, (b) 800 rpm, (c) 1200 rpm, (d) 1600 rpm.

To estimate the turbulent mixing effect in CSTR, an equation is used to describe the turbulent dissipation energy per unit mass ε [J/s·kg] (Sung *et al*., 2000):

$$\varepsilon = \frac{N_P n^3 Da^5 \rho}{g_c m} \tag{5-1}$$

where n is rotation speed (rps), Da is impeller diameter, ρ is density of reaction solution, m is mass of solution in the reactor and N_P is power number which can be correlated to the Reynolds number.

The Reynolds numbers and power number N_P can be defined as

$$Re = \frac{\rho n^2 Da^3}{\mu} \tag{5-2}$$

$$N_P = \frac{P}{\rho n^3 Da^5} \tag{5-3}$$

where μ is solution viscosity and P is the power.

Based on the turbulent dissipation energy, the Kolmogorov length λ and turbulent shear stress τ, which are the important characteristics of the turbulent mixing, can be estimated as

$$\lambda = \left(\frac{v_{ms}^3}{\varepsilon} \right)^{1/4} \tag{5-4}$$

$$\tau = u(\frac{\varepsilon}{v_{ms}})^{1/2} \tag{5-5}$$

Where v_{ms} is the kinematic viscosity of the mixed solution is defined as u/ρ and u is dynamic viscosity.

The values of these parameters for calculation are listed in Table 5-3.

Table 5-3 Experimental parameters for calculation

Density (ρ, **kg m^{-3}**)	**Viscosity** (μ, **Pa·s**)	**Impeller diameter** (Da, **m**)
1126	0.001005	0.06

Table 5-4 Reynolds number, power, turbulent dissipation energy and shear stress corresponding to the rotation speed in CSTR.

Rotation Speed (rps)	Reynolds Number	Power (W)	Turbulent Dissipation Energy (m^2/s^3)	Turbulent shear stress (τ)
6.67	1.1×10^4	1.76	0.43	0.70
13.33	4.3×10^4	8.18	2.13	1.55
20.00	9.7×10^4	15.99	4.91	2.36
26.67	1.7×10^5	23.66	7.93	3.00

The increase in the rotation speed can enhance mass transfer rate and improve collision rate. Besides, the values of turbulent energy dissipation rate ε and turbulent shear stress τ, which are shown in Table 5-4, will increase as the increasing of rotation speed. The turbulent shear stress τ influences the breakage/re-dispersion process of the aggregated particles in CSTR. At a low rotation speed (400 rpm), the shear stress is weaker than the interactive force among the aggregated primary grains. Thus the aggregated particles cannot be broke and re-dispersed, results in larger particle size and broad particle size distribution. As the increasing of rotation speed, the shear stress is increased and enough to overcome the physical interactive force. The breakage/re-dispersion process then was facilitated and exceeded agglomeration process. As a result, the particle shape become more spherical, the average particle size is decreased and the particle size distribution is narrowed. Furthermore, it is clear that the sample particles which exhibit more spherical shape and narrow particle size distribution show a higher tap density. Because the particles with spherical shape have

the smallest contact interface with other particles, the fluidic of particles is improved and the formation of bridge among particles becomes more difficult (Ying *et al*., 2001; Cho *et al*., 2005; Ying *et al*., 2004).

5.3.3 Effect of two-step methods

The effect of two-step co-precipitation method on particle morphology was investigated on optimum condition of reaction time (36 h) and stirring rate (1600 rpm). The SEM images were shown in Figure 5-8, while the results of particle size distribution were shown in Figure 5-9 and Table 5-5. As shown in Figure 5-8a, FP-IPre precursor particles with hierarchical micro/nano-structured mesoporous structure can be well synthesized by two-step co-precipitation method. The micro-sized near-spherical secondary structure of FP-Imp has an average particle size of 1.75 um, consisting of nanospheres with sizes ranging from 50 nm to 150 nm. The SEM image of FP-CoPre composites was shown in Figure 5-8b. FP-CoPre exhibited near-spherical shape with lower porosity. The average secondary particle size and primary grain size are 2.47 um and 176.6 nm respectively. The particle size distribution also became broader.

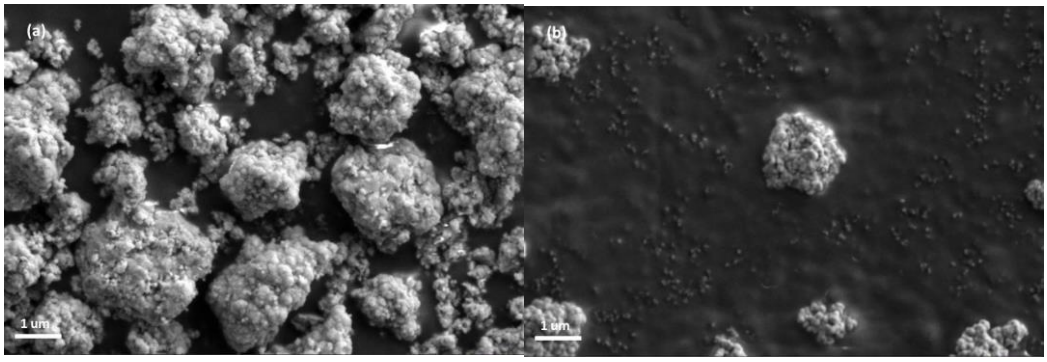

Figure 5-8 SEM images of $FePO_4 \cdot 2H_2O$ composites synthesized by different methods: (a) conventional method, (b) two-step co-precipitation.

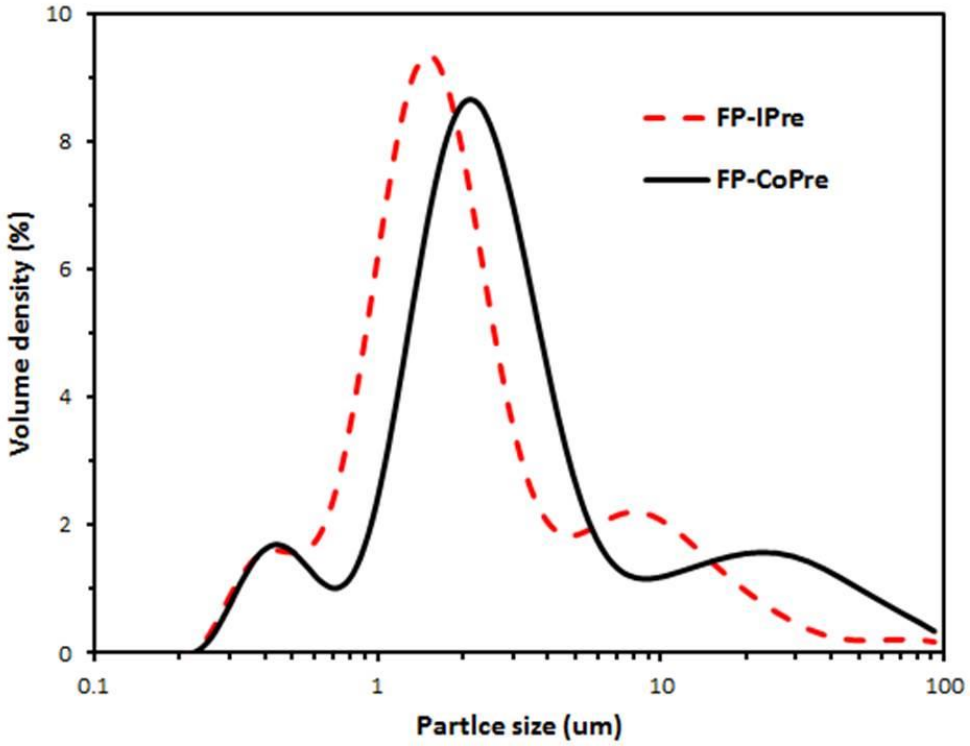

Figure 5-9 Particle size distribution of $FePO_4 \cdot 2H_2O$ composites synthesized by different synthesis method

Table 5-5 Particle size distribution results of $FePO_4$ precursors prepared by different synthesis methods.

Samples	Dx10 (um)	Average Particle Size (um, Dx50)	Dx90 (um)	Average Primary Grain Size (nm)	Surface area ($m^2 g^{-1}$)
FP-IPre	0.73	1.75	10.5	115.48	18.65
FP-CoPre	0.90	2.47	22.5	176.63	8.59

The BET specific surface area and pore size distribution of the $FePO_4$ precursors prepared by two different methods have been characterized by nitrogen adsorption-desorption analysis. The N_2 sorption isotherm of FP-IPre and FP-CoPre precursors (Figure 5-10a) were Type IV. The big hysteresis loops evidence the presence of mesopores (> 2 nm and < 50 nm). The measured BET surface area for FP-IPre and FP-CoPre precursors are 18.65 and 8.59 $m^2 g^{-1}$, respectively. The analytical results of pore size distribution based on desorption of the $FePO_4$ precursors synthesized using two different methods are shown in Figure 5-10b and c. As can be seen from the figures, both FP-IPre and FP-CoPre precursor samples feature pores in mesoporous (>2 nm and <50 nm) and macropores (> 50 nm) range. The acquirement of higher specific surface area of FP-IPre precursor is caused by the reduction of average grain size and the increase in the numbers of mesopores and macropores.

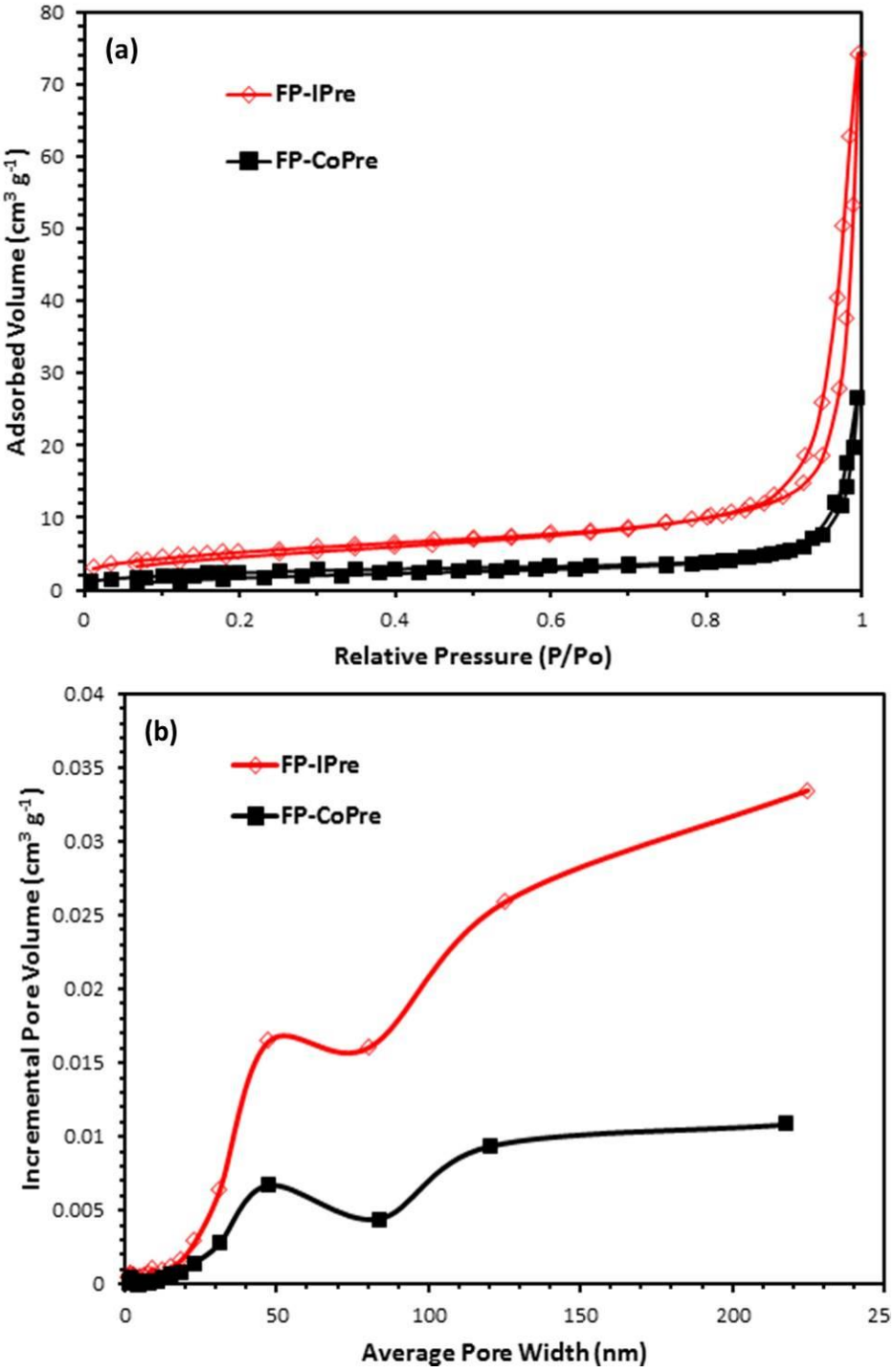
(a)
FP-IPre
FP-CoPre
Adsorbed Volume (cm3 g-1)
Relative Pressure (P/Po)
0
10
20
30
40
50
60
70
80
0
0.2
0.4
0.6
0.8
1
(b)
FP-IPre
FP-CoPre
Incremental Pore Volume (cm3 g-1)
Average Pore Width (nm)
0
0.005
0.01
0.015
0.02
0.025
0.03
0.035
0.04
0
50
100
150
200
25

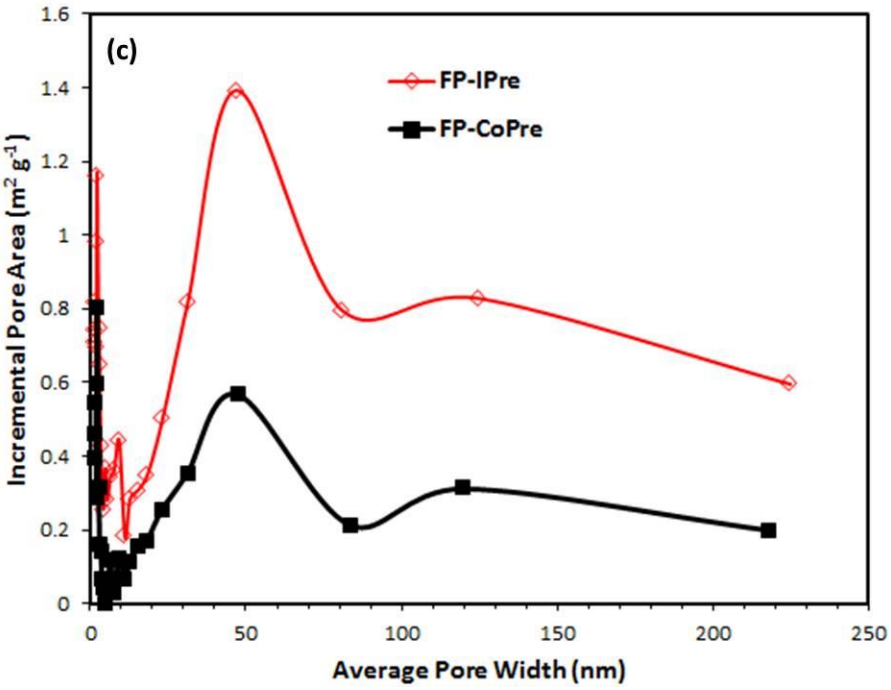

Figure 5-10 (a) N_2 adsorption-desorption isotherms of $FePO_4 \cdot 2H_2O$ composites prepared by impinging jet reaction with different feeding rate; (b) Incremental pore volume; (c) Incremental pore area

The XRD patterns of $FePO_4$ and $LiFePO_4$/C composites prepared by two different methods are shown in Figure 5-11. The XRD results of FP-IPre and FP-CoPre composites, which are pre-heated at 600 ℃ for 10 h, match well with anhydrous hexagonal structure $FePO_4$ (JCPDS card no. 29-0715, a = 5.035 Å, b = 5.035 Å, c = 11.245 Å), suggesting the formation of perfect crystalline $FePO_4$ composites after the thermal treatment. Simultaneously, it can be clearly observed that the diffraction peak intensities of FP-CoPre sample are lower than FP-IPre sample. The highest intensities of FP-CoPre and FP-IPre composites around 25.83 degree are 2475 and 2841, respectively. This may suggest that the adoption of two-step co-precipitation method can improve the crystallinity of the products. The diffraction peaks of LFP-IPre and

LFP-CoPre composites are also well indexed with $LiFePO_4$ with orthorhombic structure (JCPDS card no.40-1499, a = 10.347 Å, b = 6.019 Å, c = 4.704 Å).

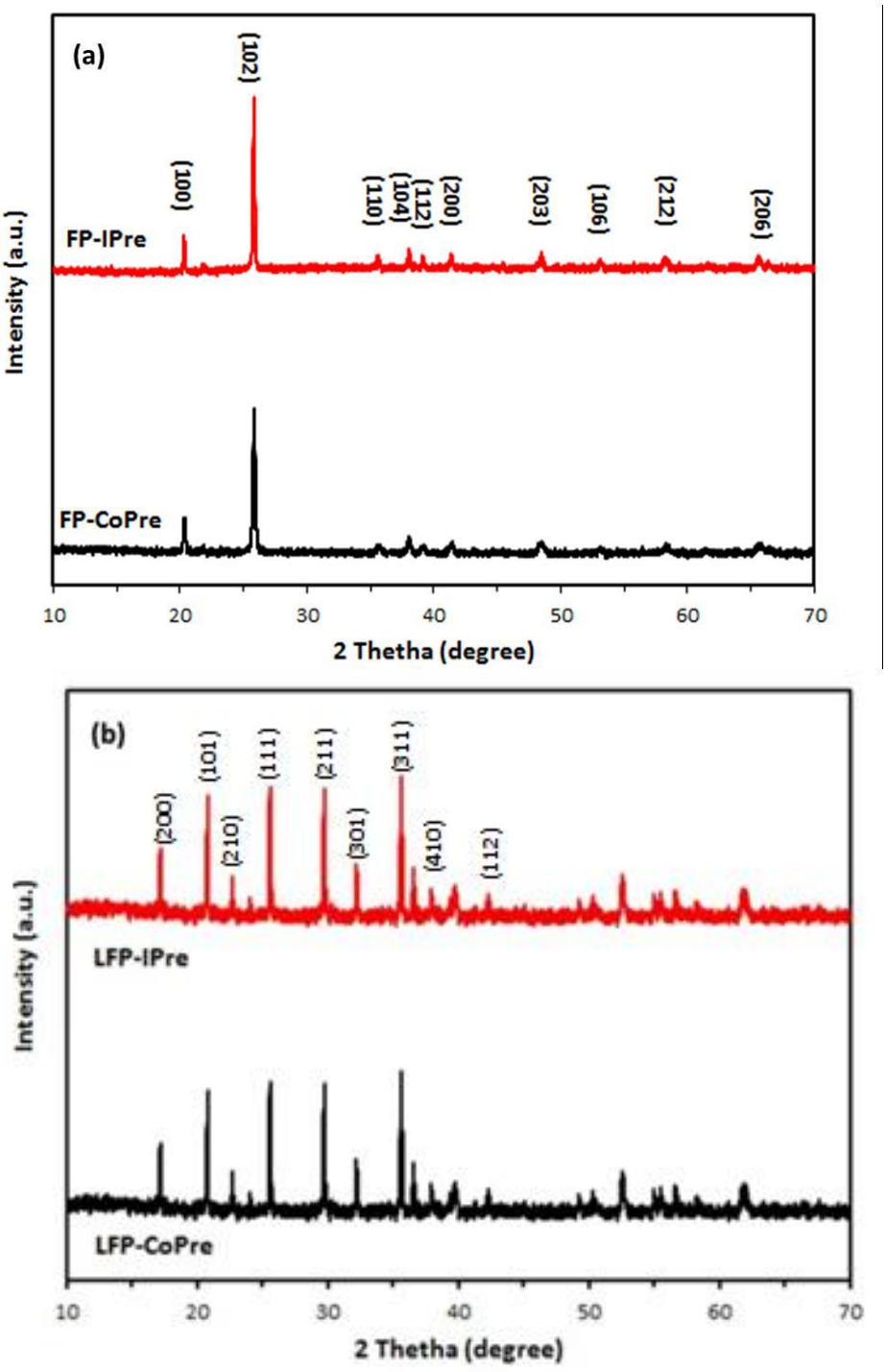

Figure 5-11 X-ray diffraction patterns of (a) $FePO_4$ and (b) $LiFePO_4$/C composites prepared by different methods.

Table 5-6 Calculated lattice parameters of as-synthesized $FePO_4$ and $LiFePO_4$/C samples

	a(Å)	b(Å)	c(Å)	V(Å^3)	Tap density (g cm^{-3})
FP-IPre	5.041	5.041	11.246	285.807	0.95
FP-CoPre	5.036	5.036	11.244	285.231	1.13
LFP-IPre	10.310	6.002	4.589	283.970	1.29
LFP-CoPre	10.336	6.006	4.697	291.580	1.50

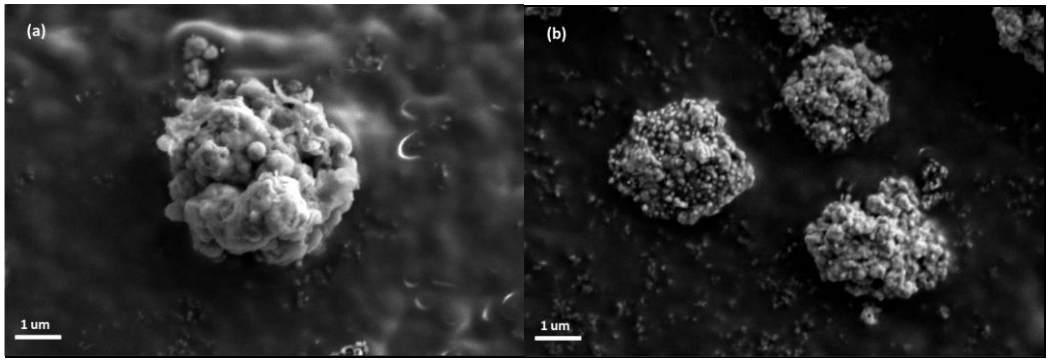

Figure 5-12 SEM images of $LiFePO_4$/C composites synthesized by different methods: (a) LFP-CoPre, (b) LFP-IPre.

The SEM images of $LiFePO_4$/C composites prepared by two different methods are shown in Figure 5-12. As the morphology of $LiFePO_4$/C was affected by the precursor significantly, the LFP-CoPre sample has near-spherical shape and features micro-scale secondary structure with lower porosity. LFP-IPre sample (Figure 5-12b) also presents near spherically shaped particles. Comparing to LFP-CoPre, LFP-IPre composites exhibit smaller secondary particle size with higher porous structure.

The electrochemical characterization of $LiFePO_4$/C prepared by different methods is shown in Figure 5-13 and Table 5-7. The LFP-IPre presents better discharge capacities from 0.1 to 5 C. The average discharge capacity of LFP-IPre is 145.6, 133.7, 118.0, 103.7, and 85.7 mAh g^{-1} at a rate of 0.1 C, 0.5 C, 1 C, 2 C and 5 C, respectively. For LFP-CoPre, the average discharge capacity can reach 120.2, 113.3, 101.3, 91.8, and 73.9 mAh g^{-1} at a rate of 0.1 C, 0.5 C, 1 C, 2 C and 5 C, respectively. The improved rate capacities can be attributed to the smaller primary grain size, enlarged specific surface area and mesoporous secondary structure. Generally, a larger specific surface area helps increase the interface between electrode and electrolyte, and provide an effective charge transfer across the interface. A reduced primary grain size helps shorten the diffusion distance of Li^+ ion, resulted in an improved electrochemical performance for $LiFePO_4$ active materials. Meanwhile, mesoporous structure can facilitate the penetration of electrolyte and improve the electronic conductivity. For cycling capability, LFP-IPre exhibited 127.7 and 132.4 mAh g^{-1} at 1^{st} and 100^{th} cycle. Similarly, the discharge capacities at 1^{st} and 100^{th} cycle of LFP-CoPre sample were 112.9 and 117.1 mAh g^{-1}. The improved cycle ability can be attributed to less side reaction. Additionally, micro-sized near-spherical secondary particle can maintain a relatively higher tap density (1.29 g cm^{-3}). Thus, for FP-IPre precursor, its hierarchical mesoporous micro/nano-structure can facilitate the electrolyte penetration, improve the electronic conductivity and guarantee a relatively higher tap density and volumetric density of the resulting LFP- IPre sample.

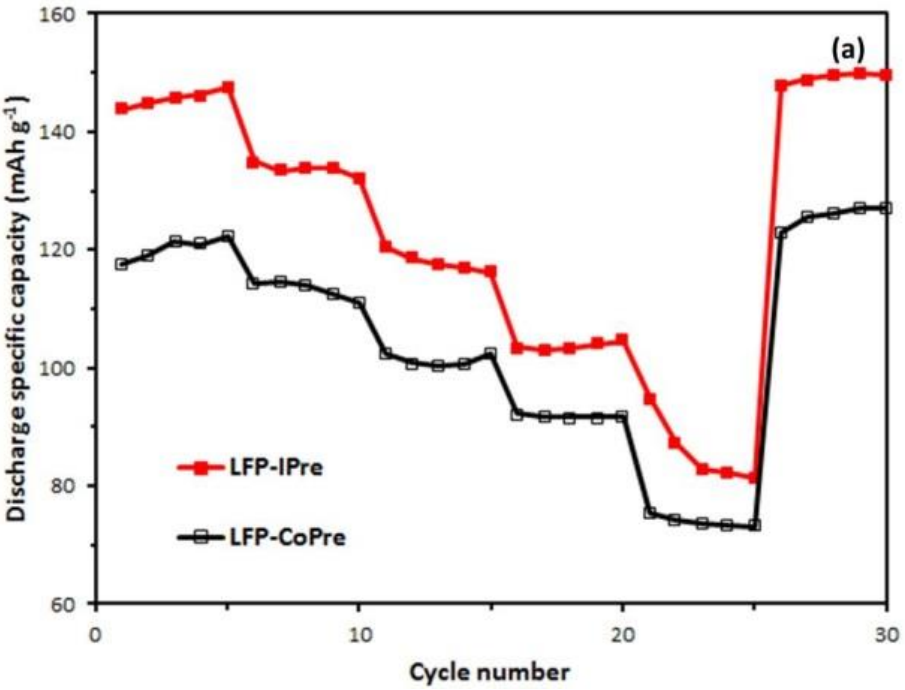
(a)
Discharge specific capacity (mAh g-1)
160
140
120
100
80
60
0
10
20
30
Cycle number
LFP-IPre
LFP-CoPre

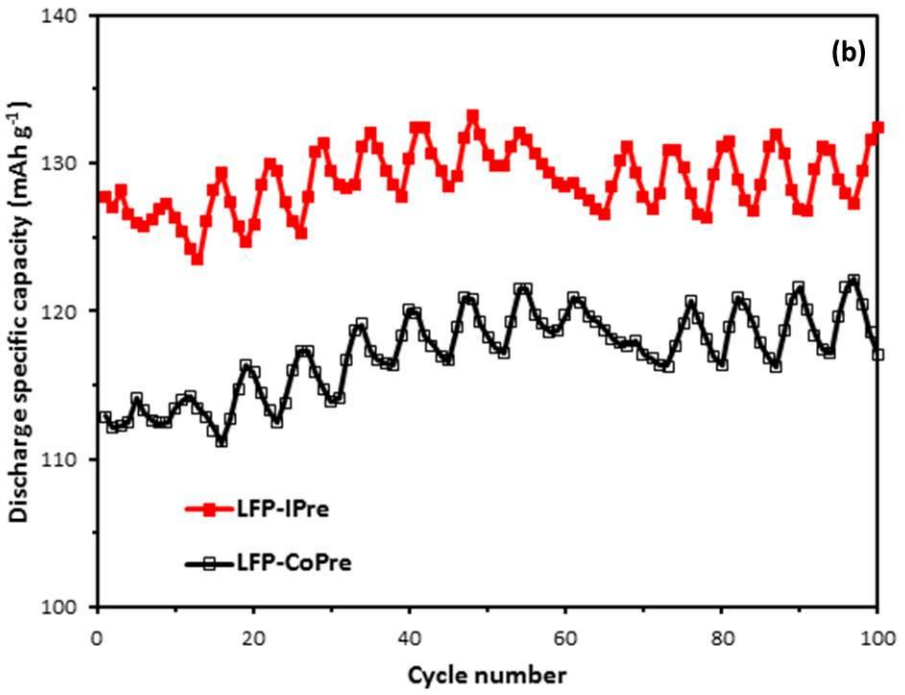
(b)
Discharge specific capacity (mAh g-1)
140
130
120
110
100
0
20
40
60
80
100
Cycle number
LFP-IPre
LFP-CoPre

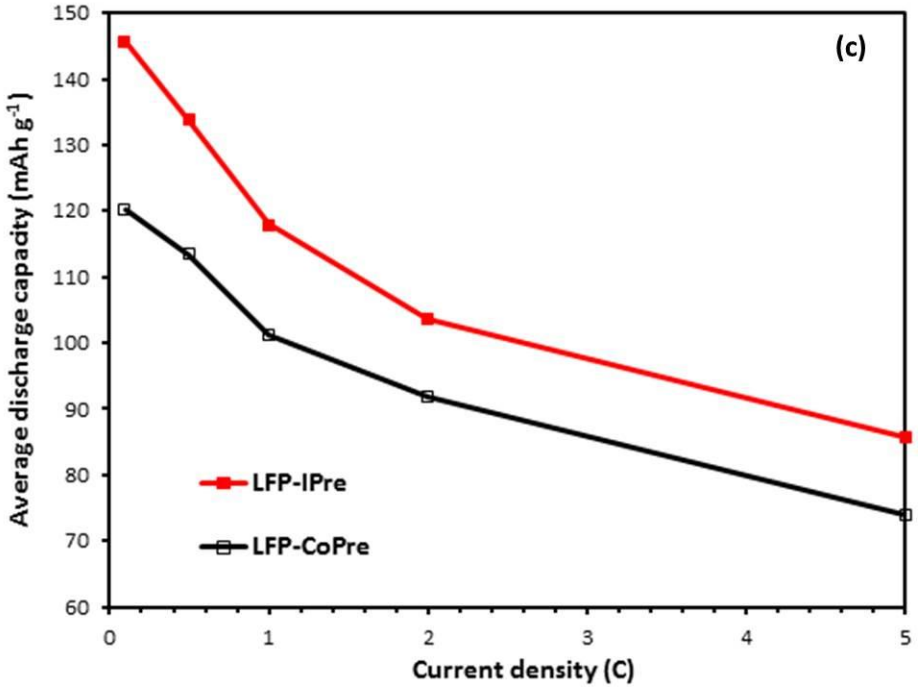

Figure 5-13 Electrochemical performance of $LiFePO_4$/C composites synthesized with different methods: (a) Rate performance at various rates, (b) Cycling performance at 0.5 C for 100 cycles, (c) Average rate capability.

Table 5-7 The comparison of electrochemical performance of the $LiFePO_4$/C synthesized by two-step co-precipitation method and conventional method.

Sample	Cycle performance at 0.5 C (mAh g^{-1})			Average Rate Performance (mAh g^{-1})				
	1st cycle	100th cycle	R_1[a](%)	0.1 C	0.5 C	1 C	2 C	5 C
LFP-IPre	127.7	132.4	103.7	145.6	133.7	118.0	103.7	85.7
LFP-CoPre	112.9	117.1	103.7	120.2	113.3	101.3	91.8	73.9

5.4 Conclusion

In this work, hierarchical micro/nano-structured porous $FePO_4$ precursor and $LiFePO_4$/C samples were synthesized by utilising two-step co-precipitation method under precisely controlled reaction time and stirring rate. The results showed that, in contrast to the $LiFePO_4$/C synthesized by conventional co-precipitation method, the $LiFePO_4$/C composites prepared by two-step co-precipitation method exhibited both excellent electrochemical performance and relatively high tap density. The excellent electrochemical performance can be attributed to the large specific surface area, mesoporous structure and nanoscale primary grains which can shorten the diffusion pathway of Li^+. And the relatively high tap density of $LiFePO_4$ was guaranteed by the micro-sized near-spherical secondary structure. It is thus concluded that two-step co-precipitation technology will be promising synthesis method for the preparation of $LiFePO_4$ composites for energy storage. The conclusions reached as the results of the current study are as follows:

(1) The proceeding of experiment leads to the decrease of primary gains size, increase of secondary particle size, and reduction of particle size distribution. However, over-increase in the mean residence time would have negative impact. Both primary grain size and secondary particle size were increased dramatically, and mesoporous structure was disappeared when the reaction time is more than 36 hours.

(2) For two-step co-precipitation method, increase in the rotation speed can narrow particle size distribution and improve sphericity of $FePO_4$ precursor particles due to the facilitation of breakage/re-dispersion process which is caused by enhanced hydrodynamic shear stress.

(3) The $LiFePO_4$/C composites synthesized by two-step co-precipitation method exhibit hierarchical mesoporous micro/nano-structure, resulting in both improved electrochemical performance and relatively higher tap density and volumetric density

References

1. Ding Y., Jiang Y., Xu F., Yin J., Ren H., Zhuo Q., Long Z., and Zhang P., 2010, Preparation of nano-structured $LiFePO_4$/graphene composites by co-precipitation method, Eletrochemistry Communication, 12, 10-13

2. Park K.S., Son J.T., Chung H.T., Kim S.J., Lee C.H., and Kim H.G., 2003, Synthesis of $LiFePO_4$ by co-precipitation and microwave heating. Electrochemistry Communications, 5, 839-842

3. Padhi K., Nanjundaswamy K. S., Masquelier C., Okada S., and Goodenough J. B., 1997, Effect of structure on the Fe^{3+}/Fe^{2+} redox couple in iron phosphates., Journal of the Electrochemistry Society, 144, 1609-1613

4. Xiang,W., Wu Z.G., Wang E.H., Chen M.Z., Song Y., Zhang J.B., Zhong Y.B., Chou S.L., Luo J.H., and Guo X.D., 2016, Confined synthesis of graphene wrapped $LiMn_{0.5}Fe_{0.5}PO_4$ composite via two step solution phase method as high performance cathode for Li-ion batteries. Journal of Power Sources, 329, 94-103

5. Naik A., Zhou J., Gao C., Liu G.Z., and Wang L., 2016, Rapid and facile synthesis of Mn doped porous $LiFePO_4$/C from iron carbonyl complex. Journal of the Energy Institute, 89, 21-29

6. Shu H., Wang X., Wu Q., Hu B., Yang X., Wei Q., Liang Q., Bai Y., Zhou M., Wu C., Chen M., Wang A., and Jiang L., 2013, Improved electrochemical performance of $LiFePO_4$/C cathode via Ni and Mn co-doping for lithium-ion batteries, Journal of Power Sources, 237, 149-155

7. Wang H., Yang Y., Liang Y., Cui L., Casalongue H.S., Li Y., Hong G., Cui Y., and Dai H., 2011, $LiMn_{1-x}Fe_xPO_4$ nanorods grown on graphene sheets for ultrahigh-rate-performance lithium ion batteries. Angewandte Chemie, 123, 7502-7506.

8. Ying J., Lei M., Jiang C., Wan C., He X., Li J., Wang L., Ren J., 2006, Preparation and characterization of high-density spherical $Li_{0.97}Cr_{0.01}FePO_4$/C cathode material for lithium ion batteries. Journal of Power Sources, 2006, 543-549

9. Shin H.C., Park S.B., Jang H., Chung K.Y., Cho W., Kim C.S., and Cho B.W., 2008, Rate performance and structural change of Cr-doped $LiFePO_4$/C during cycling, Eletrochimica Acta, 53, 7946-7951

10. Wang Y., Wang Y., Hosono E., Wang K., and Zhou H., 2008, The design of a $LiFePO_4$/carbon nanocomposite with a core-shell structure and its synthesis by an in situ polymerization restriction method. Angewandte Chemie International Edition, 47, 7461-7465

11. Sun C.S., Zhang Y., Zhang X.J. and Zhou Z., 2010, Structural and electrochemical properties of Cl-doped $LiFePO_4$/C. Journal of Power Sources, 195, 3680-3683

12. Hong J., Wang Y., He G., and He M., 2012, A new approach to $LiFePO_4$/C synthesis: The use of complex carbon source without ball milling. Materials Chemistry and Physics, 133, 573-577

13. Hsieh C., Chen I., Chen W., and Wang J., 2012, Synthesis of iron phosphate powders by chemical precipitation route for high-power lithium iron phosphate cathodes. Electrochimica Acta, 83, 202-208

14. Zhu Y., Tang S., Shi H., and Hu H., 2014, Synthesis of $FePO_4 \cdot xH_2O$ for fabricating submicrometer structured $LiFePO_4$/C by a co-precipitation method. Ceramics International, 40, 2685-2690

15. Qian L., Xia Y., Zhang W., Huang H., Gan Y., Zeng H., and Tao X., 2012, Electrochemical synthesis of mesoporous $FePO_4$ nanoparticles for fabricating high performance $LiFePO_4$/C cathode materials. Microporous and Mesoporous Materials, 152, 128-133

16. Arnold G., Garche J., Hemmer R., Strobele S., Vogler C., Wohlfahrt-Mehrens M., 2003, Fine-particle lithium iron phosphate $LiFePO_4$ synthesized by a new low-cost aqueous precipitation technique. Journal of Power Sources, 119-121, 247-251

17. Ni J.F., Zhou H.H., Chen J.T., and Zhang X.X., 2005, $LiFePO_4$ doped with ions prepared by co-precipitation method. Materials Letters, 59, 2361-2365

18. Liu H., Miao C., Meng Y., Xu Q., Zhang X. and Tang Z., 2014, Effect of graphene nanosheets content on the morphology and electrochemical performance of $LiFePO_4$ particles in lithium ion batteries, Eletrochimica Acta, 135, 311-318

19. Shi Y., Chou S., Wang J., Wexler D., Li H., Liu H. and Wu Y., 2012, Graphene wrapped $LiFePO_4$/C composites as cathode materials for Li-ion

batteries with enhanced rate capability. Journal of Materials Chemistry, 22, 16465-16470

20. Bai N., Chen H., Zhou W., Xiang K., Zhang Y., Li C., and Lu H., 2015, Preparation and electrochemical performance of $LiFePO_4$/C microspheres by a facile and novel co-precipitation. Electrochimica Acta, 167, 172-178

21. Han D., Ryu W., Kim W., Lim S., Kim Y., Eom J., and Kwon H., 2013, Tailoring crystal structure and morphology of $LiFePO_4$/C cathode materials synthesized by heterogeneous growth on nanostructured $LiFePO_4$ seed crystals. ACS Applied Materials & Interfaces, 5, 1342-1347

22. Whittingham M.S., Lithium Batteries and Cathode Materials. Chemical Review, 2004. 104: p. 4271-4301.

23. Vu A., Qian Y., and Stein A., 2012, Porous electrode materials for lithium-ion batteries - how to prepare them and what makes them special, Advanced Energy Materials, 2, 1056-1085

24. Wang, K.X., Li X.H., and Chen J.S., 2015, Surface and interface engineering of electrode materials for lithium-ion batteries. Advanced Materials, 27, 527-545.

25. Wang, M., Yang Y., and Zhang Y., 2011, Synthesis of micro-nano hierarchical structured $LiFePO_4$/C composite with both superior high-rate performance and high tap density. Nanoscale, 3, 4434-4439.

26. Thai D.K., Mayra Q.P., and Kim W.S., 2015, Agglomeration of Ni-rich hydroxide crystals in Taylor vortex flow. Powder Technology, 274, 5-13

27. Kim J.E. and Kim W.S., 2017, Synthesis of Core–Shell Particles of Nickel–Manganese–Cobalt Hydroxides in a Continuous Couette-Taylor Crystallizer. Crystal Growth & Design, 17, 3677-3686

28. Sung M.H., Choi I.S., Kim J.S., Kim W.S., 2000, Agglomeration of Yttrium Oxalate Particles Produced by Reaction Precipitation in Semi-Batch Reactor. Chemical Engineering Science, 55, 2173-2184

29. Ying J., Wan C., Jiang C., and Li Y., 2001, Preparation and characterization of high-density spherical $LiNi_{0.8}Co_{0.2}O_2$ cathode material for lithium secondary batteries. Journal of Power Sources, 99, 78-84.

30. Cho T.H., Park S.M., Yoshio M., Hirai T., and Hideshima Y., 2005, Effect of synthesis condition on the structural and electrochemical properties of $Li(Ni_{1/3}Mn_{1/3}Co_{1/3})O_2$ prepared by carbonate co-precipitation method. Journal of Power Sources, 142, 306-312

31. Ying, J., Jiang C., and Wan C., 2004, Preparation and characterization of high-density spherical LiCoO2 cathode material for lithium ion batteries. Journal of Power Sources, 129, 264-269.

CHAPTER 6: Controllable Synthesis of $(NH_4)Fe_2(PO_4)_2(OH)\cdot 2H_2O$ Using Two-Step Route: Ultrasonic-intensified Impinging Stream Pre-treatment Followed by Hydrothermal Treatment

SUMMARY

In Chapter 5, two-step co-precipitation method has been employed to prepare $LiFePO_4$ particles with hierarchical micro/nano structure. In this chapter, we introduce a two-step hydrothermal method, and investigate the effect of different parameters on the preparation of $FePO_4$ particles. $(NH_4)Fe_2(PO_4)_2(OH)\cdot 2H_2O$ and $FePO_4$ samples with different morphology are successfully synthesized via two-step synthesis route - ultrasonic-intensified impinging stream pre-treatment followed by hydrothermal treatment (UIHT) method. The effects of the adoption of ultrasonic-intensified impinging stream pre-treatment, reagent concentration (*C*), pH value of solution and hydrothermal reaction time (*T*) on the physical and chemical properties of the synthesised $(NH_4)Fe_2(PO_4)_2(OH)\cdot 2H_2O$ composites and $FePO_4$ particles were systematically investigated. Nano- seeds were firstly synthesized using the ultrasonic-intensified T-mixer and these nano-seeds were then transferred into a hydrothermal reactor, heated at 170 ℃ for 4 hours. The obtained samples were characterized by utilising XRD, BET, TG-DTA, SEM, TEM, Mastersizer 3000 and FTIR, respectively. The experimental results have indicated that the particle size and morphology of the obtained samples are remarkably affected by the use of ultrasonic-intensified

impinging stream pre-treatment, hydrothermal reaction time, reagent concentration, and pH value of solution. When such $(NH_4)Fe_2(PO_4)_2(OH)\cdot 2H_2O$ precursor samples were transformed to $FePO_4$ products after sintering at 650℃ for 10 hours, the SEM images have clearly shown that both the precursor and the final product still retain their monodispersed spherical microstructures with similar particle size of about 3 μm when the samples are synthesised at the optimised condition.

6.1 Introduction

$(NH_4)Fe_2(PO_4)_2(OH)\cdot 2H_2O$ is an isopytic mineral of $KFe_2(PO_4)_2OH\cdot 2H_2O$ (leucophosphite) and has received increasing attentions due to its magnetic properties and rich crystal chemistry (Trobajo *et al*., 2000). The synthetic $(NH_4)Fe_2(PO_4)_2(OH)\cdot 2H_2O$ has been considered as a promising material and applied in the fields of catalysts (Bonnet *et al*., 1996), magnetics (Cavellec *et al*., 1997; Zhou *et al*., 2010), optics (Cao *et al*., 2010), and lithium ion battery as positive electrode material (Ju *et al*., 2013; Li *et al*., 2014; Reale *et al*., 2003). As a functional material, the physical and chemical properties of $(NH_4)Fe_2(PO_4)_2(OH)\cdot 2H_2O$ are significantly affected by its morphology and particle size. Many methods have been developed to prepare $(NH_4)Fe_2(PO_4)_2(OH)\cdot 2H_2O$ particles, and various efforts are endeavoured to conduct the synthesis for different morphologies and particle sizes.

Shaowen Cao *et al*. (2010) proposed a simple one-step microwave-solvothermal ionic liquid method using $[BMIM][BF_4]$ to prepare $(NH_4)Fe_2(PO_4)_2(OH)\cdot 2H_2O$ composites that contained various nanostructures, such as solid micro-spheres, microspheres with the core in the hollow shell, and double-shelled hollow microspheres while the synthesis was conducted by adjusting reagent concentration and microwave heating

time (Cao *et al*., 2010). Pure and well-crystallized spheniscidite $(NH_4)Fe_2(PO_4)_2(OH)\cdot 2H_2O$ was obtained by Delacourt *et al.* when NH_3 was added as an agent to raise pH value (Reale *et al*., 2003). Ju *et al*. (2013) reported a low temperature (at 80 ℃) hydrothermal method to synthesize peanut-like microscale $(NH_4)Fe_2(PO_4)_2(OH)\cdot 2H_2O$ particles that were used as the precursor of $LiFePO_4$ positive electrode material. The as-synthesized $LiFePO_4$ composites presented desirable electrochemical performance and high tap density. Li *et al.* (2014) synthesized ellipsoid-shaped $(NH_4)Fe_2(PO_4)_2(OH)\cdot 2H_2O$ composites that have micro-nano structures for being used as the precursor of $LiFePO_4$ positive electrode material, adopting a facile chemical precipitation route. The obtained $LiFePO_4$ products exhibited excellent rate capability and good cyclic performance. Trobajo *et al.* (2000) applied the hydrothermal method for preparation of $(NH_4)Fe_2(PO_4)_2(OH)\cdot 2H_2O$ at relatively high pH values of 9-11 and used excess amount of urea. Kaipeng Wu *et al*. (2018) adopted sonochemical method to synthesise $(NH_4)Fe_2(PO_4)_2(OH)\cdot 2H_2O$ particles that possess red-blood-cell-like shape. In addition, Zhou *et al*. (2010) also used hydrothermal method to synthesise $(NH_4)Fe_2(PO_4)_2(OH)\cdot 1.5H_2O$ which exhibited the behaviour of spontaneous magnetization below 25 K. It can be claimed that as a self-assembly synthesis approach, hydrothermal method has been widely used to design and fabricate $(NH_4)Fe_2(PO_4)_2(OH)\cdot 2H_2O$ particles due to its mild operation temperature, simple process, homogeneous particle size distribution, improved cycle life and has the potential for large-scale production (Liang *et al*., 2008; Liu *et al.,* 2015). However, most of the synthesis route still needs long reaction time (up to 3 days) and additional additives (such as glycol and $C_2H_4O_4\cdot 2H_2O$).

It has been recognised that the application of high intensity ultrasonic-irradiation has a remarkable function which can significantly intensify the processes. It has been applied in industrial manufacturing process and also the material synthesis process with the features of cost-effective and environmental-friendly. It has been revealed that the particles synthesised using ultrasonic treatment usually present porous structures (Suslick and Price, 1999; Xu *et al*., 2013). Since ultrasonic wave can acoustically create the tiny cavitation, such instantaneous collapse of the created micro bubbles due to cavitation can provide the extreme conditions in a very small volume, characterised by occurrence of extremely high temperature up to 5000K, pressures up to 1000 atm, and the heating and cooling rate greater than 10^{10} Ks^{-1} inside the cavitation zone (McNamara *et al*., 1999). Thus, ultrasonic-assisted hydrothermal synthesis method has been applied to the synthesis of catalysts (Moradiyan *et al*., 2017; Khan *et al*., 2017; Li *et al*., 2010; Ezeh *et al*., 2018), zeolite (Su *et al*., 2016; Jusoh *et al*., 2017; Mu *et al*., 2017; Askari and Halladj, 2012), hydrogen storage material (Roy and Das, 2017), and MOFs (Azad *et al*., 2016).

Adoption of confined impinging T-jet mixer (CITJ) for synthesis of micro particles was also reported in the open literatures (Andreussi *et al*., 2015; Krupa *et al*., 2014). A CITJ reactor which has T-shaped branches is the simplest component that contains two inlet tubes, allowing two streams to flow in, and one outlet tube, allowing the mixture to be collected. Local intensive micro-mixing in a CITJ takes place through the collision between two impinging streams, usually resulting in a fast homogenization of reactants so that both mass transfer rate and chemical reaction rate can be effectively enhanced. The kinetic energy and mass transfer rate in the mixing zone (reactor chamber) are influenced by the pressure fluctuation while the intensive

mixing occurring in a small confined volume of reaction chamber enhances the crystallisation and promotes the growth of particle size (Huang *et al*., 2015; Siddiqui *et al*., 2009).

A novel two-step preparation route that combines ultrasound-assisted CITJ and hydrothermal treatment (UIHT) to synthesize $(NH_4)Fe_2(PO_4)_2(OH)\cdot 2H_2O$ is developed in the present study. To the best of our knowledge, the application of UIHT method to synthesis of $(NH_4)Fe_2(PO_4)_2(OH)\cdot 2H_2O$ has not been reported in the literature. The effects of the use of ultrasonic-intensified impinging streams, reagent concentration, pH value of solution, and hydrothermal reaction time on the chemical and physical properties of the synthesised particles are systematically investigated. The possible nucleation and particle growth mechanisms are discussed in detail. This paper will be organised in such a way. Section 2 presents the experimental details including materials preparation and characterisation. Section 3 discusses the effects of various conditions on properties of samples while the main conclusions reached as the result of the study will be given in Section 4.

6.2 Experimental

6.2.1 Materials preparation

The main procedures of two-step hydrothermal synthesis of $(NH_4)Fe_2(PO_4)_2(OH)\cdot 2H_2O$ and $FePO_4$ samples are shown in Figure 6-1. The experimental set-up of ultrasonic-intensified T-mixer and internal structure of T-mixer are shown in Figure 6-2. Nano-seeds were synthesized with ultrasonic-intensified T-mixer (see Figure 6-2a) in the first step, labelled as Seed-UIHT. Thereafter iron nitrate solution and diammonium phosphate solution (C= 0.5, 1.0 and

1.5 mol L^{-1}, respectively) were injected continuously and separately into an T-mixer from two inlets by using two peristaltic pumps (BT100FJ, Baoding Chuangrui Ltd, China) to precisely control flow rates at 85.74 ml min^{-1}. Meanwhile, the T-mixer was connected and irradiated by a FS-600pv horn type ultrasonic wave piezoelectric vibrator (600 W, 13 mm in diameter) with 20 kHz. The inlet ports of T-mixer were connected to two stainless steel tubes with an inner diameter of 2.5 mm. The inner diameter and length of internal chamber in the T-mixer are 3.5 mm and 17 mm, respectively. The outlet of the T-mixer which had the same diameter as the impinging stream inlets and an enlarged channel (with an inner diameter of 4 mm) was interconnected to the inner chamber of the T-mixer. The mixed solution was then transferred into a 500 ml glass beaker and vigorously stirred for 5 mins after the impinged mixing was conducted in the ultrasonic-intensified T-mixer under room temperature of 20 °C. In this step, the pH value of solution was maintained, respectively, at the given value (pH=0.8, 1.2, 1.5, and 1.8) but was added the ammonia solution (1.5 mol L^{-1}) carefully through a pH automatic controller. After that, the obtained mixture was transferred and sealed in a 100 ml Teflon-lined stainless steel autoclave, heated at 170 ℃ for up to 4 hours. The mixture was then removed from the autoclave, naturally cooling to the room temperature. The obtained samples were washed with deionized water for several times, followed by using a vacuum filter to separate the products and to dry at 80℃ overnight. These samples were labelled as Prod-UIHT. Then the as-synthesized products were calcined at 650 °C for 10 hours in the air. Such obtained product was labelled as ProdC-UIHT.

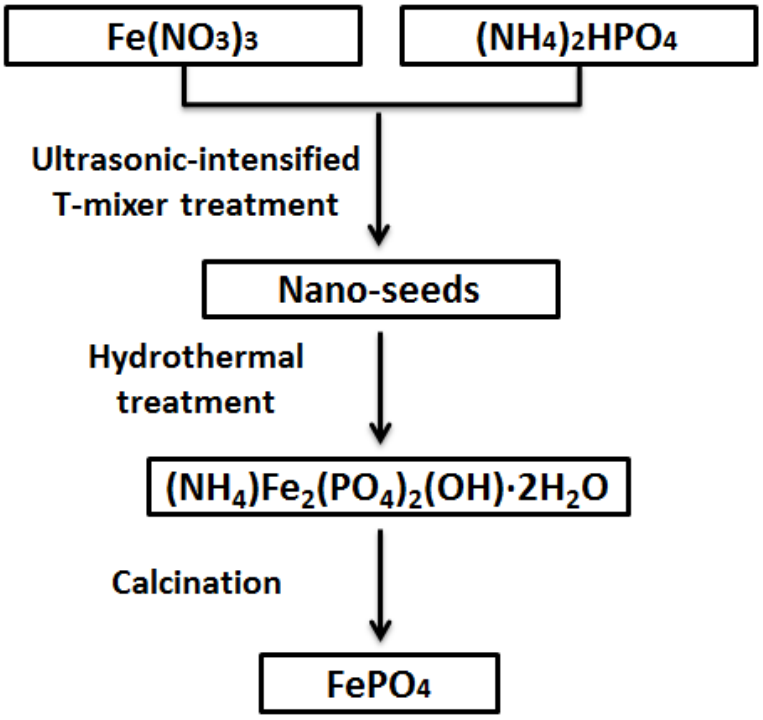

Figure 6-1 Schematic illustration of main procedures in two-step hydrothermal synthesis of $(NH_4)Fe_2(PO_4)_2(OH)\cdot 2H_2O$ and $FePO_4$ samples

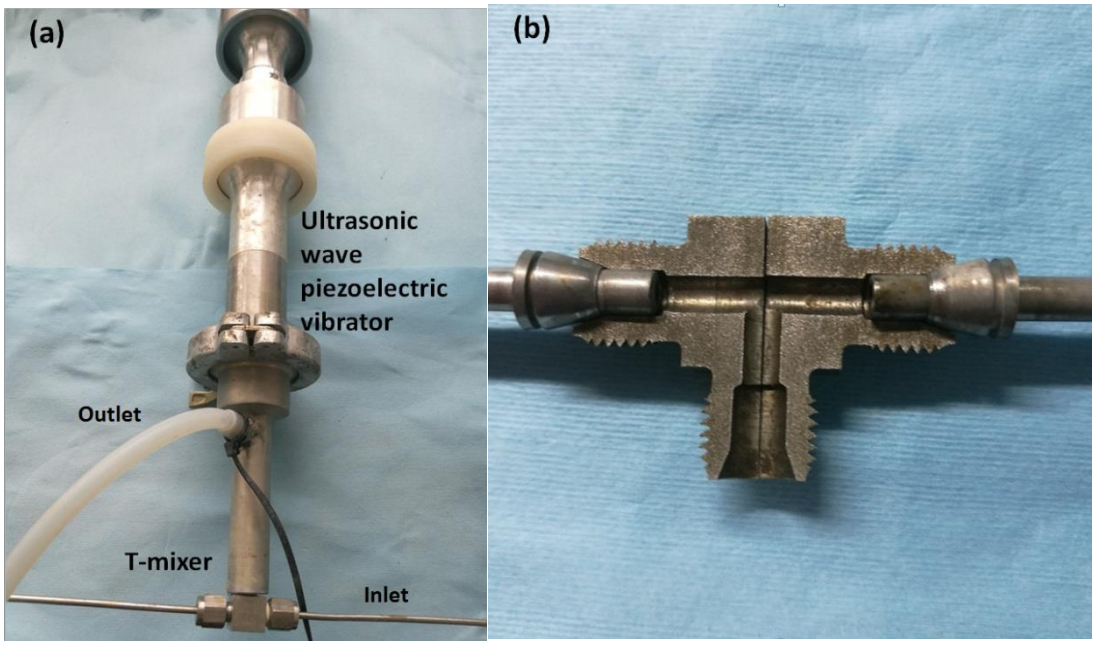

Figure 6-2 (a) Experimental set-up of ultrasonic-intensified T-mixer and (b) internal structure of T-mixer

For the comparison purpose, the samples were also prepared by adopting the conventional hydrothermal method. $Fe(NO_3)_3$ and $(NH_4)_2HPO_4$ solutions (1.0 mol L^{-1}) were directly added into a 100 ml Teflon-lined stainless steel autoclave, heated at 170 ℃ for up to 4 hours. The seeds, products, and the calcined products were labelled as Seed-HT, Prod-HT, and ProdC-HT, respectively. The conditions of different experiments are shown in Table 6-1.

6.2.2 Characterization

The crystal structure of samples was analysed using a Bruker D8 series X-ray diffraction by setting Cu Kα radiation (λ=1.5406Å). Thermogravimetric characteristics was measured by simultaneous thermal analyser (TG, NETZSCH STA 449 F3 Jupiter, Germany) at a heating rate of 10 ℃ min^{-1} in the air, varying from the room temperature to 700 ℃. The surface morphology of the obtained particles was observed by scanning electron microscope (Sigma VP, ZEISS, Germany) and transmission electron microscope (Tecnai F20, FEI, U.S). The particle size and distribution of the precursors were measured by using the laser diffraction method (Mastersizer 3000, Malvern Inc, UK). Surface area and porosity were analysed by Brunauer Emmett Teller (BET, Micromeritics ASAP 2020, U.S.A). The infrared spectra was recorded on a Fourier transform infrared spectroscopy (FTIR, Bruker V70, U.S.A) using the KBr disk technique.

Table 6- 1 Dimensions of experiments for the synthesis of samples

Experiments	Samples	Method	Reaction time (h)	pH value	Reagent concentration (*C*, mol L^{-1})
S1	Seed-UIHT	UIHT	0	0.8	1.0
S2	Prod-UIHT	UIHT	4	0.8	1.0
S3	Seed-HT	HT	0	0.8	1.0
S4	Prod-HT	HT	4	0.8	1.0
S5	UIHT-1h	UIHT	1	0.8	1.0
S6	UIHT-2h	UIHT	2	0.8	1.0
S7	UIHT-3h	UIHT	3	0.8	1.0
S8	UIHT-0.5	UIHT	4	0.8	0.5
S9	UIHT-1.5	UIHT	4	0.8	1.5
S10	UIHT-pH1.2	UIHT	4	1.2	1.0
S11	UIHT-pH1.5	UIHT	4	1.5	1.0
S12	UIHT-pH1.8	UIHT	4	1.8	1.0

6.3 Results and Discussions

6.3.1 Effect of Ultrasonic-intensified Impinging Stream Pre-treatment

The XRD patterns of the as-synthesized samples prepared by different hydrothermal methods are shown in Figure 6-3. It can be seen from the figure that the XRD pattern of Prod-HT sample was well matched with monoclinic $FePO_4 \cdot 2H_2O$ (PDF #33-0666, space group P21/n, with lattice parameters a = 0.5329 nm, b = 0.9798 nm, and c = 0.8710 nm). It is noted that that the obtained sample exhibits the same crystalline phase as that was reported by Wang *et al* (2011). Meanwhile, the XRD pattern of Prod-UIHT sample matches well with $(NH_4)Fe_2(PO_4)_2(OH) \cdot 2H_2O$ with spheniscidite structure (PDF #41-0593, space group P21/n, with lattice parameters a = 0.9750 nm, b = 0.9630 nm, and c = 0.9700 nm).

Figure 6-3b shows the XRD patterns of the as-synthesized samples after sintering at 650 ℃ for 10 hours. The major peaks of ProdC-HT sample are indexed to $FePO_4$ (PDF #29-0715, space group P321, with lattice parameters a = 0.5035 nm, b = 0.5035 nm, and c = 1.1245 nm), while the reflection peaks of $Fe_3(PO_4)_2(OH)_2$ (PDF #14-0310, space group P41212, with lattice parameters a = 0.74 nm, b = 0.74 nm, and c = 1.281 nm, which can be used as the catalyst or precursor of positive electrode material (Vedrine, 2000; Millet and Vedrine, 2001; Chen *et al*., 2014), which can be also observed in the XRD patterns. For the XRD patterns of ProdC-UIHT sample, only the reflection peaks of $FePO_4$ can be observed, indicating that the purity of decomposed $FePO_4$ sample can be further improved when using the two-step hydrothermal method. In addition, as can be seen from Table 6-2, unit volumes of Prod-HT and Prod-UIHT are 453.73 and 915.13 $Å^3$ respectively. After calcination process, the unit volume of

ProdC-HT increases to 701.73 $Å^3$, while the unit volume of ProdC-UIHT decreases to 285.53 $Å^3$. This indicates that the sample cells are affected by temperature significantly.

The reason is that, during ultrasonic irradiation, large amount of H· and OH· was generated by the sonolysis of water, which may form H_2 and H_2O_2 (Riesz *et al*., 1985; Suslick, 1990). Thus, H_2O_2 can assist to effectively avoid the reduction of Fe^{3+} during hydrothermal reaction. The main reactions in hydrothermal reaction can be assumed to follow the following steps:

$$H_2O \rightarrow H\cdot + OH\cdot$$

$$H\cdot + H\cdot \rightarrow H_2$$

$$OH\cdot + OH\cdot \rightarrow H_2O_2$$

$$H\cdot + OH\cdot \rightarrow H_2O$$

$$2Fe^{2+} + H_2O_2 + 2H\cdot \rightarrow 2Fe^{3+} + 2H_2O$$

Table 6-2 Calculated lattice parameters of as-synthesized samples prepared by two different methods.

Samples	a(Å)	b(Å)	c(Å)	V(Å^3)
Prod-HT	5.3254	9.8325	8.6653	453.73
Prod-UIHT	9.8229	9.6208	9.6835	915.13
ProdC-HT	7.4118	7.4118	12.7739	701.73
ProdC-UIHT	5.0321	5.0326	11.2750	285.53

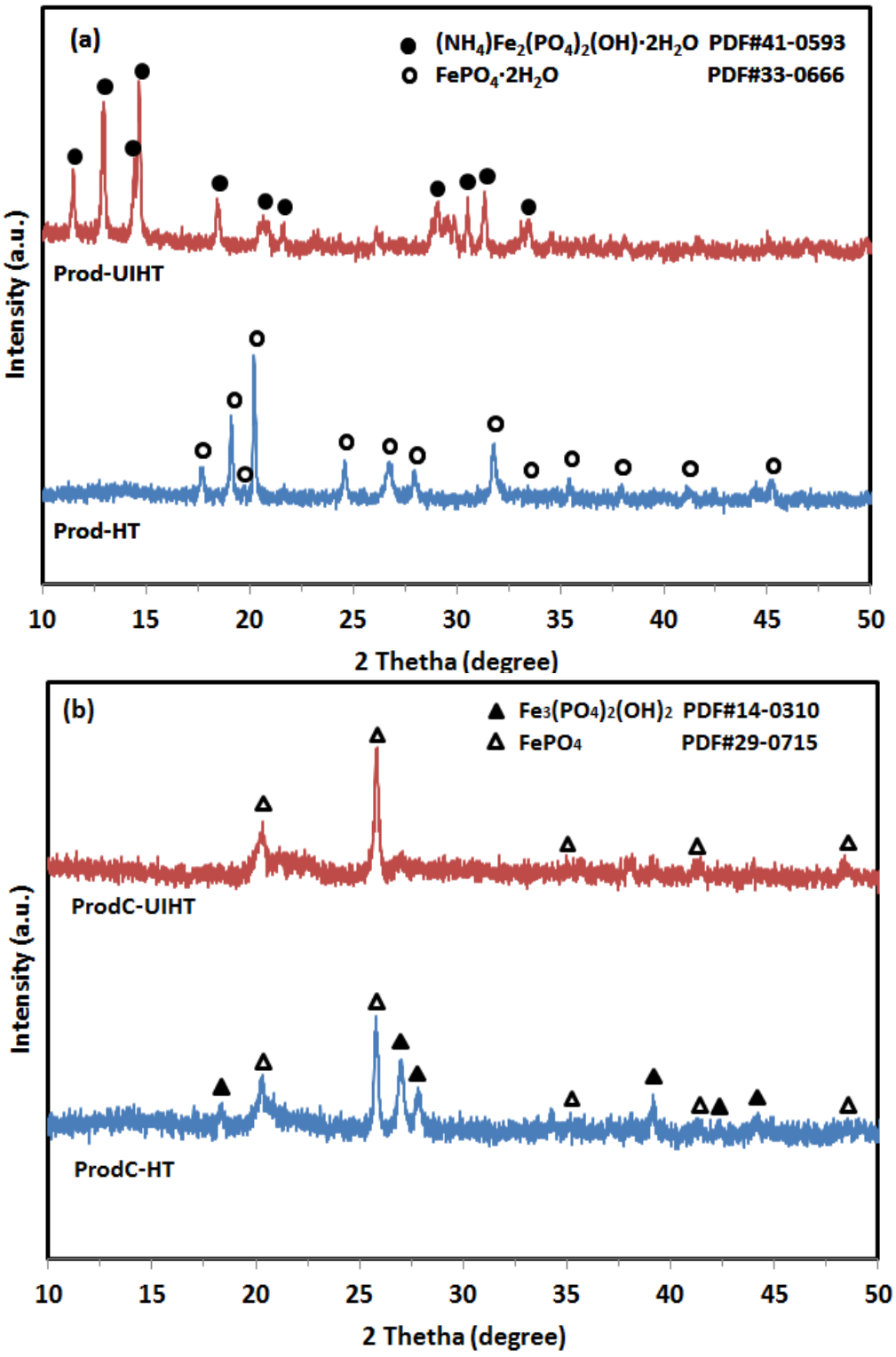

Figure 6-3 XRD patterns of samples prepared when *C*=1.0 mol L^{-1} and pH=0.8: (a) as-synthesized precursors (b) obtained products after sintering process prepared by different methods.

To investigate the presence of all bands corresponding to as-synthesized samples, FTIR spectra is shown in Figure 6-4. For Prod-UIHT sample, the absorption peaks confirm the presence of PO_4^{3-} functional group, including v_4 (O-P-O) double band of 574 and 597 cm^{-1}, v_3 (P-O) band of 1042 cm^{-1}, v_2 (O-P-O) band of 456 cm^{-1}, and v_1 (P-O) band of 996 cm^{-1} (Wang *et al*., 2014; Zhang *et al*., 2015; Shen *et al*., 2016). The stretching vibration at 1420 cm^{-1} can be attributed to the presence of NH_4^+. The occurrence of wide bands around 1629 and 3332 cm^{-1} indicates the presence of v (OH) in H_2O molecules in $(NH_4)Fe_2(PO_4)_2(OH)\cdot 2H_2O$ (Bonnet *et al*., 1996; Wu *et al*., 2018; Amer *et al*., 2014). The FTIR spectra of Prod-HT samples look similar, but the amplitude is weaker than those for Prod-UIHT sample. The difference is that stretching vibration of NH_4^+ cannot be observed in the spectra. After experiencing calcination process, the FTIR spectra of ProdC-HT sample is still at the same position, but become narrower and sharper than its precursor. For ProdC-UIHT sample, the absorption peaks at 1420 cm^{-1} and 3332 cm^{-1} in the spectra disappear, indicating the removal of NH_4^+ and H_2O in decomposed $FePO_4$ product. In addition, as both the position and intensity of the vibration in FTIR spectra can be influenced by chemical bonds and content (Garcia-Romero and Suarez, 2006), the removal of NH_4^+ and H_2O also leads to the increased intensity of FTIR spectra for ProdC-HT.

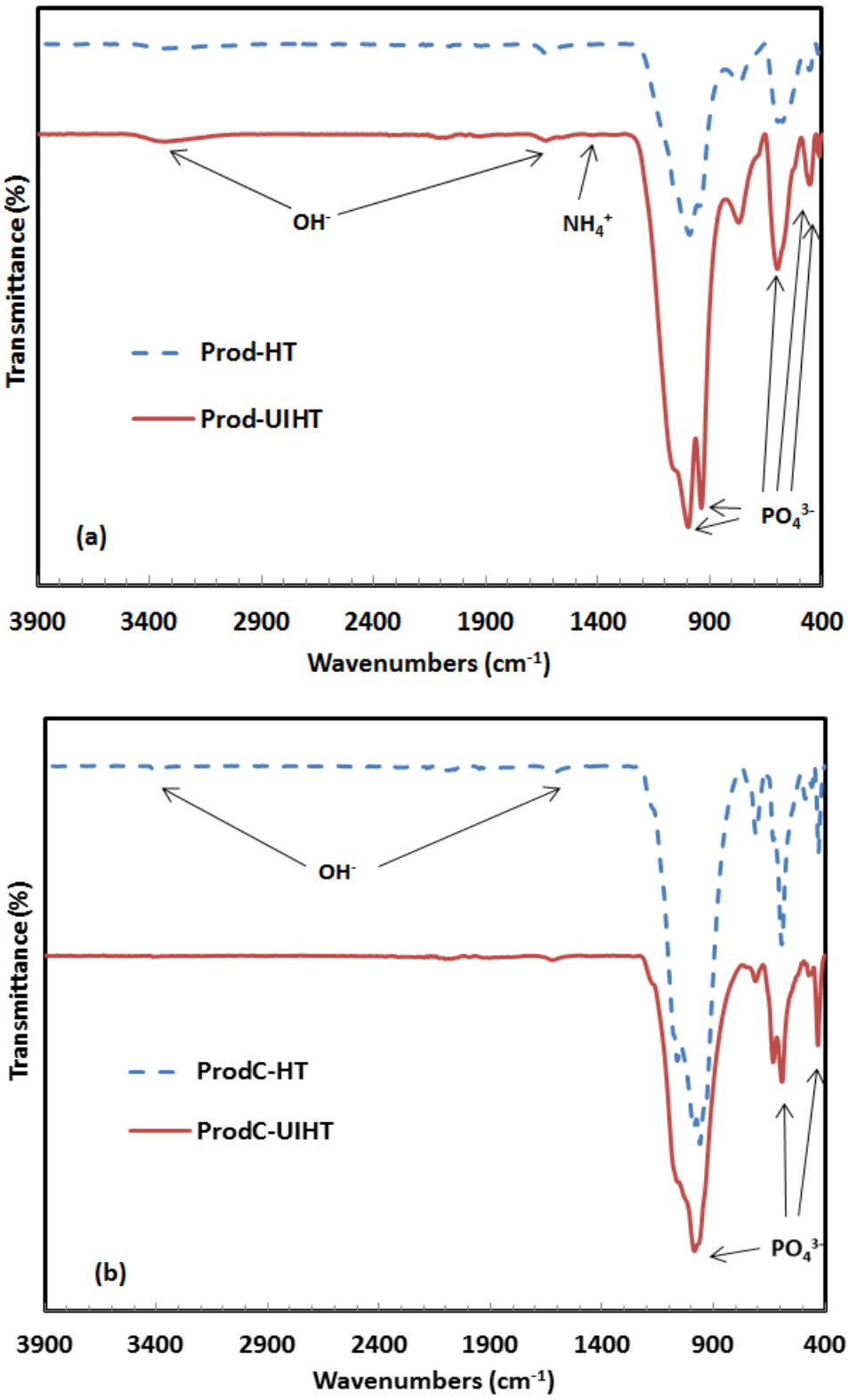

Figure 6-4 FTIR patterns of samples prepared when *C*=1.0 mol L^{-1} and pH=0.8: (a) as-synthesized precursors (b) obtained products after sintering process.

The TGA-DTG, and DTA curves of Prod-UIHT and Prod-HT are shown in Figure 6-5. It can be seen clearly from the figure that there exist three main weight loss stages as shown in Figure 6-5a. In the temperature range from 50℃ to 150 ℃, a weight loss of 2 wt% can be attributed to the removal of physical water. The second main weight loss stage takes place in the range of 150℃ to 350℃, where a weight loss of 4 wt% can be related to the elimination of coordinated water molecules. The third main weight loss of 7 wt%, occurring at the temperature ranging from 350 ℃ to 630 ℃ and peaking at appropriate 410℃, is corresponding to the decomposition of NH_4^+ and OH^-. The TGA-DTG curves of Prod-HT are shown in Figure 6-5b. It can be observed from the figure that there is one main weight loss step in the range from 100 ℃ to 200 ℃, which may be attributed to the removal of coordinated water molecules. Furthermore, a total mass loss of 19% indicates that there are two water molecules in one monoclinic $FePO_4 \cdot 2H_2O$ molecules. The DTA curves obtained from the characterisation of Prod-UIHT and Prod-HT samples are shown in Figure 6-5c. The DTA curves of two samples look the same during physical water removal process (varying from the room temperature to 120℃). It has been observed that an endothermic peak in the DTA curve of Prod-HT occurs at 175℃, corresponding to the removal of two water molecules from one $FePO_4 \cdot 2H_2O$ molecules (endothermic reaction). For the DTA curve of Prod-UIHT sample, the appearance of broad peaks at around 170 ℃ and 270 ℃ indicates the elimination of coordinated water molecules while the third peak at around 420 ℃ corresponds to the removal of NH_4^+ and OH^- (Ca *et al*., 2010).

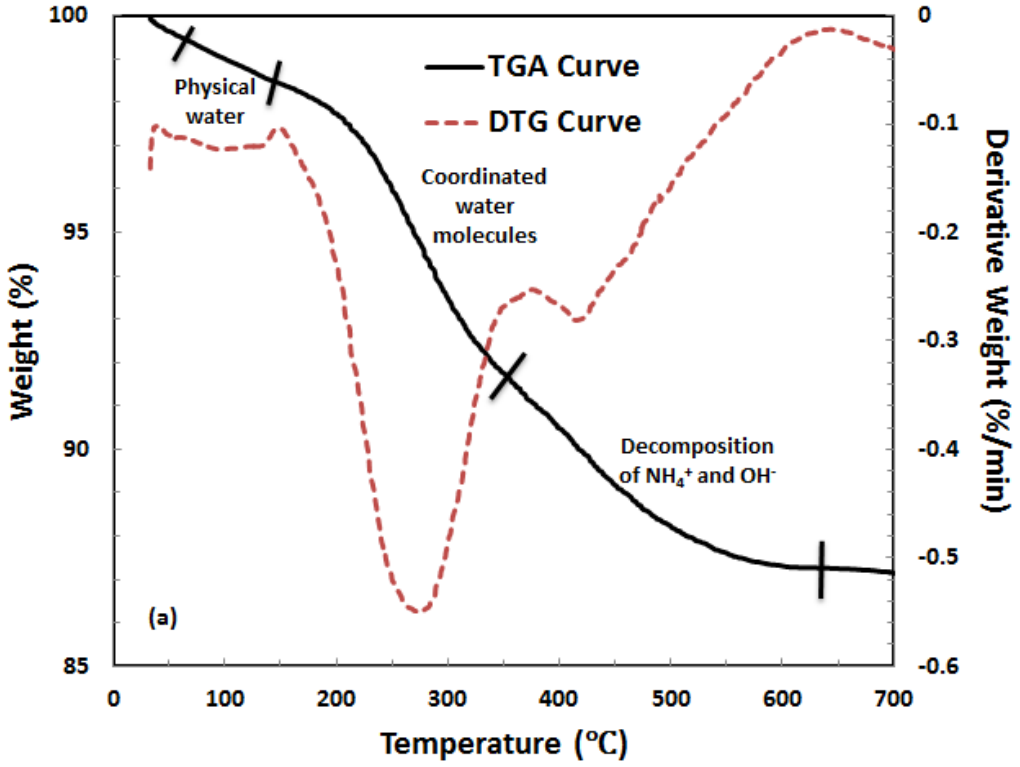
TGA Curve
DTG Curve
Physical water
Coordinated water molecules
Decomposition of NH_4^+ and OH^-
(a)
Weight (%)
Derivative Weight (%/min)
Temperature (°C)
100
95
90
85
0
-0.1
-0.2
-0.3
-0.4
-0.5
-0.6
0
100
200
300
400
500
600
700

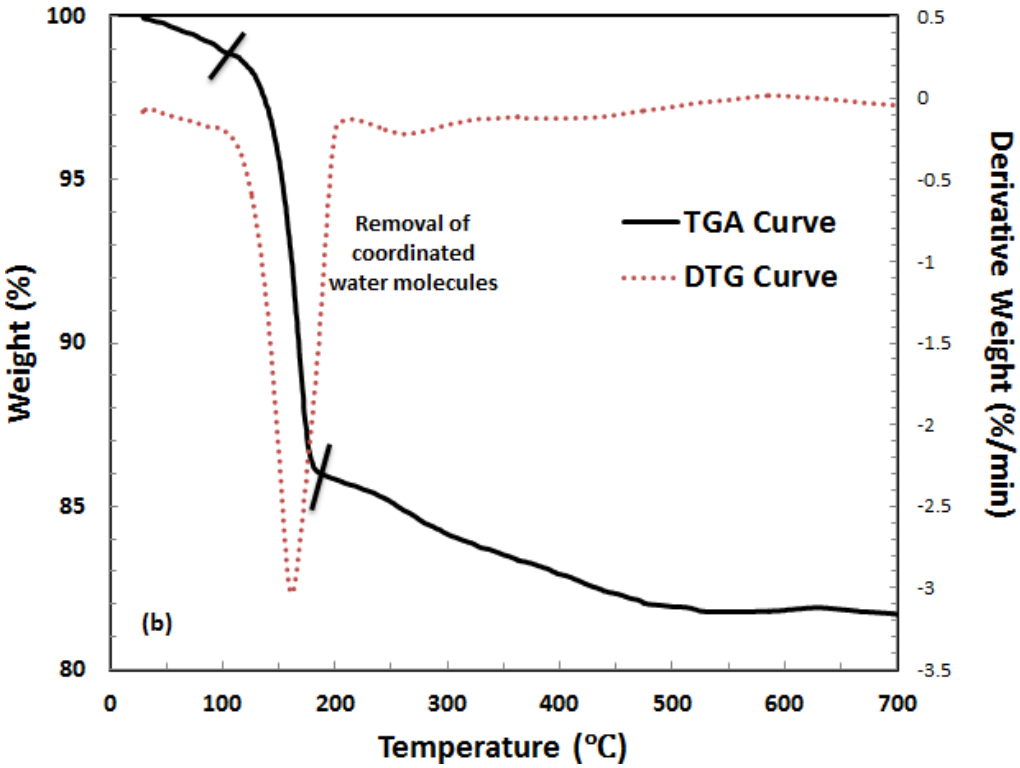
Removal of coordinated water molecules
TGA Curve
DTG Curve
(b)
Weight (%)
Derivative Weight (%/min)
Temperature (°C)
100
95
90
85
80
0.5
0
-0.5
-1
-1.5
-2
-2.5
-3
-3.5
0
100
200
300
400
500
600
700

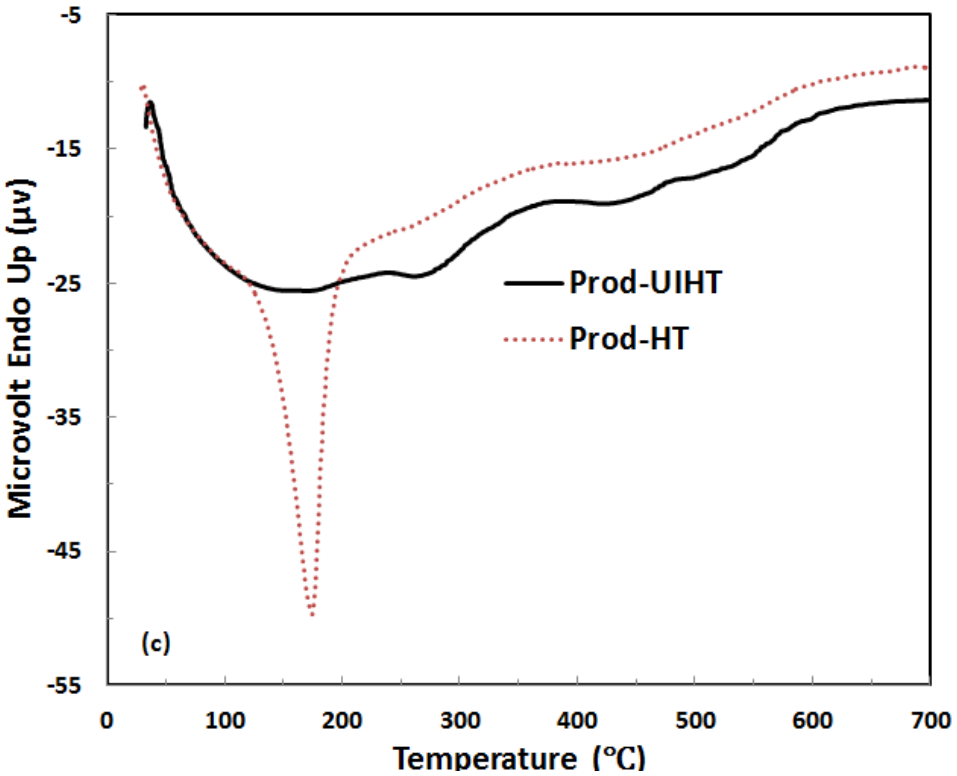

Figure 6-5 TGA-DTG curves of samples prepared when *C*=1.0 mol L^{-1} and pH=0.8: (a) Prod-UIHT and (b) Prod-HT; (c) DTA curves of Prod-UIHT and Prod-HT.

SEM and TEM images of the nano-seeds prepared by two different hydrothermal methods are shown in Figure 6-6. As show in Figures 6-6a and b, the Seed-HT nanoparticles which are highly agglomerated exhibit a near spherical or elliptical shape with a spread in particle size distribution, ranging from 50-150 nm. By comparison, due to the application of ultrasonic-intensified impinging stream pre-treatment, the Seed-UIHT samples are well-dispersed and the near spherical morphology with nuclei sizes from 30-80 nm is observed (Figure 6-6c and d).

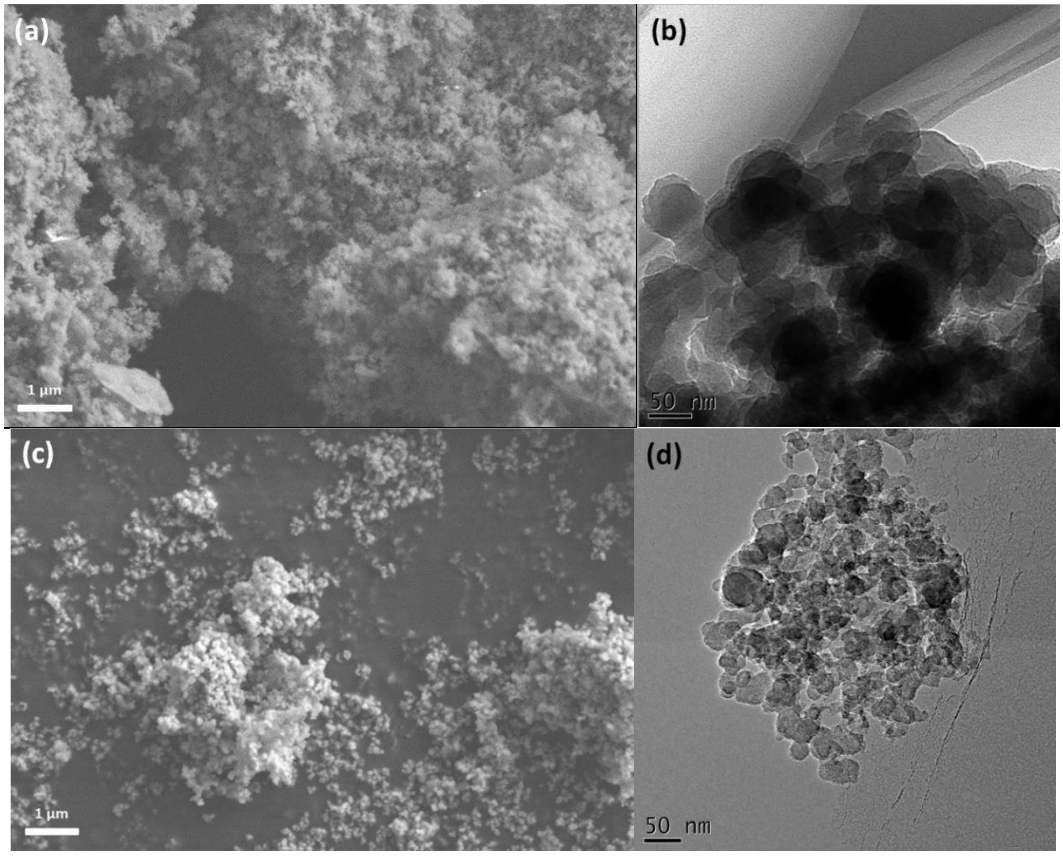

Figure 6-6 The SEM and TEM images of nano-seeds samples prepared when *C*=1.0 mol L^{-1} and pH=0.8: (a-b) Seed-HT; (c-d) Seed-UIHT.

The BET specific surface area and pore size distribution of the Seed-UIHT and Seed-HT have been characterized by nitrogen adsorption-desorption analysis. It can be seen that the N_2 adsorption isotherm of all nano-seeds (Figure 6-7a) is Type IV. Their big hysteresis loops can be evidenced by the presence of meso-pores (>2nm and <50nm) and large surface areas. The surface area, porosity and average nuclei size of Seed-UIHT and Seed-HT samples are shown in Table 6-3. The average nuclei sizes of Seed-UIHT and Seed-HT samples are 62.9 and 148.6 nm, respectively. It can be seen that the Seed-HT sample has smaller BET surface area of 40.4 m^2 g^{-1} and a lower pore volume of 0.31 cm^3 g^{-1} while the average pore width and nuclei size of Seed-HT sample are greater than the Seed-UIHT with the values of 36.9 nm and 148.6 nm,

respectively. In contrast, the Seed-UIHT sample shows a relatively smaller average pore size with the diameter of 24.6 nm, and exhibits larger BET surface area and higher total pore volume, corresponding to 95.4 m^2g^{-1} and 0.59 cm^3g^{-1} respectively. The analytical results of pore size distribution based on BJH desorption pore distribution are shown in Figure 6-7b. The Seed-UIHT has a significant amount of mesopores and small numbers of macropores in the range of 2 to 55 nm, which yields larger specific surface area and higher pore volume. The difference of BET analysis results between Seed-UIHT and Seed-HT can be attributed to application of ultrasound. The implosion of bubbles in solution induces both micro-streaming and micro-jetting. Micro-streaming caused by symmetrical implosion bubbles can enhance micromixing effect, result in increased mass transfer rate, chemical reaction rate, and nucleation rate. Meanwhile, micro-jetting caused by asymmetrical implosion bubbles can break larger particles into small pieces, and preventing agglomeration and clogging in CITJ. Therefore, the synergistic effect of micro-streaming and micro-jetting leads to the formation of nanoscale particles which have larger surface area and pore volume, as well as smaller pore width and nuclei size.

Table 6-3 N_2 adsorption-desorption analysis results of $FePO_4 \cdot 2H_2O$ precursors prepared with different synthesis methods.

Samples	Surface area ($m^2 g^{-1}$)	Average Pore Width (nm)	Total pore volume ($cm^3 g^{-1}$)	Average nuclei size (nm)
Seed-UIHT	95.4	24.6	0.59	62.9
Seed-HT	40.4	36.9	0.31	148.6

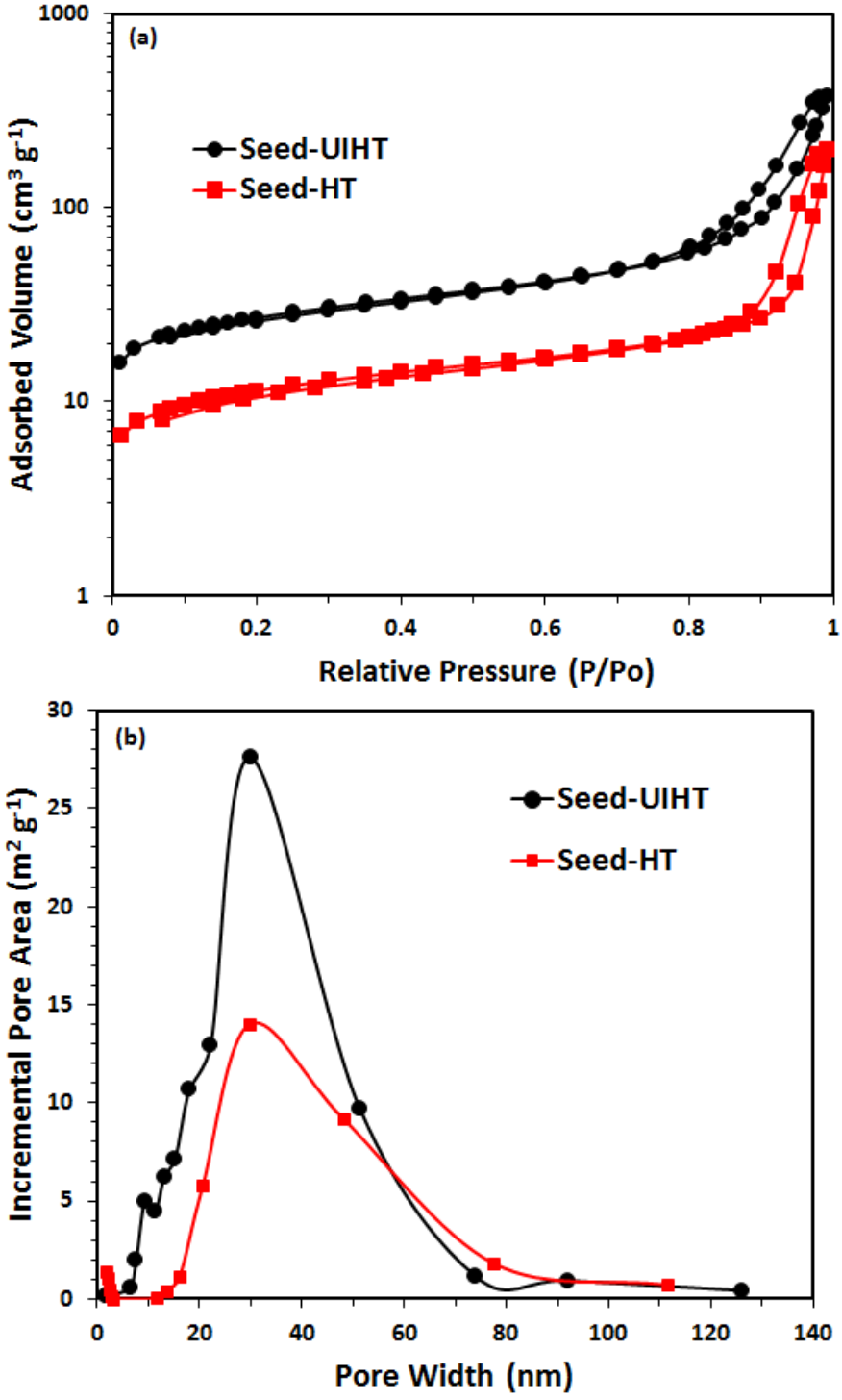

Figure 6-7 BET analysis results of nano-seeds samples prepared when *C*=1.0 mol L^{-1} and pH=0.8: (a) N_2 adsorption-desorption isotherms of Seed-UIHT and Seed-HT samples; (b) the corresponding pore-size distribution obtained. from the adsorption branch using the BJH method of Seed-UIHT and Seed-HT samples.

The SEM images of as-synthesized products are shown in Figure 6-8. It can be seen from the figure that the morphology of obtained particles is significantly affected by the presence of the nano-seeds. Figure 6-8a shows that that the Prod-HT particles do present spherical morphology but the size of the agglomerated particles is distributed diversely. The average size of larger particles can reach up to 10 um while those smaller particles have an average size of 2 um. However, as can be seen from Figure 6-8b and c, the Prod-UIHT particles not only show a spherical shape but also present a narrow size distribution with an average particle size of only 3 um. After sintering at 650 ℃ for 10 hours, the ProdC-UIHT particles (anhydrous $FePO_4$ precursor composites) still maintain micro-sized spherical secondary structures with the nano-scale porous structure being formed on the outside layer of the particles as can be seen from Figure 6-8d.

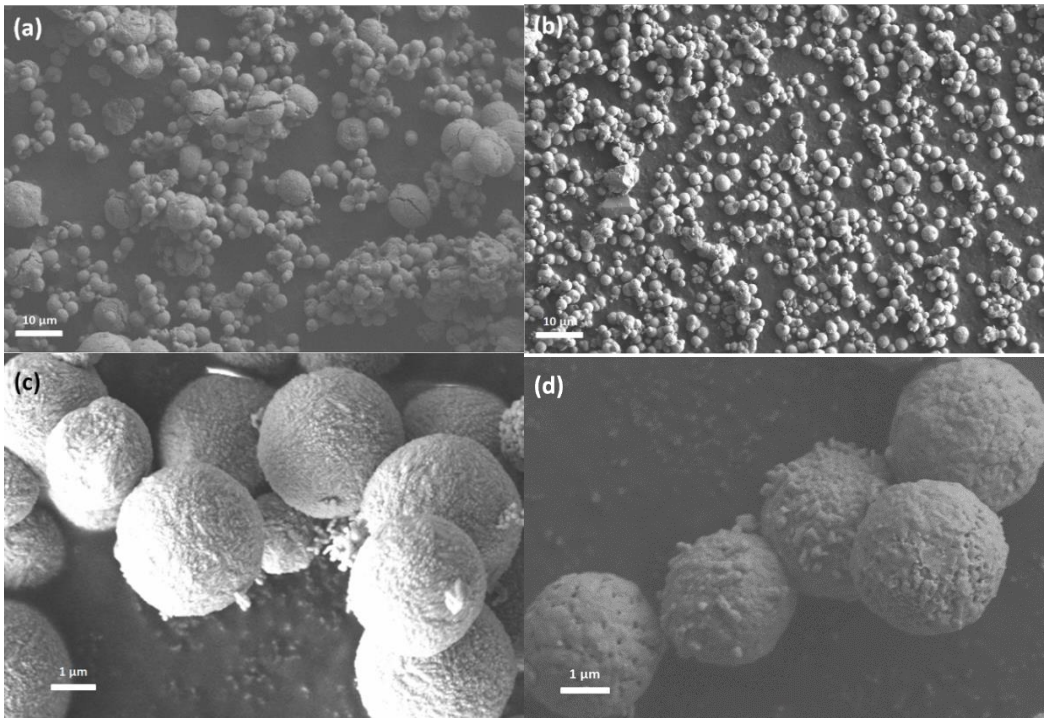

Figure 6-8 The SEM images of as-synthesized samples prepared when *C*=1.0 mol L^{-1} and pH=0.8: (a) Prod-HT; (b-c) Prod-UIHT; (d) ProdC-UIHT.

6.3.2 Formation Mechanism of $(NH_4)Fe_2(PO_4)_2(OH)\cdot 2H_2O$ and $FePO_4$ Particles

To investigate the formation mechanism of $(NH_4)Fe_2(PO_4)_2(OH)\cdot 2H_2O$ and $FePO_4$ particles by the UIHT method, time-dependent experiments have been conducted. Previous studies have suggested that the synthesis mechanism using hydrothermal treatment is consisted of three major stages, precursor dissolution, nucleation, and nuclei growth (Qin *et al*., 2010). The mechanism of the formation particles when using two-step hydrothermal method may be divided into four stages, i.e. primary nucleation, seeds dissolution, branching, and spherulitic growth (Wu *et al*., 2017). Based on the XRD, FTIR and SEM results, it is conjectured that the production of uniform and well-dispersed $(NH_4)Fe_2(PO_4)_2(OH)\cdot 2H_2O$ and $FePO_4$ particles with higher purity via UIHT is likely contributed from primary nucleation through ultrasound-intensified impinging stream pre-treatment before the hydrothermal growth occurrence. The primary nucleation will be influenced by applying ultrasonic irradiation which will affect the micro-mixing process in the T-mixer. Generally speaking, the adoption of ultrasonic irradiation is able to intensify the motion of eddies in the T-mixer. In order to estimate the characteristic micromixing time t_M, a scaling model was used to evaluate the time for diffusion which take place in the turbulence eddies with the eddy size of the order equal to the Kolmogorov length λ (Zhang *et al*., 2015; Shen *et al*., 2016).

$$t_M = \frac{(0.5\lambda)^2}{D_{eddy}} \tag{6-1}$$

where D_{eddy} is the eddy diffusivity of the reactant solutions. The Kolmogorov length λ can be estimated based on the micromixing energy dissipation rate ε [J/s·kg] and the kinematic viscosity of the mixed solution, ν_{ms}, at the point of mixing, given by

$$\lambda = \left(\frac{\nu_{ms}^3}{\varepsilon} \right)^{1/4} \tag{6-2}$$

The energy dissipation rate should be equal to the energy change associated with the energy loss (pressure drop) in the T-mixer, which can be measured by estimating the input power *P* divided by the mixed solution mass in the reactor:

$$\varepsilon = \frac{P}{\rho_{ms} V_T} \tag{6-3}$$

where V_T is the mixing volume of the T-type micromixer used in this study. For the present study, the input power *P* can be approximately assumed to be the superposition contributed from the input power for impinging stream P_{IS} and the ultrasonic irradiation P_{UI}:

$$P = P_{IS} + P_{UI} \tag{6-4}$$

The micromixing time can thus be estimated by

$$t_M = \frac{\left[0.5 \left(\frac{\rho_{ms} V_T \nu_{ms}^3}{P_{IS} + P_{UI}} \right)^{1/4} \right]^2}{D_{eddy}} \tag{6-5}$$

It can be seen from equation (5) that the micromixing time can be further reduced by imposing the ultrasonic irradiation. We noticed that the Reynolds numbers for T-shape microreactor based on the two inlets diameters can be estimated by

$$\mathrm{Re}_i = \frac{4 \rho_i Q_i}{\mu_i \pi d_i^2} \tag{6-6}$$

As the density and viscosity of $Fe(NO_3)_3$ and $(NH_4)_2HPO_4$ solutions are different, the equivalent Reynolds number used to characterise the mixing in the ISR can be defined by

$$\mathrm{Re}_{eq} = \frac{4\rho_{ms}\sum_{i=1}^{2} Q_i}{\mu_{ms}\pi d_{outlet}^2} \tag{6-7}$$

where ρ_{ms} and μ_{ms} are the density and viscosity of the fully mixed solution. The measured values of ρ_{ms} and μ_{ms} are found to be 1144.4 kg m^{-3} and 0.001005 Pa·s, respectively. The outlet diameter of T-mixer, d_{outlet} and volumetric feeding rate Q are 0.0035 m and 85.74 ml min^{-1}, which yields the estimated Reynolds number without using ultrasonic irradiation is 572, corresponding to a laminar shear flow in the T-mixer. However, the use of ultrasonic irradiation can produce a large number of micro bubbles. Such imploding bubbles can be considered as small microreactors which can generate powerful hydraulic shocks, and an environment with extremely high temperature and pressure (Mason, 1997). The hydraulic shocks caused by these bursting of the microbubbles can induce eddies that promote the regime transition from laminar to turbulent so that the turbulent energy dissipation can be enhanced. As a result, the diffusion rate or micro-mixing among these eddies are remarkably improved due to the application ultrasonic irradiation. In addition, chemical reaction rate and nucleation rate are increased due to the extremely high temperature and pressure created by imploding bubbles, which lead to the formation of large amount of nanoscale seeds. The energy transformed from ultrasound, especially from collapsing of bubbles, may overcome the Van Der Waals force and prevent agglomeration among nano-seeds. Therefore, the physical effects of ultrasonic

irradiation lead to the formation of uniform nanoscale primary seeds with an average size of 60 nm, although they are slightly agglomerated by high interfacial energy in the solution (shown in Figure 6-9a). With adopting hydrothermal treatment for 1 hour, these nano-seeds start to dissolve and hydrolyse (Figure 6-9b). When hydrothermal treatment increases to 2 hours, successive branching of nucleus is formed, grows as radial disks and fills spherical volumes (Figure 6-9c) (Beck and Andreassen, 2010; Andreassen *et al*., 2010). As hydrothermal time is increased, micro-sized spherulite grows uniformly and spherically (Figure 6-9d and e).

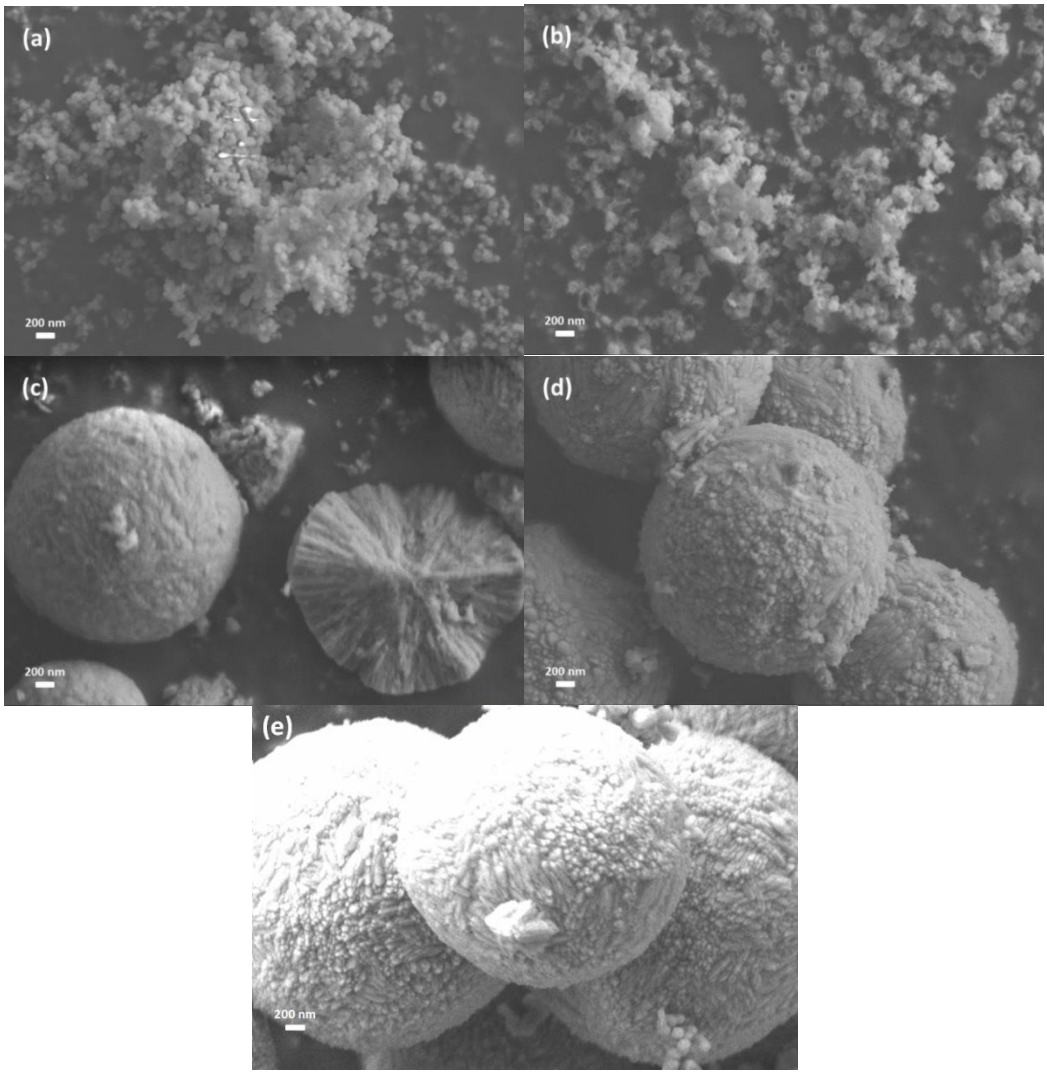

Figure 6-9 The SEM images of the samples obtained at 170 ℃ with different hydrothermal time when *C*=1.0 mol L^{-1} and pH=0.8: (a) Seed-UIHT; (b) UIHT-1h; (c) UIHT-2h; (d) UIHT-3h; (e) UIHT-4h (Prod-UIHT).

For chemical effect, the starting raw materials were dissolved into water and gives ions including NH_4^+, PO_4^{3-}, NO_3^-, Fe^{3+}, and H^+. Meanwhile, water molecules can be hydrolysed as H^+ and OH^- by ultrasound irradiation. It has been reported from the previous studies that three different kind of chemical reactions may take place at (1) inner environment of the collapsing bubbles (gas phase region); (2) the interfacial region between the bubble and bulk solution; and (3) in bulk solution region (Nithya

et al., 2015). It is noted that the raw materials used in this study are ionic and non-volatile, which are difficult to enter the phase region due to the low vapour pressure (Sivakumar *et al*., 2006). Thus, the reaction will only take place in the interfacial region between the gas and solution. The ions, including NH_4^+, PO_4^{3-}, NO_3^-, Fe^{3+}, OH^-, and H^+ ions, are homogeneously distributed in solution with the help of ultrasonic irradiation. Furthermore, the chemical bonds can be ruptured by the extremely high temperature and pressure induced by the collapsing of microbubbles so that the side reaction and the formation of by-products can be prevented. Through these actions, the $(NH_4)Fe_2(PO_4)_2(OH)\cdot 2H_2O$ particles are generated after hydrothermal treatment, and the pure $FePO_4$ particles are produced by removing $[NH_4^+]$ and $[OH^-]$ ions after sintering process. The above mentioned chemical reaction of two-step hydrothermal method can be described as:

$$2Fe^{3+} + 2PO_4^{3-} + NH_4^+ + OH^- + 2H_2O \rightarrow (NH_4)Fe_2(PO_4)_2(OH)\cdot 2H_2O\downarrow \quad (6\text{-}8)$$

$$(NH_4)Fe_2(PO_4)_2(OH)\cdot 2H_2O \rightarrow 2FePO_4 + NH_3 + 3H_2O \quad (6\text{-}9)$$

By comparison, the samples prepared by using the conventional hydrothermal method are indexed to be $FePO_4$ but the impurities, such as $Fe_3(PO_4)_2(OH)_2$, were found after sintering process. This indicates that the NH_4^+, PO_4^{3-}, NO_3^-, Fe^{3+}, OH^-, and H^+ ions are distributed in-homogeneously, resulting in the formation of amorphous by-products although they cannot be found before calcination process. This is likely due to the fact that the conventional mixing does not give out the sufficient mixing, leading to product contamination or formation of by-products (Krupa *et al*., 2014).

6.3.3 Effect of Reagent Concentration on the Synthesis of $(NH_4)Fe_2(PO_4)_2(OH)\cdot 2H_2O$ and Decomposed Products

To further investigate the effect of reagent concentration for the synthesis of $(NH_4)Fe_2(PO_4)_2(OH)\cdot 2H_2O$ particles and decomposed products, samples were prepared under precisely controlled reactant concentration (C = 0.5, 1.0 and 1.5 mol L^{-1}). The hydrothermal temperature and heating time were maintained at 170 ℃ and 4 hours, respectively. The as-synthesized samples were denoted as Prod-UIHT-0.5, Prod-UIHT-1.0, and Prod-UIHT-1.5, while the products after sintering process were labelled as ProdC-UIHT-0.5, ProdC-UIHT-1.0, and ProdC-UIHT-1.5.

The morphology of $(NH_4)Fe_2(PO_4)2(OH)\cdot 2H_2O$ particles synthesized with different reagent concentration was identified by SEM is shown in Figure 6-10. It can be seen from the figure that the Prod-UIHT-0.5 sample (Figure 6-10a) shows microscale red-blood-cell-like morphology with irregular hole in the centre, which is similar to the $(NH_4)Fe_2(PO_4)_2(OH)\cdot 2H_2O$ particles as reported by Wu *et al*. (2018). The average diameter and thickness of the particle are found to be around 4 um and 2 um, respectively. When the initial reagent concentration is increased to 1.0 mol L^{-1}, the Prod-UIHT-1.0 particles present uniform microspheres with an average particle size of 2 um (Figure 6-10b). Further increase in the feeding concentration (1.5 mol L^{-1}) results in the appearance of near-sphere $(NH_4)Fe_2(PO_4)2(OH)\cdot 2H_2O$ particles that have a spread particle size distribution (Figure 6-10c). Those large particles have an average size of 10 um. In addition, it is also observed that there exist a large number of small particles with the average size of 1 μm.

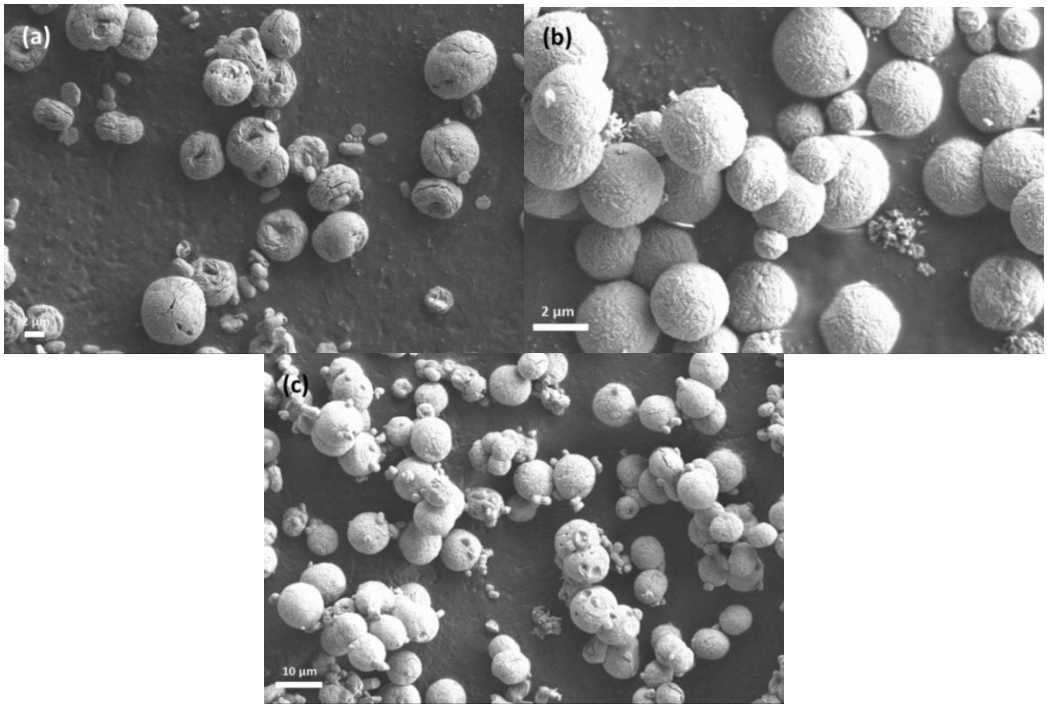

Figure 6-10 SEM images of as-synthesized $Fe_2(NH_4)(OH)(PO_4)_2(H_2O)_2$ samples synthesized with different reagent concentration at 170 ℃ for 4 hours when pH=0.8: (a) Prod-UIHT-0.5; (b) Prod-UIHT-1.0(Prod-UIHT); and (c) Prod-UIHT-1.5

The corresponding XRD patterns of the as-synthesized precursors and calcined products prepared with different reagent concentration by two-step hydrothermal method are shown in Figures 6-11. The XRD patterns of precursor samples (Figure 6-11a) are all well matched with $(NH_4)Fe_2(PO_4)_2(OH)\cdot 2H_2O$ with spheniscidite structure (PDF #41-0593). Figure 6-11b shows the XRD patterns of products after sintering process. It can be seen clearly from the figure that the major diffraction peaks take place around 20.2˚, 25.8˚, 41.2˚ and 48.4˚, which can be classified as hexagonal structure of $FePO_4$ (PDF #29-0715). The minor diffraction peaks occurring at 18.9˚, 27.0˚ and 27.8˚ indicate the formation of $Fe_3(PO_4)_2(OH)_2$ (PDF #14-0310), while the diffraction peaks appearing around 18.9˚, 20.2 ˚ and 21.3˚ reveal the presence of

$Fe_3(PO_4)_2(OH)_2 \cdot 4H_2O$ (PDF #26-1138, space group P21/c, with lattice parameters a = 1.0000 nm, b = 0.9730 nm, and c = 0.5471 nm). In addition, the calculated lattice parameters in Table 6-4 show that the unit volume of Prod-UIHT-1.0 is 915.13 $Å^3$, which is greater than the unit volume of Prod-UIHT-0.5 (911.76 $Å^3$) and Prod-UIHT-1.5 (910.34 $Å^3$). After sintering process, the unit volumes of ProdC-UIHT-0.5 and ProdC-UIHT-1.5 are 702.82 $Å^3$ and 532.64 $Å^3$, respectively, being greater than the unit volume of ProdC-UIHT-1.0 (285.53 $Å^3$).

Table 6-4 Calculated lattice parameters as-synthesized samples

Samples	a(Å)	b(Å)	c(Å)	V($Å^3$)
Prod-UIHT-0.5	9.7544	9.6301	9.7062	911.76
Prod-UIHT-1.0	9.8229	9.6208	9.6835	915.13
Prod-UIHT-1.5	9.7502	9.6372	9.6881	910.34
ProdC-UIHT-0.5	7.4174	7.4174	12.7745	702.82
ProdC-UIHT-1.0	5.0321	5.0326	11.2750	285.53
ProdC-UIHT-1.5	10.0187	9.7251	5.4667	532.64

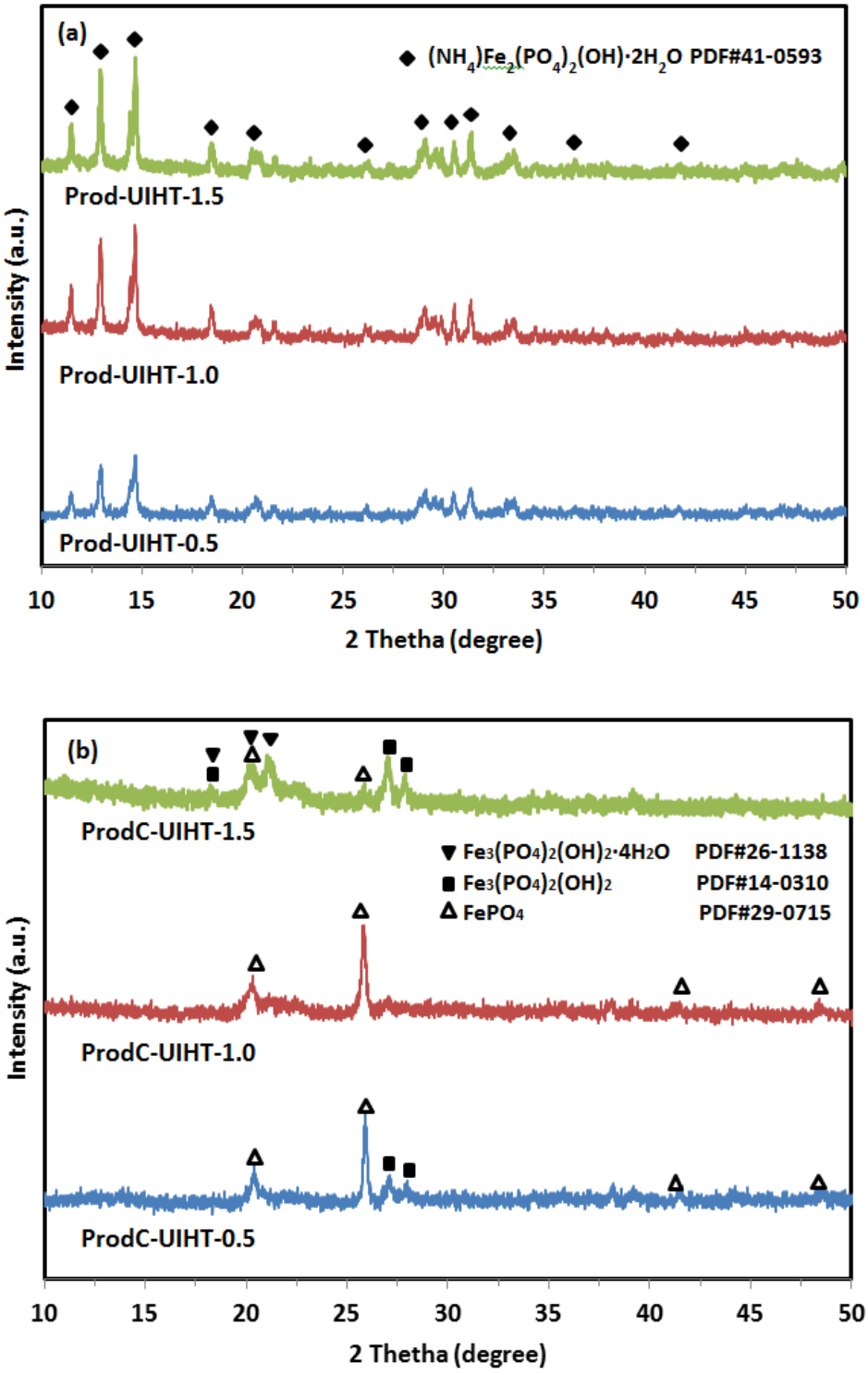

Figure 6-11 XRD patterns of samples synthesized with different reagent concentration at 170 ℃ for 4 hours when pH=0.8: (a) as-synthesized precursors (b) obtained products after sintering process

Based on the SEM and XRD results, it can be fairly claimed that the use of reagent concentration of 1.0 mol L^{-1} is likely the optimal condition for the initial reagent concentration which could be applied for the formation of uniform and spherical $(NH_4)Fe_2(PO_4)_2(OH)\cdot 2H_2O$ and decomposed $FePO_4$ particles. Previous study has demonstrated that the initial reagent concentration significantly influences the supersaturation level, nucleation rate, particle growth rate during the particle formation process (Andac *et al*., 2005; Behin *et al*., 2016). For primary nucleation, the nano-seeds prepared by raw materials of 1.0 mol L^{-1} via the ultrasonic-intensified T-mixer can have smaller nuclei size (Dong *et al*., 2017). It is commented that apart from the raw materials used for the nucleation of nano-seeds, a large amount of free ions may still exist in the solution. From the point of view of particle growth process, the adoption of higher reactant concentration can increase the supersaturation level and particle growth rate in a chemical reaction.

When the reagent concentration is 0.5 mol L^{-1}, some cracks were found on the surface of the micro-sized red-blood-cell-like particles. The appearance of these cracks is very likely caused by the shortage of free ions, result in the incomplete growth of $(NH_4)Fe_2(PO_4)_2(OH)\cdot 2H_2O$ particles. When increasing the initial reagent concentration from 0.5 to 1.0 mol L^{-1}, the relatively higher supersaturation level and sufficient free ions can be beneficial and contribute to the formation of spherical particles. However, further increment in the initial reagent concentration to 1.5 mol L^{-1} lead to the particle size increase (around 10 μm), accompanying by presence of a large number of small particles due to the excess of free ions. Thus, it can be concluded that the as-synthesized products are significantly affected by initial reagent concentration.

6.3.4 Effect of pH value on the synthesis of $(NH_4)Fe_2(PO_4)_2(OH)\cdot 2H_2O$ and decomposed products

To determine the effect of pH value on the synthesis of $(NH_4)Fe_2(PO_4)_2(OH)\cdot 2H_2O$ and $FePO_4$ particles, samples were prepared under precisely controlled pH values (pH=0.8, 1.2, 1.5, and 1.8) when the reagent concentration, hydrothermal temperature and heating time were maintained at the same condition during the synthesis process. The as-synthesized samples were denoted as Prod-UIHT-pH0.8, Prod-UIHT-pH1.2, Prod-UIHT-pH1.5, and Prod-UIHT-pH1.8 while the products after sintering process were labelled as ProdC-UIHT-pH0.8, ProdC-UIHT-pH1.2, ProdC-UIHT-pH1.5, and ProdC-UIHT-pH1.8.

The morphology of $(NH_4)Fe_2(PO_4)_2(OH)\cdot 2H_2O$ samples prepared by UIHT method at different pH values was examined by SEM is shown in Figure 6-12. The $(NH_4)Fe_2(PO_4)_2(OH)\cdot 2H_2O$ composites formed under the condition that pH = 0.8 clearly present microspheres with an average size of 3 um (see Figure 6-12a). When pH value is increased to 1.2, two $(NH_4)Fe_2(PO_4)_2(OH)\cdot 2H_2O$ micro-spheres interweave to combine and form the peanut-like micro-sized particles with an average length of 8 μm and width of 4 μm (see Figure 6-12b). As pH value further increases to 1.5, $(NH_4)Fe_2(PO_4)_2(OH)\cdot 2H_2O$ particles still show peanut-like morphology but cracks are occurring in the middle of the particle. The average length and width of the particles attain 16 μm and 10 μm, respectively (see Figure 6-12c). Further increase pH value to 1.8, $(NH_4)Fe_2(PO_4)_2(OH)\cdot 2H_2O$ particles are found to be easily agglomerated and they can form to generate even larger particles with irregular shapes (see Figure 6-12d). The reason is that, according to Derjaguin and Landau, Verwey and Overbeek (DLVO) theory, when pH value was increased and became closer to the

pH of zero net proton charge (PZNPC), the aggregation between two particles becomes faster and irreversible. Therefore, the samples can become twined (Figure 6-12b), and even contain crystallographic defects (Figure 6-12c). When pH value is further increased and above a specific point, the process is dominated by random aggregation and several particles are combined together (Figure 6-12d). Therefore, the pH value, or the concentration of $[OH]^-$, influences the particle growth orientation during hydrothermal process, resulting in the difference on the morphology of $(NH_4)Fe_2(PO_4)_2(OH)\cdot 2H_2O$ particles (Burrows *et al.*, 2013; Devasia *et al*., 1993).

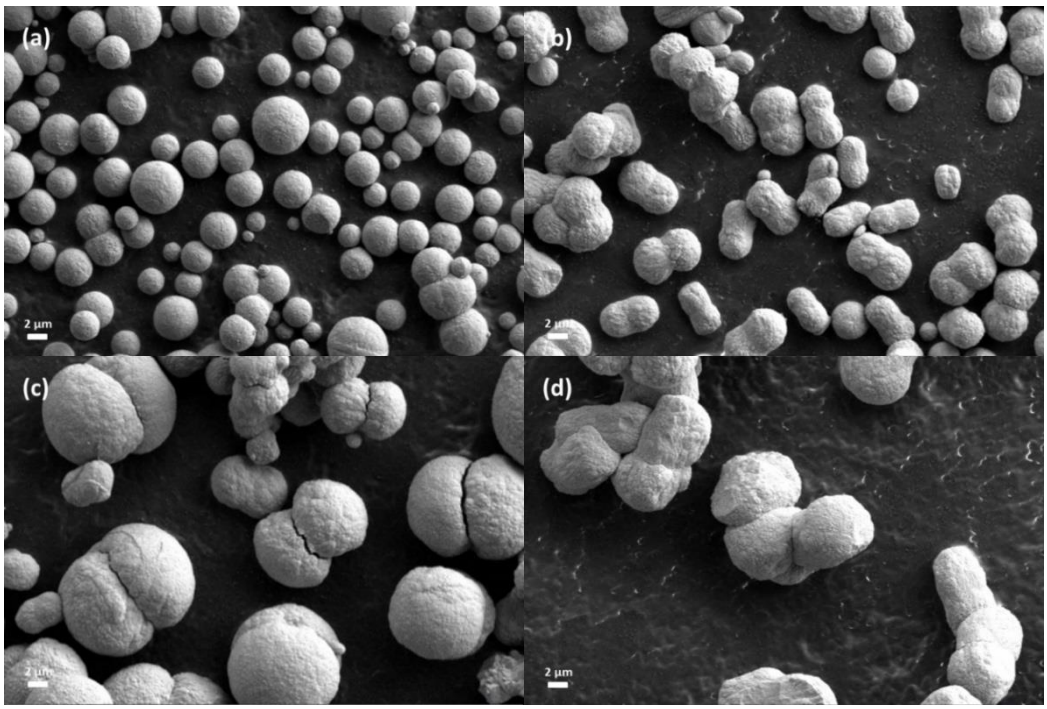

Figure 6-12 SEM images of $Fe_2(NH_4)(OH)(PO_4)_2(H_2O)_2$ composites synthesized with different pH value at 170 ℃ for 4 hours when *C*=1.0 mol L^{-1}: (a) UIHT-pH0.8 (Prod-UIHT), (b) UIHT-pH1.2, (c) UIHT-pH1.5, and (d) UIHT-pH1.8.

The corresponding XRD patterns of the as-synthesized precursors and calcined products prepared with different reagent concentration by two-step hydrothermal method are shown in Figures 6-13. The XRD patterns of as-synthesized

$(NH_4)Fe_2(PO_4)_2(OH)\cdot 2H_2O$ samples (Figure 6-13a) are all well matched with $(NH_4)Fe_2$ $(PO_4)_2(OH)\cdot 2H_2O$ with spheniscidite structure (PDF #41-0593). After sintering, all the XRD patterns of discomposed products (Figure 6-13b) match well with anhydrous hexagonal structure $FePO_4$ (PDF #29-0715). It can be seen clearly from the figure that, as pH value increases, there are no obvious difference among the XRD patterns of $(NH_4)Fe_2(PO_4)_2(OH)\cdot 2H_2O$ precursor. However, when the $FePO_4$ composites were synthesized at pH=0.8, the main diffraction peaks at $2\Theta = 20.3^0$ and 25.8^0 are lower and spread wider than those for other samples, which clearly indicates that higher pH value may lead to the high degree of crystallinity of the decomposed samples. The calculated lattice parameters of $(NH_4)Fe_2(PO_4)_2(OH)\cdot 2H_2O$ and decomposed $FePO_4$ samples are listed in Table 6-5. As seen from the table, with increasing pH value, the unit volume of $(NH_4)Fe_2(PO_4)_2(OH)\cdot 2H_2O$ sample decreases from 915.13 $Å^3$ (pH=0.8) to 794.40 $Å^3$ (pH=1.8). The same tendency is also observed for the case of decomposed $FePO_4$ samples, in which the unit volume reduces from 285.53 $Å^3$ (pH=0.8) to 246.57 $Å^3$ (pH=1.8).

Table 6-5 Calculated lattice parameters and nuclei size of as-synthesized samples

Samples	a(Å)	b(Å)	c(Å)	V(Å^3)
Prod-UIHT-pH0.8	9.8229	9.6208	9.6835	915.13
Prod-UIHT-pH1.2	9.7126	9.4408	9.3986	846.64
Prod-UIHT-pH1.5	9.4912	9.4212	9.4410	823.57
Prod-UIHT-pH1.8	9.3748	9.3179	9.3192	794.40
ProdC-UIHT-pH0.8	5.0321	5.0326	11.2750	285.53
ProdC-UIHT-pH1.2	5.0351	5.0351	11.2373	246.72
ProdC-UIHT-pH1.5	5.0320	5.0320	11.2476	246.65
ProdC-UIHT-pH1.8	5.0345	5.0345	11.2327	246.57

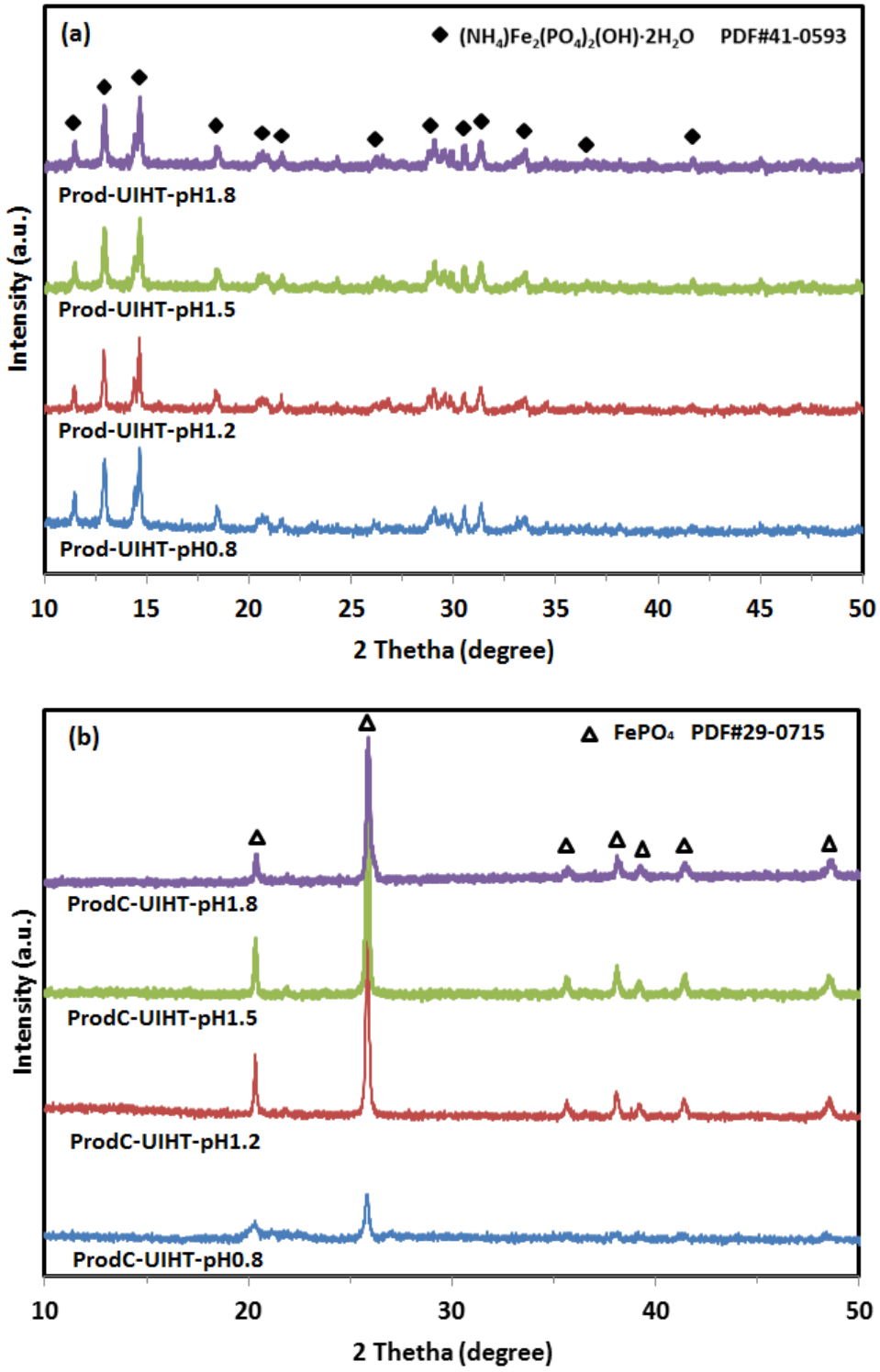

Figure 6-13 XRD patterns of samples synthesized with different pH value at 170 ℃ for 4 hours when *C*=1.0 mol L^{-1}: (a) as-synthesized precursors (b) obtained products after sintering process

Figure 6-14 shows the FTIR spectra of $(NH_4)Fe_2(PO_4)2(OH)\cdot 2H_2O$ and decomposed $FePO_4$ samples prepared at various pH conditions in the wave number region of 400–3900 cm^{-1}. The $(NH_4)Fe_2(PO_4)_2(OH)\cdot 2H_2O$ samples prepared at pH = 1.2, 1.5 and 1.8 show sharper bands at 1420 cm^{-1} and 1620 cm^{-1}. These sharper stretched vibrations correspond to the binding vibration of NH_4^+, which induced by ammonia solution used for adjusting the pH value. In addition, it is noticeable that the wide bands at 3332 cm^{-1} which indicates the v (OH) in H_2O molecules in $(NH_4)Fe_2(PO_4)_2(OH)\cdot 2H_2O$ have disappeared when pH value of solution is 1.2, 1.5 and 1.8. However, four small and spread peaks around 2800, 3100, 3300 and 3450 cm^{-1} can be still observed, suggesting the presence of v (NH), v (NH_2), and v (OH) groups (Devasia *et al*., 1993). After performing calcination, the FTIR spectra of all decomposed samples look similar. The disappearance of the absorption signals in the range of 2800 to 3450 cm^{-1} indicates the removal of H_2O. Moreover, the peak at 1420 cm^{-1} disappears for ProdC-UIHT-pH0.8, and becomes weaker for ProdC-UIHT-pH1.2, ProdC-UIHT-pH1.5, and ProdC-UIHT-pH1.8 samples, indicating that NH_4^+ functional group can be removed after calcination process.

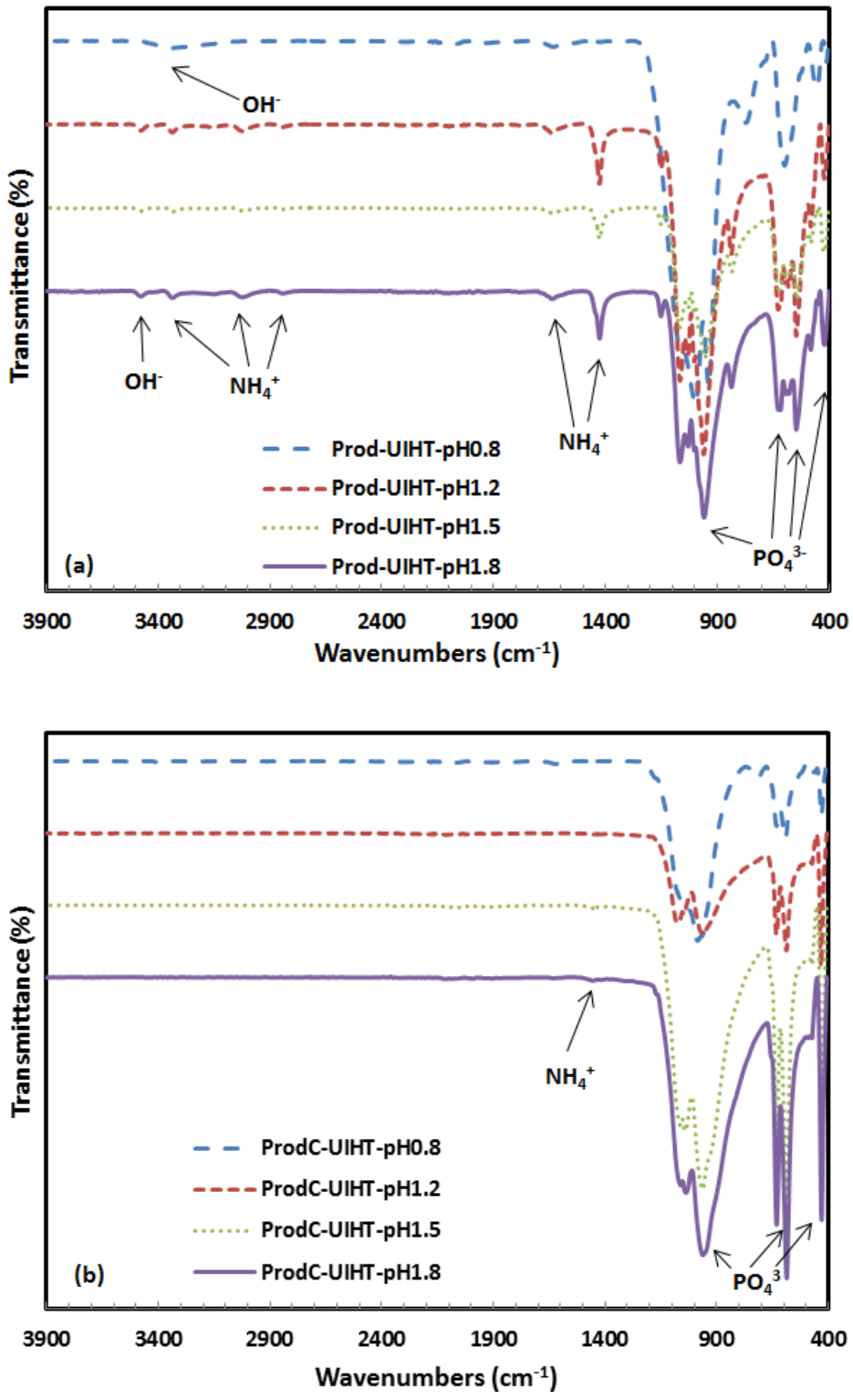

Figure 6-14 FTIR patterns of samples synthesized with different pH value at 170 ℃ for 4 hours when *C*=1.0 mol L^{-1}: (a) as-synthesized precursors (b) obtained products after sintering process

6.3.5 Electrochemical performance of $LiFePO_4$/C prepared by two-step hydrothermal method

The electrochemical performance of $LiFePO_4$/C sample prepared when pH is 0.8, reagent concentration is 1.0 mol/L by two-step hydrothermal method is shown in Figure 6-15. The average discharge capacities are 113.5, 92.9, 79.9, 68.0, and 53.6 mAh g^{-1} at a rate of 0.1 C, 0.5 C, 1 C, 2 C and 5 C, respectively. For cycling capability, $LiFePO_4$/C sample exhibited 92.0 and 82.8 mAh g^{-1} at 1^{st} and 100^{th} cycle. Comparing with the $LiFePO_4$/C samples prepared by other methods, the electrochemical performance of LiFePO4/C sample prepared by two-step hydrothermal method is not good. The reason may be attributed to that the 1-D transport path of Li^+ is blocked by impurities produced in hydrothermal reaction.

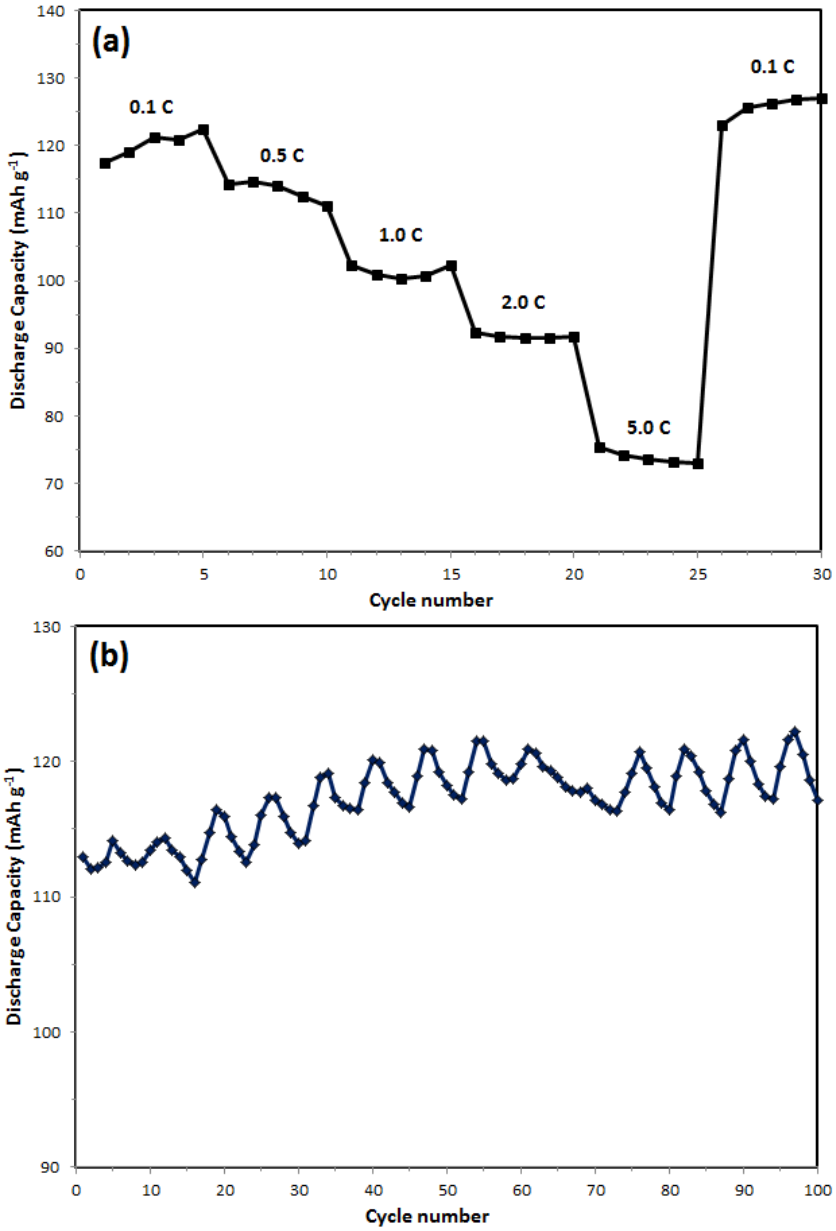

Figure 6-15 Electrochemical performance of $LiFePO_4$/C sample synthesized when pH=0.8, reagent concentration is 1.0 mol/L, temperature is 170 ℃ for 4 hours by two-step hydrothermal method: (a) Rate performance at various rates, (b) Cycling performance at 0.5 C for 100 cycles

6.4 Conclusions

Two synthesis approaches, the conventional hydrothermal method and two-step hybrid ultrasonic intensified impinging stream and hydrothermal method (ultrasonic-intensified impinging stream pre-treatment followed by hydrothermal treatment),

were applied for the synthesis of $(NH_4)Fe_2(PO_4)_2(OH)\cdot 2H_2O$ and $FePO_4$ samples under the same experimental conditions that the temperature, heating time, reactant concentration, and pH value were carefully controlled. It has been demonstrated that the adoption of ultrasonic-intensified impinging stream pretreatment can produce nano-seeds that have smaller nuclei size and narrow particle size distribution, giving out the well-dispersed spherical $(NH_4)Fe_2(PO_4)_2(OH)\cdot 2H_2O$ and decomposed $FePO_4$ samples. The conclusions reached as the results of the current study are as follows:

1. The adoption of ultrasonic-intensified impinging stream pre-treatment can effectively reduce the synthesised particle size and acquire the narrow particle size distribution of both nano-seeds and as-synthesized products.

2. The results obtained from the time-dependent experiments clearly indicate that the formation of $(NH_4)Fe_2(PO_4)_2(OH)\cdot 2H_2O$ particles by using two-step hydrothermal method consists of four major stages: primary nucleation, seeds dissolution, branching, and spherulitic growth.

3. An increase in the reactant concentration (from 0.5 to 1.0 mol L^{-1} in the present study) can improve the supersaturation level and promote the chemical reaction rate, leading to the generation of well-dispersed spherical $(NH_4)Fe_2(PO_4)_2(OH)\cdot 2H_2O$ particles. However, excess increase in the reactant concentration will diversify particle size distribution, resulting in by-products in the decomposed $FePO_4$ samples.

4. The pH value, or the concentration of $[OH]^-$, significantly affects the particle growth orientation during the hydrothermal process as clearly illustrated by the difference on the morphology of $(NH_4)Fe_2(PO_4)_2(OH)\cdot 2H_2O$ particles. In

addition, the crystallinity of decomposed $FePO_4$ samples can be improved as the result of increasing pH value.

References

1. Trobajo C., Espina A., Jaimez E., Khainakov S. A. and García J. R., 2000, Hydrothermal synthesis of iron(III) phosphates in the presence of urea, Journal Of The Chemical Society, Dalton Transactions, 5, 787-790.
2. Bonnet P., Millet J.M.M., Leclercq C., and Vedrine JC., 1996, Study of a New Iron Phosphate Catalyst for Oxidative Dehydrogenation of Isobutyric Acid, Journal of Catalysis, 158, 128-141.
3. Cavellec M., Ferey G., and Greneche J.M., 1997, Magnetic properties of synthetic spheniscidite. Journal of Magnetism and Magnetic Materials, 167, 57-64.
4. Zhou H., Duan H., Zhang H., and Ren X.M., 2010, A new pseudo-polymorph in mineral sphenicidite family $(NH_4)[Fe_2(OH)(H_2O)(PO_4)_2]\cdot 1.5H_2O$ exhibiting spontaneous magnetization below 25 K, Solid State Sciences, 12, 1816-1821.
5. Cao S.W., Zhu Y.J., and Cui J.B., 2010, Iron hydroxyl phosphate microspheres: Microwave-solvothermal ionic liquid synthesis, morphology control, and photoluminescent properties. Journal of Solid State Chemistry, 183, 1704-1709.
6. Ju S., Liu T., Peng H., Li G., and Chen K., 2013, A facile synthesis route for porous spherical $LiFePO_4$/C microscale secondary particles. Materials Letters, 93, 194-198.
7. Li J., Wu J., Wang Y., Liu G., Chen C., and Liu H., 2014, Synthesis of $LiFePO_4$ /C composite with high rate capability using spheniscidite as a facile precursor. Materials Letter, 136, 282-285.

8. Reale P., Scrosati B., Delacourt C., Wurm C., Morcrette M. and Masquelier C., 2003, Synthesis and Thermal Behavior of Crystalline Hydrated Iron(III) Phosphates of Interest as Positive Electrodes in Li Batteries. Chemistry of Materials. 15, 5051-5058.
9. Wu K., Liu D., and Tang Y., 2018, Self-assembly of red-blood-cell-like $(NH_4)[Fe_2(OH)(PO_4)_2]\cdot 2H_2O$ architectures from 2D nanoplates by sonochemical method. Ultrasonics Sonochemistry, 40, 832-836.
10. Liang G., Wang L., Ou X., Zhao X., and Xu S., 2008, Lithium iron phosphate with high-rate capability synthesized through hydrothermal reaction in glucose solution. Journal of Power Sources, 184, 538-542.
11. Liu Y., Gu J., Zhang J., Wang J., Nie N., Fu Y., Li W., and Yu F., 2015, Controllable synthesis of nano-sized $LiFePO_4$/C via a high shear mixer facilitated hydrothermal method for high rate Li-ion batteries. Electrochimica Acta, 173, 448-457.
12. Suslick K.S., Price G.J., 1999, Applications of ultrasound to materials chemistry, Annual Review of Materials Science. 29, 295-326.
13. Xu H., Zeiger B.W., and Suslick K.S., 2013, Sonochemical synthesis of nanomaterials. Chemical Society Review. 42, 2555-2567.
14. McNamara W. B., Didenko Y. T., and Suslick K. S., 1999, Sonoluminescence temperatures during multi-bubble cavitation. Nature, 401, 772-775.
15. Moradiyan E., Halladj R., Askari S., and Bijani P.M., 2017, Ultrasonic-assisted hydrothermal synthesis and catalytic behavior of a novel SAPO-34/Clinoptilolite nanocomposite catalyst for high propylene demand in MTO process. Journal of Physics and Chemistry of Solids, 107, 83-92.

16. Khan I., Ali S., Mansha M., and Qurashi A., 2017, Sonochemical assisted hydrothermal synthesis of pseudo-flower shaped Bismuth vanadate ($BiVO_4$) and their solar-driven water splitting application. Ultrasonics Sonochemistry, 36, 386-392.
17. Li H.B., Liu G.C., Chen S.Q., and Q.C. Liu, 2010, Novel Fe doped mesoporous TiO_2 microspheres: Ultrasonic–hydrothermal synthesis, characterization, and photocatalytic properties. Physica E, 42, 1844-1849.
18. Ezeh C.I., Tomatis M., Yang X.G., He J., and Sun C.G., 2018, Ultrasonic and hydrothermal mediated synthesis routes for functionalized Mg-Al LDH: Comparison study on surface morphology, basic site strength, cyclic sorption efficiency and effectiveness. Ultrasonics Sonochemistry, 40, 341-343.
19. Su S., Ma H., and Chuan X., 2016, Hydrothermal synthesis of zeolite A from K-feldspar and its crystallization mechanism. Advanced Powder Technology, 27, 139-144
20. Jusoh N., Yeong Y. F., Mohamad M., Lau K. K., and Shariff A. M., 2017, Rapid-synthesis of zeolite T via sonochemical-assisted hydrothermal growth method. Ultrasonics Sonochemistry, 34, 273-280.
21. Mu Y., Zhang Y., Fan J., and Guo C., 2017, Effect of ultrasound pretreatment on the hydrothermal synthesis of SSZ-13 zeolite. Ultrasonics Sonochemistry, 38, 430-436.
22. Askari S. and Halladj R., 2012, Ultrasonic pretreatment for hydrothermal synthesis of SAPO-34 nanocrystals. Ultrasonics Sonochemistry, 19, 554-559.
23. Roy P. and Das N., 2017, Ultrasonic assisted synthesis of Bikitaite zeolite: A potential material for hydrogen storage application. Ultrasonics Sonochemistry, 36, 466-473.

24. Azad F. N., Ghaedi M., Dashtian K., Hajati S., and Pezeshkpour V., 2016, Ultrasonically assisted hydrothermal synthesis of activated carbon-HKUST-1-MOF hybrid for efficient simultaneous ultrasound-assisted removal of ternary organic dyes and antibacterial investigation: Taguchi optimization. Ultrasonics Sonochemistry, 31, 383-393.
25. Andreussi T., Galletti C., Mauri R., Camarri S., and Salvetti M. V., 2015, Flow regimes in T-shaped micro-mixers. Computers & Chemical Engineering, 76, 150-159.
26. Krupa K., Nunes M.I., Santos R.J., and Bourne J.R., 2014, Characterization of micromixing in T-jet mixers. Chemical Engineering Science, 111, 48-55.
27. Huang Y., Wang P., Yuan Y., and Yang F., 2015, Synergistic degradation of chitosan by impinging stream and jet cavitation. Ultrasonics Sonochemistry, 27, 592-601.
28. Siddiqui S.W., Unwin P.J., Xu Z., and Kresta S.M., 2009, The effect of stabilizer addition and sonication on nanoparticle agglomeration in a confined impinging jet reactor. Colloid and Surface A: Physicochemical and Engineering Aspects, 350, 38-50.
29. Wang M., Yang Y., and Zhang Y., 2011, Synthesis of micro-nano hierarchical structured $LiFePO_4$/C composite with both superior high-rate performance and high tap density. Nanoscale, 3, 4434-4439.
30. Vedrine J. C., 2000, Partial oxidation reactions on phosphate-based catalysts. Topics in Catalysis, 11/12, 147-152.
31. Millet J. M. M. and Vedrine J.C., 2001, Importance of site isolation in the oxidation of isobutyric acid to methacrylic, Topics in Catalysis, 15, 139-144.

32. Chen R., Wu Y. and Kong X.Y., 2014, Monodisperse porous $LiFePO_4$/C microspheres derived by microwave-assisted hydrothermal process combined with carbothermal reduction for high power lithium-ion batteries. Journal of Power Sources, 258, 246-252.
33. Riesz P., Berdahl D., and Christman C.L., 1985, Free radical generation by ultrasound in aqueous and nonaqueous solutions. Environmental Health Perspectives, 64, 233-252.
34. Suslick K. S., 1990, Sonochemistry. Science, 247, 1439-1445.
35. Wang H. Q., Zhang X. H., Zheng F. H., Huang Y. G., and Li Q. Y., 2014, Surfactant effect on synthesis of core-shell $LiFePO_4$/C cathode materials for lithium-ion batteries. Journal of Solid State Electrochemistry. 19, 187-194.
36. Zhang L.L., Li H.J., Li K.Z., Fu Q.G., Zhang Y.L., and Liu S. J., 2015, Synthesis and characterization of nanobelt-shaped Na, F and carbonate multi-substituted hydroxyapatite. Materials Letter, 138, 48-51.
37. Shen J., Jin B., Jiang Q., Hu Y., and Wang X., 2016, Morphology-controlled synthesis of fluorapatite nano/microstructures via surfactant-assisted hydrothermal process. Materials & Design, 97, 204-212.
38. Amer W., Abdelouahdi K., Ramananarivo H. R., Zahouily M., Fihri A., Djessas K., Zahouily K., Varma R. S. and Solhy A., 2014, Microwave-assisted synthesis of mesoporous nano-hydroxyapatite using surfactant templates. CrystEngComm, 16, 543-549.
39. Garcia-Romero E. and M. Suarez, 2006, FTIR spectroscopic study of palygorskite: influence of the composition of the octahedral sheet. Applied Clay Science, 31, 154-163.

40. Qin X., Wang X.H., Xiang H.M., Xie J., Li J.J., and Zhou Y.C., 2010, Mechanism for Hydrothermal Synthesis of $LiFePO_4$ Platelets as Cathode Material for Lithium-Ion Batteries, Journal of Physical Chemistry C, 114, 16806-16812.
41. Wu S.G., Chen M.Y., Rohani S., Zhang D.J., Du S.C., Xu S.J., Dong W.B., and Gong J.b., 2017, Solvent-Mediated Nonoriented Self-Aggregation Transformation: A Case Study of Gabapentin. Crystal Growth & Design, 17, 4207-4216.
42. Mason T.J., 1997, Ultrasound in synthetic organic chemistry. Chemical Society Reviews. 26, 443-451
43. Beck R. and Andreassen J.P., 2010, Spherulitic Growth of Calcium Carbonate. Crystal Growth & Design, 10, 2934-2947.
44. Andreassen J.P., Flaten E. M., Beck R., and Lewis A.E., 2010, Investigations of spherulitic growth in industrial crystallization. Chemical Engineering Reseatch & Design, 88, 1163-1168.
45. Nithya V.D., Hanitha B., Surendran S., Kalpana D., and Selvan R. K., 2015, Effect of pH on the sonochemical synthesis of $BiPO_4$ nanostructures and its electrochemical properties for pseudocapacitors. Ultrasonics Sonochemistry, 22, 300-310.
46. Sivakumar M., Takami T., Ikuta H., Towata A., Yasui K., Tuziuti T., Kozuka T., Bhattacharya D., and Iida Y., 2006, Fabrication of Zinc Ferrite Nanocrystals by Sonochemical Emulsification and Evaporation Observation of Magnetization and Its Relaxation at Low Temperature. Journal of Physical Chemistry B, 110, 15234-15243.
47. Andac O., Tatlier M., Sirkecioglu A., Ece I., and Senatalar A. E., 2005, Effects of ultrasound on zeolite A synthesis. Microporous and Mesoporous Materials. 79, 225-233.

48. Behin J., Kazemian H., and Rohani S., 2016, Sonochemical synthesis of zeolite NaP from clinoptilolite. Ultrasonics Sonochemistry, 28, 400-408.
49. Dong B., Huang X.N., Yang X.G., Li G., Xia L., and Chen G. Z., 2017, Rapid preparation of high electrochemical performance $LiFePO_4$/C composite cathode material with an ultrasonic-intensified micro-impinging jetting reactor. Ultrasonics Sonochemistry, 39, 816-826.
50. Burrows N.D., Hale C.R.H., and Penn R.L., 2013, Effect of pH on the kinetics of crystal growth by oriented aggregation. Crystal Growth & Design, 13, 3396-3403
51. Devasia P., Natarajan K.A., Sathyanarayana D.N., and Rao G.R., 1993, Surface chemistry of Thiobacillus ferrooxidans relevant to adhesion on mineral surfaces. Applied and Environmental Microbiology. 59, 4051-4055.

CHAPTER 7: Conclusions and Recommendations for Future Work

7.1 Conclusions

The major conclusions derived from the present project are as follows:

1. The adoption of impinging stream reaction can be beneficial to generation of $FePO_4$ nanoparticles that have smaller primary grain size, large-mesoporous structures and higher specific surface areas. Application of ultrasonic irradiation can lead to synthesis of small-mesoporous $FePO_4$ precursors that have smaller nanoscale primary nuclei size and higher specific surface areas. It can also remarkably improve the purity of $FePO_4$ precursors due to the increased mass diffusion rate between $FePO_4$ and Li_2CO_3. The formation of small-mesopores contributes to an improved electrochemical property and relatively high volumetric energy density of LFP-UltraImp. However, the relatively higher interface area between nano-sized particles and the electrolyte may lead to undesired side reactions so as to cause reduced cycling performance.

2. The pH value of solution slightly influences the particle size and morphology of $FePO_4$ precursor but significantly affects the electrochemical properties of $LiFePO_4$ nanoparticles. For a T-type micromixer, increase in the reactant concentration can promote chemical reaction, yielding the reduced average primary grain size, increased specific surface area and total adsorption pore

volume so that the electrochemical performance can be improved. However, over-increase in the reactant concentration would have negative impact on these properties of $LiFePO_4$ nanocomposites. Increased specific surface area and total adsorption pore volume, and reduced average primary grain size can be obtained through increasing the volumetric flow rate of the reactant solutions fed into the T-type micromixer. An increase in the volumetric flow rate will reduce the size of Kolmogorov dissipation eddies (characterised by enhanced Reynolds number based on the diameter of the impinging streams), effectively reducing the micromixing time and promoting the mass transfer between the reactant solutions due to an enhanced collision rate among the turbulent eddies. However, when the volumetric feeding rate is increased to exceed a certain value, it has little impact on the reduction of primary grain size of $LiFePO_4$ nanocomposites.

3. The increasing of ultrasound intensity can reduce micromixing time, and improve both mass transfer coefficient and overall reaction rate, which result in smaller primary grain size, higher specific surface area, and narrower and sharper pore size distribution. However, over-increase in the ultrasound intensity would have negative impact, results in the increasing of average grain size, and reduction of specific surface area due to the extremely high temperature caused by higher ultrasound intensity. The purity of $FePO_4$ is affected by ultrasound pulse significantly due to the homogeneous competitive reactions between $FePO_4$ and $Fe(OH)_3$. The increasing of interval time leads to the formation of more $Fe(OH)_3$ because of the weakened micromixing effect and reduced mass transfer coefficient. Increased specific surface area and total

adsorption pore volume, and reduced average primary grain size can be obtained through increasing the volumetric flow rate, especially in ISR. The reasons are that, the energy dissipation rate and micromixing time in the T-type micromixer are only related to volumetric feeding rate *Q*. However, for UISR, the explosion of bubbles can cause hydraulic shocks and induce eddies which promote the regime transition from laminar to turbulent so that the turbulent energy dissipation can be enhanced. In addition, the micromixing effect can be improved by ultrasonic irradiation more significantly than the increasing of volumetric feeding rate.

4. Hierarchical mesoporous micro/nano-structured $FePO_4$ precursor and $LiFePO_4$/C samples can be successfully synthesized by utilising two-step co-precipitation method under precisely controlled reaction time and stirring rate. The results showed that, in contrast to the $LiFePO_4$/C synthesized by conventional co-precipitation method, the $LiFePO_4$/C composites prepared by two-step co-precipitation method exhibited both excellent electrochemical performance and relatively high tap density. The excellent electrochemical performance can be attributed to the large specific surface area, mesoporous structure and nanoscale primary grains which can shorten the diffusion pathway of Li^+. And the relatively high tap density of $LiFePO_4$ was guaranteed by the micro-sized near-spherical secondary structure. It is thus concluded that two-step co-precipitation technology will be promising synthesis method for the preparation of $LiFePO_4$ composites for energy storage. However, due to the long reaction time (up to 36 hours), two-step co-

precipitation method need to be further developed to reduce reaction time and energy consumption.

5. The adoption of ultrasonic-intensified impinging stream pre-treatment can effectively reduce the synthesised particle size and acquire the narrow particle size distribution of both nano-seeds and as-synthesized products. The results obtained from the time-dependent experiments clearly indicate that the formation of $(NH_4)Fe_2(PO_4)_2(OH)\cdot 2H_2O$ particles by using two-step hydrothermal method consists of four major stages: primary nucleation, seeds dissolution, branching, and spherulitic growth. An increase in the reactant concentration (from 0.5 to 1.0 mol L^{-1} in the present study) can improve the supersaturation level and promote the chemical reaction rate, leading to the generation of well-dispersed spherical $(NH_4)Fe_2(PO_4)_2(OH)\cdot 2H_2O$ particles. However, excess increase in the reactant concentration will diversify particle size distribution, resulting in by-products in the decomposed $FePO_4$ samples. The pH value, or the concentration of $[OH]^-$, significantly affects the particle growth orientation during the hydrothermal process as clearly illustrated by the difference on the morphology of $(NH_4)Fe_2(PO_4)_2(OH)\cdot 2H_2O$ particles. In addition, the crystallinity of decomposed $FePO_4$ samples can be improved as the result of increasing pH value. However, the electrochemical performance of $LiFePO_4$/C prepared by two-step hydrothermal method is poor. The reason may be attributed to that the 1-D transport path of Li^+ is blocked by impurities produced in hydrothermal reaction.

In conclusion, both two-step co-precipitation and two-step hydrothermal methods have potential to become promising synthesis methods for the preparation of

$LiFePO_4$ particles with hierarchical mesoporous micro/nano-structure, which can exhibit good electrochemical performance and high energy density.

7.2 Recommendations for future work

1. Based on the experimental results obtained by using ISR and UISR methods, it is possible to do CFD modelling work to simulate the fluid dynamics condition in the reactor.
2. This study was carried out to develop a novel technology for the synthesis of hierarchical micro/nano-structured porous $FePO_4$ for high performance lithium-Ion batteries. Although hierarchical micro/nano-structured porous $FePO_4$ can be prepared by two-step co-precipitation method, this method takes long reaction time (up to 36 hours). Therefore, it is necessary to attempt to reduce reaction time through other methods, such as increasing viscosity.

Ultrasonics - Sonochemistry 39 (2017) 816–826

Contents lists available at ScienceDirect

Ultrasonics - Sonochemistry

journal homepage: www.elsevier.com/locate/ultson

Rapid preparation of high electrochemical performance $LiFePO_4/C$ composite cathode material with an ultrasonic-intensified micro-impinging jetting reactor

Bin Dong[a], Xiani Huang[a], Xiaogang Yang[a,*], Guang Li[a], Lan Xia[b], George Chen[b]

[a] Department of Mechanical, Materials and Manufacturing Engineering, The University of Nottingham Ningbo China, University Park, Ningbo 315100, PR China
[b] Department of Chemical and Environmental Engineering, The University of Nottingham Ningbo China, University Park, Ningbo 315100, PR China

ARTICLE INFO

Keywords:
Ultrasonic irradiation
Impinging jetting reactor
$FePO_4$
$LiFePO_4$
Lithium ion battery

ABSTRACT

A joint chemical reactor system referred to as an ultrasonic-intensified micro-impinging jetting reactor (UIJR), which possesses the feature of fast micro-mixing, was proposed and has been employed for rapid preparation of $FePO_4$ particles that are amalgamated by nanoscale primary crystals. As one of the important precursors for the fabrication of lithium iron phosphate cathode, the properties of $FePO_4$ nano particles significantly affect the performance of the lithium iron phosphate cathode. Thus, the effects of joint use of impinging stream and ultrasonic irradiation on the formation of mesoporous structure of $FePO_4$ nano precursor particles and the electrochemical properties of amalgamated $LiFePO_4/C$ have been investigated. Additionally, the effects of the reactant concentration (C = 0.5, 1.0 and 1.5 mol L^{-1}), and volumetric flow rate (V = 17.15, 51.44, and 85.74 mL min^{-1}) on synthesis of $FePO_4{\cdot}2H_2O$ nucleus have been studied when the impinging jetting reactor (IJR) and UIJR are to operate in nonsubmerged mode. It was affirmed from the experiments that the $FePO_4$ nano precursor particles prepared using UIJR have well-formed mesoporous structures with the primary crystal size of 44.6 nm, an average pore size of 15.2 nm, and a specific surface area of 134.54 $m^2 g^{-1}$ when the reactant concentration and volumetric flow rate are 1.0 mol L^{-1} and 85.74 mL min^{-1} respectively. The amalgamated $LiFePO_4/C$ composites can deliver good electrochemical performance with discharge capacities of 156.7 mA h g^{-1} at 0.1 C, and exhibit 138.0 mA h g^{-1} after 100 cycles at 0.5 C, which is 95.3% of the initial discharge capacity.

1. Introduction

Increasingly global warming and air pollution caused by the consumption of fossil fuels have imposed the priority of using green energy. As a result, the use of rechargeable lithium-ion batteries (LIBs) has increased rapidly [1,2]. Compared with other commercial cathode materials, such as $LiCoO_2$, $LiNiO_2$, $LiMn_2O_4$ and their derivatives, olivine-structured $LiFePO_4$ is considered as one of the most promising cathode material owing to its significant advantages of nontoxicity, low cost of raw materials, good structural stability at high temperature, excellent safety performance, and relatively high theoretical specific capacity (170 mA h g^{-1}) with a flat discharge-charge potential (3.45 V vs. Li^+/Li) [3–5]. However, the poor rate performance of LiFePO4, resulting from its intrinsic low Li^+ diffusivity (10^{-17} to 10^{-14} $cm^2 s^{-1}$) and low electronic conductivity (10^{-9} to 10^{-8} S cm^{-1}), has become a technical bottleneck to confine its widely practical applications [6–8] before these drawbacks being overcome fundamentally.

The kinetics of Li^+ insertion and extraction process is the primary mechanism to determine the battery delivery rate capability of a LFP-based electrode. This kinetics involved consists of three main steps: (i) electron and Li^+ diffusion to/from the bulk material within the bulk material (solid phase); (ii) charge transfer reactions (electrochemical reactions) at the interface of the electrode/electrolyte; and (iii) Li^+ diffusion from/to the interface in electrolyte phase [9,10]. Significant amount of efforts have been made on developing new methods to facilitate the kinetics of Li^+ insertion and extraction process, and improving the rate performance of $LiFePO_4$. Reducing the particle size and preparing nano-scale cathode materials have been proved to be one of the effective ways to shorten the Li^+ diffusion path and facilitate the kinetics of steps. Additionally, fabrication of cathode material possessing the porous structures can also increase electrode/electrolyte interface area and ensure effective electrolyte permeation [11,12]. The porous structures would be beneficial to the improvement on the rate performance of LiFePO4. It should be emphasized here, however, that

* Corresponding author.
E-mail address: Xiaogang.Yang@nottingham.edu.cn (X. Yang).

http://dx.doi.org/10.1016/j.ultsonch.2017.06.010
Received 9 May 2017; Received in revised form 13 June 2017; Accepted 13 June 2017
Available online 15 June 2017

only meso- and macroporous structure is desirable, since the smaller size of micropores can hinder the reversibility of Li^+ insertion process and reduce the active interfaces of the electrode/electrolyte by an increased potential of blockage from residual carbon [13,14]. Micropores may also cause the formation of an extensive solid electrolyte interface (SEI) layer and inhibit charge transfer across the interfaces, resulting in a decrease in conductivity [15]. The application of $LiFePO_4$ in lithium ion battery requires an optimal combination of high porosity and surface area to provide excellent electrochemical properties.

There are several different preparation routes that have been attempted to develop the electrode materials for LIBs with high porosity structures. Sono-chemical synthesis is a well-known, simple and scalable technique to produce nanomaterials and the synthesized particles can have high porosities. The use of ultrasonic treatment is the other feasible way. By using ultrasonic treatment, acoustically created cavitation can be induced by ultrasonic wave while instantaneous collapse of the cavitation bubbles can create extreme conditions such as extremely high temperature up to 5000 K, pressures up to 1000 atm, and the heating and cooling rate greater than 10^{10} Ks^{-1} inside the cavitation zone. When ultrasonic treatment is applied for synthesis of the particles, the synthesized particles usually present porous structures [16,17].

Adoption of impinging stream (IS) is the other promising technology for materials synthesis and it has been widely used in industry for various applications. Liquid-continuous impinging streams are where two high speed impinging streams collide each other to form a local intensive micro-mixing have two major features: strong pressure fluctuation and many highly turbulent eddies. When this impinge streams are used for synthesis of particles, the generated turbulent micro-mixing can effectively increase local mass transfer rate and enhance the reaction rate, significantly boosting the probability of engulfed molecular diffusion by eddy collision. Meanwhile, the pressure fluctuation can also influence the energy and mass transfer in the solution [18]. Comparing to conventional stirred tanks, an impinging stream reactor (ISR) has fixed and confined volume, which lead to several orders of magnitude higher mixing intensity as well as uniform residence time when the feeding rate is kept unchanged. This kind of hydrodynamic reaction environment can enhance the control of the mixing conditions and local reactant concentrations [19].

This paper proposes three different synthesis routes, aiming to synthesis $FePO_4$ nano precursor particles that can have mesoporous structures. These obtained precursor micro or nano particles will be used to synthesize $LiFePO_4$/C composites. The effects of impinging jet stream and ultrasonic irradiation on the morphology of $FePO_4$ precursor and electrochemical properties of $LiFePO_4$/C will be investigated and the findings will be discussed. The paper is organised as follows. Section 2 will describe the experimental details for synthesis of $FePO_4$ nanocomposites. The properties of $FePO_4$ and $LiFePO_4$ synthesized by using different synthesis methods are discussed in Section 3. Finally, some important conclusions drawn from the present work are given in Section 4.

2. Materials and experimental methods

2.1. Synthesis of $FePO_4$ nanocomposites

The $Fe(NO_3)_3$ (1 mol L^{-1}) and $(NH_4)_2HPO_4$ (1 mol L^{-1}) aqueous solutions were prepared by dissolving $Fe(NO_3)_3{\cdot}9H_2O$ (Sinopharm Chemical Reagent Co., Ltd, 99%) and $(NH_4)_2HPO_4$ (Sinopharm Chemical Reagent Co., Ltd, 99%) into deionized water. A certain amount of ammonia solution was used to adjust the pH value of $(NH_4)_2HPO_4$ to maintain the desired value.

Three different methods were designed to synthesis the nanoparticles of $FePO_4$. The first type of $FePO_4$ nanoparticles were synthesized via an ultrasonic-assisted impinging stream reaction at room temperature. The two reaction solutions were added continuously into an impinging jet reactor which was irradiated by a FS-600pv horn type ultrasonic wave piezoelectric vibrator (600 W, 13 mm in diameter) with 20 kHz (as shown in Fig. 1). The inlet of impinging jetting reactor had an inner diameter of 4 mm, while the inner diameter of outlet was 15 mm. The volumetric feeding rate of solutions was maintained at 85.74 ml/min (100 rpm). The pH value of solution was maintained at 1.70 by adding the ammonia solution using a pH automatic controller. Temperature was maintained at 60 °C. The obtained products were then subsequently washed with deionized water several times, filtrated and then dried in air at 100 °C for 12 h. Then the sample was calcined in air at 600 °C for 10 h to obtain anhydrous crystalline $FePO_4$ samples. This nano $FePO_4{\cdot}xH_2O$ sample was denoted as FP-Ultraimp.

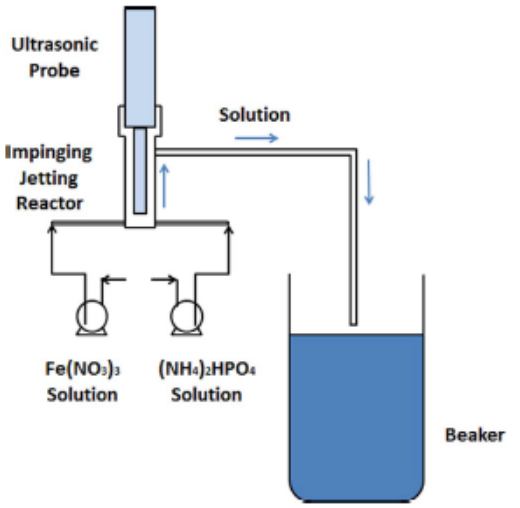

Fig. 1. Schematic diagrams of experimental setup for combined ultrasonic-assisted impinging jetting reaction method.

The second type of $FePO_4$ nanocomposites were synthesized by applying a similar impinging jet reaction to the described first method. The only difference between the first and second type of synthesis methods is only the ultrasonic irradiation step. The second type of $FePO_4{\cdot}xH_2O$ sample is not irradiated with ultrasonic waves. The obtained nano $FePO_4$ sample was referred to as FP-Imp.

The third type of $FePO_4{\cdot}xH_2O$ nanocomposites were prepared for comparison purpose by a conventional co-precipitation method. The two reaction solutions were added continuously into a stirring reactor at a constant volumetric feeding rate of 85.74 ml/min (100 rpm). The pH value of solution was also maintained at 1.70 by adding ammonia solution via pH automatic controller. After adopting the same filtration, drying and calcination procedures, the $FePO_4$ nanocomposites were obtained, named by FP-Copre.

In addition, to investigate the effect of reagent concentration and volumetric flow rate, FP-Ultraimp and FP-Imp nanocomposites were also synthesized under precisely controlled reagent concentration (C = 0.5 and 1.5 mol L^{-1}) and volumetric flow rate (V = 17.15 and 51.44 ml min^{-1}).

2.2. Synthesis of $LiFePO_4$/C composites

Three types of anhydrous $FePO_4$ samples were mixed with Li_2CO_3 (Sinopharm Chemical Reagent Co., Ltd, 99%) and glucose (Sinopharm Chemical Reagent Co., Ltd, 99%) at a desired ratio and ball-milled at 300 rpm for 6 h by a planetary ball mill, respectively. Then the mixtures were calcined in nitrogen atmosphere at 650 °C for 10 h. The obtained

$LiFePO_4$/C samples were designated as LFP- UltraImp, LFP-Imp, and LFP-Copre, respectively.

2.3. Characterization of $FePO_4$ and $LiFePO_4$/C

Thermalgravimetric was measured by simultaneous thermal analyser (TG, NETZSCH STA 449 F3 Jupiter, Germany) at a heating rate of 10 °C min^{-1} in air. The n_{Fe}/n_P ratio of $FePO_4{\cdot}2H_2O$ precursors was analysed by ICP. The crystal structure of $FePO_4$ and $LiFePO_4$/C samples were analysed by a Bruker D8 series X-ray diffraction using Cu Kα radiation (λ = 1.5406 Å) operated at 40 kV and 40 mA. The 2θ was scanned from 10 degree to 70 degree (with a resolution of 0.01 degree). The surface morphology of $FePO_4{\cdot}xH_2O$ particles were observed by scanning electron microscope (Sigma VP, ZEISS, Germany) and transmission electron microscope (Tecnai F20, FEI, U.S). Surface area, porosity and particle size are analysed by Brunauer Emmett Teller (BET, Micromeritics ASAP 2020, U.S.A). In terms of tap density measurement, a simple method described by Wang et al. (2011) was employed. In this work, about 5 g of the samples were stored in 10 ml plastic centrifugal tube and tapped on the lab bench for 10 min by hand. The measured mass and volume of samples were then recorded to calculate the tap density.

2.4. Electrode and coin cell battery preparation

The electrochemical performance was tested using a CR2032 cointype cell. The cathode material was consisted of as-synthesized $LiFePO_4$/C composite, acetylene black and polytetrafluoroethylene (PTFE) binder in a weight ratio of 80:10:10. The mixture was coating on an aluminium foil. After rolling and drying at 80 °C for 8 h. The coated aluminium was cut into circular plates. The thickness and diameter of these circular plates were 0.06 and 12 mm respectively. The loading density of $LiFePO_4$ active material was around 5.0 mg cm^{-2}. 0.1 M $LiPF_6$ dissolved in ethylene carbonate (EC)/diethyl carbonate (DEC) (1:1 vol ratio) was used as the electrolyte. Celguard 2300 microporous film was adopted as the separator. The assembly of the cells was carried out in a dry Ar-filled glove box. The cells were galvanostatically charged and discharged at various rates within the voltage range of 2.5 V and 4.2 V (versus Li/Li+) on an electrochemical test workstation (CT2001A, Wuhan LAND Electronic Co. Ltd., China). All the electrochemical tests were carried out at room temperature. Cyclic voltammetry (CV) measurement was performed on an electrochemical workstation (Shanghai Chenhua Instrument Co. Ltd., China) over the potential range of 2.5–4.2 V (vs. Li/Li^+) at a scanning rate of 0.1 mVs^{-1}.

3. Results and discussion

3.1. Properties of $FePO_4$

3.1.1. Effect of impinging jetting reaction and ultrasonic assisted impinging jetting reaction

To determine the water containing content of $FePO_4{\cdot}xH_2O$ precursors, TG-DTA examination of the FP-UltraImp precursor particles was carried out by variation of the temperature from room temperature to 600 °C in air. The variations of the moisture are shown in Fig. 2. The TGA curve shows that the mass loss of $FePO_4{\cdot}xH_2O$ samples was found to be 22.5 wt%, indicating there are two molecules in one as-synthesized iron phosphate molecule. After 500 °C, the sample has no weight loss, indicating the dehydration of $FePO_4{\cdot}2H_2O$ occurs in the range between 178 and 500 °C.

It has been reported in the literature that the n_{Fe}/n_P ratio of $FePO_4{\cdot}2H_2O$ precursors is sensitive to the pH value of the working solution [20]. To investigate the effect of impinging stream and ultrasonic irradiation on the atom ratios between Fe ion and P ion, the $FePO_4{\cdot}2H_2O$ precursors prepared with different synthesis methods are

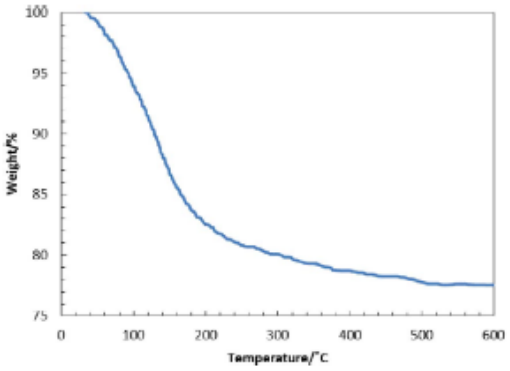

Fig. 2. TG/DTA curves of FP-UltraImp precursors at a heating rate of 10 °C min^{-1} in the air.

Table 1
The n_{Fe}/n_P ratio of $FePO_4{\cdot}2H_2O$ precursors prepared by different methods.

Samples	FP-UltraImp precursor	FP-Imp precursor	FP-Copre precursor
n_{Fe}/n_P	0.97	0.95	0.92

measured by inductively coupling the use of a plasma mass spectrometry (ICP-MS). The test results are shown in Table 1. The n_{Fe}/n_P ratio of all $FePO_4{\cdot}2H_2O$ samples obtained in this work is less than 1. The n_{Fe}/n_P ratio of FP-UltraImp precursor is 0.97, which is higher than the n_{Fe}/n_P ratio of FP-Imp precursor (0.95) and FP-Copre precursor (0.92). The ICP-MS result indicates that the n_{Fe}/n_P ratio of $FePO_4{\cdot}2H_2O$ precursors is sensitive to the synthesis method when the pH of working solution is maintained at the same value. When water is irradiated by ultrasound, large amount of $H^{\cdot}$ and $OH^{\cdot}$ are generated [21]. The main reactions are summarized below:

$$H_2O \rightarrow H^{\cdot} + OH^{\cdot}$$

$$H^{\cdot} + H^{\cdot} \rightarrow H_2$$

$$OH^{\cdot} + OH^{\cdot} \rightarrow H_2O_2$$

$$H^{\cdot} + OH^{\cdot} \rightarrow H_2O$$

For the synthesis of $FePO_4$ precursor, the main reactions are as follows:

$$Fe^{3+} + PO_4^{3-} \rightarrow FePO_4 \downarrow$$

$$Fe^{3+} + 3OH^{-} \rightarrow Fe(OH)_3 \downarrow$$

The generation of $FePO_4$ and $Fe(OH)_3$ is a homogeneous competitive-consecutive (series-parallel) reaction. Comparing with impinging jetting stream, ultrasonic irradiation can further improve micromixing effect and reduce micromixing time [22]. Therefore, with the help of ultrasound irradiation, the chemical reactions tend to produce $FePO_4$ and leading to an increased n_{Fe}/n_P ratio.

The X-ray powder diffraction (XRD) patterns of different $FePO_4$ samples, which are pre-heated at 600 °C for 10 h, are shown in Fig. 3. The calculated cell parameters and mean crystalline size of these samples are listed in Table 2. All the calculated lattice constants match well with anhydrous hexagonal structured $FePO_4$ (JCPDS card No. 29-0715, a = 5.035 Å, b = 5.035 Å, c = 11.245 Å), suggesting the formation of perfect crystalline $FePO_4$ composites after the thermal treatment. Simultaneously, it can be clearly observed that the intensities of the diffraction peaks decrease with the use of impinging jet reactor and ultrasonic irradiation, which may suggest that the adoption of impinging jet stream and ultrasonic irradiation have remarkable

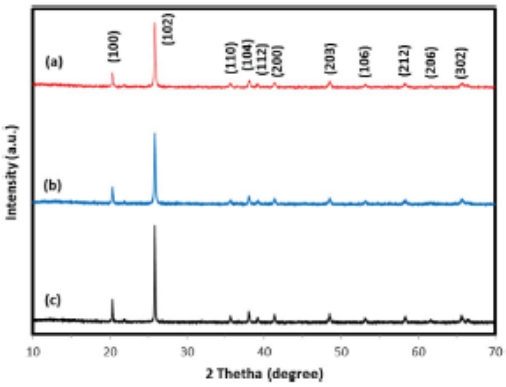

Fig. 3. X-ray diffraction patterns of different $FePO_4$ composites (a) FP-UltraImp, (b) FP-Imp, and (c) FP-Copre.

Table 2
Calculated lattice parameters and nuclei size of as-synthesized $FePO_4$ samples.

	a(Å)	b(Å)	c(Å)	V(Å^3)	Mean crystalline size(nm)
FP-UltraImp	5.0412	5.0412	11.2462	285.8075	42.9
FP-Imp	5.0365	5.0365	11.2445	285.2317	48.5
FP-Copre	5.0362	5.0362	11.2482	285.2916	82.7

effect on the crystallinity of the products. The highest intensities of FP-Copre, FP-Imp and FP-UltraImp composites around 25.83 degree are 4184, 3218 and 2949, respectively. The reason of lower intensities of FP-Imp and FP-UltraImp samples may be attributed to their smaller mean crystalline size [23].

The BET specific surface area and pore size distribution of the $FePO_4{\cdot}2H_2O$ precursors have been characterized by nitrogen adsorption-desorption analysis. It can be seen that the N_2 sorption isotherm of all $FePO_4{\cdot}2H_2O$ precursors (Fig. 4a) were Type IV. Their big hysteresis loops can be evidenced by the presence of *meso*-pores (> 2 nm and < 50 nm) and large surface areas. Table 3 shows the effect of impinging stream and ultrasonic irradiation has had on the surface area, porosity and average nuclei size of the $FePO_4{\cdot}2H_2O$ samples. The average nuclei size of three $FePO_4{\cdot}2H_2O$ precursors confirms the same trend obtained from XRD analysis. The average nuclei sizes of FP-UltraImp and FP-Imp precursors are 44.60 and 54.80 nm, respectively, which is smaller than the average nuclei size of FP-Copre precursor (77.92 nm). In addition, it can be seen that the FP-Copre precursor shows the largest average pore diameter of 23.2 nm, and exhibits the smallest BET surface area and total pore volume, corresponding to 77 $m^2\,g^{-1}$ and 0.446 $cm^3\,g^{-1}$ respectively. In contrast, the precursor of FP-UltraImp sample shows the highest BET surface area of 134.54 $m^2\,g^{-1}$ and the smallest average pore size of 15.2 nm. For the FP-Imp precursor, it has the highest pore volume of 0.663 $cm^3\,g^{-1}$. The analytical results of pore size distribution based on desorption of the $FePO_4{\cdot}2H_2O$ precursors synthesized using different methods are shown in Fig. 4b and c. It becomes clear as can be seen from the figure that the FP-Imp precursor has a significant amount of large-mesopores in the range of 20–50 nm, leading to its highest pore volume. The reason that FP-UltraImp precursors have the highest specific surface area of porosity is mainly ascribed to the small-mesopores that fall into the range from 4 to 20 nm. Obviously, both FP-UltraImp and FP-Imp precursors feature pores in mesoporous (> 2 nm and < 50 nm) range, indicating that the acquirement of large surface areas of FP-UltraImp and FP-Imp precursors are caused by not only the reduction in the average nuclei size but also the increase in the numbers of mesopores rather than micropores (< 2 nm) or macropores (> 50 nm). Generally speaking, a larger specific surface area can

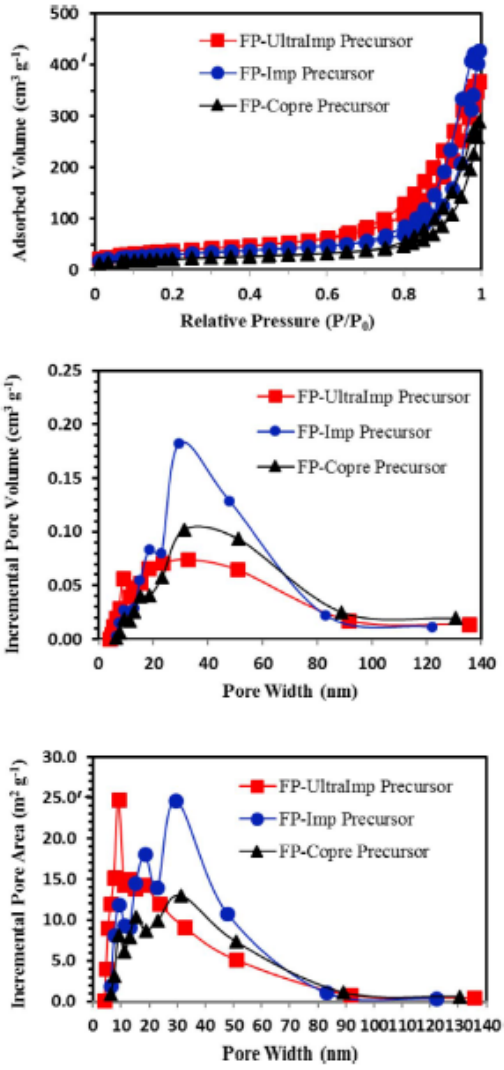

Fig. 4. The BJH desorption pore size distribution of $FePO_4{\cdot}2H_2O$ samples prepared with different synthesis methods.

Table 3
N_2 adsorption-desorption analysis results of $FePO_4{\cdot}2H_2O$ precursors prepared with different synthesis methods.

Samples	Surface area ($m^2\,g^{-1}$)	Average Pore Width (nm)	Total pore volume ($cm^3\,g^{-1}$)	Average nuclei size (nm)
FP-UltraImp precursor	134.54	15.2	0.570	44.60
FP-Imp precursor	109.49	21.4	0.663	54.80
FP-Copre precursor	77.00	23.2	0.446	77.92

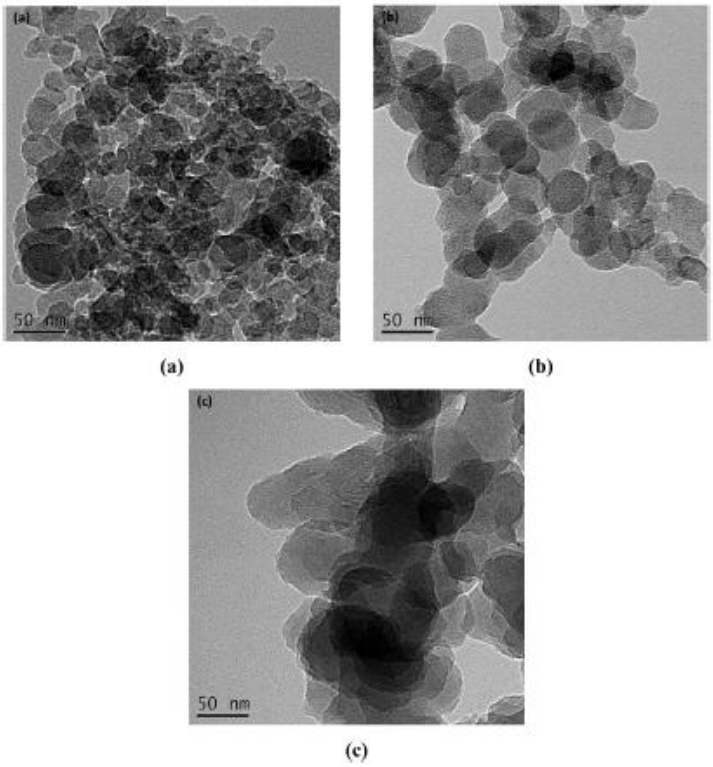

Fig. 5. TEM images of different $FePO_4$ samples (a) FP-Ultralmp, (b) FP-Imp, and (c) FP-Copre.

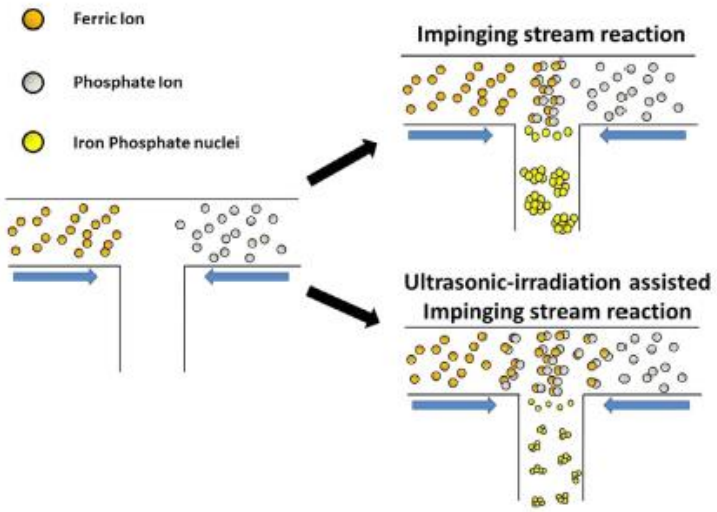

Fig. 6. Schematic illustration of the synthesis processes of impinging stream reaction and ultrasonic-assisted impinging stream reaction.

effectively increase the interface between electrode and electrolyte, thus enhancing an effective charge transfer across the interface. A reduced nuclei size is beneficial to shortening the diffusion distance of lithium ion, giving rise to an improved electrochemical performance for $LiFePO_4$. Meanwhile, mesoporous structure can facilitate the penetration of electrolyte and improve the electronic conductivity. However, it has been proved that large surface area and high pore volume of electrode materials also limits its application in industry due to the reduced

Table 4
N_2 adsorption-desorption analysis results of $FePO_4{\cdot}2H_2O$ precursors prepared with different reagent concertation by UR and UIJR methods (Volumetric feeding rate = 85.74 ml/min).

Precursors	Reactant concentration ($mol\ L^{-1}$)	Specific surface area ($m^2 g^{-1}$)	Total pore adsorption volume ($cm^3 g^{-1}$)	Average primary grain size (nm)
FP-Imp-0.5	0.5	39.53	0.203	151.78
FP-Imp-1.0	1.0	109.49	0.663	54.80
FP-Imp-1.5	1.5	71.24	0.315	84.22
FP-UltraImp-0.5	0.5	87.94	0.580	66.67
FP-UltraImp-1.0	1.0	134.54	0.570	44.60
FP-UltraImp-1.5	1.5	98.69	0.477	60.79

Table 5
N_2 adsorption-desorption analysis results of $FePO_4{\cdot}2H_2O$ precursors prepared with different volumetric feeding rate by UR and UIJR methods (Reagent concentration = 1.0 $mol\ L^{-1}$).

Precursors	Volumetric feeding rate (ml/min)	Specific surface area ($m^2 g^{-1}$)	Total pore adsorption volume ($cm^3 g^{-1}$)	Average primary grain size (nm)
FP-Imp-20	17.15 (20 rpm)	21.94	0.087	273.48
FP-Imp-60	51.44 (60 rpm)	34.75	0.263	172.69
FP-Imp-100	85.74 (100 rpm)	109.49	0.663	54.80
FP-UltraImp-20	17.15 (20 rpm)	101.89	0.652	58.89
FP-UltraImp-60	51.44 (60 rpm)	96.88	0.576	59.60
FP-UltraImp-100	85.74 (100 rpm)	134.54	0.570	44.60

tap density and volumetric energy density [24]. For FP-Ultra Imp precursor, its small-mesoporous structure is thus to play roles in facilitation of the electrolyte penetration, improvement of the electronic conductivity and maintenance of an average tap density and volumetric density of the resulting LFP-UltraImp sample.

Fig. 5 shows the TEM images of different $FePO_4$ samples after heat treatment at 600 °C for 10 h. The FP-UltraImp primary nuclei (Fig. 5a) exhibits near-spherical shape with a primary crystallite size of 20–50 nm. In Fig. 5b, the FP-Imp composites have a larger nuclei size (around 50 nm) and similar near-spherical shape with FP-UltraImp. Moreover, the pore size of FP-Imp is also larger than that of FP-UltraImp. In contrast, FP-Copre sample exhibits irregular nuclei shape and the nuclei size is increased to 50–100 nm. It can be seen clearly from the figure that all three $FePO_4$ samples still possess nano-sized nuclei and porous structure after heat treatment, which may provide high quality precursors for synthesizing $LiFePO_4$/C nanocomposites.

According to the XRD, BET and TEM results, there exists a clear tendency that the use of both ultrasonic irradiation and impinging jet reaction can have a significant effect on increasing surface area, and reducing primary grain size and pore diameter of $FePO_4{\cdot}2H_2O$ precursors. To understand the effect of ultrasonic irradiation and impinging jet stream on the formation of porous $FePO_4{\cdot}2H_2O$ precursor, a schematic illustration is presented in Fig. 6. In the impinging stream reaction, the streams of Fe^{3+} and PO_4^{3-} solutions impinge on each other directly, which can deliver a high level of supersaturation and sufficient mixing of the raw materials in an extremely short time ($\sim 10^{-7}$ s). The initial high supersaturation level can enhance the micromixing in the solution, thus facilitating nucleation rate and generating large amount of iron phosphate nuclei. The level of supersaturation level will decrease because the rapid nucleation process also consumes large amount of raw materials. Thus, particle growth process is confined, which results in a smaller average nuclei size. Additionally, it is conjectured that the improved molecular collision rate gives rise to the generation of large amount of large-mesopores as can be seen from BET analysis.

The higher BET surface area, smaller average pore width and nuclei size of FP-UltraImp precursor might be the result of joint effect of ultrasonic irradiation and high speed impinging jet streams. In joint ultrasonic-irradiation impinging stream reaction, ultrasonic irradiation can further improve the diffusion, promoting the reaction and nucleation. Therefore, the average nuclei size of FP-UltraImp precursors is smaller than FP-Imp precursors. In addition, the function of ultrasonic irradiation can prevent the agglomeration and break large agglomerated particles into smaller particles to increase surface area. The formed small-mesopores of FP-UltraImp may be attributed to the breakup of the surface film at liquid-solid interfaces which is caused by shock waves and microjets [16]. This may explain why FP-UltraImp precursor can attain the smallest average nuclei size, largest specific surface area, and small-mesopores among three preparation routes.

3.1.2. *Effect of reagent concentration*

To further understand the optimal concentration of initial reagents, $FePO_4{\cdot}2H_2O$ precursors were synthesized with three different reagent concentration (C = 0.5, 1.0 and 1.5 $mol\ L^{-1}$) by using UIJR and IJR methods and the volumetric feeding rate was maintained at 85.74 ml/min.

The BET specific surface area, total pore adsorption volume and pore size distribution of the $FePO_4{\cdot}2H_2O$ precursors synthesized under

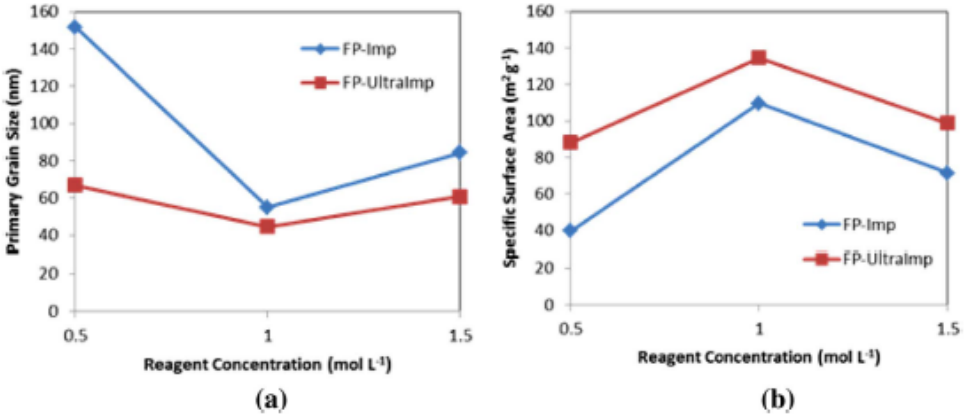

Fig. 7. The relationship between reagent concentration and (a) primary grain size; (b) specific surface area.

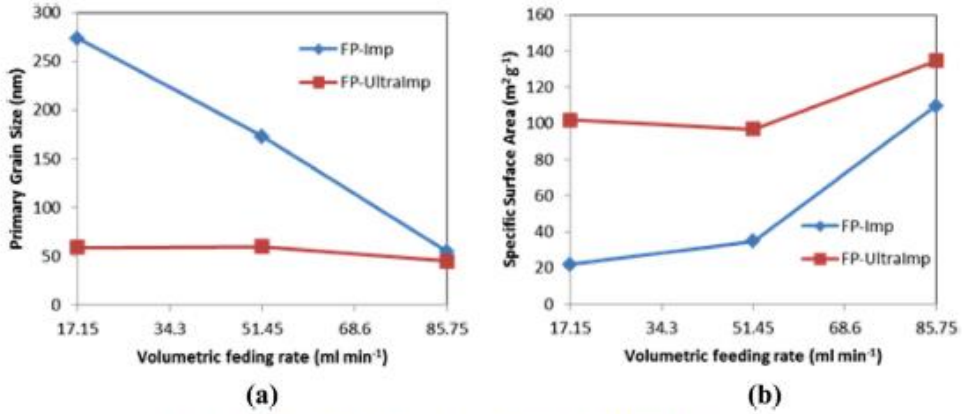

Fig. 8. The relationship between volumetric feeding rate and (a) primary grain size; (b) specific surface area.

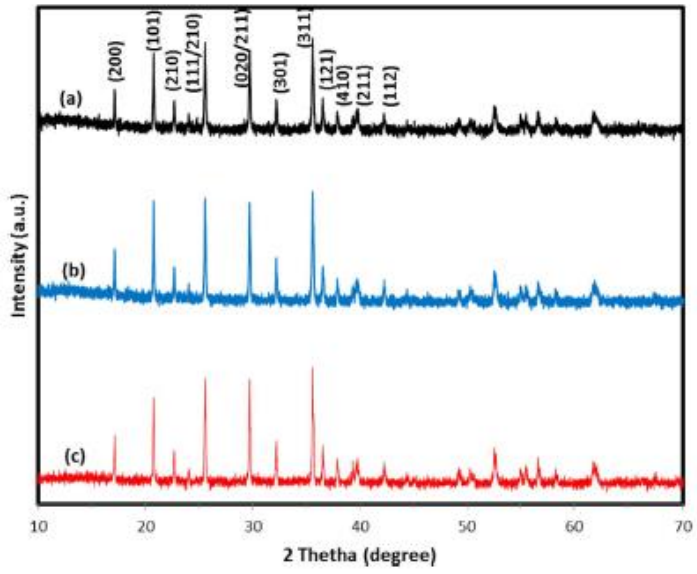

Fig. 9. X-ray diffraction patterns of as-synthesized $LiFePO_4/C$ composites: (a) LFP-UltraImp, (b) LFP-Imp, and (c) LFP-Copre.

Table 6
Lattice parameters of as-synthesized $LiFePO_4/C$ samples.

	a(Å)	b(Å)	c(Å)	V(Å^3)
LFP-UltraImp	10.3254	6.0078	4.6916	291.0337
LFP-Imp	10.3322	6.0071	4.6896	291.0673
LFP-Copre	10.3276	6.0069	4.6906	290.9901

different conditions have been characterized by nitrogen adsorption-desorption analysis. As shown in Table 4 and Fig. 7, increasing the reagent concentration had significant influence on the surface area, porosity and average nuclei size of the $FePO_4$ precursor samples.

When the reagent concentration is 1.0 mol/L, the $FePO_4$ precursor sample (FP-UltraImp-1.0) synthesized by UIJR method features largest surface area (134.54 $m^2 g^{-1}$) and smallest average nuclei size (44.60 nm). The measured BET surface area for FP-UltraImp-0.5 and FP-UltraImp-1.5 precursors is 87.94 and 98.69 $m^2 g^{-1}$, respectively. Meanwhile, the average nuclei size of these two samples is 66.67 and 60.79 nm respectively. When $FePO_4$ precursor samples are synthesized by IJR method, similar tendency can be observed and FP-Imp-1.0 relative large surface area (109.49 $m^2 g^{-1}$) and adsorption pore volume (0.663 $cm^3 g^{-1}$), as well as a smaller average primary grain size (54.80 nm).

Generally, a higher initial reactant concertation can increase supersaturation level and nucleation rate in IRJ and UIRJ reaction. However, as the volumetric feeding rate is not changed. Therefore, large amount of nanoscale FePO4 nucleus will be synthesized in a short time. Some of the nucleus might be attached to the impinging stream reactor and blocked the chamber slightly. Then heterogeneous nucleation happens on the attached nuclei. Thus, these nuclei might be agglomerated and grown up in impinging stream reactor, leading to an enlarged nuclei size, and reduced surface area and pore adsorption volume. In comparison, ultrasonic irradiation can further increase micromixing effect and prevent agglomeration in impinging jetting

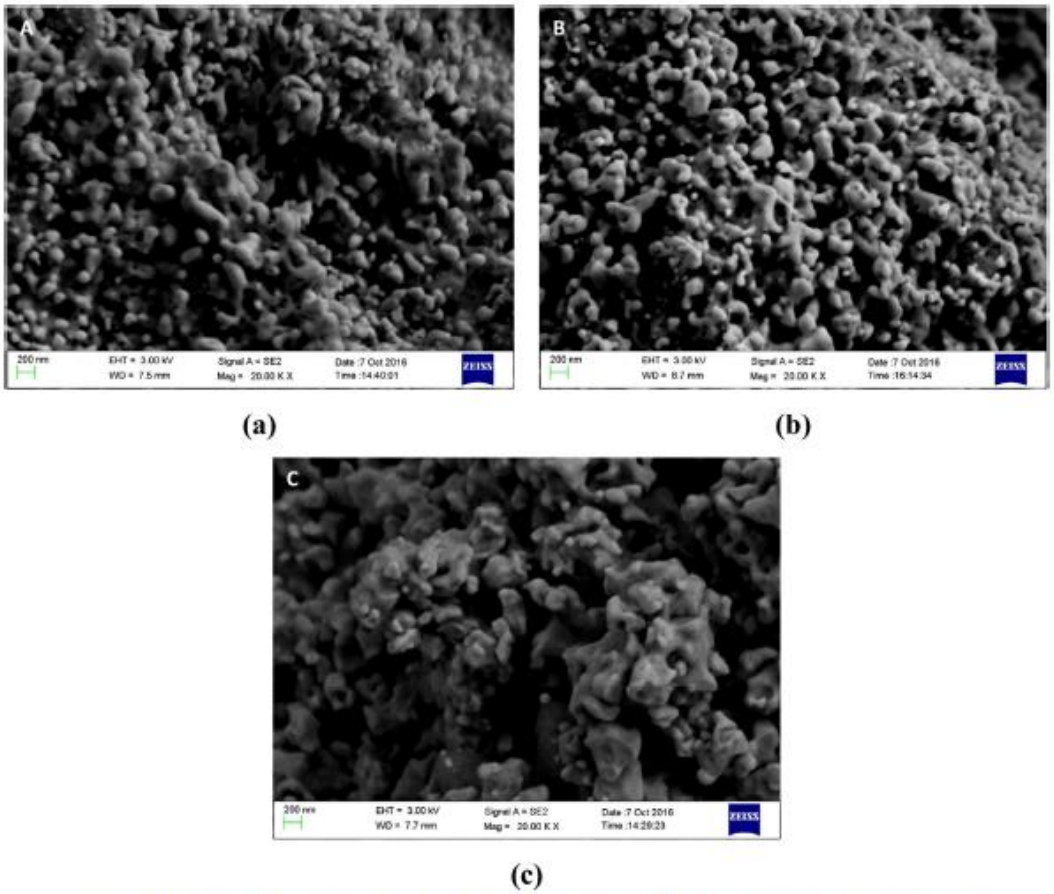

Fig. 10. SEM images of $LiFePO_4$/C composites from the precursors prepared with different methods (a) LFP-UltraImp, (b) LFP-Imp, and (c) LFP-Copre.

reactor, leading to a reduced primary grain size and enlarged surface area.

3.1.3. Effect of volumetric feeding rate

To evaluate the effect of volumetric feeding rate, $FePO_4{\cdot}2H_2O$ precursors were prepared at three different level (V = 17.15, 51.44 and 85.75 ml/min). It has been found that the increasing of volumetric feeding rate result in reduction of average primary grain size and improvement of specific surface area of $FePO_4{\cdot}2H_2O$ precursors, especially when the samples are prepared by IJR.

Table 5 and Fig. 8 show the BET analysis results of the $FePO_4{\cdot}2H_2O$ samples prepared with 3 different volumetric feeding rate by IJR and UIJR methods. When using IJR method, the surface area and total adsorption volume increase with increasing the volumetric feeding rate. The maximum specific surface area (109.49 $m^2\,g^{-1}$) and total adsorption volume (0.663 $cm^3\,g^{-1}$) were obtained when the volumetric feeding rate is 85.74 ml/min. On the contrary, it was found that the average primary grain size of $FePO_4{\cdot}2H_2O$ samples decrease significantly as the increasing of volumetric feeding rate. Therefore, the sample FP-Imp-100 precursor has the best abundant mesoporous structure. This is mainly ascribed to the reduced micromixing time and increased mass transfer rate and collision rate. When ultrasonic irradiation is applied in impinging jetting reaction, the specific surface area, total pore adsorption volume and average primary grain size changed slightly with the increasing of volumetric feeding rate, especially at a relatively lower rate (V = 17.15 and 51.44 ml/min). This indicates that the application of ultrasonic irradiation can enhance micromixing more significantly than increasing of volumetric feeding rate.

3.2. Properties of $LiFePO_4$/C

Those as-synthesized $FePO_4$ precursors by using different preparation routes as discussed in the preceding section were used for further synthesizing $LiFePO_4$/C positive electrode particles. The XRD patterns and calculated lattice parameters of the three as-synthesized $LiFePO_4$/C samples are shown in Fig. 9 and listed in Table 6. All diffraction peaks seen from XRD patterns and crystal lattice parameters are also well indexed to accord with $LiFePO_4$ which has the orthorhombic structure (JCPDS card No. 40-1499, a = 10.347 Å, b = 6.019 Å, c = 4.704 Å), suggesting all the three $LiFePO_4$/C nanocomposites were synthesized without any appreciable impurity phases.

The morphology of $LiFePO_4$/C composites prepared by different methods was also examined by scanning electron microscopy (SEM). It can be seen from Fig. 10a and b that both LFP-UltraImp and LFP-Imp samples present a similar particle morphology consisting of

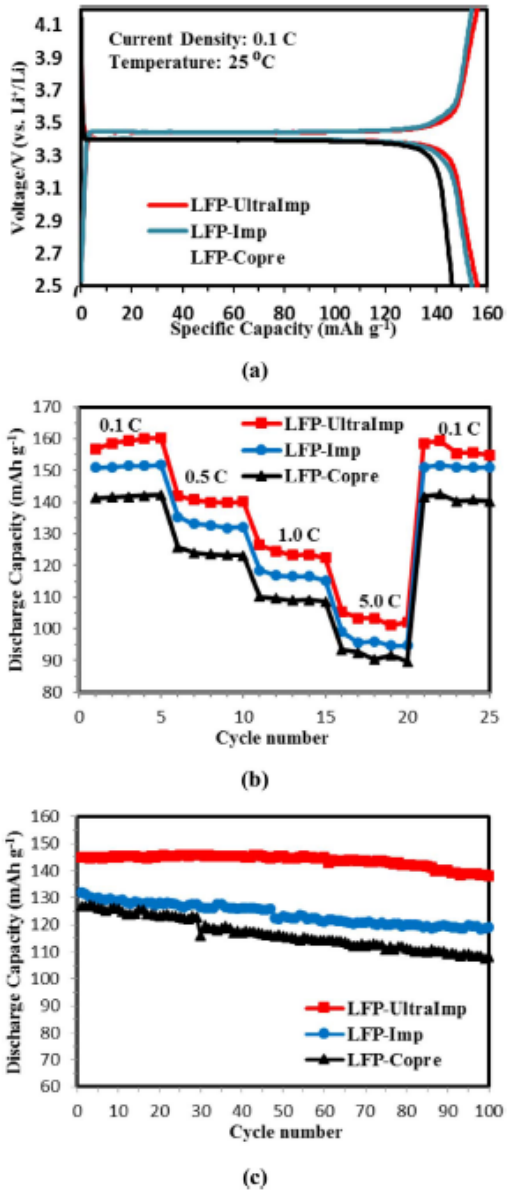

Fig. 11. Electrochemical performance of LFP-UltraImp, LFP-Imp and LFP-Copre composites (a) The initial charge/discharge curves at 0.1 C, (b) Rate performance at various rates, (c) Cycling performance at 0.5 C for 100 cycles.

nanospheres with sizes in the range of 80 nm–300 nm. These nanospheres interweave together and form high porosity structure. By comparison, Fig. 10c shows the LFP-Copre composite has a structure with lower porosity while the corresponding particle size becomes larger than those of LFP-UltraImp and LFP-Imp samples.

The electrochemical properties of all $LiFePO_4$/C samples were tested in 2032-type coin half-cells batteries. Fig. 11a shows charge/discharge

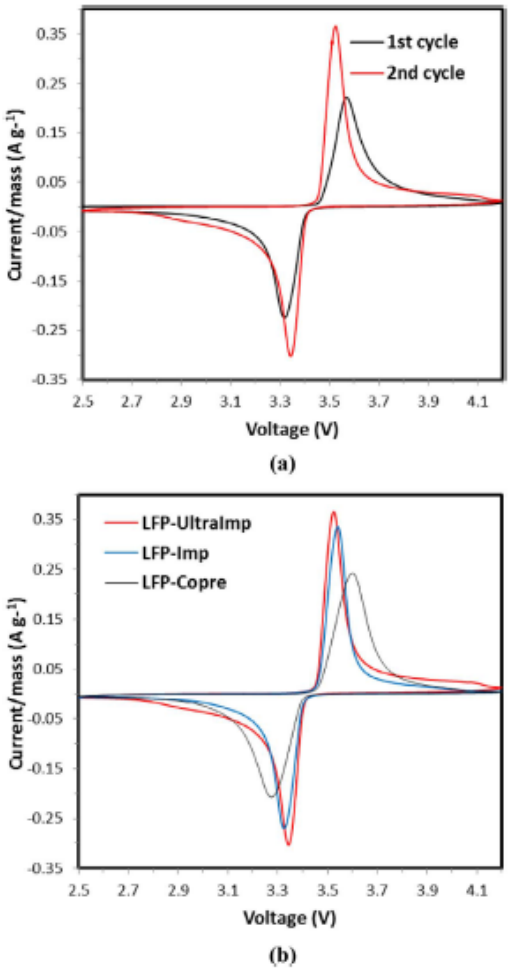

Fig. 12. Cyclic voltammogram curves of $LiFePO_4$/C samples at a scan rate of 0.1 mV s^{-1} (a) the first and second cycle of LFP-UltraImp sample, (b) the second cycle of three $LiFePO_4$/C samples.

capacities for the LFP-Copre, LFP-Imp and LFP-UltraImp composites within the voltage range of 2.5 V and 4.2 V (versus Li/Li+) at 0.1 C (17 mA g^{-1}). The charge and discharge plateaus of all three $LiFePO_4$/C samples are 3.45 V and 3.40 V respectively. At low charge/discharge rates, both LFP-UltraImp and LFP-Imp samples exhibit comparable performance. The discharge capacities of LFP-UltraImp and LFP-Imp can reach 156.7 mA h g^{-1} and 150.9 mA h g^{-1} respectively, which is higher than the discharge capacity of LFP-Copre (141.3 mA h g^{-1}). As shown in Fig. 11b, the discharge capacities of LFP-Ultra Imp at 0.5, 1, and 2 C rate can reach up to 140.7, 126.5 and 105.4 mA h g^{-1} respectively. The LFP-Imp composite delivers a discharge capacity of 135.3, 118.5 and 99.1 mA h g^{-1} at 0.5, 1 and 2 C. The LFP-UltraImp sample behaves poorly and exhibits the lowest discharge capacity, 125.8, 110.2 and 93.4 mA h g^{-1} at 0.5, 1, and 2 C. To investigate the recyclability of the as-synthesized $LiFePO_4$/C samples, the coin cells were cycled at 0.5 C for 100 cycles. As can be seen from Fig. 11c, it was found that LFP-Imp and LFP-Copre can exhibit discharge capacities of 119.1 and 108.0 mA h g^{-1} at 0.5 C after 100 cycles, which are about

90.2 and 85.0% of the initial discharge capacity respectively. In contrast, LFP-UltraImp sample delivers the best cycling stability. The LFP-UltraImp sample can show a discharge capacity of 138.0 mA h g^{-1}, with less than 4.7% loss of discharge capacity after 100 cycles at 0.5 C.

The cyclic voltammogram curves of LFP-UltraImp composite for the first two cycles are shown in Fig. 12a. During the first cycle, the oxidation and reduction peaks, which are corresponding to the charge/discharge reactions of the Fe^{3+}/Fe^{2+} redox couple, appear at 3.569 and 3.319 V. During the second cycle, the oxidation and reduction peaks take place at 3.541 and 3.326 V respectively. The voltage peak difference between oxidation and reduction is decreased from 0.25 V to 0.181 V. Meanwhile, the current/mass peaks are increased from 0.447 to 0.669 A g^{-1}. The difference of voltage and current/mass peaks indicate that electrode material is activated, and the electrochemical reversibility has been established after the first cycle [25]. In contrast, the potential difference for both LFP-Imp and LFP-Copre is only 0.215 and 0.326 V respectively (Fig. 12b). The larger and narrower current/mass peaks implicitly confirm that LFP-UltraImp composites have an improved reversibility and better kinetics of electrochemical reaction [26,27].

The better electrochemical performance of LFP-UltraImp sample can be attributed to reduced particle size, mesoporous structure and large specific surface area, as well as a higher n_{Fe}/n_P ratio. It is believed that this structure can shorten the diffusion distance of lithium ion, increase electrolyte/electrode interface area and ensure effective electrolyte permeation into electrode materials, which lead to a relatively high utilization of the active $LiFePO_4$ material. The relatively high n_{Fe}/n_P ratio of FP-UltraImp also contribute to the better electrochemical properties of LFP-UltraImp. In the lithiation/delithiation process, Li^+ moves through 1D channels which are parallel to b axis. However, 1D channel is easy to be blocked by impurities [20]. The relatively high n_{Fe}/n_P ratio of FP-UltraImp indicates that LFP-UltraImp composite has higher purity and few blocked 1D channel. Furthermore, besides good electrochemical properties, LFP-UltraImp composite also possesses higher tap density than LFP-Imp due to the smaller pore width and smaller pore volume. The tap density of LFP-UltraImp composites can reach 1.33 g cm^{-3} in contrast to 1.17 g cm^{-3} for LFP-Imp composites. All of results obtained have clearly indicated that LFP-UltraImp samples have better electrochemical properties and higher volumetric energy density, thus demonstrating that the adoption of LFP-UltraImp route is an effective way to synthesize the high performance positive electrode precursor particle materials.

4. Conclusions

Three different routes were designed for synthesis of $FePO_4$ positive electrode precursor particles, which have been used for amalgamating lithium iron phosphate cathode particles to fabricate the lithium cell battery. It has been demonstrated that the adoption of ultrasonic-assisted impinging stream reaction is an effective approach to produce high electrochemical performance positive electrode precursor particles. The LFP-UltraImp samples obtained from the experiments have shown an initial discharge capacity of 156.7 mA h g^{-1} at 0.1 C, and exhibited 138.0 mA h g^{-1} after 100 cycles at 0.5 C, which is 95.3% of the initial discharge capacity. The conclusions reached from the current study, in terms of synthesis of mesoporous $FePO_4$ precursors for improving the electrochemical performance of $LiFePO_4$/C, can be summarized:

1) The adoption of impinging stream reaction can be beneficial to generation of $FePO_4$ nanocomposites that have smaller primary grain size, large-mesoporous structures and higher specific surface areas.
2) Application of ultrasonic irradiation can lead to synthesis of small-mesoporous $FePO_4$ precursors that have nanoscale primary nuclei size and high specific surface areas. It can also remarkably improve the purity of $FePO_4$ precursors due to the increased mass diffusion rate between $FePO_4$ and Li_2CO_3.
3) The formation of small-mesopores contributes to an improved electrochemical property and relatively high volumetric energy density of LFP-UltraImp.

Acknowledgement

The authors wish to thank the support from National Natural Science Foundation of China (NSFC) (Grant Nos. 21576141, 91534118) and Zhejiang Provincial Natural Science Foundation (Grant No. LY15B060001). This work was carried out at the International Doctoral Innovation Centre (IDIC). Bin Dong would also like to acknowledge the support through the Ph.D. scholarship of the International Doctoral Innovation Centre (IDIC) of University of Nottingham Ningbo China.

References

[1] H. Shu, X. Wang, W. Wen, Q. Liang, X. Yang, Q. Wei, B. Hu, L. Liu, X. Xue, Y. Song, M. Zho, Y. Bai, L. Jiang, M. Chen, S. Yang, J. Tan, Y. Liao, H. Jiang, Effective enhancement of electrochemical properties for $LiFePO_4$/C cathode materials by Na and Ti co-doping, Eletrochim. Acta 89 (2013) 479–487.
[2] P. Gibot, M. Casas-Cabanas, L. Laffont, S. Levasseur, P. Carlach, S. Hamelet, J.M. Tamscon, C. Masquelier, Room-temperature single-phase Li insertion/extraction in nanoscale $LixFePO_4$, Nat. Mater. 7 (2008) 741–747.
[3] Y. Ding, Y. Jiang, F. Xu, J. Yin, H. Ren, Q. Zhuo, Z. Long, P. Zhang, Preparation of nano-structured LiFePO4/graphene composites by co-precipitation method, Eletrochem. Commun. 12 (2010) 10–13.
[4] K.S. Park, J.T. Son, H.T. Chung, S.J. Kim, C.H. Lee, H.G. Kim, Synthesis of $LiFePO_4$ by co-precipitation and microwave heating, Eletrochem. Commun. 5 (2003) 839–842.
[5] A.K. Padhi, K.S. Nanjundaswamy, C. Masquelier, S. Okada, J.B. Goodenough, Effect of structure on the Fe^{3+}/Fe^{2+} redox couple in iron phosphates, J. Electrochem. Soc. 144 (1997) 1609–1613.
[6] H.C. Shin, S.B. Park, H. Jang, K.Y. Chung, W. Cho, C.S. Kim, B.W. Cho, Rate performance and structural change of Cr-doped $LiFePO_4$/C during cycling, Eletrochim. Acta 53 (2008) 7946–7951.
[7] S.Y. Chung, J.T. Bloking, Y.M. Chiang, Electronically conductive phospho-olivines as lithium storage electrodes, Nat. Mater. 1 (2002) 123–128.
[8] L. Guo, Y. Zhang, L. Ma, Y. Zhang, E. Wang, Y. Bi, D. Wang, W.C. McKee, Y. Xu, J. Chen, Q. Zhang, C. Nan, L. Gu, P.G. Bruce, Z.G. Peng, Unlocking the energy capabilities of micron-sized LiFePO4, Nat. Commun. 6 (2015) 7898–7905.
[9] J. Liu, T.E. Conry, X. Song, M.M. Doeff, T.J. Richardson, Nanoporous spherical $LiFePO_4$ for high performance cathodes, Energ. Environ. Sci. 4 (2011) 885–888.
[10] J. Liu, A. Manthiram, Understanding the improvement in the electrochemical properties of surface modified 5 V $LiMn_{1.42}Ni_{0.42}Co_{0.16}O_4$ spinel cathodes in lithium-ion cells, Chem. Mater. 21 (2011) 1698–1707.
[11] A. Vu, Y. Qian, A. Stein, Porous electrode materials for lithium-ion batteries – how to prepare them and what makes them special, Adv. Energy. Mater 2 (2012) 1056–1085.
[12] K.X. Wang, X.H. Li, J.S. Chen, Surface and interface engineering of electrode materials for lithium-ion batteries, Adv. Mater. 27 (2015) 527–545.
[13] P. Adelhelm, Y.S. Hu, L. Chuenchom, M. Antonietti, B.M. Smarsly, J. Maier, Generation of hierarchical meso- and macroporous carbon from mesophase pitch by spinodal decomposition using polymer templates, Adv. Mater. 19 (2007) 4012–4017.
[14] C.M. Doherty, R.A. Caruso, C.J. Drummond, High performance LiFePO4 electrode materials: influence of colloidal particle morphology and porosity on lithium-ion battery power capability, Energy Environ. Sci. 3 (2010) 813–823.
[15] Z. Wang, F. Li, N.S. Ergang, A. Stein, Effects of hierarchical architecture on electronic and mechanical properties of nanocast monolithic porous carbons and carbon−carbon nanocomposites, Chem. Mater. 18 (2006) 5543–5553.
[16] K.S. Suslick, G.J. Price, Applications of ultrasound to materials chemistry, Annu. Rev. Mater. Sci. 29 (1999) 295–326.
[17] H. Xu, B.W. Zeiger, K.S. Suslick, Sonochemical synthesis of nanomaterials, Chem. Soc. Rev. 42 (2013) 2555–2567.
[18] Y. Huang, P. Wang, Y. Yuan, X. Ren, F. Yang, Synergistic degradation of chitosan by impinging stream and jet cavitation, Ultrason Sonochem. 27 (2015) 592–601.
[19] S.W. Siddiqui, P.J. Unwin, Z. Xu, S.M. Kresta, The effect of stabilizer addition and sonication on nanoparticle agglomeration in a confined impinging jet reactor, Colloids Surf. A Physicochem. Eng. Asp. 350 (2009) 38–50.
[20] P. Yan, L. Lu, X.M. Liu, Y. Cao, Z.P. Zhang, H. Yang, X.D. Shen, An economic and scalable approach to synthesize high power LiFePO4/C nanocomposites from nano-FePO4 precipitated from an impinging jet reactor, J. Mater. Chem. A 35 (2013) 10429–10435.
[21] J.H. Bang, K.S. Suslick, Applications of ultrasound to the synthesis of nanostructured materials, Adv. Mater. 22 (2010) 1039–1059.
[22] J. Mahajan, J.K. Donald, Micromixing effects in a two impinging jets precipitator, AIChE J. 42 (1996) 1801–1814.
[23] H. Liu, C. Miao, Y. Meng, Q. Xu, X. Zhang, Z. Tang, Effect of graphene nanosheets

content on the morphology and electrochemical performance of $LiFePO_4$ particles in lithium ion batteries, Eletrochim. Acta 135 (2014) 311–318.
[24] L. Tan, Q. Tang, X. Chen, A. Hu, W. Deng, Y. Yang, L. Xu, Mesoporous LiFePO4 microspheres embedded homogeneously with 3D CNT conductive networks for enhanced electrochemical performance, Eletrochim. Acta 137 (2014) 344–351.
[25] Y. Wang, J. Wang, J. Yang, Y. Nuli, High-rate LiFePO4 electrode material synthesized by a novel route from FePO4·4H2O, Adv. Funct. Mater. 16 (2006) 2135–2140.
[26] C.S. Sun, Y. Zhang, X.J. Zhang, Z. Zhou, Structural and electrochemical properties of Cl-doped $LiFePO_4$/C, J. Power Sources 195 (2010) 3680–3683.
[27] Y. Shi, S.L. Chou, J.Z. Wang, D. Wexler, H.J. Li, H.K. Liu, Y.P. Wu, Graphene wrapped $LiFePO_4$/C composites as cathode materials for Li-ion batteries with enhanced rate capability, J. Mater. Chem. 22 (2012) 16465–16470.

Ultrasonics - Sonochemistry 42 (2018) 452–463

Contents lists available at ScienceDirect

Ultrasonics - Sonochemistry

journal homepage: www.elsevier.com/locate/ultson

Controllable synthesis of $(NH_4)Fe_2(PO_4)_2(OH)\cdot 2H_2O$ using two-step route: Ultrasonic-intensified impinging stream pre-treatment followed by hydrothermal treatment

Bin Dong[a,b], Guang Li[a,b,*], Xiaogang Yang[a,b,*], Luming Chen[a,b], George Z. Chen[a,c]

[a] International Doctoral Innovation Centre, University of Nottingham Ningbo China, University Park, Ningbo 315100, PR China
[b] Department of Mechanical, Materials and Manufacturing Engineering, University of Nottingham Ningbo China, University Park, Ningbo 315100, PR China
[c] Department of Chemical and Environmental Engineering, University of Nottingham Ningbo China, University Park, Ningbo 315100, PR China

ARTICLE INFO

Keywords:
Ultrasonic-intensified impinging stream
Hydrothermal treatment
pH value
Reagent concentration
$(NH_4)Fe_2(PO_4)_2(OH)\cdot 2H_2O$
$FePO_4$

ABSTRACT

$(NH_4)Fe_2(PO_4)_2(OH)\cdot 2H_2O$ samples with different morphology are successfully synthesized via two-step synthesis route – ultrasonic-intensified impinging stream pre-treatment followed by hydrothermal treatment (UIHT) method. The effects of the adoption of ultrasonic-intensified impinging stream pre-treatment, reagent concentration (C), pH value of solution and hydrothermal reaction time (T) on the physical and chemical properties of the synthesised $(NH_4)Fe_2(PO_4)_2(OH)\cdot 2H_2O$ composites and $FePO_4$ particles were systematically investigated. Nano-seeds were firstly synthesized using the ultrasonic-intensified T-mixer and these nano-seeds were then transferred into a hydrothermal reactor, heated at 170 °C for 4 h. The obtained samples were characterized by utilising XRD, BET, TG-DTA, SEM, TEM, Mastersizer 3000 and FTIR, respectively. The experimental results have indicated that the particle size and morphology of the obtained samples are remarkably affected by the use of ultrasonic-intensified impinging stream pre-treatment, hydrothermal reaction time, reagent concentration, and pH value of solution. When such $(NH_4)Fe_2(PO_4)_2(OH)\cdot 2H_2O$ precursor samples were transformed to $FePO_4$ products after sintering at 650 °C for 10 h, the SEM images have clearly shown that both the precursor and the final product still retain their monodispersed spherical microstructures with similar particle size of about 3 μm when the samples are synthesised at the optimised condition.

1. Introduction

$(NH_4)Fe_2(PO_4)_2(OH)\cdot 2H_2O$ is an isopytic mineral of $KFe_2(PO_4)_2OH\cdot 2H_2O$ (leucophosphite) and has received increasing attentions due to its magnetic properties and rich crystal chemistry [1]. The synthetic $(NH_4)Fe_2(PO_4)_2(OH)\cdot 2H_2O$ has been considered as a promising material and applied in the fields of catalysts [2], magnetics [3,4], optics [5], and lithium ion battery as positive electrode material [6–8]. As a functional material, the physical and chemical properties of $(NH_4)Fe_2(PO_4)_2(OH)\cdot 2H_2O$ are significantly affected by its morphology and particle size. Many methods have been developed to prepare $(NH_4)Fe_2(PO_4)_2(OH)\cdot 2H_2O$ particles, and various efforts are endeavoured to conduct the synthesis for different morphologies and particle sizes.

Shaowen Cao et al. (2010) proposed a simple one-step microwave-solvothermal ionic liquid method using [BMIM][BF_4] to prepare $(NH_4)Fe_2(PO_4)_2(OH)\cdot 2H_2O$ composites that contained various nanostructures, such as solid micro-spheres, microspheres with the core in the hollow shell, and double-shelled hollow microspheres while the synthesis was conducted by adjusting reagent concentration and microwave heating time [5]. Pure and well-crystallized spheniscidite $(NH_4)Fe_2(PO_4)_2(OH)\cdot 2H_2O$ was obtained by Delacourt et al. when NH_3 was added as an agent to raise pH value [8]. Shuyang Ju et al. (2013) reported a low temperature (at 80 °C) hydrothermal method to synthesize peanut-like microscale $(NH_4)Fe_2(PO_4)_2(OH)\cdot 2H_2O$ particles that were used as the precursor of $LiFePO_4$ positive electrode material [6]. The as-synthesized $LiFePO_4$ composites presented desirable electrochemical performance and high tap density. Li et al. (2014) synthesized ellipsoid-shaped $(NH_4)Fe_2(PO_4)_2(OH)\cdot 2H_2O$ composites that have micro-nano structures for being used as the precursor of $LiFePO_4$ positive electrode material, adopting a facile chemical precipitation route [7]. The obtained $LiFePO_4$ products exhibited excellent rate capability and good cyclic performance. Camino Trobajo et al. (2000) applied the hydrothermal method for preparation of $(NH_4)Fe_2(PO_4)_2(OH)\cdot 2H_2O$ at relatively high pH values of 9–11 and used excess amount of urea [1]. Kaipeng Wu et al. (2018) adopted sonochemical method to synthesise $(NH_4)Fe_2(PO_4)_2(OH)\cdot 2H_2O$ particles that possess red-blood-cell-like

* Corresponding authors at: Department of Mechanical, Materials and Manufacturing Engineering, University of Nottingham Ningbo China, University Park, Ningbo 315100, PR China.
Email addresses: guang.li@nottingham.edu.cn (G. Li), xiaogang.yang@nottingham.edu.cn (X. Yang).

https://doi.org/10.1016/j.ultsonch.2017.12.008
Received 5 November 2017; Received in revised form 4 December 2017; Accepted 4 December 2017
Available online 07 December 2017
1350-4177/

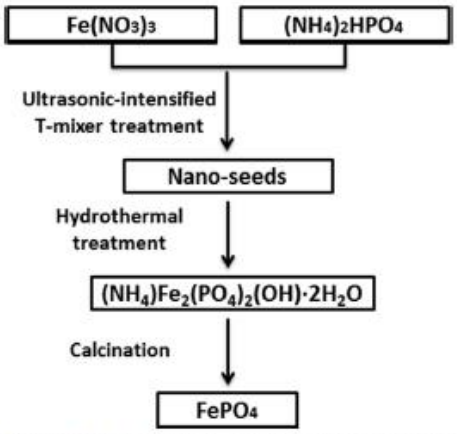

Fig. 1. Schematic illustration of main procedures in two-step hydrothermal synthesis of $(NH_4)Fe_2(PO_4)_2(OH)\cdot 2H_2O$ and $FePO_4$ samples.

shape [9]. In addition, Hong Zhou et al. (2010) also used hydrothermal method to synthesise $(NH_4)Fe_2(PO_4)_2(OH)\cdot 1.5H_2O$ which exhibited the behaviour of spontaneous magnetization below 25 K [4]. It can be claimed that as a self-assembly synthesis approach, hydrothermal method has been widely used to design and fabricate $(NH_4)Fe_2(PO_4)_2(OH)\cdot 2H_2O$ particles due to its mild operation temperature, simple process, homogeneous particle size distribution, improved cycle life and has the potential for large-scale production [10,11]. However, most of the synthesis route still needs long reaction time (up to 3 days) and additional additives (such as glycol and $C_2H_4O_4\cdot 2H_2O$).

It has been recognised that the application of high intensity ultrasonic-irradiation has a remarkable function which can significantly intensify the processes. It has been applied in-industrial manufacturing process and also the material synthesis process with the features of cost-effective and environmental-friendly. It has been revealed that the particles synthesized using ultrasonic treatment usually present porous structures [12,13]. Since ultrasonic wave can acoustically create the tiny cavitation, such instantaneous collapse of the created micro bubbles due to cavitation can provide the extreme conditions in a very small volume, characterised by occurrence of extremely high temperature up to 5000 K, pressures up to 1000 atm, and the heating and cooling rate greater than 10^{10} Ks^{-1} inside the cavitation zone [14]. Thus, ultrasonic-assisted hydrothermal synthesis method has been applied to the synthesis of catalysts [15–18], zeolite [19–22], hydrogen storage material [23], and MOFs [24].

Table 1
Dimensions of experiments for the synthesis of samples.

Experiments	Samples	Method	Reaction time (h)	pH value	Reagent concentration (C, mol L^{-1})
S1	Seed-UIHT	UIHT	0	0.8	1.0
S2	Prod-UIHT	UIHT	4	0.8	1.0
S3	Seed-HT	HT	0	0.8	1.0
S4	Prod-HT	HT	4	0.8	1.0
S5	UIHT-1h	UIHT	1	0.8	1.0
S6	UIHT-2h	UIHT	2	0.8	1.0
S7	UIHT-3h	UIHT	3	0.8	1.0
S8	UIHT-0.5	UIHT	4	0.8	0.5
S9	UIHT-1.5	UIHT	4	0.8	1.5
S10	UIHT-pH1.2	UIHT	4	1.2	1.0
S11	UIHT-pH1.5	UIHT	4	1.5	1.0
S12	UIHT-pH1.8	UIHT	4	1.8	1.0

Adoption of confined impinging T-jet mixer (CITJ) for synthesis of micro particles was also reported in the open literatures [25,26]. A CITJ reactor which has T-shaped branches is the simplest component that contains two inlet tubes, allowing two streams to flow in, and one outlet tube, allowing the mixture to be collected. Local intensive micro-mixing in a CITJ takes place through the collision between two impinging streams, usually resulting in a fast homogenization of reactants so that both mass transfer rate and chemical reaction rate can be effectively enhanced. The kinetic energy and mass transfer rate in the mixing zone (reactor chamber) are influenced by the pressure fluctuation [27] while the intensive mixing occurring in a small confined volume of reaction chamber enhances the crystallisation and promote the growth of particle size [28].

A novel two-step preparation route that combines ultrasound-assisted CITJ and hydrothermal treatment (UIHT) to synthesize $(NH_4)Fe_2(PO_4)_2(OH)\cdot 2H_2O$ is developed in the present study. To the best of our knowledge, the application of UIHT method to synthesis of $(NH_4)Fe_2(PO_4)_2(OH)\cdot 2H_2O$ has not been reported in the literature. The effects of the use of ultrasonic-intensified impinging streams, reagent concentration, pH value of solution, and hydrothermal reaction time on the chemical and physical properties of the synthesized particles are

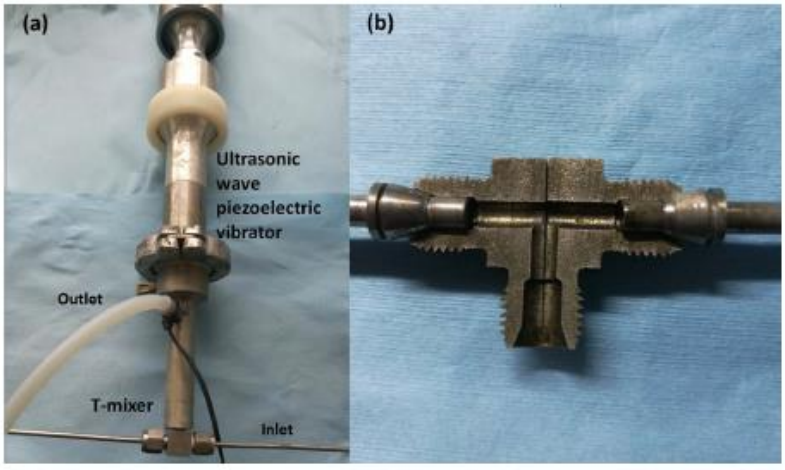

Fig. 2. (a) Experimental set-up of ultrasonic-intensified T-mixer and (b) internal structure of T-mixer.

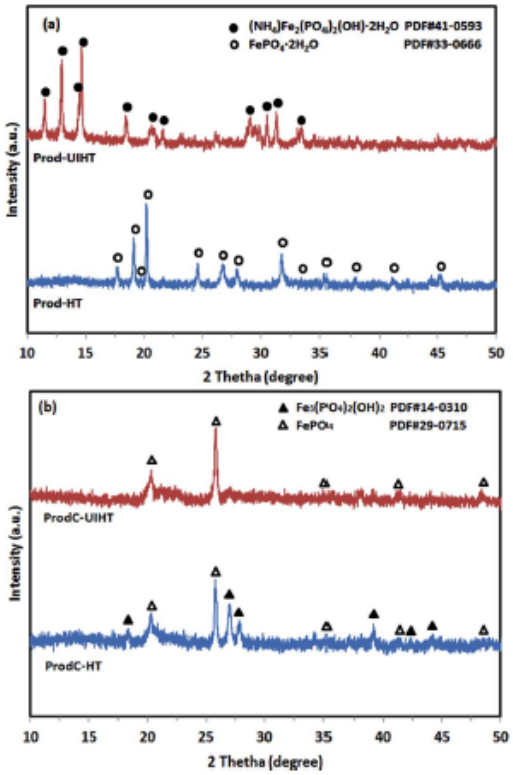

Fig. 3. XRD patterns of samples prepared when $C = 1.0\ mol\ L^{-1}$ and pH = 0.8: (a) as-synthesized precursors (b) obtained products after sintering process prepared by different methods.

Table 2
Calculated lattice parameters of as-synthesized samples prepared by two different methods.

Samples	a(Å)	b(Å)	c(Å)	V(Å³)
Prod-HT	5.3254	9.8325	8.6653	453.73
Prod-UIHT	9.8229	9.6208	9.6835	915.13
ProdC-HT	7.4118	7.4118	12.7739	701.73
ProdC-UIHT	5.0321	5.0326	11.2750	285.53

systematically investigated. The possible nucleation and particle growth mechanisms are discussed in detail. This paper will be organised in such a way. Section 2 presents the experimental details including materials preparation and characterisation. Section 3 discusses the effects of various conditions on properties of samples while the main conclusions reached as the result of the study will be given in Section 4.

2. Experimental

2.1. Materials preparation

The main procedures of two-step hydrothermal synthesis of $(NH_4)Fe_2(PO_4)_2(OH)\cdot 2H_2O$ and $FePO_4$ samples are shown in Fig. 1. The experimental set-up of ultrasonic-intensified T-mixer and internal structure of T-mixer are shown in Fig. 2. Nano-seeds were synthesized with ultrasonic-intensified T-mixer (see Fig. 2a) in the first step, labelled as

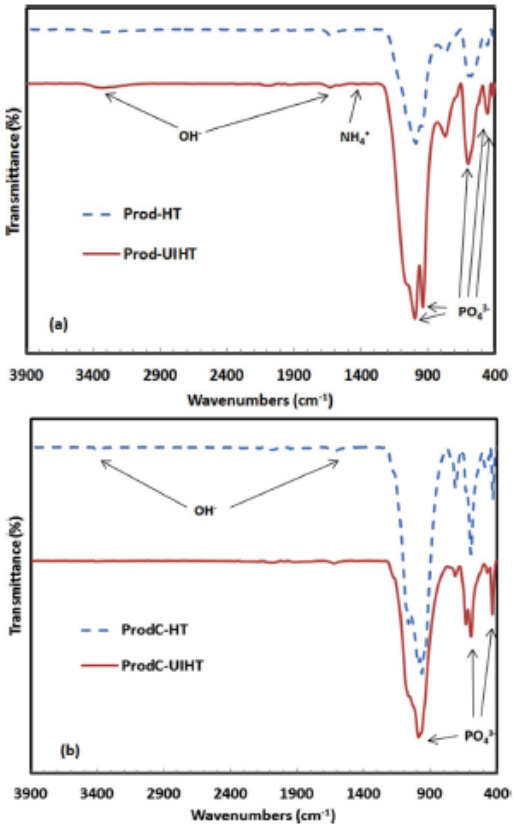

Fig. 4. FTIR patterns of samples prepared when $C = 1.0\ mol\ L^{-1}$ and pH = 0.8: (a) as-synthesized precursors (b) obtained products after sintering process.

Seed-UIHT. Thereafter iron nitrate solution and diammonium phosphate solution ($C = 0.5$, 1.0 and 1.5 mol L^{-1}, respectively) were injected continuously and separately into an T-mixer from two inlets by using two peristaltic pumps (BT100FJ, Baoding Chuangrui Ltd, China) to precisely control flow rates at 85.74 ml min^{-1}. Meanwhile, the T-mixer was connected and irradiated by a FS-600pv horn type ultrasonic wave piezoelectric vibrator (600 W, 13 mm in diameter) with 20 kHz. The inlet ports of T-mixer were connected to two stainless steel tubes with an inner diameter of 2.5 mm. The inner diameter and length of internal chamber in the T-mixer are 3.5 mm and 17 mm, respectively. The outlet of the T-mixer which had the same diameter as the impinging stream inlets and an enlarged channel (with an inner diameter of 4 mm) was interconnected to the inner chamber of the T-mixer. The mixed solution was then transferred into a 500 ml glass beaker and vigorously stirred for 5 min after the impinged mixing was conducted in the ultrasonic-intensified T-mixer under room temperature of 20 °C. In this step, the pH value of solution was maintained, respectively, at the given value (pH = 0.8, 1.2, 1.5, and 1.8) but was added the ammonia solution (1.5 mol L^{-1}) carefully through a pH automatic controller. After that, the obtained mixture was transferred and sealed in a 100 ml Teflon-lined stainless steel autoclave, heated at 170 °C for up to 4 h. The mixture was then removed from the autoclave, naturally cooling to the room temperature. The obtained samples were washed with deionized water for several times, followed by using a vacuum filter to separate the products and to dry at 80 °C overnight. These samples were labelled

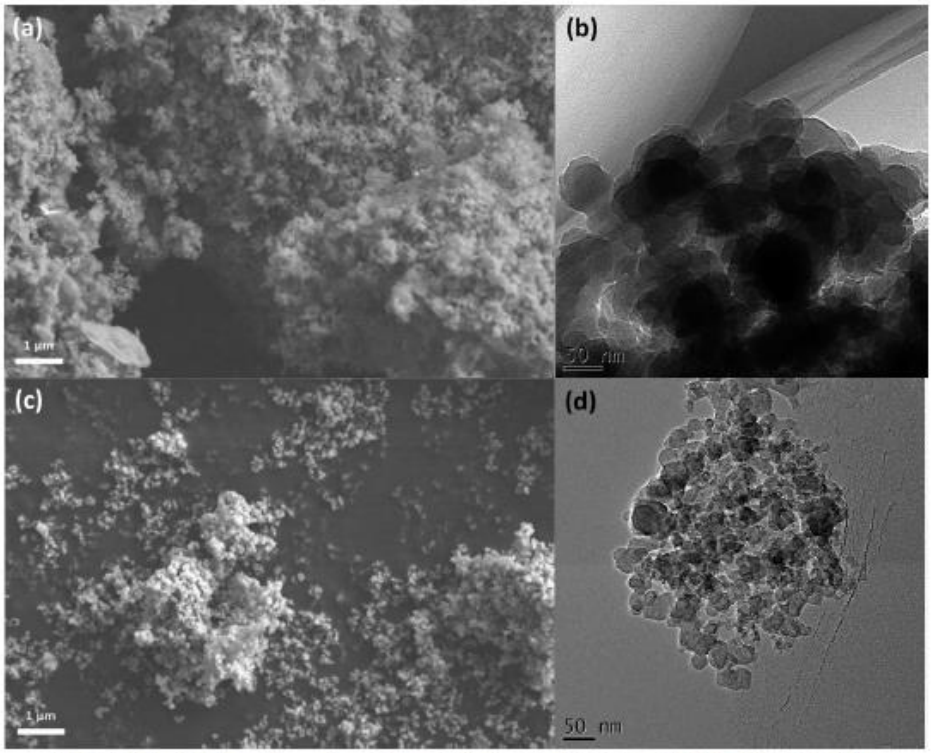

Fig. 5. The SEM and TEM images of nano-seeds samples prepared when $C = 1.0\ mol\ L^{-1}$ and pH = 0.8: (a-b) Seed-HT; (c-d) Seed-UIHT.

as Prod-UIHT. Then the as-synthesized products were calcined at 650 °C for 10 h in the air. Such obtained product was labelled as ProdC-UIHT.

For the comparison purpose, the samples were also prepared by adopting the conventional hydrothermal method. $Fe(NO_3)_3$ and $(NH_4)_2HPO_4$ solutions ($1.0\ mol\ L^{-1}$) were directly added into a 100 ml Teflon-lined stainless steel autoclave, heated at 170 °C for up to 4 h. The seeds, products, and the calcined products were labelled as Seed-HT, Prod-HT, and ProdC-HT, respectively. The conditions of different experiments are shown in Table 1.

2.2. Characterization

The crystal structure of samples was analysed using a Bruker D8 series X-ray diffraction by setting Cu Kα radiation (λ = 1.5406 Å). Thermogravimetric characteristics was measured by simultaneous thermal analyser (TG, NETZSCH STA 449 F3 Jupiter, Germany) at a heating rate of $10\ °C\ min^{-1}$ in the air, varying from the room temperature to 700 °C. The surface morphology of the obtained particles was observed by scanning electron microscope (Sigma VP, ZEISS, Germany) and transmission electron microscope (Tecnai F20, FEI, U.S). The particle size and distribution of the precursors were measured by using the laser diffraction method (Mastersizer 3000, Malvern Inc, UK). Surface area and porosity were analysed by Brunauer Emmett Teller (BET, Micromeritics ASAP 2020, U.S.A). The infrared spectra was recorded on a Fourier transform infrared spectroscopy (FTIR, Bruker V70, U.S.A) using the KBr disk technique.

3. Results and discussions

3.1. Effect of ultrasonic-intensified impinging stream pre-treatment

The XRD patterns of the as-synthesized samples prepared by different hydrothermal methods are shown in Fig. 3. It can be seen from the figure that the XRD pattern of Prod-HT sample was well matched with monoclinic $FePO_4{\cdot}2H_2O$ (PDF #33-0666, space group P21/n, with lattice parameters a = 0.5329 nm, b = 0.9798 nm, and c = 0.8710 nm). It is noted that that the obtained sample exhibits the same crystalline phase as that was reported by Wang et al. [29]. Meanwhile, the XRD pattern of Prod-UIHT sample matches well with $(NH_4)Fe_2(PO_4)_2(OH){\cdot}2H_2O$ with spheniscidite structure (PDF #41-0593, space group P21/n, with lattice parameters a = 0.9750 nm, b = 0.9630 nm, and c = 0.9700 nm).

Fig. 3b shows the XRD patterns of the as-synthesized samples after sintering at 650 °C for 10 h. The major peaks of ProdC-HT sample are indexed to $FePO_4$ (PDF #29-0715, space group P321, with lattice parameters a = 0.5035 nm, b = 0.5035 nm, and c = 1.1245 nm), while the reflection peaks of $Fe_3(PO_4)_2(OH)_2$ (PDF #14-0310, space group P41212, with lattice parameters a = 0.74 nm, b = 0.74 nm, and c = 1.281 nm, which can be used as the catalyst [30,31] or precursor of positive electrode material [32], which can be also observed in the XRD patterns. For the XRD patterns of ProdC-UIHT sample, only the reflection peaks of $FePO_4$ can be observed, indicating that the purity of decomposed $FePO_4$ sample can be further improved when using the two-step hydrothermal method. In addition, as can be seen from Table 2, unit volumes of Prod-HT and Prod-UIHT are 453.73 and 915.13 $Å^3$ respectively. After calcination process, the unit volume of ProdC-HT

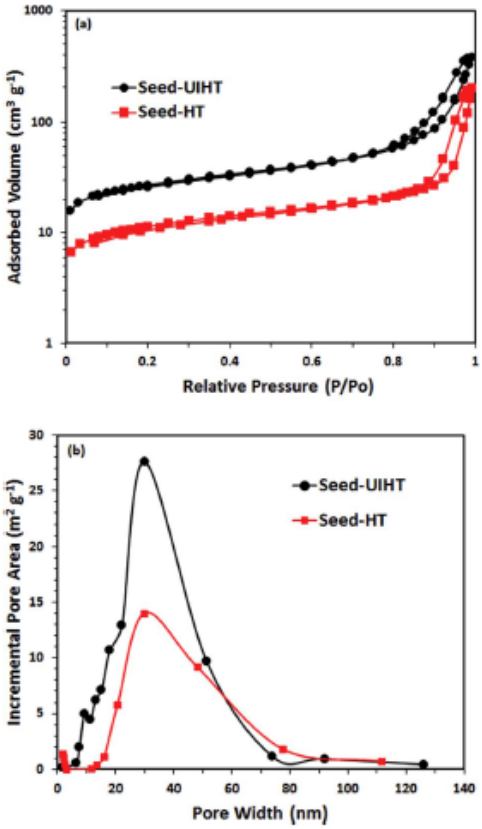

Fig. 6. BET analysis results of nano-seeds samples prepared when $C = 1.0\ mol\ L^{-1}$ and pH = 0.8: (a) N_2 adsorption-desorption isotherms of Seed-UIHT and Seed-HT samples; (b) the corresponding pore-size distribution obtained from the adsorption branch using the BJH method of Seed-UIHT and Seed-HT samples.

Table 3
N_2 adsorption-desorption analysis results of $FePO_4{\cdot}2H_2O$ precursors prepared with different synthesis methods.

Samples	Surface area ($m^2 g^{-1}$)	Average Pore Width (nm)	Total pore volume ($cm^3 g^{-1}$)	Average nuclei size (nm)
Seed-UIHT	95.4	24.6	0.59	62.9
Seed-HT	40.4	36.9	0.31	148.6

increases to 701.73 Å^3, while the unit volume of ProdC-UIHT decreases to 285.53 Å^3. This indicates that the sample cells are affected by temperature significantly.

The reason is that, during ultrasonic irradiation, large amount of H· and OH· was generated by the sonolysis of water, which may form H_2 and H_2O_2 [33,34]. Thus, H_2O_2 can assist to effectively avoid the reduction of Fe^{3+} during hydrothermal reaction. The main reactions in hydrothermal reaction can be assumed to follow the following steps:

$$H_2O \rightarrow H\cdot + OH\cdot$$

$$H\cdot + H\cdot \rightarrow H_2$$

$$OH\cdot + OH\cdot \rightarrow H_2O_2$$

$$H\cdot + OH\cdot \rightarrow H_2O$$

$$2Fe^{2+} + H_2O_2 + 2H\cdot \rightarrow 2Fe^{3+} + 2H_2O$$

To investigate the presence of all bands corresponding to as-synthesized samples, FTIR spectra is shown in Fig. 4. For Prod-UIHT sample, the absorption peaks confirm the presence of PO_4^{3-} functional group, including v_4 (O–P–O) double band of 574 and 597 cm^{-1}, v_3 (P–O) band of 1042 cm^{-1}, v_2 (O–P–O) band of 456 cm^{-1}, and v_1 (P–O) band of 996 cm^{-1} [35–37]. The stretching vibration at 1420 cm^{-1} can be attributed to the presence of NH_4^+. The occurrence of wide bands around 1629 and 3332 cm^{-1} indicates the presence of v (OH) in H_2O molecules in $(NH_4)Fe_2(PO_4)_2(OH){\cdot}2H_2O$ [2,9,38]. The FTIR spectra of Prod-HT samples look similar, but the amplitude is weaker than those for Prod-UIHT sample. The difference is that stretching vibration of NH_4^+ cannot be observed in the spectra. After experiencing calcination process, the FTIR spectra of ProdC-HT sample is still at the same position, but become narrower and sharper than its precursor. For ProdC-UIHT sample, the absorption peaks at 1420 cm^{-1} and 3332 cm^{-1} in the spectra disappear, indicating the removal of NH_4^+ and H_2O in decomposed $FePO_4$ product. In addition, as both the position and intensity of the vibration in FTIR spectra can be influenced by chemical bonds and content [39], the removal of NH_4^+ and H_2O also leads to the increased intensity of FTIR spectra for ProdC-HT.

The TGA-DTG, and DTA curves of Prod-UIHT and Prod-HT are shown in Fig. S1. It can be seen clearly from the figure that there exist three main weight loss stages as shown in Fig. S1a. In the temperature range from 50 °C to 150 °C, a weight loss of 2 wt% can be attributed to the removal of physical water. The second main weight loss stage takes place in the range of 150–350 °C, where a weight loss of 4 wt% can be related to the elimination of coordinated water molecules. The third main weight loss of 7 wt%, occurring at the temperature ranging from 350 °C to 630 °C and peaking at appropriate 410 °C, is corresponding to the decomposition of NH_4^+ and OH^-. The TGA-DTG curves of Prod-HT are shown in Fig. S1b. It can be observed from the figure that there is one main weight loss step in the range from 100 °C to 200 °C, which may be attributed to the removal of coordinated water molecules. Furthermore, a total mass loss of 19% indicates that there are two water molecules in one monoclinic $FePO_4{\cdot}2H_2O$ molecules. The DTA curves obtained from the characterisation of Prod-UIHT and Prod-HT samples are shown in Fig. S1c. The DTA curves of two samples look the same during physical water removal process (varying from the room temperature to 120 °C). It has been observed that an endothermic peak in the DTA curve of Prod-HT occurs at 175 °C, corresponding to the removal of two water molecules from one $FePO_4{\cdot}2H_2O$ molecules (endothermic reaction). For the DTA curve of Prod-UIHT sample, the appearance of broad peaks at around 170 °C and 270 °C indicates the elimination of coordinated water molecules while the third peak at around 420 °C corresponds to the removal of NH_4^+ and OH^- [5].

SEM and TEM images of the nano-seeds prepared by two different hydrothermal methods are shown in Fig. 5. As show in Fig. 5a-b, the Seed-HT nanoparticles which are highly agglomerated exhibit a near spherical or elliptical shape with a spread in particle size distribution, ranging from 50 to 150 nm. By comparison, due to the application of ultrasonic-intensified impinging stream pre-treatment, the Seed-UIHT samples are well-dispersed and the near spherical morphology with nuclei sizes from 30 to 80 nm is observed (Fig. 5c-d).

The BET specific surface area and pore size distribution of the Seed-UIHT and Seed-HT have been characterized by nitrogen adsorption-desorption analysis. It can be seen that the N_2 adsorption isotherm of all nano-seeds (Fig. 6a) is Type IV. Their big hysteresis loops can be evidenced by the presence of meso-pores (> 2nm and < 50 nm) and large surface areas. The surface area, porosity and average nuclei size of Seed-UIHT and Seed-HT samples are shown in Table 3. The average nuclei sizes of Seed-UIHT and Seed-HT samples are 62.9 and 148.6 nm, respectively. It can be seen that the Seed-HT sample has smaller BET

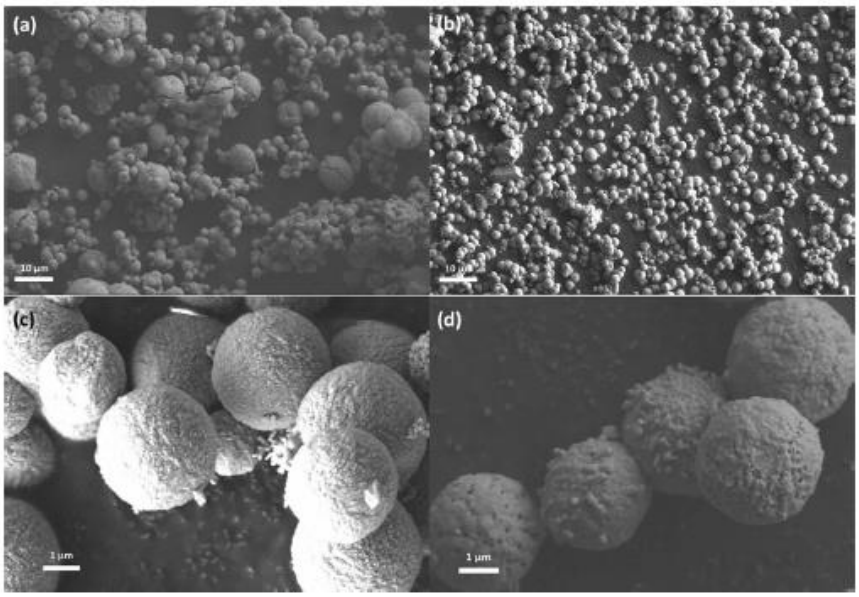

Fig. 7. The SEM images of as-synthesized samples prepared when $C = 1.0\,mol\,L^{-1}$ and pH = 0.8: (a) Prod-HT; (b-c) Prod-UIHT; (d) ProdC-UIHT.

surface area of $40.4\,m^2\,g^{-1}$ and a lower pore volume of $0.31\,cm^3\,g^{-1}$ while the average pore width and nuclei size of Seed-HT sample are greater than the Seed-UIHT with the values of 36.9 nm and 148.6 nm, respectively. In contrast, the Seed-UIHT sample shows a relatively smaller average pore size with the diameter of 24.6 nm, and exhibits larger BET surface area and higher total pore volume, corresponding to $95.4\,m^2\,g^{-1}$ and $0.59\,cm^3\,g^{-1}$ respectively. The analytical results of pore size distribution based on BJH desorption pore distribution are shown in Fig. 6b. The Seed-UIHT has a significant amount of mesopores and small numbers of macropores in the range of 2–55 nm, which yields larger specific surface area and higher pore volume. The difference of BET analysis results between Seed-UIHT and Seed-HT can be attributed to application of ultrasound. The implosion of bubbles in solution induces both micro-streaming and micro-jetting. Micro-streaming caused by symmetrical implosion bubbles can enhance micromixing effect, result in increased mass transfer rate, chemical reaction rate, and nucleation rate. Meanwhile, micro-jetting caused by asymmetrical implosion bubbles can break larger particles into small pieces, and preventing agglomeration and clogging in CITJ. Therefore, the synergistic effect of micro-streaming and micro-jetting leads to the formation of nanoscale particles which have larger surface area and pore volume, as well as smaller pore width and nuclei size.

The SEM images of as-synthesized products are shown in Fig. 7. It can be seen from the figure that the morphology of obtained particles is significantly affected by the presence of the nano-seeds. Fig. 7a shows that that the Prod-HT particles do present spherical morphology but the size of the agglomerated particles is distributed diversely. The average size of larger particles can reach up to 10 um while those smaller particles have an average size of 2 μm. However, as can be seen from Fig. 7b and c, the Prod-UIHT particles not only show a spherical shape but also present a narrow size distribution with an average particle size of only 3 um. After sintering at 650 °C for 10 h, the ProdC-UIHT particles (anhydrous $FePO_4$ precursor composites) still maintain micro-sized spherical secondary structures with the nano-scale porous structure being formed on the outside layer of the particles as can be seen from Fig. 7d.

3.2. Formation mechanism of $(NH_4)Fe_2(PO_4)_2(OH)\cdot 2H_2O$ and $FePO_4$ particles

To investigate the formation mechanism of $(NH_4)Fe_2(PO_4)_2(OH)\cdot 2H_2O$ and $FePO_4$ particles by the UIHT method, time-dependent experiments have been conducted. Previous studies have suggested that the synthesis mechanism using hydrothermal treatment is consisted of three major stages, precursor dissolution, nucleation, and nuclei growth [40]. The mechanism of the formation particles when using two-step hydrothermal method may be divided into four stages, i.e. primary nucleation, seeds dissolution, branching, and spherulitic growth [41]. Based on the XRD, FTIR and SEM results, it is conjectured that the production of uniform and well-dispersed $(NH_4)Fe_2(PO_4)_2(OH)\cdot 2H_2O$ and $FePO_4$ particles with higher purity via UIHT is likely contributed from primary nucleation through ultrasound-intensified impinging stream pre-treatment before the hydrothermal growth occurrence. The primary nucleation will be influenced by applying ultrasonic irradiation which will affect the micro-mixing process in the T-mixer. Generally speaking, the adoption of ultrasonic irradiation is able to intensify the motion of eddies in the T-mixer. In order to estimate the characteristic micromixing time t_M, a scaling model was used to evaluate the time for diffusion which take place in the turbulence eddies with the eddy size of the order equal to the Kolmogorov length λ [36,37].

$$t_M = \frac{(0.5\lambda)^2}{D_{eddy}} \tag{1}$$

where D_{eddy} is the eddy diffusivity of the reactant solutions. The Kolmogorov length λ can be estimated based on the micromixing energy dissipation rate ε [J/s·kg] and the kinematic viscosity of the mixed solution, ν_{mix}, at the point of mixing, given by

$$\lambda = \left(\frac{\nu_{mix}^3}{\varepsilon}\right)^{1/4} \tag{2}$$

The energy dissipation rate should be equal to the energy change

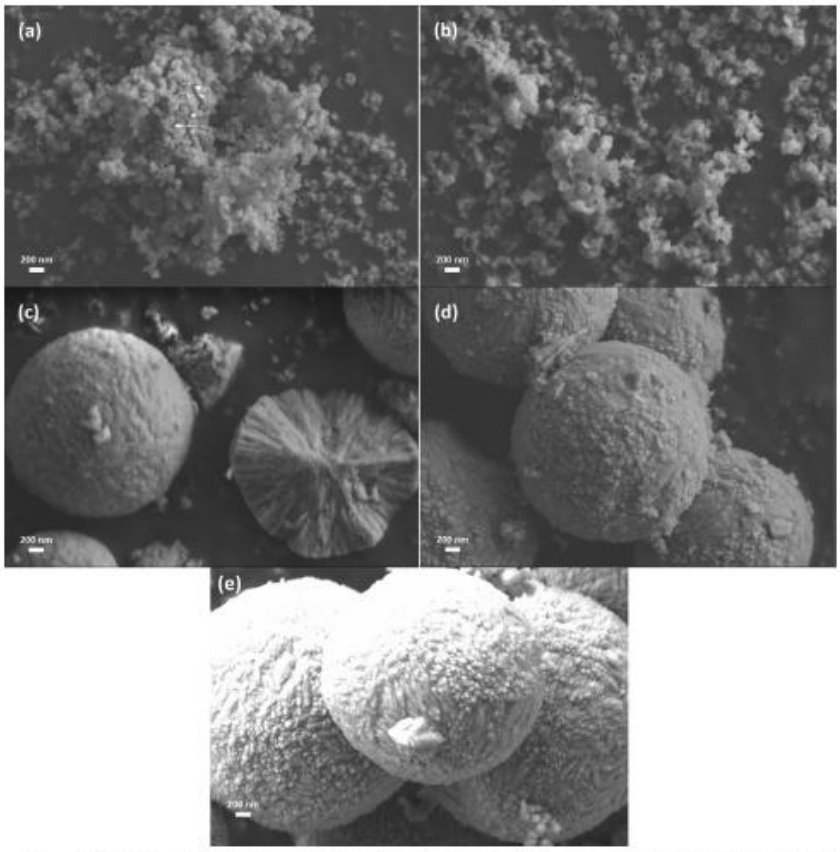

Fig. 8. The SEM images of the samples obtained at 170 °C with different hydrothermal time when $C = 1.0$ mol L^{-1} and pH = 0.8: (a) Seed-UBHT; (b) UBHT-1h; (c) UBHT-2h; (d) UBHT-3h; (e) UBHT-4h (Prod-UBHT).

associated with the energy loss (pressure drop) in the T-mixer, which can be measured by estimating the input power P divided by the mixed solution mass in the reactor:

$$\varepsilon = \frac{P}{\rho_{ms} V_T} \tag{3}$$

where V_T is the mixing volume of the T-type micromixer used in this study. For the present study, the input power P can be approximately assumed to be the superposition contributed from the input power for impinging stream P_{IS} and the ultrasonic irradiation P_{UI}:

$$P = P_{IS} + P_{UI} \tag{4}$$

The micromixing time can thus be estimated by

$$t_M = \frac{\left[0.5\left(\frac{\rho_{ms} V_T \nu_{ms}^2}{P_{IS}+P_{UI}}\right)^{1/4}\right]^2}{D_{addy}} \tag{5}$$

It can be seen from Eq. (5) that the micromixing time can be further reduced by imposing the ultrasonic irradiation. We noticed that the Reynolds numbers for T-shape microreactor based on the two inlets diameters can be estimated by

$$\mathrm{Re}_i = \frac{4\rho_i Q_i}{\mu_i \pi d_i} \tag{6}$$

As the density and viscosity of $Fe(NO_3)_3$ and $(NH_4)_2HPO_4$ solutions are different, the equivalent Reynolds number used to characterise the mixing in the ISR can be defined by

$$\mathrm{Re}_{eq} = \frac{4\rho_{ms} \sum_{i=1}^{2} Q_i}{\mu_{ms} \pi d_{outlet}} \tag{7}$$

where ρ_{ms} and μ_{ms} are the density and viscosity of the fully mixed solution. The measured values of ρ_{ms} and μ_{ms} are found to be 1144.4 kg m^{-3} and 0.001005 Pa-s, respectively. The outlet diameter of T-mixer, d_{outlet} and volumetric feeding rate Q are 0.0035 m and 85.74 ml min^{-1}, which yields the estimated Reynolds number without using ultrasonic irradiation is 572, corresponding to a laminar shear flow in the T-mixer. However, the use of ultrasonic irradiation can produce a large number of micro bubbles. Such imploding bubbles can be considered as small microreactors which can generate powerful hydraulic shocks, and an environment with extremely high temperature and pressure [42]. The hydraulic shocks caused by these bursting of the microbubbles can induce eddies that promote the regime transition from laminar to turbulent so that the turbulent energy dissipation can be enhanced. As a result, the diffusion rate or micro-mixing among these eddies are remarkably improved due to the application ultrasonic irradiation. In addition, chemical reaction rate and nucleation rate are increased due to the extremely high temperature and pressure created

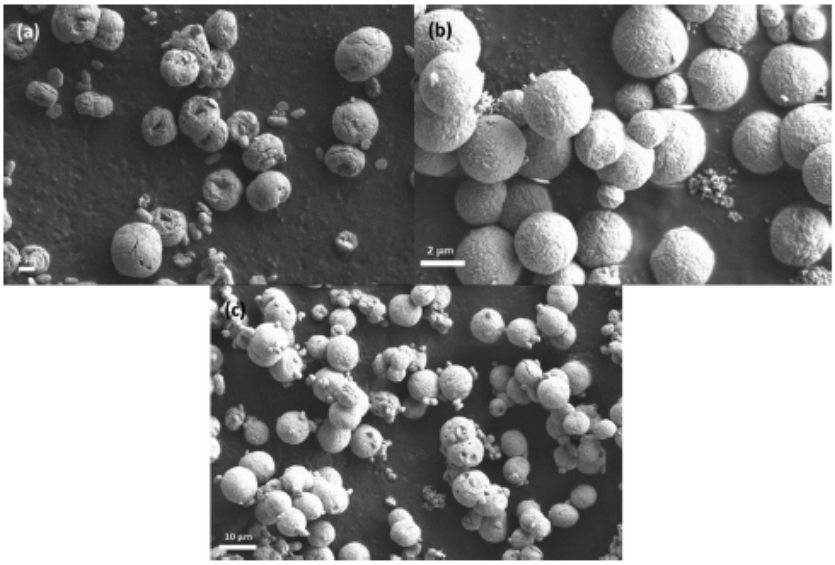

Fig. 9. SEM images of as-synthesized $Fe_2(NH_4)(OH)(PO_4)_2(H_2O)_2$ samples synthesized with different reagent concentration at 170 °C for 4 h when pH = 0.8: (a) Prod-UIHT-0.5; (b) Prod-UIHT-1.0(Prod-UIHT); and (c) Prod-UIHT-1.5.

by imploding bubbles, which lead to the formation of large amount of nanoscale seeds. The energy transformed from ultrasound, especially from collapsing of bubbles, may overcome the Van Der Waals force and prevent agglomeration among nano-seeds. Therefore, the physical effects of ultrasonic irradiation lead to the formation of uniform nanoscale primary seeds with an average size of 60 nm, although they are slightly agglomerated by high interfacial energy in the solution (shown in Fig. 8a). With adopting hydrothermal treatment for 1 h, these nano-seeds start to dissolve and hydrolyse (Fig. 8b). When hydrothermal treatment increases to 2 h, successive branching of nucleus is formed, grows as radial disks and fills spherical volumes (Fig. 8c) [43,44]. As hydrothermal time is increased, micro-sized spherulite grows uniformly and spherically (Fig. 8d-e).

For chemical effect, the starting raw materials were dissolved into water and gives ions including NH_4^+, PO_4^{3-}, NO_3^-, Fe^{3+}, and H^+. Meanwhile, water molecules can be hydrolysed as H^+ and OH^- by ultrasound irradiation. It has been reported from the previous studies that three different kind of chemical reactions may take place at (1) inner environment of the collapsing bubbles (gas phase region); (2) the interfacial region between the bubble and bulk solution; and (3) in bulk solution region [45]. It is noted that the raw materials used in this study are ionic and non-volatile, which are difficult to enter the phase region due to the low vapour pressure [46]. Thus, the reaction will only take place in the interfacial region between the gas and solution. The ions, including NH_4^+, PO_4^{3-}, NO_3^-, Fe^{3+}, OH^-, and H^+ ions, are homogeneously distributed in solution with the help of ultrasonic irradiation. Furthermore, the chemical bonds can be ruptured by the extremely high temperature and pressure induced by the collapsing of microbubbles so that the side reaction and the formation of by-products can be prevented. Through these actions, the $(NH_4)Fe_2(PO_4)_2(OH)\cdot 2H_2O$ particles are generated after hydrothermal treatment, and the pure $FePO_4$ particles are produced by removing $[NH_4^+]$ and $[OH^-]$ ions after sintering process. The above mentioned chemical reaction of two-step hydrothermal method can be described as:

$$2Fe^{3+} + 2PO_4^{3-} + NH_4^+ + OH^- + 2H_2O \rightarrow (NH_4)Fe_2(PO_4)_2(OH)\cdot 2H_2O\downarrow \quad (8)$$

$$(NH_4)Fe_2(PO_4)_2(OH)\cdot 2H_2O \rightarrow 2FePO_4 + NH_3 + 3H_2O \quad (9)$$

By comparison, the samples prepared by using the conventional hydrothermal method are indexed to be $FePO_4$ but the impurities, such as $Fe_3(PO_4)_2(OH)_2$, were found after sintering process. This indicates that the NH_4^+, PO_4^{3-}, NO_3^-, Fe^{3+}, OH^-, and H^+ ions are distributed in-homogeneously, resulting in the formation of amorphous by-products although they cannot be found before calcination process. This is likely due to the fact that the conventional mixing does not give out the sufficient mixing, leading to product contamination or formation of by-products [26].

3.3. Effect of reagent concentration on the synthesis of $(NH_4)Fe_2(PO_4)2(OH)\cdot 2H_2O$ and decomposed products

To further investigate the effect of reagent concentration for the synthesis of $(NH_4)Fe_2(PO_4)_2(OH)\cdot 2H_2O$ particles and decomposed products, samples were prepared under precisely controlled reactant concentration (C = 0.5, 1.0 and 1.5 mol L^{-1}). The hydrothermal temperature and heating time were maintained at 170 °C and 4 h, respectively. The as-synthesized samples were denoted as Prod-UIHT-0.5, Prod-UIHT-1.0, and Prod-UIHT-1.5, while the products after sintering process were labelled as ProdC-UIHT-0.5, ProdC-UIHT-1.0, and ProdC-UIHT-1.5.

The morphology of $(NH_4)Fe_2(PO_4)2(OH)\cdot 2H_2O$ particles synthesized with different reagent concentration was identified by SEM is shown in Fig. 9. It can be seen from the figure that the Prod-UIHT-0.5 sample (Fig. 9a) shows microscale red-blood-cell-like morphology with irregular hole in the centre, which is similar to the $(NH_4)Fe_2(PO_4)2(OH)\cdot 2H_2O$ particles as reported by Wu et al. (2018) [9]. The average diameter and thickness of the particle are found to be around 4 μm and 2 μm, respectively. When the initial reagent concentration is increased to 1.0 mol L^{-1}, the Prod-UIHT-1.0 particles present uniform microspheres with an average particle size of 2 μm (Fig. 9b). Further increase in the feeding concentration (1.5 mol L^{-1}) results in the appearance of near-sphere $(NH_4)Fe_2(PO_4)2(OH)\cdot 2H_2O$ particles that have a spread particle size distribution (Fig. 9c). Those large particles have an average

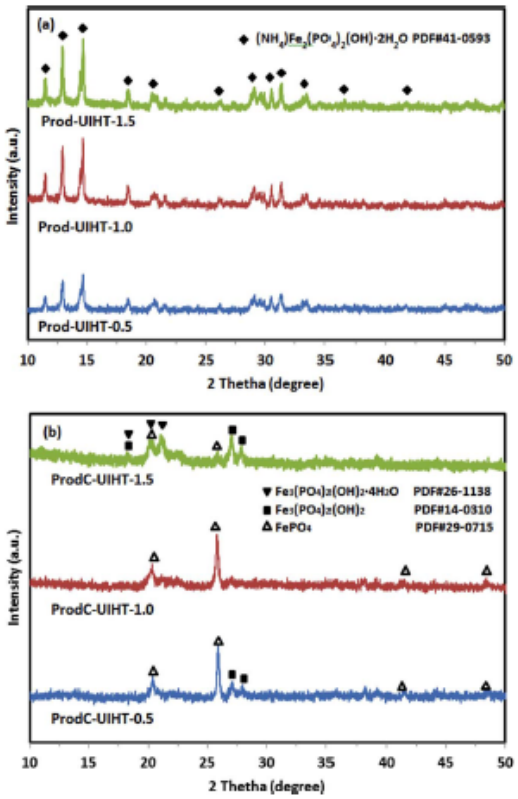

Fig. 10. XRD patterns of samples synthesized with different reagent concentration at 170 °C for 4 h when pH = 0.8: (a) as-synthesized precursors (b) obtained products after sintering process.

Table 4
Calculated lattice parameters as-synthesized samples.

Samples	a(Å)	b(Å)	c(Å)	V(Å^3)
Prod-UIHT-0.5	9.7544	9.6301	9.7062	911.76
Prod-UIHT-1.0	9.8229	9.6208	9.6835	915.13
Prod-UIHT-1.5	9.7502	9.6372	9.6881	910.34
ProdC-UIHT-0.5	7.4174	7.4174	12.7745	702.82
ProdC-UIHT-1.0	5.0321	5.0326	11.2750	285.53
ProdC-UIHT-1.5	10.0187	9.7251	5.4667	532.64

size of 10 μm. In addition, it is also observed that there exist a large number of small particles with the average size of 1 μm.

The corresponding XRD patterns of the as-synthesized precursors and calcined products prepared with different reagent concentration by two-step hydrothermal method are shown in Fig. 10. The XRD patterns of precursor samples (Fig. 10a) are all well matched with $(NH_4)Fe_2(PO_4)_2(OH)\cdot 2H_2O$ with spheniscidite structure (PDF #41-0593). Fig. 10b shows the XRD patterns of products after sintering process. It can be seen clearly from the figure that the major diffraction peaks take place around 20.2°, 25.8°, 41.2° and 48.4°, which can be classified as hexagonal structure of $FePO_4$ (PDF #29-0715). The minor diffraction peaks occurring at 18.9°, 27.0° and 27.8° indicate the formation of $Fe_3(PO_4)_2(OH)_2$ (PDF #14-0310), while the diffraction peaks appearing around 18.9°, 20.2° and 21.3° reveal the presence of $Fe_3(PO_4)_2(OH)_2\cdot 4H_2O$ (PDF #26-1138, space group P21/c, with lattice parameters a = 1.0000 nm, b = 0.9730 nm, and c = 0.5471 nm). In addition, the calculated lattice parameters in Table 4 show that the unit volume of Prod-UIHT-1.0 is 915.13 Å^3, which is greater than the unit volume of Prod-UIHT-0.5 (911.76 Å^3) and Prod-UIHT-1.5 (910.34 Å^3). After sintering process, the unit volumes of ProdC-UIHT-0.5 and ProdC-UIHT-1.5 are 702.82 Å^3 and 532.64 Å^3, respectively, being greater than the unit volume of ProdC-UIHT-1.0 (285.53 Å^3).

Based on the SEM and XRD results, it can be fairly claimed that the use of reagent concentration of 1.0 mol L^{-1} is likely the optimal condition for the initial reagent concentration which could be applied for the formation of uniform and spherical $(NH_4)Fe_2(PO_4)_2(OH)\cdot 2H_2O$ and decomposed $FePO_4$ particles. Previous study has demonstrated that the initial reagent concentration significantly influences the supersaturation level, nucleation rate, particle growth rate during the particle formation process [47,48]. For primary nucleation, the nano-seeds prepared by raw materials of 1.0 mol L^{-1} via the ultrasonic-intensified T-mixer can have smaller nuclei size [49]. It is commented that apart from the raw materials used for the nucleation of nano-seeds, a large amount of free ions may still exist in the solution. From the point of view of particle growth process, the adoption of higher reactant concentration can increase the supersaturation level and particle growth rate in a chemical reaction.

When the reagent concentration is 0.5 mol L^{-1}, some cracks were found on the surface of the micro-sized red-blood-cell-like particles. The appearance of these cracks is very likely caused by the shortage of free ions, result in the incomplete growth of $(NH_4)Fe_2(PO_4)_2(OH)\cdot 2H_2O$ particles. When increasing the initial reagent concentration from 0.5 to 1.0 mol L^{-1}, the relatively higher supersaturation level and sufficient free ions can be beneficial and contribute to the formation of spherical particles. However, further increment in the initial reagent concentration to 1.5 mol L^{-1} lead to the particle size increase (around 10 μm), accompanying by presence of a large number of small particles due to the excess of free ions. Thus, it can be concluded that the as-synthesized products are significantly affected by initial reagent concentration.

3.4. Effect of pH value on the synthesis of $(NH_4)Fe_2(PO_4)2(OH)\cdot 2H_2O$ and decomposed products

To determine the effect of pH value on the synthesis of $(NH_4)Fe_2(PO_4)_2(OH)\cdot 2H_2O$ and $FePO_4$ particles, samples were prepared under precisely controlled pH values (pH = 0.8, 1.2, 1.5, and 1.8) when the reagent concentration, hydrothermal temperature and heating time were maintained at the same condition during the synthesis process. The as-synthesized samples were denoted as Prod-UIHT-pH0.8, Prod-UIHT-pH1.2, Prod-UIHT-pH1.5, and Prod-UIHT-pH1.8 while the products after sintering process were labelled as ProdC-UIHT-pH0.8, ProdC-UIHT-pH1.2, ProdC-UIHT-pH1.5, and ProdC-UIHT-pH1.8.

The morphology of $(NH_4)Fe_2(PO_4)_2(OH)\cdot 2H_2O$ samples prepared by UIHT method at different pH values was examined by SEM is shown in Fig. 11. The $(NH_4)Fe_2(PO_4)_2(OH)\cdot 2H_2O$ composites formed under the condition that pH = 0.8 clearly present microspheres with an average size of 3 um (see Fig. 11a). When pH value is increased to 1.2, two $(NH_4)Fe_2(PO_4)_2(OH)\cdot 2H_2O$ micro-spheres interweave to combine and form the peanut-like micro-sized particles with an average length of 8 μm and width of 4 μm (see Fig. 11b). As pH value further increases to 1.5, $(NH_4)Fe_2(PO_4)_2(OH)\cdot 2H_2O$ particles still show peanut-like morphology but cracks are occurring in the middle of the particle. The average length and width of the particles attain 16 μm and 10 μm, respectively (see Fig. 11c). Further increase pH value to 1.8, $(NH_4)Fe_2(PO_4)_2(OH)\cdot 2H_2O$ particles are found to be easily agglomerated and they can form to generate even larger particles with irregular shapes (see Fig. 11d). The reason is that, according to Derjaguin and Landau, Verwey and Overbeek (DLVO) theory, when pH value was increased and became closer to the pH of zero net proton charge (PZNPC), the aggregation between two particles becomes faster and irreversible.

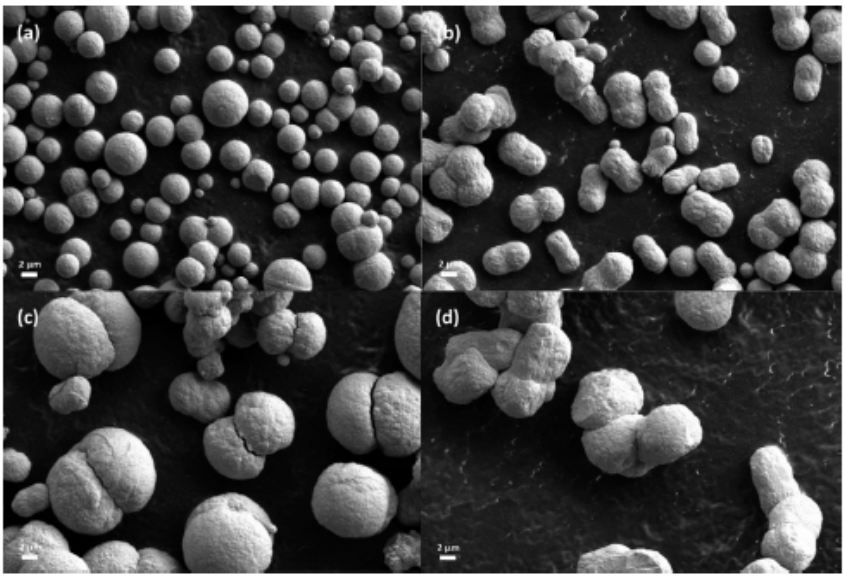

Fig. 11. SEM images of $Fe_2(NH_4)(OH)(PO_4)_2(H_2O)_2$ composites synthesized with different pH value at 170 °C for 4 h when $C = 1.0\,mol\,L^{-1}$: (a) UIHT-pH0.8 (Prod-UIHT), (b) UIHT-pH1.2, (c) UIHT-pH1.5, and (d) UIHT-pH1.8.

Therefore, the samples can become twined (Fig. 11b), and even contain crystallographic defects (Fig. 11c). When pH value is further increased and above a specific point, the process is dominated by random aggregation and several particles are combined together (Fig. 11d). Therefore, the pH value, or the concentration of $[OH]^-$, influences the particle growth orientation during hydrothermal process, resulting in the difference on the morphology of $(NH_4)Fe_2(PO_4)_2(OH)\cdot 2H_2O$ particles [50,51].

The corresponding XRD patterns of the as-synthesized precursors and calcined products prepared with different reagent concentration by two-step hydrothermal method are shown in Fig. 12. The XRD patterns of as-synthesized $(NH_4)Fe_2(PO_4)_2(OH)\cdot 2H_2O$ samples (Fig. 12a) are all well matched with $(NH_4)Fe_2$ $(PO_4)_2(OH)\cdot 2H_2O$ with spheniscidite structure (PDF #41-0593). After sintering, all the XRD patterns of discomposed products (Fig. 12b) match well with anhydrous hexagonal structure $FePO_4$ (PDF #29-0715). It can be seen clearly from the figure that, as pH value increases, there are no obvious difference among the XRD patterns of $(NH_4)Fe_2(PO_4)_2(OH)\cdot 2H_2O$ precursor. However, when the $FePO_4$ composites were synthesized at pH = 0.8, the main diffraction peaks at $2\theta = 20.3°$ and 25.8° are lower and spread wider than those for other samples, which clearly indicates that higher pH value may lead to the high degree of crystallinity of the decomposed samples. The calculated lattice parameters of $(NH_4)Fe_2(PO_4)_2(OH)\cdot 2H_2O$ and decomposed $FePO_4$ samples are listed in Table 5. As seen from the table, with increasing pH value, the unit volume of (NH_4) $Fe_2(PO_4)_2(OH)\cdot 2H_2O$ sample decreases from 915.13 $Å^3$ (pH = 0.8) to 794.40 $Å^3$ (pH = 1.8). The same tendency is also observed for the case of decomposed $FePO_4$ samples, in which the unit volume reduces from 285.53 $Å^3$ (pH = 0.8) to 246.57 $Å^3$ (pH = 1.8).

Fig. 13 shows the FTIR spectra of $(NH_4)Fe_2(PO_4)2(OH)\cdot 2H_2O$ and decomposed $FePO_4$ samples prepared at various pH conditions in the wave number region of 400–3900 cm^{-1}. The (NH_4) $Fe_2(PO_4)_2(OH)\cdot 2H_2O$ samples prepared at pH = 1.2, 1.5 and 1.8 show sharper bands at 1420 cm^{-1} and 1620 cm^{-1}. These sharper stretched vibrations correspond to the binding vibration of NH_4^+, which induced by ammonia solution used for adjusting the pH value. In addition, it is noticeable that the wide bands at 3332 cm^{-1} which indicates the ν (OH) in H_2O molecules in $(NH_4)Fe_2(PO_4)_2(OH)\cdot 2H_2O$ have disappeared when pH value of solution is 1.2, 1.5 and 1.8. However, four small and spread peaks around 2800, 3100, 3300 and 3450 cm^{-1} can be still observed, suggesting the presence of ν (NH), ν (NH_2), and ν (OH) groups [51]. After performing calcination, the FTIR spectra of all decomposed samples look similar. The disappearance of the absorption signals in the range of 2800–3450 cm^{-1} indicates the removal of H_2O. Moreover, the peak at 1420 cm^{-1} disappears for ProdC-UIHT-pH0.8, ProdC-UIHT-pH1.2, ProdC-UIHT-pH1.5, and ProdC-UIHT-pH1.8 samples, indicating that NH_4^+ functional group can be removed after calcination process.

4. Conclusions

Two synthesis approaches, the conventional hydrothermal method and two-step hybrid ultrasonic intensified impinging stream and hydrothermal method (ultrasonic-intensified impinging stream pre-treatment followed by hydrothermal treatment), were applied for the synthesis of $(NH_4)Fe_2(PO_4)_2(OH)\cdot 2H_2O$ and $FePO_4$ samples under the same experimental conditions that the temperature, heating time, reactant concentration, and pH value were carefully controlled. It has been demonstrated that the adoption of ultrasonic-intensified impinging stream pretreatment can produce nano-seeds that have smaller nuclei size and narrow particle size distribution, giving out the well-dispersed spherical $(NH_4)Fe_2(PO_4)_2(OH)\cdot 2H_2O$ and decomposed $FePO_4$ samples. The conclusions reached as the results of the current study are as follows:

(1) The adoption of ultrasonic-intensified impinging stream pre-treatment can effectively reduce the synthesized particle size and acquire the narrow particle size distribution of both nano-seeds and as-synthesized products.
(2) The results obtained from the time-dependent experiments clearly indicate that the formation of $(NH_4)Fe_2(PO_4)_2(OH)\cdot 2H_2O$ particles by using two-step hydrothermal method consists of four major

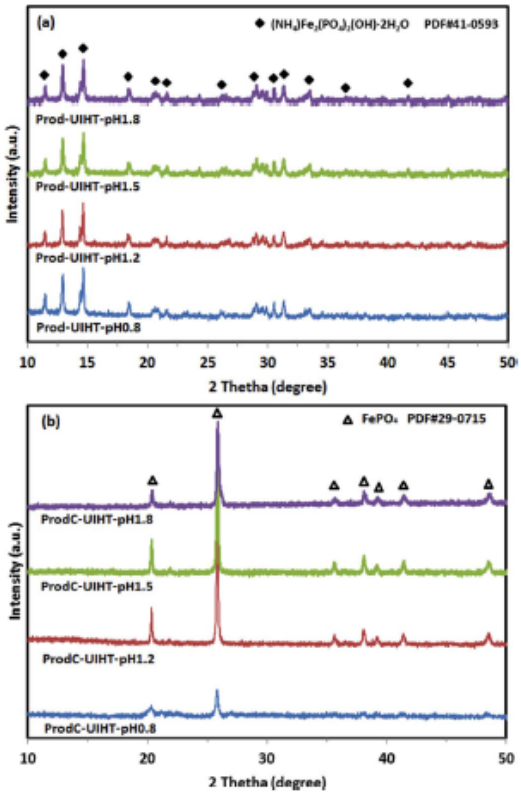

Fig. 12. XRD patterns of samples synthesized with different pH value at 170 °C for 4 h when $C = 1.0\ mol\ L^{-1}$: (a) as-synthesized precursors (b) obtained products after sintering process.

Table 5
Calculated lattice parameters and nuclei size of as-synthesized samples.

Samples	a(Å)	b(Å)	c(Å)	V(Å^3)
Prod-UIHT-pH0.8	9.8229	9.6208	9.6835	915.13
Prod-UIHT-pH1.2	9.7126	9.4408	9.3986	846.64
Prod-UIHT-pH1.5	9.4912	9.4212	9.4410	823.57
Prod-UIHT-pH1.8	9.3748	9.3179	9.3192	794.40
ProdC-UIHT-pH0.8	5.0321	5.0326	11.2750	285.53
ProdC-UIHT-pH1.2	5.0351	5.0351	11.2373	246.72
ProdC-UIHT-pH1.5	5.0320	5.0320	11.2476	246.65
ProdC-UIHT-pH1.8	5.0345	5.0345	11.2327	246.57

stages: primary nucleation, seeds dissolution, branching, and spherulitic growth.

(3) An increase in the reactant concentration (from 0.5 to 1.0 mol L^{-1} in the present study) can improve the supersaturation level and promote the chemical reaction rate, leading to the generation of well-dispersed spherical $(NH_4)Fe_2(PO_4)_2(OH)\cdot 2H_2O$ particles. However, excess increase in the reactant concentration will diversify particle size distribution, resulting in by-products in the decomposed $FePO_4$ samples.

(4) The pH value, or the concentration of $[OH]^-$, significantly affects the particle growth orientation during the hydrothermal process as clearly illustrated by the difference on the morphology of $(NH_4)Fe_2(PO_4)_2(OH)\cdot 2H_2O$ particles. In addition, the crystallinity of decomposed $FePO_4$ samples can be improved as the result of increasing pH value.

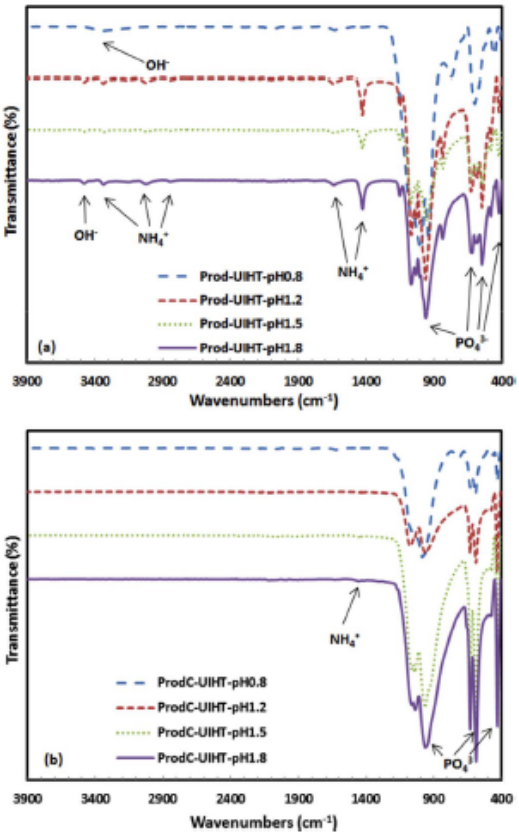

Fig. 13. FTIR patterns of samples synthesized with different pH value at 170 °C for 4 h when $C = 1.0\ mol\ L^{-1}$: (a) as-synthesized precursors (b) obtained products after sintering process.

Acknowledgement

This work was financially supported by National Natural Science Foundation of China (NSFC) (Grant No. 21576141, 91534118) and Zhejiang Provincial Natural Science Foundation (Grant No. LY15B060001). Support from Engineering and Physical Sciences Research Council (Grant No. EP/J000582/1, GR/R68078) and Ningbo Municipal Government (3315 Plan, 2014A35001-1) was also acknowledged. This work was carried out at the International Doctoral Innovation Centre (IDIC). Bin Dong would also like to acknowledge the support through the Ph.D. scholarship of the International Doctoral Innovation Centre (IDIC) of University of Nottingham Ningbo China.

Appendix A. Supplementary data

Supplementary data associated with this article can be found, in the online version, at http://dx.doi.org/10.1016/j.ultsonch.2017.12.008.

References

[1] C. Trobajo, A. Espina, E. Jaimez, S.A. Khainakov, J.R. García, Hydrothermal

synthesis of iron(III) phosphates in the presence of urea, J. Chem. Soc., Dalton Trans. 5 (2000) 787–790.
[2] P. Bonnet, J.M.M. Millet, C. Leclercq, J.C. Vedrine, Study of a new iron phosphate catalyst for oxidative dehydrogenation of isobutyric acid, J. Catal. 158 (1996) 128–141.
[3] M. Cavellec, G. Ferey, J.M. Greneche, Magnetic properties of synthetic phenisicidite, J. Magn. Magn Mater. 167 (1997) 57–64.
[4] H. Zhou, H. Duan, H. Zhang, X.M. Ren, A new pseudo-polymorph in mineral sphenicidite family (NH4)[Fe2(OH)(H2O)(PO4)2]·1.5H2O exhibiting spontaneous magnetization below 25 K, Solid State Sci. 12 (2010) 1816–1821.
[5] S.W. Cao, Y.J. Zhu, J.B. Cui, Iron hydroxyl phosphate microspheres: microwave-solvothermal ionic liquid synthesis, morphology control, and photoluminescent properties, J. Solid State Chem. 183 (2010) 1704–1709.
[6] S. Ju, T. Liu, H. Peng, G. Li, K. Chen, A facile synthesis route for porous spherical LiFePO4/C microscale secondary particles, Mater. Lett. 93 (2013) 194–198.
[7] J. Li, J. Wu, Y. Wang, G. Liu, C. Chen, H. Liu, Synthesis of LiFePO4/C composite with high rate capability using sphenisicidite as a facile precursor, Mater. Lett. 136 (2014) 282–285.
[8] P. Reale, B. Scrosati, C. Delacourt, C. Wurm, M. Morcrette, C. Masquelier, Synthesis and thermal behavior of crystalline hydrated iron(III) phosphates of interest as positive electrodes in Li batteries, Chem. Mater. 15 (2003) 5051–5058.
[9] K. Wu, D. Liu, Y. Tang, Self-assembly of red-blood-cell-like (NH4)[Fe 2 (OH)(PO 4) 2]·2H 2 O architectures from 2D nanoplates by sonochemical method, Ultrason. Sonochem. 40 (2018) 832–836.
[10] G. Liang, L. Wang, X. Ou, X. Zhao, S. Xu, Lithium iron phosphate with high-rate capability synthesized through hydrothermal reaction in glucose solution, J. Power Sources 184 (2008) 538–542.
[11] Y. Liu, J. Gu, J. Zhang, J. Wang, N. Nie, Y. Fu, W. Li, F. Yu, Controllable synthesis of nano-sized LiFePO4/C via a high shear mixer facilitated hydrothermal method for high rate Li-ion batteries, Electrochim. Acta 173 (2015) 448–457.
[12] K.S. Suslick, G.J. Price, Applications of ultrasound to materials chemistry, Annu. Rev. Mater. Sci. 29 (1999) 295–326.
[13] H. Xu, B.W. Zeiger, K.S. Suslick, Sonochemical synthesis of nanomaterials, Chem. Soc. Rev. 42 (2013) 2555–2567.
[14] W.B. McNamara, Y.T. Didenko, K.S. Suslick, Sonoluminescence temperatures during multi-bubble cavitation, Nature 401 (1999) 772–775.
[15] E. Moradiyan, R. Halladj, S. Askari, P.M. Bijani, Ultrasonic-assisted hydrothermal synthesis and catalytic behavior of a novel SAPO-34/Clinoptilolite nanocomposite catalyst for high propylene demand in MTO process, J. Phys. Chem. Solids 107 (2017) 83–92.
[16] S. Khan, M. Ali, A. Mansha Qurashi, Sonochemical assisted hydrothermal synthesis of pseudo-flower shaped Bismuth vanadate (BiVO4) and their solar-driven water splitting application, Ultrason. Sonochem. 36 (2017) 386–392.
[17] H.B. Li, G.C. Liu, S.Q. Chen, Q.C. Liu, Novel Fe doped mesoporous TiO2 microspheres: ultrasonic-hydrothermal synthesis, characterization, and photocatalytic properties, Physica E 42 (2010) 1844–1849.
[18] C.I. Ezeh, M. Tomatis, X.G. Yang, J. He, C.G. Sun, Ultrasonic and hydrothermal mediated synthesis routes for functionalized Mg-Al LDH: comparison study on surface morphology, basic site strength, cyclic sorption efficiency and effectiveness, Ultrason. Sonochem. 40 (2018) 341–343.
[19] S. Su, H. Ma, X. Chuan, Hydrothermal synthesis of zeolite A from K-feldspar and its crystallization mechanism, Adv. Powder Technol. 27 (2016) 139–144.
[20] N. Jusoh, Y.F. Yeong, M. Mohamad, K.K. Lau, A.M. Shariff, Rapid-synthesis of zeolite T via sonochemical-assisted hydrothermal growth method, Ultrason. Sonochem. 34 (2017) 273–280.
[21] Y. Mu, Y. Zhang, J. Fan, C. Guo, Effect of ultrasound pretreatment on the hydrothermal synthesis of SSZ-13 zeolite, Ultrason. Sonochem. 38 (2017) 430–436.
[22] S. Askari, R. Halladj, Ultrasonic pretreatment for hydrothermal synthesis of SAPO-34 nanocrystals, Ultrason. Sonochem. 19 (2012) 554–559.
[23] P. Roy, N. Das, Ultrasonic assisted synthesis of Bikitaite zeolite: a potential material for hydrogen storage application, Ultrason. Sonochem. 36 (2017) 466–473.
[24] F.N. Azad, M. Ghaedi, K. Dashtian, S. Hajati, V. Pezeshkpour, Ultrasonically assisted hydrothermal synthesis of activated carbon-HKUST-1-MOF hybrid for efficient simultaneous ultrasound-assisted removal of ternary organic dyes and antibacterial investigation: Taguchi optimization, Ultrason. Sonochem. 31 (2016) 383–393.
[25] T. Andreussi, C. Galletti, R. Mauri, Simone Camarri, M.V. Salvetti, Flow regimes in T-shaped micro-mixers, Comput. Chem. Eng. 76 (2015) 150–159.
[26] K. Krupa, M.I. Nunes, R.J. Santos, J.R. Bourne, Characterization of micromixing in T-jet mixers, Chem. Eng. Sci. 111 (2014) 48–55.
[27] Y. Huang, P. Wang, Y. Yuan, F. Yang, Synergistic degradation of chitosan by impinging stream and jet cavitation, Ultrason. Sonochem. 27 (2015) 592–601.
[28] S.W. Siddiqui, P.J. Unwin, Z. Xu, S.M. Kresta, The effect of stabilizer addition and sonication on nanoparticle agglomeration in a confined impinging jet reactor, Colloid Surf. A 350 (2009) 38–50.
[29] M. Wang, Y. Yang, Y. Zhang, Synthesis of micro-nano hierarchical structured LiFePO(4)/C composite with both superior high-rate performance and high tap density, Nanoscale 3 (2011) 4434–4439.
[30] J.C. Vedrine, Partial oxidation reactions on phosphate-based catalysts, Top. Catal. 11 (12) (2000) 147–152.
[31] J.M.M. Millet, J.C. Vedrine, Importance of site isolation in the oxidation of isobutyric acid to methacrylic, Top. Catal. 15 (2001) 139–144.
[32] R. Chen, Y. Wu, X.Y. Kong, Monodisperse porous LiFePO4/C microspheres derived by microwave-assisted hydrothermal process combined with carbothermal reduction for high power lithium-ion batteries, J. Power Sources 258 (2014) 246–252.
[33] P. Riesz, D. Berdahl, C.L. Christman, Free radical generation by ultrasound in aqueous and nonaqueous solutions, Environ. Health Persp. 64 (1985) 233–252.
[34] K.S. Suslick, Sonochemistry, Science 247 (1990) 1439–1445.
[35] H.Q. Wang, X.H. Zhang, F.H. Zheng, Y.G. Huang, Q.Y. Li, Surfactant effect on synthesis of core-shell LiFePO4/C cathode materials for lithium-ion batteries, J. Solid State Electr. 19 (2014) 187–194.
[36] L.L. Zhang, H.J. Li, K.Z. Li, Q.G. Fu, Y.L. Zhang, S.J. Liu, Synthesis and characterization of nanobelt-shaped Na, F and carbonate multi-substituted hydroxyapatite, Mater. Lett. 138 (2015) 48–51.
[37] J. Shen, B. Jin, Q. Jiang, Y. Hu, X. Wang, Morphology-controlled synthesis of fluorapatite nano/microstructures via surfactant-assisted hydrothermal process, Mater. Des. 97 (2016) 204–212.
[38] W. Amer, K. Abdelouahdi, H.R. Ramananarivo, M. Zahouily, A. Fihri, K. Djessas, K. Zahouily, R.S. Varma, A. Solhy, Microwave-assisted synthesis of mesoporous nano-hydroxyapatite using surfactant templates, CrystEngComm 16 (2014) 543–549.
[39] E. Garcia-Romero, M. Suarez, FTIR spectroscopic study of palygorskite: influence of the composition of the octahedral sheet, Appl. Clay Sci. 31 (2006) 154–163.
[40] X. Qin, X.H. Wang, H.M. Xiang, J. Xie, J.J. Li, Y.C. Zhou, Mechanism for hydrothermal synthesis of LiFePO4 platelets as cathode material for lithium-ion batteries, J. Phys. Chem. C 114 (2010) 16806–16812.
[41] S.G. Wu, M.Y. Chen, S. Rohani, D.J. Zhang, S.C. Du, S.J. Xu, W.B. Dong, J.B. Gong, Solvent-mediated nonoriented self-aggregation transformation: a case study of gabapentin, Cryst. Growth Des. 17 (2017) 4207–4216.
[42] T.J. Mason, Ultrasound in synthetic organic chemistry, Chem. Soc. Rev. 26 (1997) 443–451.
[43] R. Beck, J.P. Andreassen, Spherulitic growth of calcium carbonate, Cryst. Growth Des. 10 (2010) 2934–2947.
[44] J.P. Andreassen, E.M. Flaten, R. Beck, A.E. Lewis, Investigations of spherulitic growth in industrial crystallization, Chem. Eng. Res. Des. 88 (2010) 1163–1168.
[45] V.D. Nithya, B. Haritha, S. Surendran, D. Kalpana, R.K. Selvan, Effect of pH on the sonochemical synthesis of BiPO4 nanostructures and its electrochemical properties for pseudocapacitors, Ultrason. Sonochem. 22 (2015) 300–310.
[46] M. Sivakumar, T. Takami, H. Ikuta, A. Towata, K. Yasui, T. Tuziuti, T. Kozuka, D. Bhattacharya, Y. Iida, Fabrication of zinc ferrite nanocrystals by sonochemical emulsification and evaporation observation of magnetization and its relaxation at low temperature, J. Phys. Chem. B 110 (2006) 15234–15243.
[47] Andac, M. Tatlier, A. Sirkecioglu, I. Ece, A.E. Senatalar, Effects of ultrasound on zeolite A synthesis, Microporous Mesoporous Mater. 79 (2005) 225–233.
[48] J. Behin, H. Kazemian, S. Rohani, Sonochemical synthesis of zeolite NaP from clinoptilolite, Ultrason. Sonochem. 28 (2016) 400–408.
[49] B. Dong, X.N. Huang, X.G. Yang, G. Li, L. Xia, G.Z. Chen, Rapid preparation of high electrochemical performance LiFePO4/C composite cathode material with an ultrasonic-intensified micro-impinging jetting reactor, Ultrason. Sonochem. 39 (2017) 816–826.
[50] N.D. Burrows, C.R.H. Hale, R.L. Penn, Effect of pH on the kinetics of crystal growth by oriented aggregation, Cryst. Growth Des. 13 (2013) 3396–3403.
[51] P. Devasia, K.A. Natarajan, D.N. Sathyanarayana, G.R. Rao, Surface chemistry of Thiobacillus ferrooxidans relevant to adhesion on mineral surfaces, Appl. Environ. Microb. 59 (1993) 4051–4055.